frontiers | Research Topics

Innovative research on coronary artery hemodynamics, heart treatment and cardiovascular medicine

Edited by
Kelvin Kian Loong Wong, Dhanjoo Ghista, Ruizheng Shi and W. J. Zhang

Published in
Frontiers in Cardiovascular Medicine

ISSN 1664-8714
ISBN 978-2-8325-2650-7
DOI 10.3389/978-2-8325-2650-7

About Frontiers

Frontiers is more than just an open access publisher of scholarly articles: it is a pioneering approach to the world of academia, radically improving the way scholarly research is managed. The grand vision of Frontiers is a world where all people have an equal opportunity to seek, share and generate knowledge. Frontiers provides immediate and permanent online open access to all its publications, but this alone is not enough to realize our grand goals.

Frontiers journal series

The Frontiers journal series is a multi-tier and interdisciplinary set of open-access, online journals, promising a paradigm shift from the current review, selection and dissemination processes in academic publishing. All Frontiers journals are driven by researchers for researchers; therefore, they constitute a service to the scholarly community. At the same time, the *Frontiers journal series* operates on a revolutionary invention, the tiered publishing system, initially addressing specific communities of scholars, and gradually climbing up to broader public understanding, thus serving the interests of the lay society, too.

Dedication to quality

Each Frontiers article is a landmark of the highest quality, thanks to genuinely collaborative interactions between authors and review editors, who include some of the world's best academicians. Research must be certified by peers before entering a stream of knowledge that may eventually reach the public - and shape society; therefore, Frontiers only applies the most rigorous and unbiased reviews. Frontiers revolutionizes research publishing by freely delivering the most outstanding research, evaluated with no bias from both the academic and social point of view. By applying the most advanced information technologies, Frontiers is catapulting scholarly publishing into a new generation.

What are Frontiers Research Topics?

Frontiers Research Topics are very popular trademarks of the *Frontiers journals series*: they are collections of at least ten articles, all centered on a particular subject. With their unique mix of varied contributions from Original Research to Review Articles, Frontiers Research Topics unify the most influential researchers, the latest key findings and historical advances in a hot research area.

Find out more on how to host your own Frontiers Research Topic or contribute to one as an author by contacting the Frontiers editorial office: frontiersin.org/about/contact

Innovative research on coronary artery hemodynamics, heart treatment and cardiovascular medicine

Topic editors

Kelvin Kian Loong Wong — University of Saskatchewan, Canada
Dhanjoo Ghista — Other, United States
Ruizheng Shi — Central South University, China
W. J. Zhang — University of Saskatchewan, Canada

Topic Coordinator

Xuefei Deng — Anhui Medical University, China

Citation

Wong, K. K. L., Ghista, D., Shi, R., Zhang, W. J., eds. (2023). *Innovative research on coronary artery hemodynamics, heart treatment and cardiovascular medicine*. Lausanne: Frontiers Media SA. doi: 10.3389/978-2-8325-2650-7

Table of contents

frontiers | Frontiers in Cardiovascular Medicine

CASE REPORT
published: 16 June 2022
doi: 10.3389/fcvm.2022.904400

Case Report: Tachycardia, Hypoxemia and Shock in a Severely Burned Pediatric Patient

Jianshe Shi[1†], *Chuheng Huang*[1†], *Jialong Zheng*[1], *Yeqing Ai*[1], *Hiufang Liu*[1], *Zhiqiang Pan*[1], *Jiahai Chen*[1], *Runze Shang*[2], *Xinya Zhang*[3], *Shaoliang Dong*[3], *Rongkai Lin*[2], *Shurun Huang*[4], *Jianlong Huang*[5*] and *Chenghua Zhang*[2*]

[1] Department of Surgical Intensive Care Unit, Huaqiao University Affiliated Strait Hospital, Quanzhou, China, [2] Department of General Surgery, Huaqiao University Affiliated Strait Hospital, Quanzhou, China, [3] School of Medicine, Huaqiao University, Quanzhou, China, [4] Department of Burn, Huaqiao University Affiliated Strait Hospital, Quanzhou, China, [5] Key Laboratory of Intelligent Computing and Information Processing, Quanzhou Normal University, Quanzhou, China

OPEN ACCESS

Edited by:
Ruizheng Shi,
Central South University, China

Reviewed by:
Zhonghua Shi,
Academic Medical Center, Netherlands
Junping Tian,
Capital Medical University, China

***Correspondence:**
Jianlong Huang
robotics@qztc.edu.cn
Chenghua Zhang
zch180@263.net

[†]These authors have contributed equally to this work

Specialty section:
This article was submitted to General Cardiovascular Medicine, a section of the journal Frontiers in Cardiovascular Medicine

Received: 25 March 2022
Accepted: 19 May 2022
Published: 16 June 2022

Citation:
Shi J, Huang C, Zheng J, Ai Y, Liu H, Pan Z, Chen J, Shang R, Zhang X, Dong S, Lin R, Huang S, Huang J and Zhang C (2022) Case Report: Tachycardia, Hypoxemia and Shock in a Severely Burned Pediatric Patient. Front. Cardiovasc. Med. 9:904400. doi: 10.3389/fcvm.2022.904400

Background: Severely burned children are at high risk of secondary intraabdominal hypertension and abdominal compartment syndrome (ACS). ACS is a life-threatening condition with high mortality and requires an effective, minimally invasive treatment to improve the prognosis when the condition is refractory to conventional therapy.

Case presentation: A 4.5-year-old girl was admitted to our hospital 30 h after a severe burn injury. Her symptoms of burn shock were relieved after fluid resuscitation. However, her bloating was aggravated, and ACS developed on Day 5, manifesting as tachycardia, hypoxemia, shock, and oliguria. Invasive mechanical ventilation, vasopressors, and percutaneous catheter drainage were applied in addition to medical treatments (such as gastrointestinal decompression, diuresis, sedation, and neuromuscular blockade). These treatments did not improve the patient's condition until she received continuous renal replacement therapy. Subsequently, her vital signs and laboratory data improved, which were accompanied by decreased intra-abdominal pressure, and she was discharged after nutrition support, antibiotic therapy, and skin grafting.

Conclusion: ACS can occur in severely burned children, leading to rapid deterioration of cardiopulmonary function. Patients who fail to respond to conventional medical management should be considered for continuous renal replacement therapy.

Keywords: tachycardia, hypoxemia, shock, abdominal compartment syndrome, pediatric, severe burns, continuous renal replacement therapy

CASE PRESENTATION

A 4.5-year-old girl was transferred to the emergency department of our tertiary care center, with burns covering 40% of her body surface area from boiling water. She received no intravenous fluid administration within 30 h post-scalding and complained of tachycardia, dizziness, weakness, and oliguria. Her physical examination at admission showed that her blood pressure was 98/73 mmHg, her body temperature was 37.3°C, her pulse rate was 164 beats per minute, and her respiration rate

was 25 breaths per minute. The pulse oxygen oximeter read 95% on room air. The patient presented with clammy extremities and an increased capillary refill time. While receiving appropriate first aid and wound assessment, she was resuscitated immediately using lactated ringer's injection based on a potential diagnosis of burn shock from her focused history taking, signs, and symptoms. Then, the patient was quickly and gently transferred to the burn center of our hospital for further treatment.

Laboratory investigations revealed a serum creatinine level of 97.3 μmol/L and an arterial blood serum lactate level of 5.2 mmol/L. These data indicated acute kidney injury induced by hypovolemic shock and confirmed the fluid resuscitation requirement. After resuscitation to correct dangerous deficits in accordance with the Parkland Formula, the patient's vital signs, mental status, capillary refill time, and serum creatinine level improved, and reached a target of 0.5–1.0 ml/kg/h^{-1} of urine output, indicating adequate fluid resuscitation. Then, the fluid rates were adjusted accordingly based on the monitoring results. The patient's condition improved as expected within the first 2 days. When the patient showed signs of bloating on the 3rd day, a nasogastric tube was inserted, and gastrointestinal prokinetic agents were administered to prevent abdominal over distension. During the aggravation of bloating on the 4th day, the volume of fluid administration was increased in accordance with the trend of decreased urine output. The daily fluid balances are summarized in **Figure 1**. On the 5th day of hospitalization, she developed hypoxemia, tachypnoea, hypotension, and oliguria. Blood pressure was 75/53 mmHg, body temperature was 37.2°C, pulse rate was 155 beats per minute, and respiration rate was 45 breaths per minute. The PaO_2/FiO_2 ratio was 126 mmHg, with 10 L/min oxygen flow delivered by nasal cannula. Her intra-abdominal pressure (IAP) increased to and remained above 15 mmHg as measured from the intrabladder pressure. The central venous pressure increased to a level above 14 cmH_2O, the extravascular lung water index increased to >10 ml/kg, and the B-type natriuretic peptide level was >35,000 pg/ml. The urine output was <0.3 ml/kg·h^{-1}, with serum creatinine at 81 μmol/L. The patient was unresponsive to furosemide. These findings indicated the development of secondary abdominal compartment syndrome (ACS), coupled with refractory fluid overload. The patient was intubated and mechanically ventilated immediately, and norepinephrine (1.6 μg/kg·min^{-1}) was administered to maintain mean arterial pressure above 70 mmHg. A neuromuscular blocking agent (cisatracurium besylate) was administered upon sedation and analgesia to improve thoracic and abdominal wall compliance. To manage the increased IAP, a percutaneous catheter was inserted into the abdominal cavity for drainage with ultrasound guidance, and 1,100 ml of fluid was drained within 28 h. The IAP decreased to 11 mmHg, but the clinical condition did not improve. Then, continuous renal replacement therapy (CRRT) was performed with an ultrafiltration flow rate of 20–25 ml/kg·h^{-1}. After 40 h of hemofiltration, 5,080 ml of fluid was removed in total. IAP declined to 7 mmHg immediately and then dropped to 5 mmHg. The patient's vital signs subsequently stabilized, the B-type natriuretic peptide level decreased to 5,204 pg/ml, and urine output increased to 1.3 ml/kg·h^{-1}. CRRT was terminated on Day 7, and mechanical ventilation was weaned on Day 8. The trends of the laboratory tests and vital parameters are presented in **Figure 2**. After recovering from ACS, the patient continued to improve under routine enteral nutrition support and antibiotic therapy. No significant infections were observed. Skin grafting was performed on Day 17. The patient fully recovered and was discharged from the hospital 34 days after her admission.

DISCUSSION

ACS in children is defined as a sustained elevated IAP (>10 mmHg) associated with new-onset or worsening organ dysfunction (1). Secondary ACS occurs in the absence of injury or disease in the abdominal or pelvic area. A study showed that 10–30% of patients with a burn injury, covering more than 20% of the total body surface, develop secondary ACS, and the mortality ranges from 40 to 100% (2–6).

The pathophysiology of secondary ACS is identical to that of primary ACS. As the IAP increases, cardiac output is reduced as a result of decreased central venous return and a consequently diminished right ventricular end-diastolic volume. Initially, high IAP increases systemic vascular resistance, and a "normal" blood pressure may be observed. Paradoxically, intracardiac filling pressures, such as pulmonary artery occlusion pressure and central venous pressure, typically increase with a rising IAP despite the reduced venous return and cardiac output. Then, the increased after load will undermine the contractibility of the cardiac muscle, tampering with the cardiac output. In clinical settings, this will manifest as tachycardia and shock. Beyond the heart, ACS also affects the lungs, kidneys, and other organs. During ACS, the diaphragm shifts cranially, leading to lower respiratory compliance, which increases the effort needed for breathing and the mismatch of perfusion and ventilation. Patients will present with elevated peak pressures, a decreased P/F ratio, hypoxemia, hypercarbia, and atelectasis. IAH may significantly compress the kidney and diminish renal perfusion. Studies have shown that acute renal dysfunction may develop even at relatively low levels of IAP. Renal dysfunction presents as oliguria, progressing to anuria due to a reduced glomerular filtration rate. In addition, ACS also leads to mesenteric, gastrointestinal, and neurological complications secondary to decreased cardiac output and direct compression from IAH (7–10). The pathophysiology of ACS is illustrated in **Figure 3**.

The mechanism of secondary ACS can be related to visceral, peritoneal, and retroperitoneal edema induced by inflammation or fluid resuscitation (11), which are commonly reported in burned children (12). Burn injury is characterized by a hypermetabolic response with physiological, catabolic, and immune effects. Burn areas larger than 15% of the total body surface will lead to a systemic inflammatory response, resulting in disruption of the endothelial glycocalyx, as well as alterations in the structure and function of the extracellular matrix (13–15). This will increase vascular permeability and promote the leakage of plasma fluid to the extracellular space and the interstitial compartment (16). Delayed or insufficient

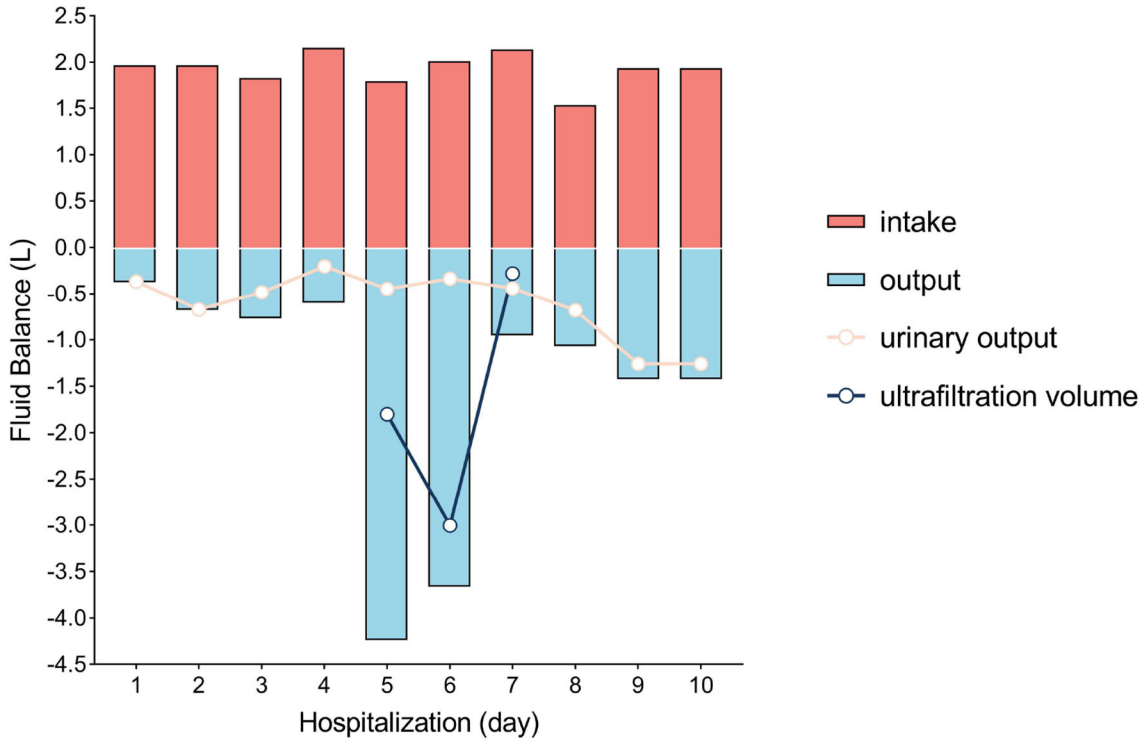

FIGURE 1 | Fluid balance in the first 10 days of hospitalization. Day 1 was defined as the time between hospital admission and the next morning (14 h).

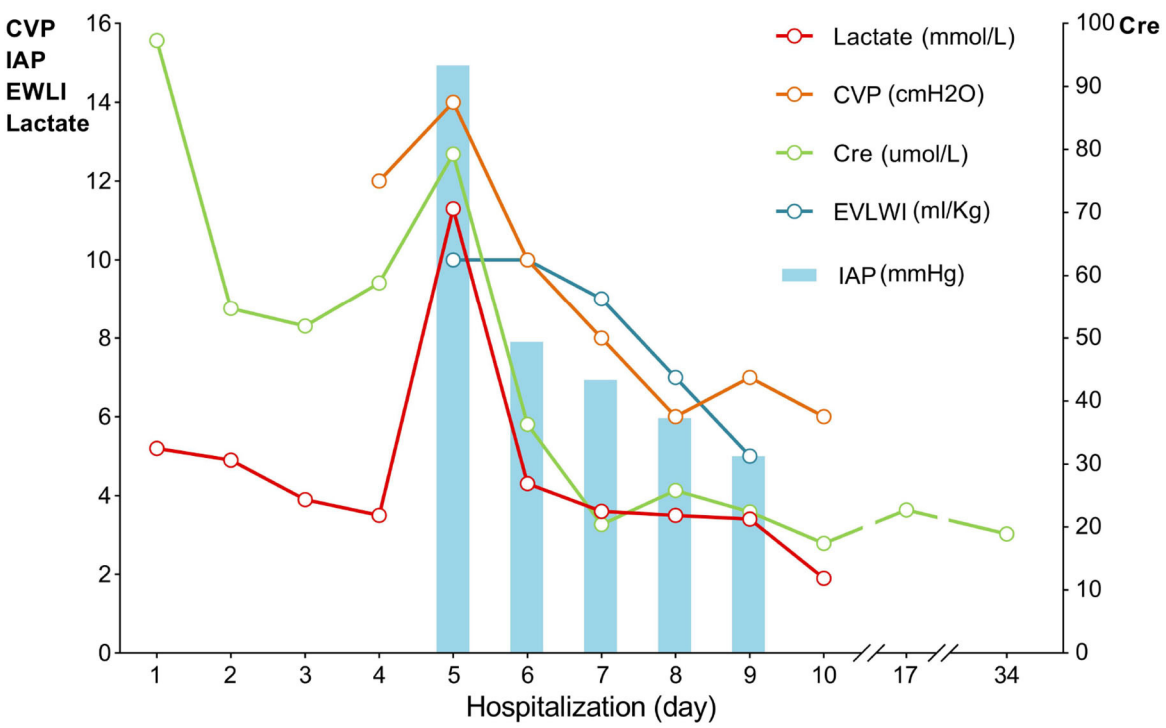

FIGURE 2 | Trends of vital parameters during hospitalization. CVP, central venous pressure; IAP, intra-abdominal pressure; EVLWI, extravascular lung water index; Lac, lactate, Cre, serum creatinine.

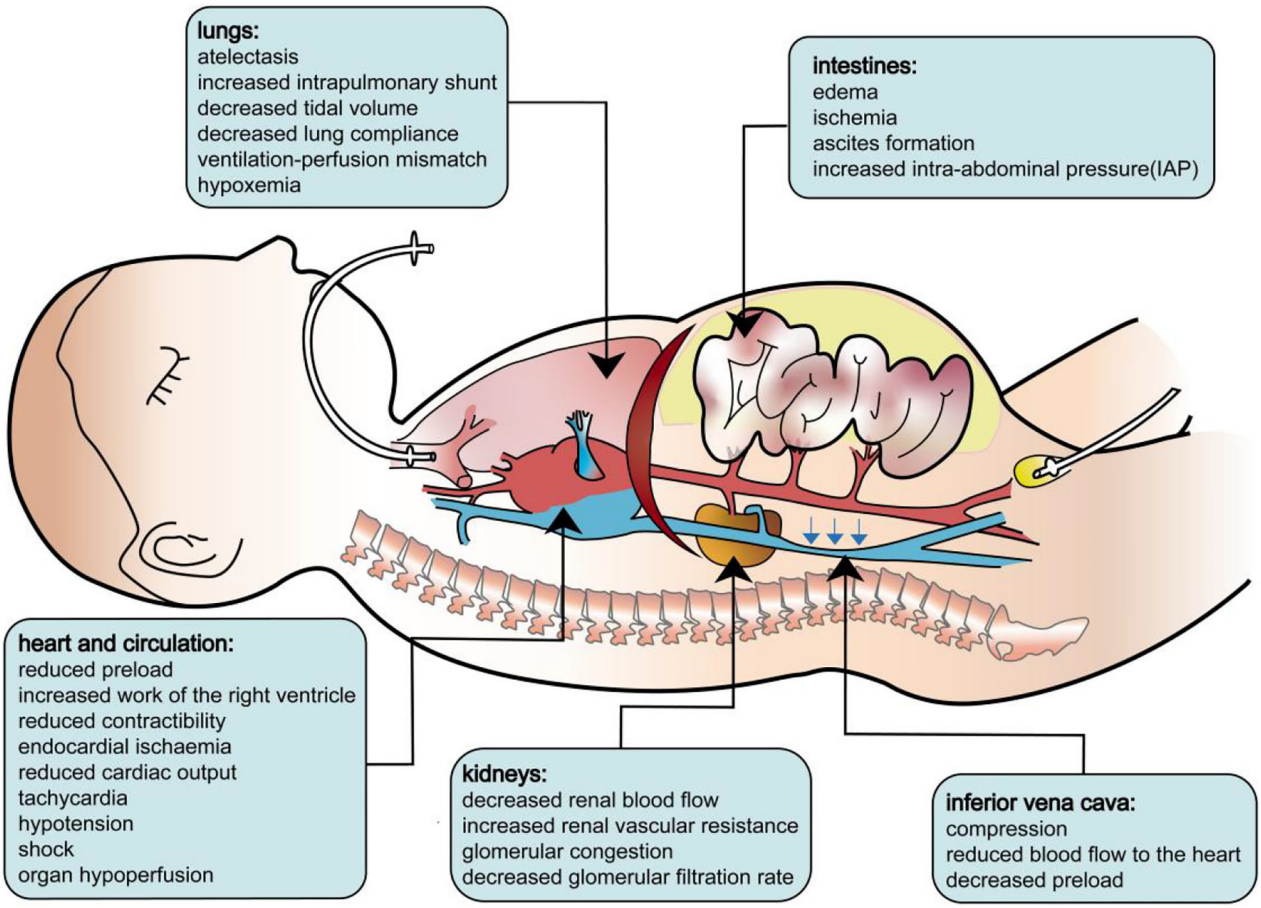

FIGURE 3 | Pathophysiology of abdominal compartment syndrome.

fluid resuscitation may lead to burn shock, poor tissue perfusion, multiple organ dysfunction, and death (17); moreover, fluid overload also results in edema associated with organ dysfunction (as depicted in **Figure 4**). However, commonly applied fluid resuscitation strategies may be complicated by swelling of the viscera due to inflammation and resuscitation *per se*. Excessive fluid resuscitation, typically using too much crystalloid, may lead to ACS and pulmonary edema (18). This is known as the concept of "fluid creep," (19) which is reported in 30–90% of severely burned patients (20). Therefore, aggressive fluid resuscitation must be balanced against the possibility of "fluid creep"-induced secondary ACS. The life-threatening ACS in this patient could have resulted from delayed fluid resuscitation, severe burns, and fluid overload.

ACS in burn patients usually develops with three particular events: ∼4 days post-injury, following a surgical procedure, and during a period of sepsis. In our case, the child developed ACS 5 days following the burn injury. It is important to know that a reduced urine output or a raised serum lactate may not be because of hypovolemia, IAH could also be a potential cause. Early detection of IAH allows physicians to intervene before the development of ACS. A routine fluid responsiveness assessment [such as passive leg-raising technique (21) and measurement of the inferior vena cava diameters by ultrasound (22)] is helpful for detecting hypovolemia. However, this would become complex and challenging in the advent of ACS. In patients with persistent oliguria and negative fluid responsiveness, IAP should be measured, especially in the aforementioned three circumstances. Current methods of IAP measurement and their reliability have been comprehensively reviewed (1). In brief, bladder pressure (at the end of expiration) is recommended for patients who require ongoing monitoring. In addition, ultrasound may be a useful tool for identifying compression and evaluating bowel movement and abdominal and bowel contents, but its reliability and feasibility in the diagnosis of ACS require further investigation.

Once the diagnosis of ACS is established, medical management should focus on three key areas: management of intraluminal contents, management of the abdominal wall, and management of systemic fluid balance. A comprehensive review of these medical management strategies has been published previously (1). When medical management fails, further advanced management should be considered (1, 23). In general, emergency decompressive surgery is considered but has high morbidity and mortality (24). Some evidence has shown the effectiveness of percutaneous drainage in burned patients with ACS, and this procedure is supported by the

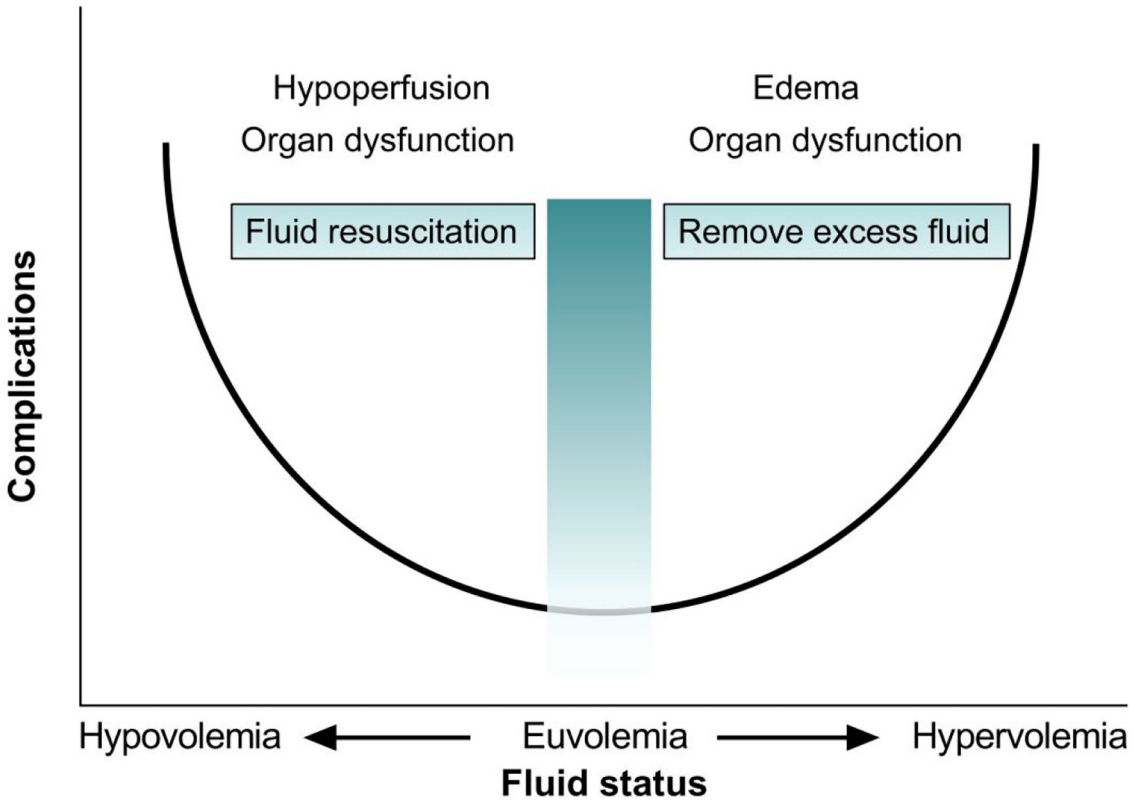

FIGURE 4 | Relation between fluid volume status and complications.

World Society of Abdominal Compartment Syndrome (1). In our case, ultrasound-guided percutaneous catheter drainage was successfully performed, with a significant decrease in IAP from 15 to 11 mmHg. However, the clinical condition of the patient did not improve.

CRRT is commonly used for critically ill patients with acute renal failure, fluid overload, and sepsis. In adult burned patients, the effectiveness of CRRT has been reported in reversing septic shock and improving acute renal failure (25). However, its effect on pediatric burned patients is unknown. To the best of our knowledge, this is the first case of the use of CRRT in a pediatric burned patient with ACS. In our case, the patient was prescribed a dose of 20–25 ml/kg·h^{-1} ultrafiltration for 40 h. The excessive fluid was successfully removed, accompanied by a decrease in B-type natriuretic peptide levels, and ACS was reversed. Our case showed that, in pediatric burned patients, CRRT can be beneficial by effectively removing inflammatory mediators, excessive fluid, and accumulated metabolic products while minimizing the effect on hemodynamics. Compared to decompressive laparotomy, CRRT provides a less invasive and promising measure for secondary ACS in severely burned children.

CONCLUSION

In severely burned children, secondary ACS can develop after a few days of fluid resuscitation, which requires routine IAP monitoring in these patients. In patients with refractory ACS, CRRT could be considered when other medical treatments fail. This report highlights the role of the interprofessional team in managing severely burned patients.

DATA AVAILABILITY STATEMENT

The original contributions presented in the study are included in the article/**Supplementary Material**, further inquiries can be directed to the corresponding authors.

ETHICS STATEMENT

The studies involving human participants were reviewed and approved by the Medical Ethics Research Committee of Huaqiao University Affiliated Strait Hospital. Written informed consent to participate in this study was provided by the participants' legal guardian/next of kin. Written informed consent was obtained from the minor(s)' legal guardian/next of kin for the publication of any potentially identifiable images or data included in this article.

AUTHOR CONTRIBUTIONS

SD and CH designed the research. JS, RL, and SH performed the research. JZ, ZP, RS, JC, and YA collected clinical data. JS,

XZ, and HL analyzed the data. JS was responsible for patient treatment and drafted the manuscript. CZ and JH reviewed and revised the manuscript. All authors read and approved the final manuscript.

FUNDING

This research was supported by Science and Technology Program of Quanzhou (Grant Nos. 2021CT0010, 2019C080R, and 2021N003S).

ACKNOWLEDGMENTS

We would like to thank all of the doctors, nurses, technicians, and the patient involved at the participating center for their dedication to the study.

SUPPLEMENTARY MATERIAL

The Supplementary Material for this article can be found online at: https://www.frontiersin.org/articles/10.3389/fcvm.2022.904400/full#supplementary-material

REFERENCES

1. Kirkpatrick AW, Roberts DJ, De Waele J, Jaeschke R, Malbrain ML, De Keulenaer B, et al. Intra-abdominal hypertension and the abdominal compartment syndrome: updated consensus definitions and clinical practice guidelines from the world society of the abdominal compartment syndrome. *Intensive Care Med.* (2013) 39:1190–206. doi: 10.1007/s00134-013-2906-z
2. Wise R, Jacobs J, Pilate S, Jacobs A, Peeters Y, Vandervelden S, et al. Incidence and prognosis of intra-abdominal hypertension and abdominal compartment syndrome in severely burned patients: pilot study and review of the literature. *Anaesthesiol Intensive Ther.* (2016) 48:95–109. doi: 10.5603/AIT.a2015.0083
3. Strang SG, Van Lieshout EM, Breederveld RS, Van Waes OJ. A systematic review on intra-abdominal pressure in severely burned patients. *Burns.* (2014) 40:9–16. doi: 10.1016/j.burns.2013.07.001
4. Ramirez JI, Sen S, Palmieri TL, Greenhalgh DG. Timing of laparotomy and closure in burn patients with abdominal compartment syndrome: effects on survival. *J Am Coll Surg.* (2018) 226:1175–80. doi: 10.1016/j.jamcollsurg.2018.03.032
5. Steinau G, Kaussen T, Bolten B, Schachtrupp A, Neumann UP, Conze J, et al. Abdominal compartment syndrome in childhood: diagnosis, therapy and survival rate. *Pediatr Surg Int.* (2011) 27:399–405. doi: 10.1007/s00383-010-2808-x
6. Ejike JC, Mathur M, Moores DC. Abdominal compartment syndrome: focus on the children. *Am Surg.* (2011) 77 (Suppl. 1):S72–7.
7. Mohmand H, Goldfarb S. Renal dysfunction associated with intra-abdominal hypertension and the abdominal compartment syndrome. *J Am Soc Nephrol.* (2011) 22:615–21. doi: 10.1681/ASN.2010121222
8. De Waele JJ, De Laet I, Malbrain ML. Understanding abdominal compartment syndrome. *Intensive Care Med.* (2016) 42:1068–70. doi: 10.1007/s00134-015-4089-2
9. De Waele JJ, De Laet I, Kirkpatrick AW, Hoste E. Intra-abdominal hypertension and abdominal compartment syndrome. *Am J Kidney Dis.* (2011) 57:159–69. doi: 10.1053/j.ajkd.2010.08.034
10. Dalfino L, Tullo L, Donadio I, Malcangi V, Brienza N. Intra-abdominal hypertension and acute renal failure in critically ill patients. *Intensive Care Med.* (2008) 34:707–13. doi: 10.1007/s00134-007-0969-4
11. Ball CG, Kirkpatrick AW, McBeth P. The secondary abdominal compartment syndrome: not just another post-traumatic complication. *Can J Surg.* (2008) 51:399–405.
12. Greenhalgh DG, Warden GD. The importance of intra-abdominal pressure measurements in burned children. *J Trauma.* (1994) 36:685–90. doi: 10.1097/00005373-199405000-00015
13. Fernández-Sarmiento J, Salazar-Peláez LM, Carcillo JA. The endothelial glycocalyx: a fundamental determinant of vascular permeability in sepsis. *Pediatr Crit Care Med.* (2020) 21:e291–300. doi: 10.1097/PCC.0000000000002266
14. Joffre J, Hellman J, Ince C, Ait-Oufella H. Endothelial responses in sepsis. *Am J Respir Crit Care Med.* (2020) 202:361–70. doi: 10.1164/rccm.201910-1911TR
15. Prowle JR, Kirwan CJ, Bellomo R. Fluid management for the prevention and attenuation of acute kidney injury. *Nat Rev Nephrol.* (2014) 10:37–47. doi: 10.1038/nrneph.2013.232
16. Williams FN, Herndon DN, Jeschke MG. The hypermetabolic response to burn injury and interventions to modify this response. *Clin Plast Surg.* (2009) 36:583–96. doi: 10.1016/j.cps.2009.05.001
17. Schulman CI, King DR. Pediatric fluid resuscitation after thermal injury. *J Craniofac Surg.* (2008) 19:910–2. doi: 10.1097/SCS.0b013e318175b566
18. Zak AL, Harrington DT, Barillo DJ, Lawlor DF, Shirani KZ, Goodwin CW. Acute respiratory failure that complicates the resuscitation of pediatric patients with scald injuries. *J Burn Care Rehabil.* (1999) 20:391–9. doi: 10.1097/00004630-199909000-00011
19. Saffle JI. The phenomenon of "fluid creep" in acute burn resuscitation. *J Burn Care Res.* (2007) 28:382–95. doi: 10.1097/BCR.0B013E318053D3A1
20. Saffle JR. Fluid creep and over-resuscitation. *Crit Care Clin.* (2016) 32:587–98. doi: 10.1016/j.ccc.2016.06.007
21. Monnet X, Marik P, Teboul JL. Passive leg raising for predicting fluid responsiveness: a systematic review and meta-analysis. *Intensive Care Med.* (2016) 42:1935–47. doi: 10.1007/s00134-015-4134-1
22. Orso D, Paoli I, Piani T, Cilenti FL, Cristiani L, Guglielmo N. Accuracy of ultrasonographic measurements of inferior vena cava to determine fluid responsiveness: a systematic review and meta-analysis. *J Intensive Care Med.* (2020) 35:354–63. doi: 10.1177/0885066617752308
23. De Laet IE, Malbrain MLNG, De Waele JJ. A clinician's guide to management of intra-abdominal hypertension and abdominal compartment syndrome in critically ill patients. *Crit Care.* (2020) 24:97. doi: 10.1186/s13054-020-2782-1
24. di Natale A, Moehrlen U, Neeser HR, Zweifel N, Meuli M, Mauracher AA, et al. Abdominal compartment syndrome and decompressive laparotomy in children: a 9-year single-center experience. *Pediatr Surg Int.* (2020) 36:513–21. doi: 10.1007/s00383-020-04632-0
25. Chung KK, Coates EC, Smith DJ Jr, Karlnoski RA, Hickerson WL, Arnold-Ross AL, et al. Randomized controlled evaluation of high-volume hemofiltration in adult burn patients with Septic shoCk and acUte kidnEy injury (RESCUE) investigators. High-volume hemofiltration in adult burn patients with septic shock and acute kidney injury: a multicenter randomized controlled trial. *Crit Care.* (2017) 21:289. doi: 10.1186/s13054-017-1878-8

Conflict of Interest: The authors declare that the research was conducted in the absence of any commercial or financial relationships that could be construed as a potential conflict of interest.

frontiers | Frontiers in Cardiovascular Medicine

ORIGINAL RESEARCH
published: 22 July 2022
doi: 10.3389/fcvm.2022.927671

Evaluation of Exercise Tolerance in Non-obstructive Hypertrophic Cardiomyopathy With Myocardial Work and Peak Strain Dispersion by Speckle-Tracking Echocardiography

Ye Su[1,2], Qionghui Peng[2], Lixue Yin[1,2] and Chunmei Li[1,2]**

[1] School of Medicine, University of Electronic Science and Technology of China, Chengdu, China, [2] Department of Cardiovascular Ultrasound, Sichuan Provincial People's Hospital, University of Electronic Science and Technology of China, Chinese Academy of Sciences Sichuan Translational Medicine Research Hospital, Chengdu, China

OPEN ACCESS

Edited by:
Ruizheng Shi,
Central South University, China

Reviewed by:
He Huang,
Sichuan University, China
Mingxing Xie,
Huazhong University of Science and Technology, China
Yu Kang,
Chengdu University of Traditional Chinese Medicine, China

***Correspondence:**
Lixue Yin
yinlixue_cardiac@163.com;
YSCSRMYY@163.com
Chunmei Li
licmxxg@163.com

Specialty section:
This article was submitted to Cardiovascular Imaging, a section of the journal Frontiers in Cardiovascular Medicine

Received: 24 April 2022
Accepted: 17 June 2022
Published: 22 July 2022

Citation:
Su Y, Peng Q, Yin L and Li C (2022) Evaluation of Exercise Tolerance in Non-obstructive Hypertrophic Cardiomyopathy With Myocardial Work and Peak Strain Dispersion by Speckle-Tracking Echocardiography. Front. Cardiovasc. Med. 9:927671. doi: 10.3389/fcvm.2022.927671

Background: The aim of this study was to evaluate exercise tolerance in non-obstructive hypertrophic cardiomyopathy (HCM) by investigating the value of myocardial work (MW) combined with strain peak dispersion.

Methods: A total of 65 patients with non-obstructive HCM and normal left ventricular ejection fraction were enrolled and 60 healthy subjects were selected as controls. The automated function imaging (AFI)-two-dimensional ultrasonic speckle-tracking technology was used to obtain the values for peak global longitudinal strain (GLS), longitudinal strain peak time dispersion (PSD), 18-segment systolic longitudinal peak strain (LPS), 18-segment longitudinal strain peak time (TTPLS), global waste work (GWW), global constructive work (GCW), global work index (GWI), global work efficiency (GWE), and exercise metabolic equivalents (METS).

Results: (1) Values for LV-GLS (−17.77 ± 0.20 vs. −21.66 ± 0.42%) were lower and PSD (95.10 ± 8.15 vs. 28.97 ± 1.50 ms) was prolonged in patients with HCM ($p < 0.01$). (2) An increasing trend was shown in the basal segment < intermediate segment < apical segment for both patients with HCM and controls, although each segment had lower values in the HCM group. (3) TTPLS was prolonged in the HCM group ($p < 0.01$). (4) GWE, GWI, and GCW were all lower ($p < 0.01$) and GWW was higher in patients with HCM ($p < 0.01$). (5) Values of GWE were less than 92.5%, GWI less than 1,200 mmHg, GCW less than 1,399 mmHg, these abnormal values are helpful for the diagnosis of impaired exercise tolerance and poor prognosis (6) The METS and LV-GLS of HCM in the asymmetric group were significantly lower than that in AHCM group, but the PSD was significantly greater than that in the AHCM group. Values of LPS-BL (−13.13% ± 2.51% vs −10.17% ± 2.20%) in the apical HCM group were better than in the asymmetric HCM group ($p < 0.05$).

Conclusion: GCW, GWI, and GWE can be safely measured by resting echocardiography to evaluate exercise tolerance in patients with HCM who cannot perform an exercise-based examination. Such measurements provide a basis for clinical decisions regarding exercise and drug prescription.

Keywords: myocardial work, peak strain dispersion, exercise tolerance, hypertrophic cardiomyopathy, global longitudinal strain (GLS)

INTRODUCTION

Many patients with non-obstructive hypertrophic cardiomyopathy (HCM) and preserved ejection fraction have no obvious symptoms at rest in the early stages, and most patients seek medical attention due to limitations on daily exercise or activities. HCM is one of the main causes of sudden death in young people following activity (1), and previous studies have estimated that its contribution to sudden cardiac death may be as high as 10.3% (2). Such statistics illustrate the urgent need for more sensitive and comprehensive techniques to detect abnormal cardiac function in patients with HCM. Subtle myocardial systolic and diastolic dysfunctions occur that are not always detectable using standard echocardiographic parameters such as left ventricular ejection fraction (LVEF). Previous studies have shown that LV global longitudinal strain (LV-GLS), measured using speckle-tracking echocardiography, is often impaired and constitutes an adverse outcome predictor in HCM patients with preserved LVEF. However, LV-GLS remains load-dependent limiting the assessment of LV function under certain hemodynamic conditions such as abnormal blood pressure. A novel speckle-tracking echocardiographic technique evaluates myocardial performance by constructing an LV pressure–strain loop (PSL) and integrating non-invasively measured arterial blood pressure and longitudinal strain. This approach allows the detection parameters of the same cardiac cycle to be measured, excludes the influence of heart rate (HR) inconsistency on the analysis, and quantitatively analyzes and evaluates myocardial function (3). The derived parameters from LVPSL can not only reflect the global and regional LV function but also reflect the synchronization and direction of LV contraction (4). Previous studies (5–7) have confirmed that non-invasively and invasively measured LVPSL have good consistency and correlation, the myocardial work (MW) assessed using non-invasive LVPSL is reduced and associated with LV fibrosis in patients with HCM. However, the relationship between MW and exercise tolerance in HCM is currently unknown. Therefore, the aims of this study were (1) to describe the global and segmental indices of MW in different HCM phenotypes and (2) to evaluate the relationship of MW with exercise tolerance.

Research Subjects

A total of 65 patients (45 males, 20 females, mean age: 47.54 ± 1.93 years) with non-obstructive HCM, including 34 patients with apical hypertrophy and 31 patients with asymmetric hypertrophy, diagnosed in Sichuan Provincial People's Hospital between January and December 2019, were consecutively enrolled. The inclusion criteria were as follows: presence of HCM diagnosed according to the 2017 Chinese Guidelines for the Diagnosis and Treatment of Hypertrophic Cardiomyopathy in Adults and the 2014 ESC Guidelines. The exclusion criteria were as follows: obstruction of the left or middle left ventricular outflow tract, hypertension, coronary heart disease, moderate or higher aortic stenosis, or other distinct diseases causing cardiac hypertrophy. A total of 60 age-matched healthy subjects who were followed up in Sichuan Provincial People's Hospital in 2019 were selected as controls. Clinical data and echocardiographic parameters of all participants were collated.

Instruments and Methods

A GE Vivid E95 color Doppler ultrasound diagnostic apparatus with 4V-D probe (frequency 1.5–4.0 MHz) (GE Medical Systems, Milwaukee, WI, United States) was used. All subjects had discontinued beta-blockers or calcium channel blockers for at least 24 h. 2 experienced sonographers Physicians performed echocardiography, by continuously acquire three-plane dynamic images of the apex for at least 4 cardiac cycles (image frame rate 60 frames/s), images were digitally stored and analyzed offline using EchoPAC (203) workstation, and performed the synchronous recording of electrocardiogram, measured resting systolic and diastolic blood pressure. All patients with HCM underwent symptom-limited treadmill exercise and electrocardiogram (ECG) using Bruce protocol immediately after resting standard transthoracic echocardiography. The study by Mendes et al. (8) included participants (112 healthy adults) with different levels of fitness, ages, and genders to increase the representation of the population and found that metabolic equivalents (METS) $\leq$6.8 had higher specificity and relatively higher accuracy. The authors also reported a maximal reduction in errors in activity intensity assessment, considered to be associated with reduced exercise tolerance and poor long-term prognosis. The study divided all subjects into group A (METS $\leq$6.8) and group B (METS $>$6.8) and also sorted them according to different hypertrophic segments apical HCM (AHCM), or asymmetric HCM for further statistical analysis (8).

SunTech Tango synchronized ambulatory blood pressure monitor (SunTech Medical Instruments, Morrisville, NC, United States) and Mortara X-Scribe tablet motion analysis system (Mortara Instrument, Milwaukee, WI, United States) were used to perform the symptom-limited treadmill exercise and an ECG and blood pressure during and after exercise. Before the examination, all subjects had discontinued beta-blockers or calcium channel blockers for at least 24 h. Resting systolic and diastolic blood pressure were measured, and a synchronous electrocardiogram recording was taken. All participants

signed informed consent after confirming that they had no contraindications to exercise testing. The BRUCE protocol was performed at the exercise stage. When subjects reached the target HR or one of the following symptoms occurred, the exercise stopped: (1) ST-segment elevation >1.0 mm in no pathological Q-wave lead (except V1 or aVR), (2) systolic blood pressure decreased >10 mmHg with other evidence of ischemia, (3) moderate to severe angina pectoris, (4) CNS symptoms, such as ataxia, dizziness, and syncope, (5) signs of hypoperfusion, such as cyanosis and pallor, (6) persistent ventricular tachycardia, and (7) technical difficulties in checking ECG or systolic blood pressure (9). ECG, exercise blood pressure, and METS were recorded. All subjects exercised to target heart rate (THR) if no symptoms restricted exercise. THR was calculated according to the following formula: THR = 220-age.

All parameter measurements and analyses were made in accordance with the American Society of Echocardiography (ASE) guidelines (10–12). Measurements were made along the short-axis views orthogonal to the circumference of the endocardium and epicardium, wherever maximal wall thickness occurs, ensuring that the cut was not oblique to the long axes of the LV. The criteria for the diagnosis of asymmetric HCM include the following: interventricular septum or anterolateral or inferior wall thickness ≥15 mm in one or more myocardial segments. The criteria for the diagnosis of AHCM include the following: apical wall thickness ≥15 mm in one or more myocardial segments or when the ratio between apical and basal wall thickness exceeds 1.3:1.

The following parameters were measured and calculated during offline data analysis: (1) conventional parameters: left ventricular end-diastolic volume (LVEDV), left ventricular end-systolic volume (LVESV), and LVEF were measured using the Simpson method. LV dimensions such as LV septal thickness (IVS), LV posterior wall thickness (LVPW), and left atrial (LA) diameter were measured from the parasternal long-axis view, and maximum LV wall thickness was assessed from three short-axis views from base to apex to identify the different phenotypes of left ventricular hypertrophy (LVH); (2) myocardial strain: 2D strain imaging was performed by using three consecutive cardiac cycles, and speckle-tracking analysis of the LV was performed in three apical (4, 2, and 3 chambered) views. The 17 regions of interest were automatically created and manually adjusted when necessary and then obtained the parameters including GLS, longitudinal strain peak time dispersion (PSD), 17-segment systolic longitudinal peak strain (LPS), 17-segment longitudinal strain peak time (TTPLS), the basal, mid, and apical segment longitudinal systolic peak strain (LPS-BL, LPS-ML, and LPS-AL), and longitudinal strain peak time [basal segment (BLST), middle segment (MLST), and apical segment (ALST)] and then calculated by averaging the peak longitudinal strain and time of corresponding segments. (3) MW: a non-invasive LVPSL was then constructed using the software (EchoPAC 203) and adjusted according to the duration of the ejection and isovolumetric phases, which were defined by the opening and closure of the mitral and aortic valves. During the LV ejection period, the total work within the area of the LVPSL during the LV ejection period represented the myocardial global work index (GWI), the MW performed during segmental shortening represented global constructive work (GCW), and the MW performed during segmental elongation represented global waste work (GWW) and calculated as the averages of each LV segment values according to the 17-segment model. Global cardiac efficiency (GCE) was an average of all segmental values expressed as GCW/(GCW + GWW) × 100%. (4) Exercise METS.

Statistical Methods

All statistical analyses were performed using the SPSS version 23.0 software (IBM SPSS Statistics, version 23). Continuous variables are expressed as means ± standard deviations. Comparisons between groups were made by two independent samples *t*-tests, and a value of $p < 0.05$ was considered to be statistically significant. Multivariate linear regression analysis was used to identify independent factors indicating exercise intolerance in patients with HCM. The sensitivity and specificity of variables for the prediction of exercise intolerance were identified by receiver operating characteristic (ROC) curves.

RESULTS

1. Among the 65 patients, 31 cases had mild mitral regurgitation, 11 had moderate mitral regurgitation, 2 had severe mitral regurgitation, 28 had mild tricuspid regurgitation, and 10 had moderate tricuspid regurgitation. All subjects with HCM included experienced non-obstructive HCM but 20 patients had increased outflow tract velocity.
2. Comparison of general information and conventional echocardiographic parameters (**Table 1**).

There was no significant difference in age, HR, blood pressure, and ESV between the two groups ($p > 0.05$). Although E/e, e, LA, and LAVI were statistically different in the control and HCM groups, these values had no correlation with METS ($p > 0.05$). Global work efficiency (GWE) (r = 0.278), GWI (r = 0.391),

TABLE 1 | Comparison of general information.

Variable	Normal group	HCM group	*P*
Age (year)	46.75 ± 1.76	47.54 ± 1.93	0.079
EDV (ml)	108.89 ± 4.31	77.61 ± 5.17	0*
ESV (ml)	26.02 ± 1.92	27.89 ± 1.90	0.376
EF (%)	73.33 ± 6.49	69.81 ± 5.99	0.014*
SBP (mmHg)	125.21 ± 9.79	142.05 ± 1.30	0.342
DBP (mmHg)	75.32 ± 1.30	75.85 ± 1.06	0.729
BSA (m^2)	1.78 ± 0.02	1.86 ± 0.03	0.027*
HR (bpm)	74.82 ± 1.84	69.72 ± 2.07	0.079
E/e	8.87 ± 1.81	19.06 ± 1.07	0*
e (m/s)	0.1 ± 0.001	0.05 ± 0.002	0*
LA (mm)	31.40 ± 2.77	38.37 ± 5.57	0*
LAVI (ml/m^2)	26.9 ± 3.96	39.6 ± 1.69	0*

*$P < 0.05$.

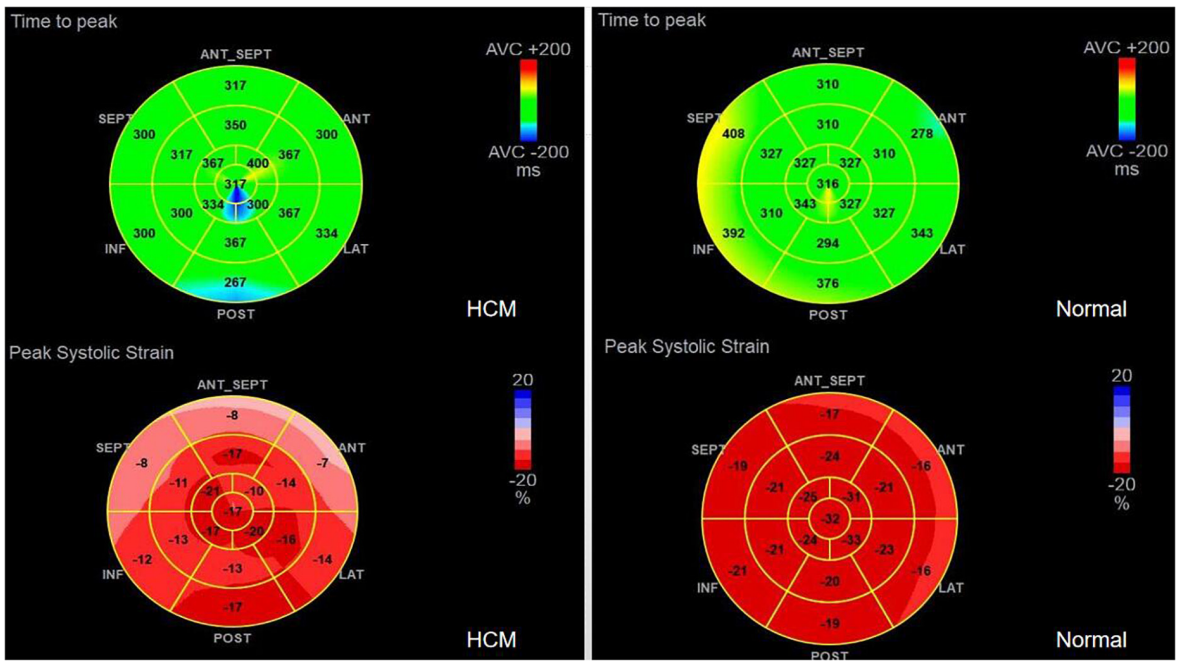

FIGURE 1 | PSD AND PSS in HCM and Normal group.

TABLE 2 | Comparison of myocardial work and strain between normal group and HCM group.

Variable	Normal group	HCM group	*P*
BLST (ms)	359.86 ± 6.74	396.32 ± 9.99	0.007*
MLST (ms)	344.28 ± 6.73	396.56 ± 13.87	0.002*
ALST (ms)	339.59 ± 6.90	401.74 ± 14.55	0.001*
PSD (ms)	28.97 ± 1.50	95.10 ± 8.15	0*
LV-GLS (%)	−21.66 ± 0.42	−17.77 ± 0.20	0.026*
LPS-BL (%)	−19.46 ± 0.21	−9.34 ± 1.03	0*
LPS-ML (%)	−20.86 ± 1.98	−11.52 ± 0.83	0*
LPS-AL (%)	−25.2 ± 0.73	−14.84 ± 1.37	0*
GWE (%)	97.7 ± 0.16	87.46 ± 6.10	0*
GWI (mmHg%)	2,014.5 ± 355.28	1,243.53 ± 424.52	0*
GCW (mmHg%)	2,309.03 ± 425.77	1,375.3 ± 436.67	0*
GWW (mmHg%)	39.93 ± 3.79	119.77 ± 13.19	0*

*$P < 0.05$.

and GCW (r = 0.372) had positive correlation with METS (all *P*-values < 0.05).

3 Comparison of strain and myocardial work

1. TTPLS: Compared with the normal group, the BLST (396.32 ± 99.9) ms, MLST (396.56 ± 13.87) ms, and ALST (401.74 ± 14.55) ms of the HCM group were significantly prolonged, and the PSD of the HCM group was significantly prolonged and higher than that of the normal group (95.10 ± 8.15 vs. 28.97 ± 1.50) ($p < 0.01$) (**Figure 1** and **Table 2**).
2. LV-GLS in the HCM group was significantly lower than that in the normal group (−17.77 ± 0.20% vs. −21.66 ± 0.42%) ($p < 0.05$) (**Figure 1** and **Table 2**).
3. LV-LPS: An increasing trend was shown in the basal segment (LPS-BL) < intermediate segment (LPS-ML) < apical segment (LPS-AL) for both patients with HCM and controls, although each segment had lower values in the HCM group. The LPS-BL, LPS-ML, and LPS-AL of the HCM group were significantly lower than the corresponding segments of the normal group (−9.34 ± 1.03% vs. −19.46 ± 0.21%), (−11.52 ± 0.83% vs. −20.86 ± 1.98%), and (−14.84 ± 1.37% vs. −25.2 ± 0.73%) ($p < 0.01$) (**Table 2**).
4. GWE (87.46 ± 6.10%), GWI (1,243.53 ± 424.52 mmHg%), and GCW (1,375.3 ± 436.67 mmHg%) in the HCM group were significantly lower than those in the control group ($p < 0.01$), and only GWW (119.77 ± 13.19 mmHg%) was significantly higher than that in the normal group ($p < 0.01$; **Figure 2** and **Table 2**).
5. In **Table 3**, a comparison of asymmetric HCM and AHCM found that the METS and LV-GLS of HCM in the asymmetric group were significantly lower than that in the AHCM group, but the PSD was significantly greater than that in the AHCM group. Values of LPS-BL (−13.13 ± 2.51% vs. −10.17 ± 2.20%) in the AHCM group were better than that in the asymmetric HCM group ($p < 0.05$). There were no significant differences between the asymmetric HCM and AHCM groups concerning values for LPS-ML, LPS-AL, GWE, GWI, GCW, and GWW.
6. The HCM group was divided into group A (METS ≤ 6.8) and group B (METS > 6.8) according to METS (8): the results showed that the resting state GWE is less than 92.5%, GWI is

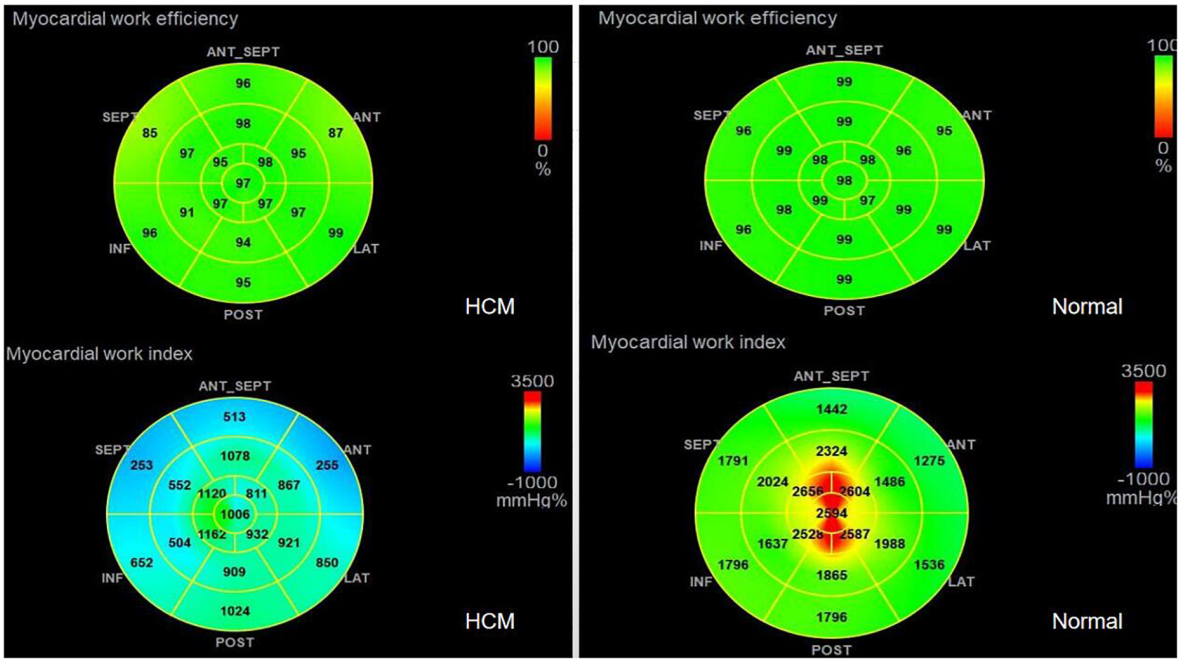

FIGURE 2 | Comparison of GWE and GWI in HCM and Normal group.

TABLE 3 | Comparison of myocardial work and strain between asymmetric and apical groups.

Variable	Asymmetric HCM (*N* = 34)	Apical HCM (*N* = 31)	*P*
METS	8.91 ± 0.43	10.17 ± 0.12	0.007*
SBP (mmHg)	128.37 ± 2.59	123.60 ± 3.12	0.204
DBP (mmHg)	76.07 ± 1.52	76.03 ± 1.94	0.988
GWE (%)	89.06 ± 1.05	88.13 ± 1.57	0.58
GWI (mmHg%)	1,395.3 ± 88.34	1,264.8 ± 84.43	0.227
GCW (mmHg%)	1,528.13 ± 93.72	1,427.97 ± 84.97	0.37
GWW (mmHg%)	119.53 ± 10.06	128.63 ± 16.95	0.642
LV-GLS (%)	−17.55 ± 0.27	−18.43 ± 0.13	0.007*
LPS-BL (%)	−10.17 ± 2.20	−13.13 ± 2.51	0.022*
LPS-ML (%)	−12.48 ± 3.21	−14.02 ± 3.90	0.320
LPS-AL (%)	−18.89 ± 2.76	−15.17 ± 3.65	0.355
PSD (ms)	115.93 ± 7.92	91.9 ± 8.34	0.033*
BLST (ms)	403.20 ± 27.61	397.54 ± 37.20	0.861
MLST (ms)	405 ± 22.46	390.66 ± 47.75	0.668
ALST (ms)	381.56 ± 44.85	384.81 ± 24.35	0.885

*$P < 0.05$.

less than 1,200 mmHg%, and GCW is less than 1,399 mmHg%, which were helpful for the diagnosis of impaired exercise tolerance (**Table 4** and **Figures 3**, **4**).

DISCUSSION

Hypertrophic cardiomyopathy is an autosomal dominant disorder with a high degree of heterogeneity in its clinical presentation. Exertional dyspnea, chest pain, fatigue, and presyncope or syncope are all common in patients with HCM. Possible mechanisms include increased myocardial oxygen consumption and demand after exercise, decreased myocardial blood supply, abnormal vasomotor responses, and vascular remodeling (13). Regardless of symptom status, the ACCF/AHA guidelines recommend lifestyle optimization at the time of HCM diagnosis. Low-intensity aerobic exercise is recommended to achieve and maintain cardiovascular fitness (14). Therefore, the assessment of exercise tolerance is particularly important for patients with HCM. The main findings of this study may be summarized as follows: (1) The left ventricular longitudinal contractility, systolic synchrony, and myocardial function were impaired in patients with HCM in whom the ejection fraction had been preserved in the resting state. (2) Patients with HCM showed decreased MW and work efficiency and increased GWW. (3) Myocardial contractility, systolic synchronization, and exercise tolerance were significantly lower in the patients with asymmetric HCM than in the AHCM group. (4) Values of GWW, GLS, GWI, PSD, GWE, and GCW have utility for the estimation of the intensity range of exercise tolerance.

The sinus node normally sends a discharge impulse down the ventricle through the bundle of His from the endocardium to the epicardium which travels from the apex to the bottom of the heart. Synchronous contraction of the myocardium completes the "pump function." The quantification of time synchronization of electromechanical conduction (*via* PSD measurement) on the basis of strain may be used to study myocardial contractile function. Haland et al. (15) and Candan et al. (16) showed that the reduction of LV-GLS and the prolongation of PSD in HCM may be helpful for the early identification of the condition requiring implantable cardioverter defibrillator (ICD) treatment. Such measurements are useful

TABLE 4 | Specificity and sensitivity analysis in HCM.

Variable	AUC	Cut-off value	Sensitivity	Specificity	Asymptotic significance b
GWE (%)	0.645	92.50%	0.898	0.375	0.043*
GWI (mmHg%)	0.784	1,200	0.6738	0.812	0.001*
GCW (mmHg%)	0.751	1,399	0.653	0.812	0.003*
LV-GLS	0.517	/	/	/	0.843

*$P < 0.05$.

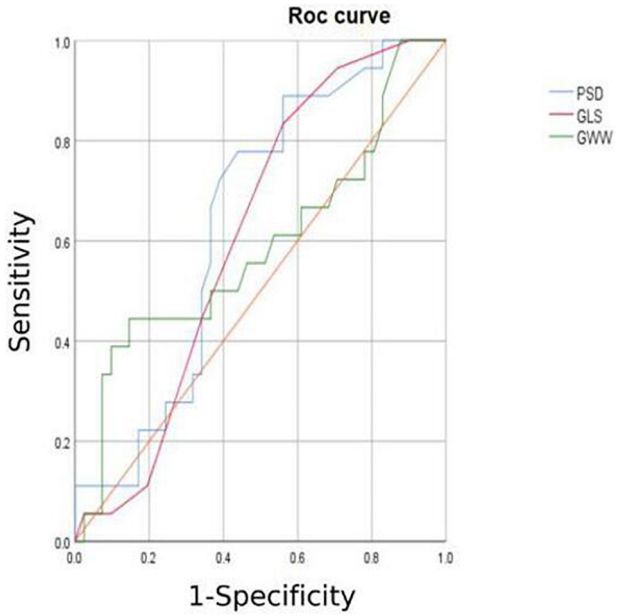

FIGURE 3 | ROC curve of GLS AND PSD.

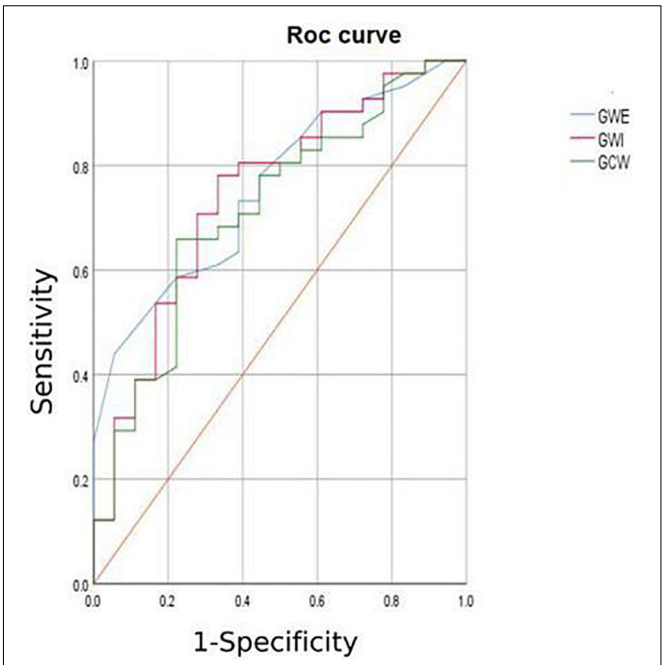

FIGURE 4 | ROC curve of myocardial work.

to guide clinicians and inform targeted early-stage treatment plans, thus improving patient outcomes. The cardiomyocytes in patients with HCM show a disordered hypertrophic arrangement with the appearance of fibrosis and increased cellular oxygen consumption and metabolic coronary intima damage results (17, 18). Cardiomyocyte hypertrophy is accompanied by fibrosis, effective cardiomyocytes per unit area decrease, and myocardial oxygen consumption increases significantly after exercise; the increase of intramyocardial vascular pressure per unit area and a relative decrease of myocardial blood supply per unit area reduce blood supply and result in decreased myocardial strain and increased systolic heterogeneity among different myocardial segments. This study found that patients with HCM, in whom ejection fraction at rest was normal, had reduced segmental strain and LV-GLS in combination with prolonged TTPLS and PSD. These findings show that left ventricular contraction mechanics and synchronicity have been significantly damaged, suggesting that LVGLS and PSD measurements would detect abnormal left ventricular systolic function in subclinical segments. Such findings are consistent with the results of Panoulas et al. (19).

The occurrence of abnormal left ventricular mechanics in HCM with preserved ejection fraction accounts for exercise intolerance. Anatomical studies show that LV-GLS largely depends on the subendocardial layer of the myocardium which is the most sensitive to ischemia (20). A retrospective study involving more than 3,000 patients with HCM showed that abnormal LV-GLS is associated with adverse cardiovascular events and ventricular arrhythmias, accounting, at least in part, for high rates of sudden death in young patients with HCM (21). Increased PSD and the deterioration of synchrony may be related to myocardial scarring and HR. Abd-Elmoniem et al. (22) found that myocardial scarring caused a loss of synchrony by reducing wave propagation speed in the infarct and surrounding areas. Furthermore, exercise increases the HR, shortens the diastolic period, and causes increased myocardial oxygen consumption leading to an imbalance between supply and demand. LPS is obtained by using two-dimensional speckle-tracking imaging (2D-STI) technology, the principle of which relies on spots in the region of interest for use as tissue markers. The software automatically matches the best mode to track and identify changes in the spatial position of the spot signals in the region of interest, calculating the strain of each myocardial segment to represent deformability (23). This study found an increasing trend in the basal segment (BL) < intermediate segment (ML) < apical segment (AL) for both patients with HCM and controls. Each segment produced lower values in the HCM group. Left ventricular contraction proceeds from the apex to the bottom of the heart and BL in the AHCM group > BL in the asymmetric HCM group ($p < 0.05$). During the development of asymmetric HCM, the septum or other ventricular walls are thickened and the ventricular septum not only undertakes the function of left ventricular contraction

but also connects the outflow tract and the mitral valve. This process may be influenced by the abnormal hemodynamic impact caused by the hypertrophic myocardium. Wall fibrosis and exercise involvement are more obvious in the case of asymmetric HCM when, especially after exercise, the HR increases and the left ventricle presents a hyperdynamic state. There was no statistical difference between ML and AL for the two groups. Although hypertrophy affects the local myocardial segment, electrical and mechanical effects on cardiomyocytes extend to adjacent regions with delayed electrical activity and reduced mechanical activity.

In combination with decreased coronary perfusion, induced myocardial ischemia and blood flow redistribution, and decreased myocardial strain (24), where all aggravate the impairment of synchrony, the co-existence of these types of damage leads to mutual aggravation. Abnormalities of electromechanical motion reduce the mechanical efficiency of left ventricular ejection, increasing energy loss and ineffective work and reducing overall work and efficiency (25–27). When this situation is prolonged, myocardial contractile function gradually deteriorates and may even lead to heart failure. Schrub et al. (28) and Duchenne et al. (29) found that GWW increased but GWE decreased when the left ventricular PSD was enlarged in HCM and this may be related to the decreased metabolic activity of the ventricular septum. This study also found PSD in asymmetric HCM > PSD in AHCM (115.93 ± 7.92 vs. 91.9 ± 8.34; $p = 0.033$). Moreover, Aalen et al. (30) found that HCM patients with reduced synchrony had a more sensitive ventricular septum and lower exercise tolerance. This finding was confirmed by METS in this study (asymmetric HCM: 8.91 ± 0.43 vs. AHCM: 10.17 ± 0.12; $p = 0.007$). Ma et al. (31) also showed that the incidence of myocardial fibrosis and the proportion of fibrotic myocardial mass were higher in patients with asymmetric HCM than that in those with AHCM which is similar to the current findings. MRI data required for the verification of the degree and extent of myocardial fibrosis were not available for this study. However, this can be inferred from PSD, LV-GLS, and LPS values and the PSD for the asymmetric group was found to be significantly larger than that of the AHCM group. Myocardial fibrosis causes a loss of synchrony by reducing wave propagation speed in fibrotic areas (22), and previous studies have established the molecular basis to be enhanced actin-myosin interaction that delays and weakens cardiomyocyte contraction (32). Thus, as the intensity decreases, the measured LV-GLS decreases. Only eight subjects with HCM enrolled in this study had received cardiac MRI at the time of writing, and statistical analysis could not be completed for the whole sample. It is the intention of the authors to wait until all patients have completed cardiac MRI before adding MRI parameters to the comparison analysis. A statistical analysis of the diagnostic capacity of MW parameters for exercise tolerance was conducted separately in asymmetrical HCM and AHCM. We found that only LV-GLS had statistical differences [area under the curve (AUC) 0.739] in the asymmetric HCM group and only GWI (AUC 0.852) in the AHCM group. Considering the small sample size of METS (less than 6.8) in the respective groups, statistical deviation is possible, precluding a discussion of the diagnostic utility of exercise tolerance by an echocardiographic parameter in the separate cases of asymmetrical and AHCM. However, the enrollment of patients with HCM continues in an attempt to expand the sample size. We hope that follow-up studies can be performed and contributed to the discussion of this component. In general, patients with HCM have worse synchrony, increased GWW, and significantly decreased GCW, GWI, and GWE, and those with asymmetric HCM had lower strain, worse synchrony, and lower METS. Myocardial electrical conduction and mechanical contraction start from the apex and travel to the bottom of the heart. Segmental myocardial strain in the healthy subject shows the trend: BL < ML < AL with the BL being dominated by longitudinal contraction and the apical segment by torsion. The heart of the patient with HCM shows a similar trend but BL strain in the asymmetric HCM group was significantly lower than that in the AHCM group ($p < 0.05$). The balance between asymmetric HCM mechanics and intracardiac hydrodynamics may be lost and hypertrophy of the BL may lead to more turbulent inflow and outflow, resulting in greater energy loss. However, further and more detailed histopathological studies are required for verification. Schrub showed that the GWE of the interventricular septum was the best predictor of exercise capacity and that dispersion was related to the uneven distribution of MW in patients with dilated cardiomyopathy (DCM) (28). Marwick et al. demonstrated that in heart failure with preserved ejection fraction, GCW better-reflected exercise tolerance than GLS: when GCW increased significantly, exercise tolerance improved (33). Selecting for METS greater than or less than 6.8, this study found that AUC values for GWE (0.645), GWI (0.784), and GCW (0.751) were all higher than that for LV-GLS (0.517), in agreement with the above results. When values of GWE were less than 92.5%, GWI less than 1,200 mmHg, and GCW less than 1,399 mmHg, these are reference values with utility in the diagnosis of impaired exercise tolerance and poor prognosis.

LIMITATIONS

This study was limited to a single center. In order to exclude differences caused by ethnicity of the geographical population, the study collected matched healthy control participants from the same area and hospital as enrolled patients with HCM. In addition, the sample size was small and the conclusions require further studies with larger sample sizes or multicenters to make up for current deficiencies. Diastolic function can be reflected by parameters such as E/e, e, and LAVI. Among the 65 patients with HCM, 31 cases had mild mitral regurgitation, 11 had moderate mitral regurgitation, 2 had severe mitral regurgitation, 28 had mild tricuspid regurgitation, and 10 had moderate tricuspid regurgitation. All subjects had non-obstructive HCM but 20 patients also had increased outflow tract velocity. Therefore, the degree of mitral regurgitation, the increased outflow tract velocity, the smaller cardiac chamber caused by ventricular wall hypertrophy, the volume load of the left ventricle, and the high hemodynamic state in the cardiac chamber may all affect E, e, E/e, LA, LAVI, and other parameters for the evaluation of diastolic function. The above parameters were found to have no significant

correlation with METS at rest but this finding cannot rule out the existence of a correlation between E, e, E/e, LA, LAVI, the diastolic reserve function of HCM during the exercising state, and METS. Therefore, relevant guidelines (10) suggest that the diastolic evaluation of patients with HCM should be combined with other influencing factors. This study focused on MW, and further diastolic function parameters which were analyzed in our follow-up study have not been included in this report.

CONCLUSION

GWI, GWE, and GCW can be safely measured by resting echocardiography to evaluate exercise tolerance in patients with HCM who cannot perform an exercise-based examination. Such measurements provide a basis for clinical decisions regarding exercise and drug prescription.

DATA AVAILABILITY STATEMENT

The raw data supporting the conclusions of this article will be made available by the authors, without undue reservation.

ETHICS STATEMENT

The studies involving human participants were reviewed and approved by the Human Body Research Institution Committee of Sichuan Provincial People's Hospital. The patients/participants provided their written informed consent to participate in this study.

AUTHOR CONTRIBUTIONS

YS, LY, and CL: conception and design. LY: administrative support. CL: provision of study materials or patients. YS and QP: collection and assembly of data, and data analysis and interpretation. All authors contributed to manuscript writing and final approval of the manuscript.

FUNDING

This study was supported by the Fundamental Research Funds for the Central Universities (Grant No. ZYGX2020ZB038) and the Sichuan Provincial Department of Science and Technology Project (Grant Nos. 2018JY0649 and 2020YFS0404).

REFERENCES

1. Huang X, Yue Y, Wang Y, Deng Y, Liu L, Di Y, et al. Clinical study of left ventricular volume and systolic function in patients with hypertrophic cardiomyopathy by ultrasound speckle tracking technique. *Chin J Ultras Med.* (2013) 29:492–449.
2. Ullal AJ, Abdelfattah RS, Ashley EA, Froelicher VF. Hypertrophic cardiomyopathy as a cause of sudden cardiac death in the young: a meta-analysis. *Am J Med.* (2016) 129:486.e–96.e. doi: 10.1016/j.amjmed.2015.12.027
3. Mondillo S, Galderisi M, Mele D, Cameli M, Lomoriello VS, Zacà V, et al. Speckle-tracking echocardiography : a new technique for assessing myocardial function. *J Ultrasound Med.* (2011) 30:71–83.
4. Zhao Q, Liu L, Cui C, et al. Quantitative study of left ventricular pressure-strain loop on global myocardial work in patients with non-obstructive hypertrophic cardiomyopathy. *Chin J Ultrasound Med.* (2020) 36:795–8.
5. Manganaro R, Marchetta S, Dulgheru R, Ilardi F, Sugimoto T, Robinet S, et al. Echocardiographic reference ranges for normal non-invasive myocardial work indices:results from the EACVI NORRE study. *Eur Heart J Cardiovasc Imaging.* (2019) 20:582–90. doi: 10.1093/ehjci/jey188
6. Hubert A, Le Rolle V, Leclercq C, Galli E, Samset E, Casset C, et al. Estimation of myocardial work from pressure-strain loops analysis : an experimental evaluation. *Eur Heart J Cardiovasc Imaging.* (2018) 19:372–371.
7. Manganaro R, Marchetta S, Dulgheru R, Sugimoto T, Tsugu T, Ilardi F, et al. Correlation between non -invasive myocardial work indices and main parameters of systolic and diastolic function:results from the EACVI NORRE study. *Eur Heart J Cardiovasc Imaging.* (2020) 21:533–41. doi: 10.1093/ehjci/jez203
8. Mendes MA, da Silva I, Ramires V, Reichert F, Martins R, Ferreira R, et al. Metabolic equivalent of task (METs) thresholds as an indicator of physical activity intensity. *PLoS One.* (2018) 13:e0200701. doi: 10.1371/journal.pone.0200701
9. Gibbons RJ, Balady GJ, Bricker JT, Chaitman BR, Fletcher GF, Froelicher VF, et al. ACC/AHA 2002 guideline update for exercise testing: summary article: a report of the American College of Cardiology/American Heart Association Task Force on Practice Guidelines (Committee to Update the 1997 Exercise Testing Guidelines). *Circulation.* (2002) 106:1883–92. doi: 10.1161/01.cir.0000034670.06526.15
10. Lang RM, Badano LP, Mor-Avi V, Afilalo J, Armstrong A, Ernande L, et al. Recommendations for cardiac chamber quantification by echocardiography in adults: an update from the American Society of Echocardiography and the European Association of Cardiovascular Imaging. *J Am Soc Echocardiogr.* (2015) 28:1.e–39.e. doi: 10.1016/j.echo.2014.10.003
11. Makavos G, Kairis C, Tselegkidi ME, Karamitsos T, Rigopoulos AG, Noutsias M, et al. Hypertrophic cardiomyopathy: an updated review on diagnosis, prognosis, and treatment. *Heart Fail Rev.* (2019) 24:439–59. doi: 10.1007/s10741-019-09775-4
12. Turvey L, Augustine DX, Robinson S, Oxborough D, Stout M, Smith N, et al. Transthoracic echocardiography of hypertrophic cardiomyopathy in adults: a practical guideline from the British Society of Echocardiography. *Echo Res Pract.* (2021) 8:G61–86. doi: 10.1530/ERP-20-0042
13. Olivotto I, Maron MS, Adabag AS, Casey SA, Vargiu D, Link MS, et al. Gender-related differences in the clinical presentation and outcome of hypertrophic cardiomyopathy. *J Am Coll Cardiol.* (2005) 46:480–7. doi: 10.1016/j.jacc.2005.04.043
14. Gersh BJ, Maron BJ, Bonow RO, Dearani JA, Fifer MA, Link MS, et al. ACCF/AHA guideline for the diagnosis and treatment of hypertrophic cardiomyopathy: executive summary: a report of the American College of Cardiology Foundation/American Heart Association Task Force on Practice Guidelines. *J Am Coll Cardiol.* (2011) 58:2703–38. doi: 10.1016/j.jacc.2011.10.825
15. Haland TF, Almaas VM, Hasselberg NE, Saberniak J, Leren IS, Hopp E, et al. Strain echocardiography is related to fibrosis and ventricular arrhythmias in hypertrophic cardiomyopathy. *Eur Heart J Cardiovasc Imaging.* (2016) 17:613–21. doi: 10.1093/ehjci/jew005
16. Candan O, Gecmen C, Bayam E, Guner A, Celik M, Doðan C. Mechanical dispersion and global longitudinal strain by speckle tracking echocardiography: predictors of appropriate implantable cardioverter defibrillator therapy in hypertrophic cardiomyopathy. *Echocardiography.* (2017) 34:835–42. doi: 10.1111/echo.13547
17. Kaesler N, Babler A, Floege J, Kramann R. Cardiac remodeling in chronic kidney disease[J]. *Toxins.* (2020) 12:161.

18. Moisi MI, Rus M, Bungau S, Zaha DC, Uivarosan D, Fratila O, et al. Acute coronary syndromes in chronic kidney disease : clinical and therapeutic characteristics. *Medicina.* (2020) 56:118.
19. Panoulas VF, Sulemane S, Konstantinou K, Bratsas A, Elliott SJ, Dawson D, et al. Early detection of subclinical left ventricular myocardial dysfunction in patients with chronic kidney disease. *Eur Heart J Cardiovasc Imaging.* (2015) 16:539–48.
20. Wang TT, Kwon HS, Dai G, Wang R, Mijailovich SM, Moss RL, et al. Resolving myoarchitectural disarray in the mouse ventricular wall with diffusion spectrum magnetic resonance imaging. *Ann Biomed Eng.* (2010) 38:2841–50. doi: 10.1007/s10439-010-0031-5
21. Tower-Rader A, Mohananey D, To A, Lever HM, Popovic ZB, Desai MY. Prognostic value of global longitudinal strain in hypertrophic cardiomyopathy: a systematic review of existing literature. *JACC Cardiovasc Imaging.* (2019) 12:1930–42. doi: 10.1016/j.jcmg.2018.07.016
22. Abd-Elmoniem KZ, Tomas MS, Sasano T, Vonken EJ, Youssef A, Agarwal H, et al. Assessment of distribution and evolution of mechanical dyssynchrony in a porcine model of myocardial infarction by cardiovascular magnetic resonance. *J Cardiovasc Magn Reson* (2012) 14:1. doi: 10.1186/1532-429X-14-1
23. Reant P, Labrousse L, Lafitte S, Bordachar P, Pillois X, Tariosse L, et al. Experimental validation of circumferential, longitudinal, and radial 2 dimensional strain during dobutamine stress echocardiography in ischemic conditions. *J Am Coll Cardiol.* (2008) 51:149–57. doi: 10.1016/j.jacc.2007.07.088
24. Muser D, Tioni C, Shah R, Selvanayagam JB, Nucifora G. Prevalence, correlates, and prognostic relevance of myocardial mechanical dispersion as assessed by feature-tracking cardiac magnetic resonance after a first ST-segment elevation myocardial infarction. *Am J Cardiol.* (2017) 120:527–33. doi: 10.1016/j.amjcard.2017.05.019
25. Christophe L, Owen F, Richard T. Systolic improvement and mechanical resynch- ronization does not require electrical syn- chrony in the dialated failing heart with left bundle-branch block. *Circulation.* (2002) 106:1760–3. doi: 10.1161/01.cir.0000035037.11968.5c
26. Yu CM, Chan YS, Zhang Q, Yip GW, Chan CK, Kum LC, et al. Benefits of cardiac resyn- chronization therapy for heart failure patients with narrow QRS complexes and coexisting systolic asynchrony by echocardiography. *J Am Coll Cardiol.* (2006) 48:2251–7. doi: 10.1016/j.jacc.2006.07.054
27. Wierzbowska-Drabik K, Plewka M, Kasprzak JD. Variability of longitudinal strain in left ventricular segments supplied by non- stenosed coronary artery: insights from speckle tracking analysis of dobutamine stress echocardiograms in patients with high coro- nary risk profile. *Arch Med Sci.* (2017) 13:82–92. doi: 10.5114/aoms.2016.60603
28. Schrub F, Schnell F, Donal E, Galli E. Myocardial work is a predictor of exercise tolerance in patients with dilated cardiomyopathy and left ventricular dyssynchrony. *Int J Cardiovasc Imaging.* (2020) 36:45–53. doi: 10.1007/s10554-019-01689-4
29. Duchenne J, Turco A, Ünlü S, Pagourelias ED, Vunckx K, Degtiarova G, et al. Left ventricular remodeling results in homogenization of myocardial work distribution. *Circ Arrhythm Electrophysiol.* (2019) 12:e007224. doi: 10.1161/CIRCEP.118.007224
30. Aalen J, Storsten P, Remme EW, Sirnes PA, Gjesdal O, Larsen CK, et al. Afterload hypersensitivity in patients with left bundle branch block. *JACC Cardiovasc Imaging* (2018) 12:967–77. doi: 10.1016/j.jcmg.2017.11.025
31. Ma X, Zhao L, Ge H, Zhang H, Li Z, Yan Z, et al. Characteristics of cardiac magnetic resonance imaging in asymmetric hypertrophic cardiomyopathy and apical hypertrophic cardiomyopathy. *Chin General Med.* (2015) 18:2166–9.
32. Burke MA, Cook SA, Seidman JG, Seidman CE. Clinical and mechanistic insights into the genetics of cardiomyopathy. *J Am Coll Cardiol.* (2016) 68:2871–86.
33. Marwick TH, Mysiak A, Kosowski W, Kosmala W. Usefulness of myocardial work measurement in the assessment of left ventricular systolic reserve response to spironolactone in heart failure with preserved ejection fraction. *Eur Heart J Cardiovasc Imaging.* (2019) 20:1138–46. doi: 10.1093/ehjci/jez027

Conflict of Interest: The authors declare that the research was conducted in the absence of any commercial or financial relationships that could be construed as a potential conflictof interest.

Publisher's Note: All claims expressed in this article are solely those of the authors and do not necessarily represent those of their affiliated organizations, or those of the publisher, the editors and the reviewers. Any product that may be evaluated in this article, or claim that may be made by its manufacturer, is not guaranteed or endorsed by the publisher.

frontiers | Frontiers in Cardiovascular Medicine

TYPE Original Research
PUBLISHED 25 July 2022
DOI 10.3389/fcvm.2022.930745

OPEN ACCESS

EDITED BY
Kelvin Kian Loong Wong,
University of Saskatchewan, Canada

REVIEWED BY
Latha Rajendran,
Anna University, India
Defu Qiu,
China University of Mining and Technology, China
Weili Liu,
Xinjiang University, China

*CORRESPONDENCE
Lisha Zhong
zhonglisha@swmu.edu.cn
Zhiwei Huang
hzwnet@swmu.edu.cn

†These authors have contributed equally to this work

SPECIALTY SECTION
This article was submitted to General Cardiovascular Medicine, a section of the journal Frontiers in Cardiovascular Medicine

RECEIVED 28 April 2022
ACCEPTED 04 July 2022
PUBLISHED 25 July 2022

CITATION
Luo J, Zhang G, Su Y, Lu Y, Pang Y, Wang Y, Wang H, Cui K, Jiang Y, Zhong L and Huang Z (2022) Quantitative analysis of heart rate variability parameter and mental stress index.
Front. Cardiovasc. Med. 9:930745.
doi: 10.3389/fcvm.2022.930745

Quantitative analysis of heart rate variability parameter and mental stress index

Jiasai Luo[1†], Guo Zhang[1,2†], Yiwei Su[1], Yi Lu[1], Yu Pang[1], Yuanfa Wang[1], Huiqian Wang[1], Kunfeng Cui[1], Yuhao Jiang[1], Lisha Zhong[1,2*] and Zhiwei Huang[1,2,3,4*]

[1]Chongqing Key Laboratory of Photoelectronic Information Sensing and Transmitting Technology, Chongqing University of Posts and Telecommunications, Chongqing, China, [2]School of Medical Information and Engineering, Southwest Medical University, Luzhou, China, [3]State Key Laboratory of Bioelectronics, Southeast University, Nanjing, China, [4]Central Nervous System Drug Key Laboratory of Sichuan Province, Luzhou, China

Background: Cardiovascular disease not only occurs in the elderly but also tends to become a common social health problem. Considering the fast pace of modern life, quantified heart rate variability (HRV) indicators combined with the convenience of wearable devices are of great significance for intelligent telemedicine. To quantify the changes in human mental state, this article proposes an improved differential threshold algorithm for R-wave detection and recognition of electrocardiogram (ECG) signals.

Methods: HRV is a specific quantitative indicator of autonomic nerve regulation of the heart. The recognition rate is increased by improving the starting position of R wave and the time-window function of the traditional differential threshold method. The experimental platform is a wearable sign monitoring system constructed based on body area networks (BAN) technology. Analytic hierarchy process (AHP) is used to construct the mental stress assessment model, the weight judgment matrix is constructed according to the influence degree of HRV analysis parameters on mental stress, and the consistency check is carried out to obtain the weight value of the corresponding HRV analysis parameters.

Results: Experimental results show that the recognition rate of R wave of real-time 5 min ECG data collected by this algorithm is >99%. The comprehensive index of HRV based on weight matrix can greatly reduce the deviation caused by the measurement error of each parameter. Compared with traditional characteristic wave recognition algorithms, the proposed algorithm simplifies the process, has high real-time performance, and is suitable for wearable analysis devices with low-configuration requirements.

Conclusion: Our algorithm can describe the mental stress of the body quantitatively and meet the requirements of application demonstration.

KEYWORDS

heart rate variability, electrocardiogram, mental stress index, body area networks, quantitative analysis

Introduction

With the influence of people's habits, diet, and environment, the death rate of cardiovascular diseases such as hypertension, coronary heart disease, and heart disease increases rapidly, and the clinical manifestations are hemiplegia, cerebral infarction, stroke, and even sudden death (1). Heart rate decreases with age. Cardiovascular disease not only occurs in the elderly but also tends to be younger (2). Heart rate variability (HRV) refers to the variation of heartbeat cycle and is a research hotspot in electrocardiogram (ECG) signal processing field in recent years (3). It contains information about the regulation of neurohumoral factors in the cardiovascular system and is a specific quantitative indicator reflecting the regulation of autonomic nerves in the heart (4). It is also the most accurate and sensitive detection indicator to judge whether patients with diabetes are accompanied by autonomic nervous system damage (5). By studying the variation of heart rate, we can reflect the influence of nervous system on cardiovascular activity. It is of great clinical immune diseases (6), rehabilitation and intensity design (7), surgical risk assessment (8), and intelligent telemedicine (9). At present, three methods, namely, resting-state HRV, task HRV, and variable HRV, are used to measure HRV. The measurement of HRV in resting state mainly refers to the way of collecting HRV in the quiet state. The measurement of HRV in the task investigates the differences in HRV of subjects under different task states. The variable HRV investigates the change in HRV, such as the change in HRV before and after a task or operation, in order to infer the effect or effect of the task or operation. Luque-Casado's research showed that the cognitive workload under execution conditions changed with the change in tasks (10). Sustained attention is a key process affecting HRV, and there is a separation between subjective and objective cognitive workload.

There are two main methods to analyze HRV, namely, time-domain analysis and spectrum analysis. In time-domain analysis, the time-domain parameters commonly used include standard deviation of normal to normal (SDNN) and root mean square successive difference (RMSSD). SDNN is generally obtained by 24 h dynamic ECG, which reflects the regulation ability of autonomic nervous system, and further reflects an individual's stress ability and resistance to pressure. RMSSD is used to assess the regulatory function and activity of the cardiac vagus nerve or parasympathetic nerve.

The spectral analysis of HRV transforms the time series of R–R interval to the frequency by mathematical transformation method, forms the spectrum curve, and analyzes the shape of the spectrum curve. Spectral analysis is usually performed at high frequency (HF, 0.15–0.40 Hz) and low frequency (LF, 0.04–0.15 Hz). HF describes parasympathetic nerve activity level, whereas LF is a sympathetic nerve activity characteristic indicator, and its ratio is negatively correlated with albumin level (11).

HRV index can be used to identify sympathetic and parasympathetic nerve activity, which can help patients with cardiovascular disease to make accurate clinical warning and take a good treatment plan. Penttila et al. (12) evaluated the applicability of these four different parameters in cardiac vagus outflow and demonstrated that these parameters are more suitable for measuring cardiac vagal outflow during free breathing. La Rovere et al. (13) quantified HRV by measuring the SDNN R–R interval with a large amount of data, which might contribute to post-infarction risk stratification. Rossi et al. (14) applied ultra-short HRV to research the influence of data loss caused by motion artifacts, which played a significant role in obtaining reliable HRV signals. After controlling for environmental and personal confounding factors, Tang et al. (15) used a linear mixed-effects model to analyze the above frequency-domain and time-domain parameters, and proved that temperature changes on the day of onset might significantly reduce cardiac autonomic nervous function. Yang et al. (16) confirmed that lower HRV was associated with a higher risk of all-cause and cardiovascular death in hemodialysis population, and that lower SDANN and LF/HF were the predictors of both all-cause and cardiovascular mortality.

HRV analysis is an important means to evaluate the state of autonomic nervous system regulating the cardiovascular system. Quantitative evaluation can directly reflect the mental state of patients, which is helpful for the evaluation of psychiatric treatment programs and detection of specific drug effects. Sripanidkulchai et al. (17) studied the effects of standard Kaempferia Parviflora (KP) extracted on physical fitness and HRV parameters of adolescent sports school students in a randomized double-blind controlled trial. The experiment proved that KP extract had an anti-stress effect on HRV parameters, which can promote its application in sports training and exercise. Yoo et al. (18) evaluated the relationship between stress measured by HRV and academic achievement of medical students during their internship.

In this article, the recognition of R characteristic wave for ECG signal, HRV parameter calculation, and mental stress (MS) evaluation was studied. The detection and recognition of the waveform is the prerequisite to judging the parameters of ECG signal. The detection and recognition of QRS waveform is the basis of ECG signal detection. If there is error detection and missing detection phenomenon of QRS waveform, it will certainly affect the judgment of P wave and T wave, and also affect the result of disease classification of ECG signal. To solve this problem, an improved difference threshold algorithm is proposed to detect R wave. The traditional difference threshold algorithm is improved in two aspects, starting point and sliding window width, to improve the accuracy of R-wave recognition. The evaluation model of MS is constructed by analytic hierarchy process (AHP), and it is verified that the algorithm can quantitatively describe the MS of the body through comparative experiments.

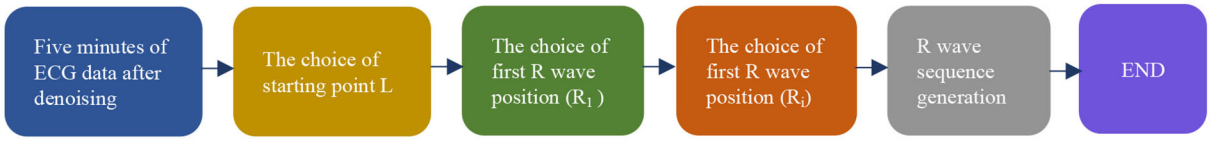

FIGURE 1
Flowchart of R-wave detection.

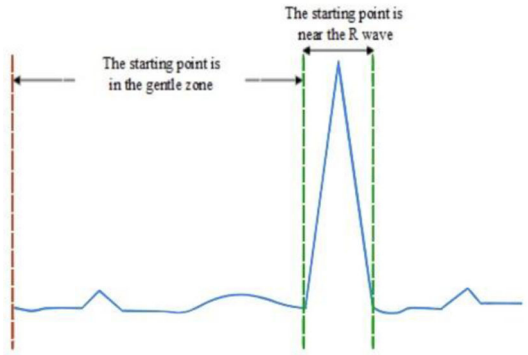

FIGURE 2
Schematic diagram of starting point selection area for R-wave detection.

Materials and methods

Differential threshold R-wave detection algorithm

QRS-wave group is the most unique and easily recognized characteristic wave in ECG signal. The characteristics of R wave in wave group are particularly obvious, and the change in rising slope and falling slope is most obvious. Differential threshold R-wave detection algorithm uses the slope characteristics of the rise and fall of R wave to recognize the R wave of ECG signal. In this article, an improved differential threshold algorithm is proposed to improve the accuracy of R-wave recognition. The whole detection process of the proposed algorithm is shown in Figure 1.

The selection of initial position is very important to accurately locate all R waves. As shown in Figure 2, the starting point of R wave may occur in the following two situations. In the first case, the starting point is in the stationary part of ECG signal, which can quickly and accurately locate R wave. The second case is that the starting point is around the R wave, and when the maximum and minimum values are compared after the first-order difference, the maximum value will appear before the minimum value, which may increase the miss and fallout ratio of the R-wave recognition (19).

To prevent the second situation mentioned above, the initial detection time of R wave should be avoided near the R wave. First, the ECG data during the period [1:t] are intercepted to find out the maximum ECG data A_{max}. Then, another period ECG data during [t+1:2×t] is intercepted to find out the maximum ECG data B_{max}. Finally, the value of Amax is required to compare with the value of $1.8 \times B_{max}$. If A_{max} is greater, it indicates that the initial position is near the R wave. $2 \times t$ will be used as the initial position for R-wave recognition. Otherwise, the initial position of R-wave detection is set as 1. After the ECG signal detection point L is selected, a segment of ECG signal X_{wf} is intercepted through the time-window function W_f, and the signal sequence is searched to locate the position point R_1 corresponding to the maximum value. At the same time, the first-order difference of X_{wf} will be carried out, and the comparison between the differential signal and the original ECG signal is shown in Figure 3.

After the differential signal dif(t) of signal segment X_{wf} is calculated, the minimum and maximum values of the differential signal dif(t) are first located to correspond to the time points t_{min} and t_{max} of ECG signal. Then, the position point R' corresponding to the maximum value of ECG signal in the time period is found. Finally, a comparison is performed to judge whether R_1 and R' are the same point. If they are the same point, then that point is the R-wave position. Otherwise, the smaller one is the R-wave position. Once the position of the first R wave is determined, as shown in Figure 4, the initial point L is some distance away from that position, which means that $L = R + T_1$. The same process is then performed to determine the location of the second R wave. The calculated time interval between these two R waves is defined as the RR interval (20).

Similarly, after the second R-wave position is determined, the delayed T_1 position is set as the initial point. Then, the ECG signal sequence is intercepted according to the dynamic time-window function W_f, and the position of R wave in this segment of ECG signal is located. In this process, if R_1 and R' are not at the same position, the absolute values of R_1R and $R'R$ are, respectively, subtracted from the previous RR interval. The position point with small difference is the position point of R wave.

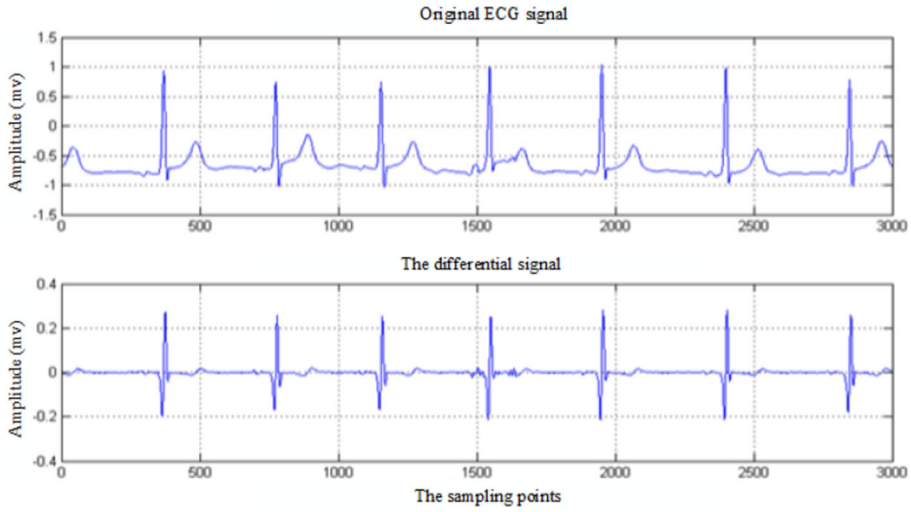

FIGURE 3
Comparison between the original ECG signal and differential signal.

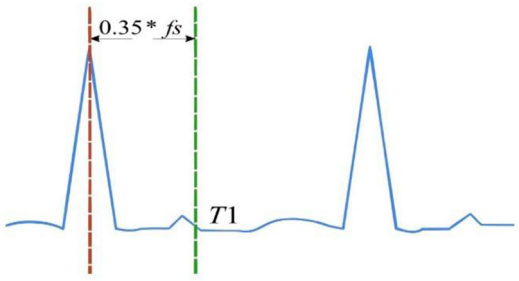

FIGURE 4
Schematic diagram of selecting the starting point for the latter R wave.

Mental stress model construction based on HRV signal

The HRV analysis is essentially a quantitative analysis of sinus heart rate. When premature beats or severe arrhythmias appear in the signals, HRV analysis will lose its significance. Therefore, the RR interval sequence will be processed to some extent in the actual analysis process as shown in Figure 5. First, the absolute value of the difference between two adjacent RR intervals is set as t_{RR}, and the critical value is set as 0.12 s. If there are 256 consecutive intervals, which are all less than the critical value when scanning the RR interval sequence, these data will be used as an HRV signal. Otherwise, it is necessary to estimate, in turn, to throw out any RR intervals in the sequence that do not satisfy the condition. Finally, the remaining RR intervals are pieced together to form HRV signals (21).

When researchers evaluate body pressure, there is no clear judgment standard so far, and most of them determine the stress state of the subjects by observing too many indicators of HRV. In the process of HRV analysis, no matter the time-domain parameters, frequency-domain parameters, or non-linear parameters, any single parameter cannot accurately represent the MS changes of the body (22). Therefore, the AHP is proposed to conduct quantitative evaluation in this article as shown in Figure 6. By obtaining the body pressure index, testers can intuitively understand their own pressure status.

In this article, some HRV analysis parameters are selected as pressure evaluation indexes by analyzing the experimental results. Among the time-domain parameters, SDNN, PNN50, and HR are selected as pressure indicators. While TP, HF, and LF/HF are frequency-domain parameter, VAI, HRD, and HLE are non-linear parameter. The hierarchical structure of the pressure model constructed according to the pressure index is shown in Table 1. Here, G represents the target layer of the model, G_i represents the criterion layer of the model, and G_{ij} represents the scheme layer of the model. The body pressure value can be obtained by comprehensively weighing each level index of the hierarchical model. This process represents the MS in the form of mathematics, instead of the subjective judgment before.

The judgment matrix is constructed using the 1–9 scale method, which represents the ratio of the index and the importance degree of the index to the upper index in the form of numbers. The larger the ratio a/b is, the more important index a is to the upper index relative to index b. In the judgment matrix constructed using the 1–9 scale method, element a_{ij} represents the ratio of the importance of the ith element and the jth element to the upper index (23).

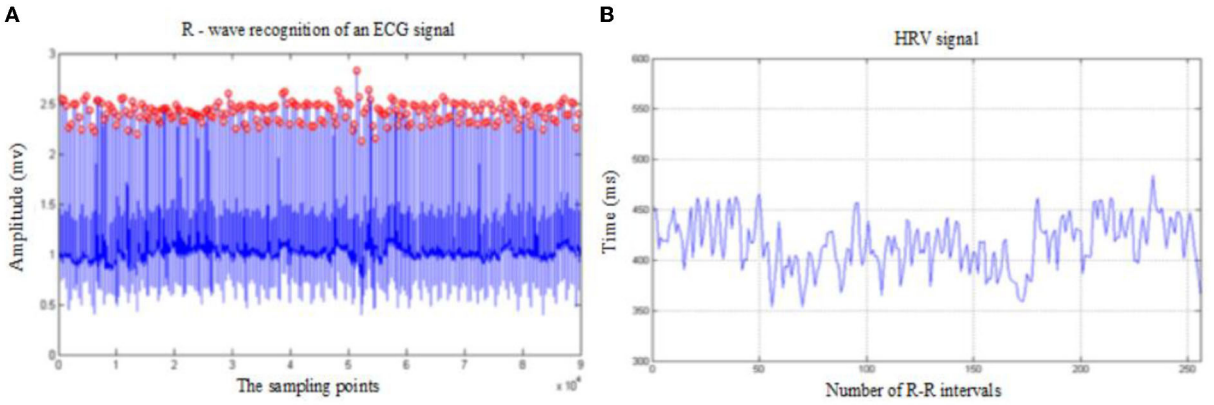

FIGURE 5
(A) The R-wave recognition effect diagram; **(B)** the generated HRV signal diagram.

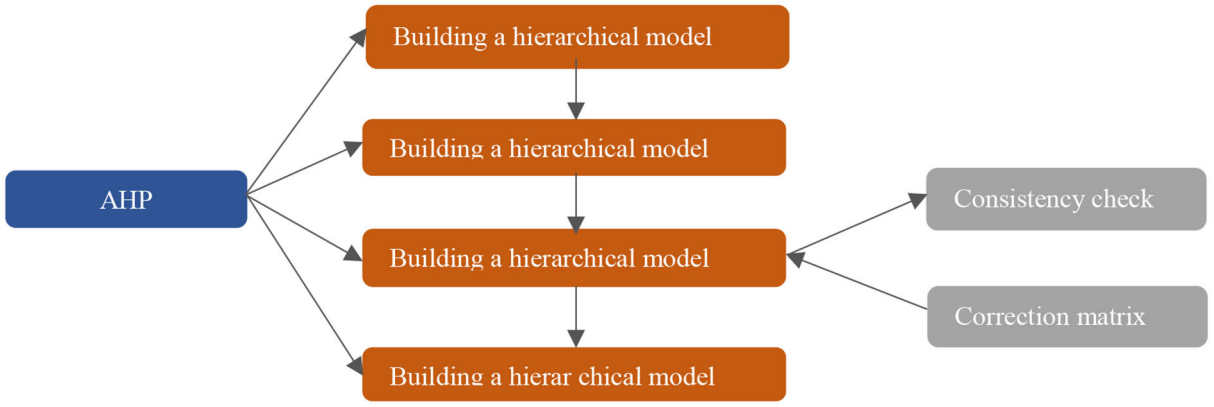

FIGURE 6
Schematic representation of the AHP.

TABLE 1 Pressure indicator architecture.

Target layer (G)	Criterion layer (G_i)		Scheme layer (G_{ij})	
Body pressure index, G	Frequency domain	G_1	LF/HF	G_{11}
			TP	G_{12}
	Time domain	G_2	SDNN	G_{21}
			PNN50	G_{22}
			HR	G_{23}
	Non-linear	G_3	HLE	G_{31}
			HRD	G_{32}
			VAI	G_{33}

The 1–9 scale method is used to construct the weight judgment matrix according to the influence degree of each parameter on MS (24). The weight judgment matrix of the constructed criterion layer is as follows:

$$A = \begin{bmatrix} 1 & 4 & 5 \\ 1/4 & 1 & 3 \\ 1/5 & 1/3 & 1 \end{bmatrix} \quad (1)$$

The weight judgment matrices B_1, B_2, and B_3 of frequency-domain parameters, time-domain parameters, and non-linear parameters of scheme layer G_{ij} are respectively expressed as follows:

$$B_1 = \begin{bmatrix} 1 & 3 \\ 1/3 & 1 \end{bmatrix} B_2 \begin{bmatrix} 1 & 1 & 3 \\ 1 & 1 & 3 \\ 1/3 & 1/3 & 1 \end{bmatrix} B_3 \begin{bmatrix} 1 & 3 & 4 \\ 1/3 & 1 & 2 \\ 1/4 & 1/2 & 1 \end{bmatrix} \quad (2)$$

According to the above analysis, the weight value of each element in set $G = \{G_1, G_2, G_3\}$ is expressed as $\beta = \{\beta_1, \beta_2, \beta_3\}$.

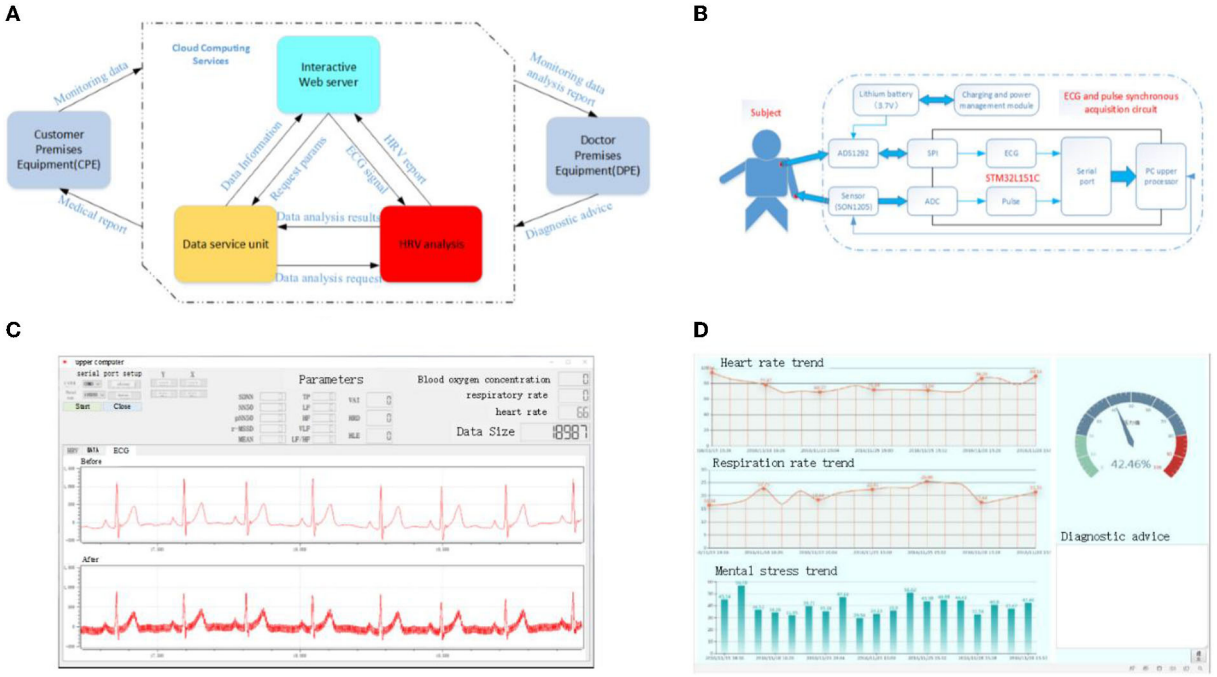

FIGURE 7
Schematic representation of the experimental test platform for HRV. **(A)** Overall structure diagram of the server, **(B)** schematic diagram of the customer premises equipment, **(C)** data acquisition interface of upper computer, and **(D)** electronic medical record interface.

The weight value of each element in the parameter set $G_1 = \{G_{11}, G_{12}\}$ in the frequency domain is expressed as $\lambda_1 = \{\lambda_{11}, \lambda_{12}\}$. The weight value of each element in the parameter set $G_2 = \{G_{21}, G_{22}, G_{23}\}$ in the time domain is expressed as $\lambda_2 = \{\lambda_{21}, \lambda_{22}, \lambda_{23}\}$. Similarly, the weight value of each element in the non-linear parameter set $G_3 = \{G_{31}, G_{32}, G_{33}\}$ is expressed as $\lambda_3 = \{\lambda_{31}, \lambda_{32}, \lambda_{33}\}$. The body pressure evaluation model of the criterion layer, expressed as $Z_{G_i} = f\left(G_{ij}, \lambda_{ij}\right)$, is constructed by combining the weight of each parameter. Here, G_{ij} is HRV analysis parameter value, and λ_{ij} is the corresponding weight value. The calculation method of criterion layer is as follows:

$$Z_{G1} = \left(\lambda_{11} \times \frac{G_{11}}{15} + \lambda_{12} \times \frac{G_{12}}{9000}\right) \times 100\% \quad (3)$$

$$Z_{G_2} = \left(\lambda_{21} \times \frac{200 - G_{21}}{200} + \lambda_{22} \times \frac{60 - G_{22}}{60} + \lambda_{23} \times \frac{G_{23}}{100}\right) \times 100\% \quad (4)$$

$$Z_{G3} = \left(\lambda_{31} \times \frac{G_{31}}{10} + \lambda_{32} \times \frac{0.4 - G_{32}}{0.4} + \lambda_{33} \times \frac{10 - G_{33}}{10}\right) \times 100\% \quad (5)$$

After the value of the secondary model Z_{G_i} is calculated, the body pressure value is calculated by combining the weight of the criterion layer β_i. The calculation formula of pressure index of the target layer model is shown in the following formula:

$$Z = \sum_{i=1}^{k} 100\beta_i \times Z_{G_i} \quad (6)$$

Results

Experimental test platform

The test platform in this article is a wearable sign monitoring system constructed based on BAN technology. The overall design structure block diagram of the system is shown in Figure 7A. It includes a three-layer structure of customer-premises equipment (CPE), cloud computing services, and doctor-premises equipment (DPE). The ECG signal is collected by the client and sent to a remote data center to obtain a diagnostic report. On the one hand, the remote data center receives the collected user data, calculates the HRV signal, and transmits the calculation results to the doctor. On the other hand, it receives the medical report transmitted by the doctor and feeds it back to the client. The doctor side will present the final HRV data calculation results, and the doctor can control the patient's status in real time for timely diagnosis and treatment advice. The hardware circuit diagram of the

CPE in this experiment is shown in Figure 7B. The device simultaneously collects ECG and pulse signals of the human body. The ECG signal is collected by CM5 bipolar chest lead, with two lead wires as positive pole LA and negative pole RA. The electrode is attached to the human body, and the ECG signal is transmitted to the acquisition circuit board through the lead wire. The ADS1292R chip amplifies the analog ECG signal, converts A/D into digital signal, and sends it to the MCU processing circuit through SPI interface. The microcontroller assembles the collected ECG and pulse signals into frames, sends them to the USB-serial circuit, and then the computer. At this point, the synchronous collection of ECG and pulse is completed. The data collection interface of the upper computer is shown in Figure 7C. The HRV time-domain, frequency–domain, and non-linear data can be presented by calculation. Figure 7D is the doctor-side diagnosis and treatment interface, which can intuitively display the patient's current MS status and query the historical changes of MS, and provide the best diagnosis and treatment suggestions accordingly.

The test data are measured in cooperation with Southwest Medical University. The ages of subjects are between 20 and 40 years, and the data are collected for 5 min at a time. The Institution Research Ethics Board of Southwest Medical University approved this experiment, and all experiments

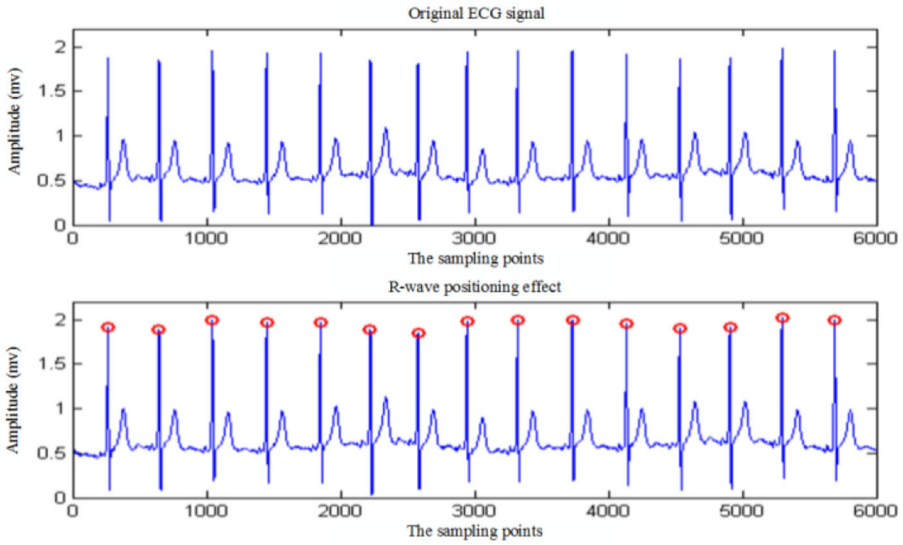

FIGURE 8
R-wave detection of ECG signal without noise interference.

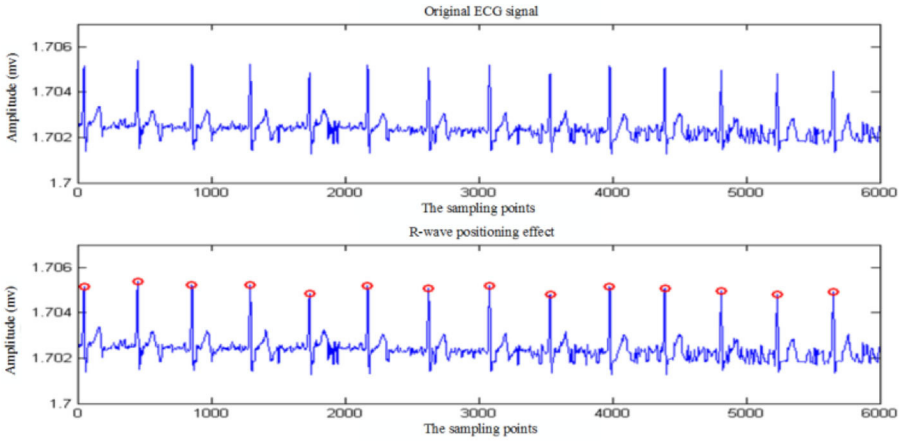

FIGURE 9
R-wave detection of ECG signal with noise interference.

are performed in accordance with relevant guidelines and regulations. In addition, all volunteers who provide data have agreed to use the data for publication and informed consent is obtained from all subjects.

Verification of R-wave detection algorithm

To verify the accuracy and anti-jamming ability of the R-wave detection algorithm, the R-wave location simulation of ECG signals under different conditions is carried out by using this algorithm on the test platform. The positioning effect diagram of ECG signal without noise interference is shown in Figure 8, and the one with noise interference is shown in Figure 9.

Real-time collection of 5 min ECG data using the algorithm presented in this article is used to identify R wave. The simulation results show that the algorithm recognition rate of R wave reaches 100%. To further verify the accuracy of the algorithm, 30 min ECG data from the MIT/BIH ECG database is used to detect and identify R characteristic waves. Table 2 shows the statistics of the recognition rate of the R-wave recognition algorithm for partial ECG data randomly selected from the MIT/BIH database. As shown in Table 2, the average R-wave recognition rate of this algorithm for the electrical signals in the center of the MIT/BIH database is ~99.69%, which is mainly caused by excessive noise interference in the signals.

The R-wave recognition algorithm proposed in this article has the following advantages over the traditional R-wave recognition algorithm. On the one hand, the algorithm improves the R-wave recognition rate and avoids missing and wrong detection of short-range ECG signals. On the other hand, the algorithm is easy to implement and the computation is small, so it is suitable for the analysis equipment with a high real-time requirement.

Contrastive experimental verification of mental states under different conditions

In this article, a comparative experiment is carried out according to the difference of motion state and environmental factors. It is found that muscle tension and mental activity could increase after exercise. In this experiment, HRV analysis parameters are used to calculate and compare MS values to verify the validity of the pressure model. Table 3 shows the

TABLE 3 Comparison of random experimental data and pressure index before and after exercise.

No.	State	VAI	HRD	HLE	HR	SDNN	PNN50	TP	LF/HF
1	Before	1.11	0.07	5.01	81	54.20	4.70	1,365	0.29
	After	0.73	0.07	7.48	99	35.26	1.90	1,929	10.45
2	Before	1.06	0.06	5.64	80	42.63	5.10	1,914	0.30
	After	0.88	0.05	6.71	102	21.43	1.10	3,924	3.86
3	Before	1.39	0.06	5.80	73	34.01	9.80	1,700	0.51
	After	0.89	0.06	6.35	95	24.36	1.90	2,042	7.28
4	Before	1.08	0.08	5.22	79	68.98	5.90	4,920	0.21
	After	0.03	0.05	5.26	100	63.36	1.20	6,743	2.23
5	Before	1.27	0.07	5.76	80	46.17	7.90	1,675	1.26
	After	0.91	0.07	6.21	98	30.12	2.80	2,485	2.05

TABLE 2 R-wave detection statistics of partial ECG data in the MIT/BIH database.

File No.	No. of standard QRS	Missing detection	Fault detection	Incorrect total	Recognition rate
100	2,273	0	1	1	99.91%
102	2,187	0	2	2	99.91%
103	2,084	1	2	3	99.86%
104	2,229	1	5	6	99.73%
105	2,572	2	6	8	99.69%
107	2,137	0	5	5	99.77%
109	2,532	1	8	9	99.64%
123	1,518	2	1	3	99.80%
208	2,955	0	9	9	99.70%
210	2,650	5	8	13	99.51%
215	3363	5	7	12	99.64%
219	2,154	0	5	5	99.77%
230	2,256	2	1	3	99.87%
Total	30,910	19	60	79	99.69%

10.3389/fcvm.2022.930745

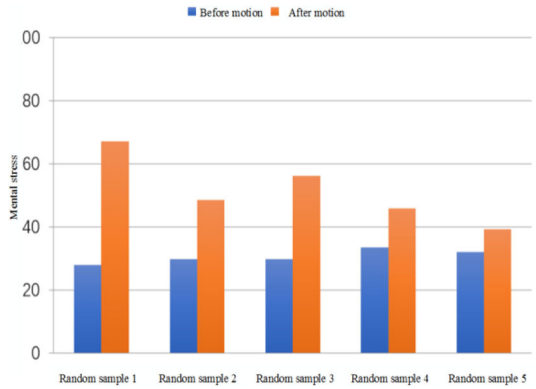

FIGURE 10
Comparison of mental stress before and after exercise for random sample.

comparison of experimental data of five randomly selected subjects in the database in two environments. From Figure 10, we can see the calculated quantitative indexes of MS before and after exercise. It can be seen from the figure that the MS value obtained by comprehensive calculation after exercise is significantly increased compared with that before exercise, which is in line with the objective fact, indicating that this model can be used for stress assessment caused by exercise.

Drastic changes in the environment may stress the subjects. The validity of the pressure evaluation model is verified by comparing the pressure values of the test subjects under two conditions. As we all know, virtual reality (VR) video has a certain auxiliary effect on mental illness and is being used by many psychiatrists to assist diagnosis and treatment. On account of this reason, VR video is used in this article to create different conditions for the subjects.

VR videos tested include soothing landscapes and a scary movie. First, the subject's MS is calculated and recorded while the subject is relaxed by watching the soothing landscapes. Every subject is then left alone in a dark room to watch a horror movie clip. The corresponding MS in a state of anxiety and tension is calculated and recorded. Table 4 shows the comparison of experimental data of five randomly selected subjects in the database in two conditions. Figure 11 shows the comparison of MS values.

According to the results of the experiment, the subjects are relaxed when watching the scenery videos, with almost no psychological or physical stress. The value of the corresponding MS is small, and the average value is ∼30. After watching the scary video, the psychological activity of the subjects is greater and even produces a sense of fear. As can be seen from Figure 11, the value of MS increases significantly. Although there are individual differences, the increase is generally more than 60%, and the biggest change even reaches 106.7%. This quantitative description is capable of reflecting the changes of MS effectively brought by different stimuli to the organism.

TABLE 4 Comparison of random experimental data and pressure index before and after watching.

No.	State	VAI	HRD	HLE	HR	SDNN	PNN50	TP	LF/HF
1	Before	1.12	0.05	5.86	77	52.85	4.11	1,728	0.76
	After	0.65	0.05	7.07	90	37.44	0.98	3,415	5.25
2	Before	2.52	0.06	5.12	70	32.29	0.78	2,992	0.35
	After	1.11	0.06	7.48	97	21.58	0	4,469	3.88
3	Before	1.06	0.05	4.96	72	48.04	2.54	2,210	0.26
	After	0.84	0.03	6.71	98	34.41	0	5,264	3.94
4	Before	2.61	0.11	5.63	80	51.7	9.59	2,426	0.9
	After	1.05	0.06	6.68	87	44.42	0.78	3,262	6.5
5	Before	1.26	0.07	5.35	77	52.85	2.15	822	1.01
	After	0.65	0.05	7.27	90	25.29	0.39	3,415	8.18

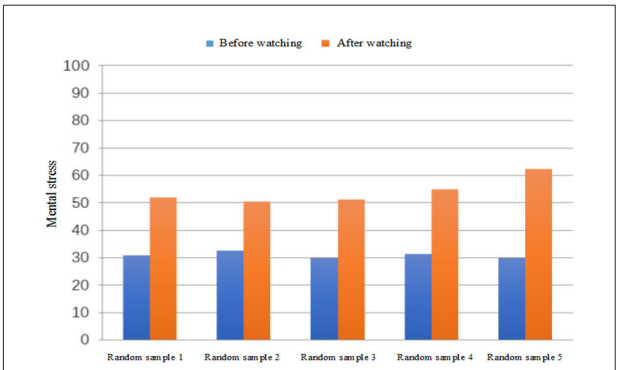

FIGURE 11
Comparison of mental stress before and after watching the video.

Error analysis of measurement data

Considering the influence of subjects, environment, and measuring instruments, there will be some errors in the actual measurement. To reduce the error, we calculate the average of multiple measurements. Table 5 shows all error rates of HRV parameters.

The result shows that the errors of SDNN in the time domain range from 0.16 to 17.27%, PNN50 range from 0.53 to 26.36%, HR range from 0.42 to 3.02%, and LF/HF range from 3.20 to 34.48%. Total power (TP) error is between 1.92 and 36.35%. The errors of relative dispersion of non-linear parameters HRD, Lyapunov index HLE, and vector angle index (VAI) are 0.19–14.96%, 0.42–7.26%, and 0.57–12.68%, respectively. The error of the final calculated MS index is between 0.57 and 9.68%, which meets the requirements of application demonstration.

TABLE 5 Error rate of HRV parameters.

No.	SDNN	pNN50	HR	LF/HF	TP	HRD	HLE	VAI	MS
1	2.94%	3.82%	1.29%	23.97%	4.28%	2.95%	0.59%	0.57%	4.71%
2	5.53%	15.41%	1.41%	16.35%	1.92%	5.56%	0.42%	1.16%	7.76%
3	4.35%	4.37%	1.62%	6.09%	7.19%	5.16%	3.72%	12.68%	1.98%
4	2.81%	3.82%	0.79%	24.00%	4.27%	6.72%	1.76%	1.65%	1.24%
5	3.42%	8.41%	1.27%	24.09%	4.73%	9.06%	0.55%	5.39%	2.97%
6	11.01%	8.27%	0.67%	18.79%	6.32%	4.83%	7.26%	9.65%	4.26%
7	6.52%	17.07%	2.12%	19.00%	5.05%	2.28%	1.34%	2.82%	5.71%
8	2.99%	26.36%	2.56%	18.89%	3.37%	3.00%	2.72%	9.93%	8.74%
9	2.98%	22.50%	3.55%	18.30%	2.33%	2.98%	3.20%	1.00%	9.68%
10	4.79%	20.03%	4.42%	28.22%	36.35%	6.25%	6.53%	11.80%	9.34%
11	17.27%	13.49%	1.92%	18.86%	23.27%	13.03%	1.59%	3.84%	0.57%
12	0.16%	19.08%	1.40%	6.57%	4.96%	0.19%	3.46%	8.85%	5.77%
13	3.96%	1.55%	2.53%	3.20%	3.29%	2.98%	1.25%	7.72%	1.77%
14	14.97%	16.17%	1.14%	20.64%	10.96%	14.96%	6.60%	8.21%	3.13%
15	3.96%	0.53%	1.63%	34.48%	13.33%	3.98%	1.55%	0.39%	5.26%
16	3.24%	0.70%	0.47%	29.74%	22.32%	5.68%	2.47%	3.02%	0.86%
17	13.18%	22.17%	1.15%	25.24%	23.61%	3.41%	2.81%	3.22%	2.58%
18	5.31%	13.46%	2.44%	6.78%	10.10%	5.31%	3.07%	3.32%	0.78%
19	6.09%	15.00%	3.02%	7.45%	6.75%	5.39%	3.18%	1.90%	1.72%
20	4.27%	19.99%	1.55%	19.15%	7.92%	3.41%	2.81%	1.61%	4.10%

Discussion

In this study, we construct the quantitative description model of mental stress, propose an improved differential threshold method to detect, and recognize R waves of ECG signals accurately and reliably. Both these research findings shed light on the accurate HRV measurement and quantitative detection of mental stress, likely playing a role in the treatment of mental illness.

By analyzing HRV time-domain and frequency-domain indexes, researchers aim to quantitatively study the relationship between HRV indexes and sympathetic nerve activity level and special diseases. Penttila et al. (12) studied the applicability of four different measures of HRV in the assessment of cardiac vagal outflow. However, its research tended to be in the category of free breathing and could not be directly quantified. Recent research by Rovere (13) introduced Baroreflex Sensitivity (BRS) for risk stratification after infarction on the basis of traditional time-domain parameter SDNN. Based on 24 h Holter recording and rate–pressure response to intravenous phenylephrine, they unveiled that low values of either HRV (SDNN $<$ 70 ms) or BRS ($<$3 ms per mmHg) carried a significant multivariate risk of cardiac mortality. However, the results of this study have great limitations, especially for patients with low BRS. Furthermore, as a time-domain parameter, SDNN has a great interference and error in the measurement process. Yang et al. (16) confirmed that the reduction in HRV was associated with a high risk of all-cause and cardiovascular death in hemodialysis population. Decreased SDANN and LF/HF were identified as predictors of both all-cause and cardiovascular mortality, while the utility of other HRV metrics requires further investigation. Tang's (15) study showed that temperature variability decreased both frequency-domain and time-domain HRV parameters, which is a possible predictor for adverse cardiac events. Consistent with these results, we found that HRV index can effectively predict the occurrence of some diseases, but also can be used as the evaluation basis of some diseases. Through the above experiments, we verified the changes of HRV indicators under different emotions and different sports states, and gave quantitative descriptions to intuitively evaluate the changes in their diseases.

To truly estimate disease status through HRV index, accurate measurement and calculation of acquisition parameters are very important. Rossi et al. (14) simulated missing values induced by motion artifacts (from 0 to 70%) in an ultra-short-time window by the random walk Gilbert burst model in 22 young healthy subjects to obtain reliable HRV parameters from device. Tang's (15) study integrated eight measurement parameters in time domain and frequency domain to ensure the reliability of calculation results. Although there is extensive evidence that multiparameter comprehensive measurement can effectively reduce measurement error and improve data reliability, we show

for the first time that the comprehensive index of HRV based on weight matrix in Equation (6) can greatly reduce the deviation caused by the measurement error of each parameter as shown in Table 5.

This study has some limitations. One limitation is that the all participants are adults. Future studies could be performed in order to detect individual characteristics such as gender, age, and individual habits. Another limitation is the lack of a broader stimulus. Future studies could be performed in order to consider stimulating factor such as sadness, shock, and weightlessness.

Conclusion

The quantitative analysis of HRV can reflect the regulation of the autonomic nervous system to the cardiovascular system. Not only can it help patients and doctors diagnose or predict cardiovascular disease, but it can also be used to assess psychological conditions such as stress. In this article, an improved differential threshold method is used to detect and recognize R waves of ECG signals. To improve the recognition rate, the traditional difference threshold method is improved through a novel algorithm for locating initial position of R wave and improved time-window function. The experimental results show that the recognition rate of R wave in 5 min ECG data collected in real time is >99%. Compared with traditional characteristic wave recognition algorithms, the proposed algorithm simplifies process, has high real-time performance, and is suitable for wearable analysis devices with low-configuration requirements. The accurate recognition of ECG signal R characteristic wave goes far toward obtaining an accurate HRV signal. The AHP is used to construct the mental stress evaluation model in this article. According to the influence degree of HRV analysis parameters on mental stress, the weight judgment matrix is constructed and the consistency is verified. Then, the weight values of the corresponding HRV analysis parameters are calculated. In the end, according to the value range of the parameters selected by the model and the ratio relationship between the parameters and mental stress, the mental stress evaluation model is constructed. The validity of the mental stress model is verified by comparing the mental stress values of the subjects in different states and different environments. The experimental results show that the mental stress model can describe the mental stress of the body quantitatively.

Data availability statement

The original contributions presented in the study are included in the article/supplementary materials, further inquiries can be directed to the corresponding author/s.

Ethics statement

Ethical review and approval was not required for the study on human participants in accordance with the local legislation and institutional requirements. The patients/participants provided their written informed consent to participate in this study. Written informed consent was obtained from the individual(s) for the publication of any potentially identifiable images or data included in this article.

Author contributions

JL and GZ: writing the manuscript. YS and YL: collecting the data. YP and YW: designing the research. HW, KC, and YJ: statistical analysis. LZ and ZH: obtaining funding. All authors have read and approved the final manuscript.

Funding

This project was funded by Central Nervous System Drug Key Laboratory of Sichuan Province, Medical Engineering and Medical Informatics Integration and Transformational Medicine of Luzhou Key Laboratory and also supported by the National Natural Science Foundation of China (No. 62171073, No. U21A20447, and No. 61971079), China Postdoctoral Science Foundation (No. 2021M693931 and No. 2021MD703941), Science and Technology Research Program of Chongqing Municipal Education Commission (KJQN202000604 and KJQN202100602), Nature Science Foundation of Chongqing (cstc2020jcyj-cxttX0002, cstc2021jscx-gksbx0051, and cstc2021jcyj-bsh0221), Science and Technology Department of Sichuan Province (2020YFQ0025, 2020YJ0151, and 2022NSFSC0508), Key Research Project of Southwest Medical University (2021ZKZD019), Project of Central Nervous System Drug Key Laboratory of Sichuan Province (200018-01SZ, 200020-01SZ, 200027-01SZ, 200028-01SZ, and 210022-01SZ), and Open Research Fund of State Key Laboratory of Bioelectronics, Southeast University (No. SKLB2022-P06).

Conflict of interest

The authors declare that the research was conducted in the absence of any commercial or financial relationships that could be construed as a potential conflict of interest.

Publisher's note

All claims expressed in this article are solely those of the authors and do not necessarily represent those of their affiliated

organizations, or those of the publisher, the editors and the reviewers. Any product that may be evaluated in this article, or claim that may be made by its manufacturer, is not guaranteed or endorsed by the publisher.

References

1. Park M, Heo Y J. Biosensing technologies for chronic diseases. BioChip Journal, (2021). 15:1–13. doi: 10.1007/s13206-021-00014-3

2. Siontis KC, Noseworthy PA, Attia ZI, Friedman PA. Artificial intelligence-enhanced electrocardiography in cardiovascular disease management. *Nat Rev Cardiol.* (2021) 18:465–78. doi: 10.1038/s41569-020-00503-2

3. Namazi H. Complexity and information-based analysis of the Heart Rate Variability (HRV) while sitting, hand biking, walking, and running. *Fractals*, (2021) 29:2150201. doi: 10.1142/S0218348X21502017

4. Johnston BW, Barrett-Jolley R, Krige A, Welters ID. Heart rate variability: measurement and emerging use in critical care medicine. *J Intens Care Soc.* (2020) 21:148–57. doi: 10.1177/1751143719853744

5. Castaldo R, Montesinos L, Melillo P, James C, Pecchia L. Ultra-short term HRV features as surrogates of short term HRV: a case study on mental stress detection in real life. *BMC Med Inform Decis Making.* (2019) 19:12. doi: 10.1186/s12911-019-0742-y

6. Zhao Q, Ren H, Han Z. Mesenchymal stem cells: immunomodulatory capability and clinical potential in immune diseases. *J Cell Immunother.* (2016) 2:3–20. doi: 10.1016/j.jocit.2014.12.001

7. Vorwerg S, Stamm O, Menant A, Alex S, Müller-Werdan U. Observational study in cardiac rehabilitation groups phase III: a comparison of perceived and measured training intensity during a moderate-intensity workout. *Eur J Phys Rehabil Med.* (2020) 57:414–23 doi: 10.23736/S1973-9087.20.06379-0

8. Nayar SK, Li D, Ijaiya B, Lloyd D, Bharathan R. Waterlow score for risk assessment in surgical patients: a systematic review. *Ann R Coll Surg Engl.* (2021) 103:312–7. doi: 10.1308/rcsann.2020.7136

9. Zhong Y, Xu ZH, Cao L. Intelligent IoT-based telemedicine systems implement for smart medical treatment. *Pers Ubiquit Comput.* (2021) 1–11. doi: 10.1007/s00779-021-01633-1

10. Luque-Casado A, Perales JC, Cárdenas D, Sanabria D. Heart rate variability and cognitive processing: the autonomic response to task demands. *Biol Psychol.* (2016) 113:83–90. doi: 10.1016/j.biopsycho.2015.11.013

11. Matusik PS, Matusik PT, Stein PK. Heart rate variability in patients with systemic lupus erythematosus: a systematic review and methodological considerations. *Lupus.* (2018) 27:1225–39. doi: 10.1177/0961203318771502

12. Penttilä J, Helminen A, Jartti T, Kuusela T, Huikuri HV, Tulppo MP, et al. Time domain, geometrical and frequency domain analysis of cardiac vagal outflow: effects of various respiratory patterns. *Clin Physiol.* (2001) 21:365–76. doi: 10.1046/j.1365-2281.2001.00337.x

13. La Rovere MT, Pinna GD, Raczak G. Baroreflex sensitivity: measurement and clinical implications. *Ann Noninv Electrocardiol.* (2008) 13:191–207. doi: 10.1111/j.1542-474X.2008.00219.x

14. Rossi A, Pedreschi D, Clifton DA, Morelli D. Error estimation of ultra-short heart rate variability parameters: effect of missing data caused by motion artifacts. *Sensors.* (2020) 20:7122. doi: 10.3390/s20247122

15. Tang M, He Y, Zhang X, Li H, Huang C, Wang C, et al. The acute effects of temperature variability on heart rate variability: a repeated-measure study. *Environ Res.* (2021) 194:110655. doi: 10.1016/j.envres.2020.110655

16. Yang L, Zhao Y, Qiao B, Wang Y, Zhang L, Cui T, et al. Heart rate variability and prognosis in hemodialysis patients: a meta-analysis. *Blood Purific.* (2021) 50:298–308. doi: 10.1159/000511723

17. Sripanidkulchai B, Promthep K, Tuntiyasawasdikul S, Tabboon P, Areemit R. Supplementation of Kaempferia parviflora extract enhances physical fitness and modulates parameters of heart rate variability in adolescent student-athletes: a randomized, double-blind, placebo-controlled clinical study. *J Dietary Suppl.* (2022) 19:149–67. doi: 10.1080/19390211.2020.1852356

18. Yoo HH, Yune SJ, Im SJ, Kam BS, Lee SY. Heart rate variability-measured stress and academic achievement in medical students. *Med Princ Pract.* (2021) 30:193–200. doi: 10.1159/000513781

19. Ucak S, Dissanayake HU, Sutherland K, de Chazal P, Cistulli PA. Heart rate variability and obstructive sleep apnea: current perspectives and novel technologies. *J Sleep Res.* (2021) 30:e13274. doi: 10.1111/jsr.13274

20. Hasty F, García G, Dávila H, Wittels SH, Hendricks S, Chong S. Heart rate variability as a possible predictive marker for acute inflammatory response in COVID-19 patients. *Milit Med.* (2021) 186:e34–8. doi: 10.1093/milmed/usaa405

21. Forte G, Morelli M, Casagrande M. Heart rate variability and decision-making: autonomic responses in making decisions. *Brain Sci.* (2021) 11:243. doi: 10.3390/brainsci11020243

22. Namazi H, Baleanu D, Krejcar O. Age-based analysis of heart rate variability (HRV) for patients with congestive heart failure. *Fractals.* (2021) 29:2150135. doi: 10.1142/S0218348X21501358

23. Koch C, Wilhelm M, Salzmann S, Reif W, Euteneuer F. A meta-analysis of heart rate variability in major depression. *Psychol Med.* (2019) 49:1948–57. doi: 10.1017/S0033291719001351

24. Mather M, Thayer JF. How heart rate variability affects emotion regulation brain networks. *Curr Opin Behav Sci.* (2018) 19:98–104. doi: 10.1016/j.cobeha.2017.12.017

frontiers | Frontiers in Cardiovascular Medicine

TYPE Original Research
PUBLISHED 09 September 2022
DOI 10.3389/fcvm.2022.925571

OPEN ACCESS

EDITED BY
Ruizheng Shi,
Central South University, China

REVIEWED BY
Defu Qiu,
China University of Mining and Technology, China
Yu Lu,
Shenzhen Technology University, China

*CORRESPONDENCE
Xiliang Zhu
zhuxiliang@zzu.edu.cn

SPECIALTY SECTION
This article was submitted to General Cardiovascular Medicine, a section of the journal Frontiers in Cardiovascular Medicine

RECEIVED 21 April 2022
ACCEPTED 10 August 2022
PUBLISHED 09 September 2022

CITATION
Zhu X, Xiao X, Wang S, Chen X, Lu G and Li X (2022) Rosendaal linear interpolation method appraising of time in therapeutic range in patients with 12-week follow-up interval after mechanical heart valve replacement. *Front. Cardiovasc. Med.* 9:925571. doi: 10.3389/fcvm.2022.925571

Rosendaal linear interpolation method appraising of time in therapeutic range in patients with 12-week follow-up interval after mechanical heart valve replacement

Xiliang Zhu[1]*, Xijun Xiao[2], Sheng Wang[1], Xianjie Chen[1], Guoqing Lu[1] and Xiaoyang Li[1]

[1]Department of Cardiovascular Surgery, Henan Province People's Hospital, Zhengzhou University, Zhengzhou, Henan, China, [2]Department of Cardiovascular Surgery, West China Hospital, Sichuan University, Chengdu, China

Background: The objective of this study was to evaluate the quality of anticoagulation by the time in therapeutic range (TTR) for patients with 12-week INR follow-up interval.

Materials and methods: From January 2018 to December 2020, a selective group of patients who underwent mechanical valve replacement and followed up at our anticoagulation clinic for adjustment of warfarin dose were enrolled. The incidences of complications of anticoagulation therapy were reported by linearized rates. TTR was calculated by the Rosendaal linear interpolation method.

Results: Two hundred and seventy-four patients were eligible for this study. The mean age of these patients was 52.8 ± 12.7 years, and 65.7% (180 cases) of them were females. The mean duration of warfarin therapy was 16.7 ± 28.1 months. A total of 1309 INR values were collected, representing 66789 patient days. In this study, the mean TTR was 63.7% ± 18.6%, weekly doses of warfarin were 20.6 ± 6.0 mg/weekly, and the mean monitoring interval for the patient was 53.6 ± 27.1 days. There were 153 cases in good TTR group (TTR ≥ 60%) and 121 cases in poor TTR group (TTR < 60%). The calculated mean TTR in both groups was 42.6% ± 22.1% and 74.8% ± 10.4%, respectively. Compared with the TTR ≥ 60% group, the TTR < 60% group exhibited a more prevalence of female gender (p = 0.001), atrial fibrillation (p < 0.001), NYHA ≥ III (p < 0.001), and lower preoperative left ventricular ejection fraction (LVEF, p = *0.032*). In multivariate analysis, female gender (p = 0.023) and atrial fibrillation (p = 0.011) were associated with TTR < 60%. The incidence of major bleeding and thromboembolic events was 2.7% and 1.1% patient-years, respectively. There was one death which resulted from cerebral hemorrhage. The incidence of death was 0.5% patient-years. The

difference in anticoagulation-related complications between the TTR < 60% group and the TTR ≥ 60% group was not statistically significant.

Conclusion: For patients with stable international normalized ratio monitoring results who are follow-up at anticoagulation clinics, a 12-week monitoring interval has an acceptable quality of anticoagulation. The female gender and atrial fibrillation were associated with TTR < 60%.

KEYWORDS

warfarin, time in therapeutic range (TTR), international normalized ratio (INR), mechanical heart valve (MHV), oral anticoagulant

Introduction

Patients with mechanical heart valve prostheses need to receive oral anticoagulant therapy for life long, or they may accompany with valve thrombosis and subsequent systemic embolism (1). Warfarin, a common vitamin K antagonist, has been demonstrated to be effective for the prevention and treatment of those thromboembolic complications (2, 3). However, its limitations are also remarkable, including a narrow therapeutic range, intra- and inter-patient variability in dose response, and susceptibility to drug–drug and drug–food interactions (1, 4). For this reason, it is important to periodically monitor and adjust the dose to keep the international normalized ratio (INR) in the target range as long as possible.

The interval between INR monitoring and stable doses of oral anticoagulants continues to be controversial (5). The American College of Chest Physicians (ACCP) recommends 4 weeks as the maximum interval for patients' follow-up. Other studies suggest that it can be extended to 12 weeks for patients with stable INR monitoring results and point out that every 4-week follow-up may increase the possibility of testing results out of the target range and the burden of anticoagulant treatment in these patients (6–9). The clinical outcomes of 12-week intervals of assessment have been found to be safe and to be equal to assessments every 4 weeks in other studies (7, 9). Despite this, there is still a lack of evidence supporting the longer monitoring interval in the literature or in clinical practice.

Time in the therapeutic range (TTR), which estimates the percentage of time a patient's INR is within the therapeutic treatment range or goal, is commonly used in the assessment of anticoagulant quality (8, 10–14). Studies indicated that patient with higher TTR is directly correlated with the reduction in risk of thromboembolism complications and major bleeding (15, 16). Lee et al. (14) showed that a 10% increase in time spent out of TTR is related to a 10–12% decrease in the risk thromboembolic events and a 29% decrease in the risk of mortality. Therefore, the objective of this study was to evaluate the quality of anticoagulation in our hospital by the TTR for patients with 12-week INR monitoring interval and to identify the predictors of poor TTR in patients with mechanical heart valve prostheses.

Materials and methods

Patients

The retrospective research was conducted in Henan Province People's Hospital. From January 2018 to December 2020, a selective group of patients who received warfarin treatment and followed up at our anticoagulation clinic were enrolled. All of them had undergone mechanical valve replacement. Patients were seen as qualified to participate in the research if they meet the following criteria: (1) aged at 18 years old or above, (2) accepted warfarin treatment for at least 12 months, and (3) had a stable dose for the previous 12 weeks. Patients were excluded from this study under the following conditions: (1) monitoring interval > 13 weeks; (2) ethnic minorities of China.

Referring to our anticoagulation clinic's anticoagulant criteria, the target range for INR in our hospital is 1.5 to 2.5. INR < 1.5 is defined as subtherapeutic range while INR > 2.5 as supratherapeutic range. We adjust the dose and monitoring intervals according to the protocol in **Table 1**. We recommend 4 weeks as the maximum monitoring interval for patients who underwent mechanical heart valve replacement within postoperative 6 months. After 6-month intensive INR monitoring, 12 weeks is recommended to the patient who keep a stable dose for 12 weeks.

Time in therapeutic range

Time in therapeutic range (TTR) is defined as the number of person-day within a pre-determined therapeutic

TABLE 1 Dose adjustment protocol according to international normalized ratio (INR) value in our anticoagulation clinical.

INR value	Action
<1.5	Increasing the dosage of 0.625 mg/day
1.5–2.5	Maintain dose
>2.5 and ≤3.5	Omit one dose, and reducing the dosage of 0.625 mg/day, weekly control until level stabilizes
>3.5	Omit three dose, and reducing the dosage of 0.625 mg/day, weekly control until level stabilizes

Patient with INR >5 is referred to the emergency department. INR: international normalized ratio.

TABLE 2 Clinical characteristics of patients.

Characteristics	Value
Age, years	52.8 ± 12.7
Female, n (%)	180 (65.7%)
Diabetes mellitus, n (%)	32 (11.7%)
Hypertension, n (%)	41 (15.0%)
Smoking, n (%)	48 (16.8%)
NYHA ≥ III, n (%)	205 (74.8%)
Creatinine, μmoI/L	73.4 ± 17.8
Total cholesterol, mmol/L	3.2 ± 0.7
HbA1c, %	6.1 ± 1.0
Echocardiography	
LVEDD, mm	48.1 ± 4.7
LVEF, %	59.5 ± 5.9
Operations	
MVR, n (%)	137 (50.0%)
MVR and AVR, n (%)	94 (34.3%)
AVR, n (%)	43 (15.7%)
Number of INR values	4.8 ± 1.6
weekly doses of warfarin	20.6 ± 6.0

AVR, aortic valve replacement; MVR, mitral valve replacement; LVEDD, left ventricular end-diastolic dimension; LVEF, left ventricular ejection fraction; NYHA, New York heart association.

range divided by the total number of person-days on warfarin (10, 17). TTR was calculated by the Rosendaal linear interpolation method that assumes a linear relationship exists between two INR values and allows one to allocate a specific INR value to each day for each patient (10, 17). Enrolled patients were divided into the "poor" TTR (TTR < 60%) group and the "good" TTR (TTR ≥ 60%) group. The clinical characteristics of patients are shown in Table 2.

Data collection

The approach to follow-up is to review the electronic record system and conduct a telephone interview. The clinical data of patients include the type of mechanical valve, age, gender, INR values, intervals of INR monitoring, duration of anticoagulant management, warfarin dose, and anticoagulation-related complications.

Anticoagulation-related complications included major bleeding events, thromboembolic events, and death. Major bleeding events were defined as bleeding that should receive hospital treatment, such as cerebral hemorrhage, gastrointestinal hemorrhage, and hematuria. Other bleeding events, including epistaxis, gingival bleeding, and ecchymosis, were classified as minor bleeding events. Thromboembolic events include cerebral vascular embolism, systemic embolism, and atrial thrombosis. Death was evaluated by the medical record or a death certificate for relationship with bleeding or thromboembolism.

This retrospective study followed the tenets of Declaration of Helsinki and was approved by the ethics review board of Henan Province People's Hospital. A waiver of consent was received from them at the same time.

Statistical analysis

Continuous variables were described in the form of means ± standard deviation (SD) and were analyzed with Student's *t*-test. Categorical data were reported as rates and were analyzed with the chi-squared test. Independent predictors for TTR < 60% were evaluated with the logistic regression model. Variables with $p < 0.20$ in univariate analysis were incorporated into multivariate analysis. A two-sided $p < 0.05$ was regarded as statistically significant. The incidences of valve-related complications were reported by linearized rates. All data were analyzed with Statistical Package for Social Sciences (SPSS V17.0, Chicago, Illinois, United States).

Results

Two hundred and seventy-four patients were eligible for this study. As shown in Table 2, patients are classified based on their clinical characteristics. The mean age of these patients was 52.8 ± 12.7 years, 65.7% (180 cases) of them were female and 34.3% (94 cases) were male. The mean duration of warfarin therapy was 16.7 ± 28.1 months. Operations of these patients were as follows: 50.0% (137 cases) patients were performed mitral valve replacement (MVR), 15.7% (43 cases) were performed aortic valve replacement (AVR), and 34.3% (94 cases) were performed MVR and AVR.

A total of 1309 INR values were collected, representing 66789 patient days, each patient with a mean of 4.8 ± 1.6

TABLE 3 Univariate analyses of preoperative variables associated with TTR < 60%.

Characteristics	TTR < 60% (n = 121)	TTR ≥ 60% (n = 153)	p
Age, years)	53.3 ± 11.2	51.9 ± 13.8	0.227
Female, n (%)	91(75.3%)	89(58.2%)	0.010
Diabetes mellitus, n (%)	18(14.9%)	14(9.1%)	0.143
Hypertension, n (%)	19(15.7%)	22(14.4%)	0.760
Smoking, n (%)	25(20.7%)	21(13.7%)	0.127
Atrial fibrillation, n (%)	88(68.6%)	82(53.6%)	<0.001
NYHA ≥ III, n (%)	103(85.1%)	102(67.5%)	<0.001
Creatinine, μmoI/L	75.5 ± 16.6	71.3 ± 19.1	0.331
Total cholesterol, mmol/L	3.2 ± 0.8	3.3 ± 0.6	0.757
HbA1c, %	6.3 ± 1.1	5.9 ± 0.9	0.291
Echocardiography			
LVEDD, mm	47.8 ± 4.5	48.2 ± 4.8	0.679
LVEF, %	56.8 ± 6.1	60.5. ± 5.7	0.032
Operations			0.170
MVR, n (%)	66(54.5%)	71(46.4%)	
MVR and AVR, n (%)	34(28.1%)	60(39.2%)	
AVR, n (%)	21(17.4%)	22(14.4%)	
Number of INR values, n	4.6 ± 1.7	5.0 ± 1.5	0.153
weekly doses of warfarin, mg	19.8 ± 6.7	21.2 ± 5.8	0.258

AVR, aortic valve replacement; INR, international normalized ratio; MVR, mitral valve replacement; LVEDD, left ventricular end-diastolic dimension; LVEF, left ventricular ejection fraction; NYHA, New York heart association; TTR, time in the therapeutic range.

TABLE 4 Multivariate analysis of predictors of TTR < 60%.

Factors	Odds ratio	95% CI	p
Female	1.21	1.08–2.17	0.023
Atrial fibrillation	2.27	1.23–4.29	0.011

INR values. In this study, the mean TTR was 63.7% ± 18.6%, weekly doses of warfarin were 20.6 ± 6.0 mg/weekly, and the mean monitoring interval for the patient was 53.6 ± 27.1 days. There were 153 cases in good TTR group (TTR ≥ 60%) and 121 cases in poor TTR group (TTR < 60%). The calculated mean TTRs for both group were 42.6% ± 22.1% and 74.8% ± 10.4%.

Univariate analyses of preoperative variables associated with TTR < 60% are shown in Table 3. Compared with the TTR ≥ 60% group, the TTR < 60% group exhibited a more prevalence of female gender (p = 0.001), atrial fibrillation (p < 0.001), NYHA ≥ III (p < 0.001), and lower preoperative left ventricular ejection fraction (LVEF, p = 0.032). The mean age in the TTR ≥ 60% group was 51.9 ± 13.8, and the mean age in the TTR < 60% group was 53.3 ± 11.2; there was no statistical significance (p = 0.2227). Although the prevalence rates of diabetes mellitus (p = 0.143), hypertension (p = 0.760), and smoking (p = 0.127) in the TTR < 60% group were even higher, it was not statistically significant. In multivariate analysis, female gender (p = 0.023) and atrial fibrillation (p = 0.011) were associated with TTR < 60%. Multivariate analysis of predictors of TTR < 60% is shown in Table 4.

In this study, the average duration was 16.7 ± 28.1 months. There were three major bleeding events during follow-up: two cases of gastrointestinal bleeding and one case of cerebral hemorrhage. The occurrence rate of major bleeding events was 1.6% patient-years. There were two thromboembolic events: one case of cerebral embolism and one case of atrial thrombosis. The occurrence rate of thromboembolic events was 1.1% patient-years. There was one case of death which resulted from cerebral hemorrhage. The incidence of death was 0.5% patient-years. The difference in anticoagulation-related complications between the TTR < 60% group and the TTR ≥ 60% group was not statistically significant (p = 0.090, Table 5).

Discussion

In China, keeping high frequency (4-week intervals) of INR monitoring after discharging from the hospital is a significant challenge due to geographical restriction, limited economic resource, and less medical knowledge (18). To reduce patients' burdens of anticoagulant therapy, a longer interval of 12 weeks was used for patients with stable warfarin doses (5, 7). Studies have shown that longer intervals (> 4 weeks) for INR monitoring are non-inferior

TABLE 5 Characteristics of warfarin treatment during the study.

Characteristics	All patients (n = 274)	TTR < 60% (n = 121)	TTR ≥ 60% (n = 153)	p
Number of INR values	4.8 ± 1.6	4.6 ± 1.7	5.0 ± 1.5	0.153
Weekly doses of warfarin	20.6 ± 6.0	19.8 ± 6.7	21.2 ± 5.8	0.258
Mean monitoring interval, days	53.6 ± 27.1	58.1 ± 33.7	51.8 ± 20.1	0.069
Anticoagulation follow-up times, months	16.7 ± 28.1	18.9 ± 31.4	15.3 ± 26.8	0.171
Anticoagulation-related complications, n (%)	6(2.2%)	4(3.3%)	2(1.3%)	0.687
Major bleeding events, n	3	2	1	
Thromboembolic events, n	2	1	1	
Death, n	1	1	0	

INR, international normalized ratio; TTR, time in the therapeutic range.

to every 4 weeks in TTR with the incidence of anticoagulant complications (7). Meanwhile, owing to the dietary habit and pharmaceutical interferon, the short interval of 4 weeks will more than likely result in more unnecessary dose adjustment, which further destabilized the anticoagulant level (18, 19).

In our study, the average TTR for patients with a 12-week INR follow-up interval has reached to 63.7%. A majority of the previous studies have reported that it ranges between 40 and 78% (11, 12, 20, 21), even under clinical trials with point-of-care home monitoring or computer assisting dose system (11, 22). According to the previous studies, the anticoagulation-related complication is associated with TTR. Yet, there is no specific benchmark of TTR being regarded as completely safe (23, 24). In a study, a TTR of greater than 65% indicated an effective anticoagulation strategy. There existed a target threshold TTR (estimated between 58 and 65%) below which anticoagulation had little benefit (25). Another study found a reduction in the risk of stroke in patients with TTR over 60% and an improved survival rate in patients with TTR over 40% (24). According to Lee and colleagues (14), 90 patients who receive warfarin therapy with atrial fibrillation had an average TTR of 60.6%. In a study published by Hong and colleagues (26), 1,230 AF patients aged 70.1 ± 9.7 years were involved, and their mean TTR was only 49.1%. To sum up, compared with these studies, TTR in our study was acceptable. However, this result may be the consequence of sampling difference. In this study, a stable warfarin dose was administered to all participants for more than 12 months. Patients of not monitoring regularly, taking amiodarone, ethnic minorities, and younger than 18 years old were excluded as they may have a significant effect in anticoagulation quality.

This study has demonstrated that female gender and atrial fibrillation are associated with TTR < 60%. Avarello and colleagues (27) found a lower TTR in females than males in a large population of anticoagulated patients followed at a University hospital anticoagulant clinic. They indicated female is an independent predictor of poor TTR. Henderson and colleagues (28) reported female gender was associated with a 10.1% decrease in TTR. Apostolakis et al. (29) evaluated factors affecting quality of anticoagulation control among patients with vitamin K antagonist. They indicated that female gender were also more likely to have poor TTR values.

Although the occurrence rate of major bleeding and thromboembolic events was lower (1, 3), we do not think the management of anticoagulants in our study is better than others. Some studies showed that anticoagulation-related complications occurred more frequently in the first 6 months after surgery, especially bleeding events (30, 31). Besides that, it may be associated with the different criteria of bleeding and thromboembolic events or patient's medical knowledge (3, 30). Therefore, a low incidence rate of anticoagulation-related complications was found in our study, and it is not enough to evaluate the quality of patients.

There are some limitations in this study. First, it is a retrospective research and is a single-center study. Second, the result of TTR in this study is sampled from not a large number of patients. Third, the result of TTR is based on patients who had at least two INR values, and not all patients were included in the whole observation period. This point may also influence the results of TTR (20).

Conclusion

The study used TTR to evaluate the quality of anticoagulation management. There reached an acceptable result of TTR for patients with 12-week INR follow-up interval in stable PT monitoring results. We also found that female gender and atrial fibrillation were associated with TTR < 60%. However, future well-designed prospective studies with a large sample size and detailed analyses of anticoagulation-related complications are still warranted to confirm our findings.

Data availability statement

The original contributions presented in this study are included in the article/supplementary material, further inquiries can be directed to the corresponding author.

Ethics statement

The studies involving human participants were reviewed and approved by Henan Province People's Hospital. The patients/participants provided their written informed consent to participate in this study.

Author contributions

XZ and XX conceived and designed the experiments. XZ and SW performed the experiments. XZ and XC analyzed the data. XZ, GL, and XL contributed reagents, materials, and analysis tools. XZ wrote the manuscript. All authors contributed to the article and approved the submitted version.

Acknowledgments

We acknowledge the generous assistance of Qian Li for statistical analysis.

Conflict of interest

The authors declare that the research was conducted in the absence of any commercial or financial relationships that could be construed as a potential conflict of interest.

Publisher's note

References

1. Cannegieter SC, Rosendaal FR, Briët E. Thromboembolic and bleeding complications in patients with mechanical heart valve prostheses. *Circulation.* (1994) 89:635–41. doi: 10.1161/01.CIR.89.2.635

2. Takarada K, Sato M, Goto M, Saito A, Ikeda Y, Fujita S, et al. Long-term PT-INR levels and the clinical events in the patients with non-valvular atrial fibrillation: A special reference to low-intensity warfarin therapy. *J Cardiol.* (2014) 64:127–32. doi: 10.1016/j.jjcc.2013.11.015

3. Labaf A, Grzymala-Lubanski B, Stagmo M, Lövdahl S, Wieloch M, Själander A, et al. Thromboembolism, major bleeding and mortality in patients with mechanical heart valves- a population-based cohort study?. *Thromb Res.* (2014) 134:354–9. doi: 10.1016/j.thromres.2014.06.007

4. Witt DM, Delate T, Clark NP, Martell C, Tran T, Crowther MA, et al. Twelve-month outcomes and predictors of very stable INR control in prevalent warfarin users. *J Thromb Haemost.* (2010) 8:744–9. doi: 10.1111/j.1538-7836.2010.03756.x

5. Clark NP. Frequency of monitoring, non-adherence, and other topics dear to an anticoagulation clinic provider. *J Thromb Thrombolysis.* (2013) 35:320–4. doi: 10.1007/s11239-013-0887-y

6. Carris NW, Spinelli A, Pierini D, Taylor JR, Anderson KV, Sando K, et al. Feasibility of extended-interval follow-up for patients receiving warfarin. *Cardiovasc Ther.* (2015) 33:98–103. doi: 10.1111/1755-5922.12115

7. Schulman S, Parpia S, Stewart C, Rudd-Scott L, Julian JA, Levine M, et al. Warfarin dose assessment every 4 weeks versus every 12 weeks in patients with stable international normalized ratios: A randomized trial. *Ann Intern Med.* (2015) 155:653–9. doi: 10.7326/0003-4819-155-10-201111150-00003

8. Rose AJ, Ozonoff A, Berlowitz DR, Henault LE, Hylek EM. Warfarin dose management affects INR control. *J Thromb Haemost.* (2009) 7:94–101. doi: 10.1111/j.1538-7836.2008.03199.x

9. Rose AJ, Ozonoff A, Henault LE, Hylek EM. Warfarin for atrial fibrillation in community-based practise. *J Thromb Haemost.* (2008) 6:1647–54. doi: 10.1111/j.1538-7836.2008.03075.x

10. Rodriguez F, Hong C, Chang Y, Oertel LB, Singer DE, Green AR, et al. Limited English proficient patients and time spent in therapeutic range in a warfarin anticoagulation clinic. *J Am Heart Assoc.* (2013) 2:e000170. doi: 10.1161/JAHA.113.000170

11. Ansell J. Point-of-care patient self-monitoring of oral vitamin K antagonist therapy. *J Thromb Thrombolysis.* (2013) 35:339–41. doi: 10.1007/s11239-013-0878-z

12. Wan Y, Heneghan C, Perera R, Roberts N, Hollowell J, Glasziou P, et al. Anticoagulation control and prediction of adverse events in patients with atrial fibrillation: A systematic review. *Circ Cardiovasc Qual Outcomes.* (2008) 1:84–91. doi: 10.1161/CIRCOUTCOMES.108.796185

13. Ansell J, Hirsh J, Hylek E, Jacobson A, Crowther M, Palareti G. Pharmacology and management of the vitamin K antagonists: American College of Chest Physicians evidence-based clinical practice guidelines. *Chest.* (2008) 133:160S–98S. doi: 10.1378/chest.08-0670

14. Lee SL, Ong TJ, Mazlan-Kepli W, Mageswaran A, Tan KH, Abd-Malek AM, et al. Patients'time in therapeutic range on warfarin among atrial fibrillation patients in Warfarin Medication Therapy Adherence Clinic. *World J Cardiol.* (2021) 13:10. doi: 10.4330/wjc.v13.i9.483

15. Gallego P, Vilchez JA, Lane DA. Apixaban compared with warfarin for stroke prevention in atrial fibrillation. *Circulation.* (2013) 127:2163–5. doi: 10.1161/CIRCULATIONAHA.113.003132

16. Farsad BF, Abbasinazari M, Dabagh A, Bakshandeh H. Evaluation of time in therapeutic range (TTR) in patients with non-valvular atrial fibrillation receiving treatment with warfarin in Tehran, Iran: A cross-sectional study. *J Clin Diagn Res.* (2016) 10:FC04–06. doi: 10.7860/JCDR/2016/21955.8457

17. Schmitt L, Speckman J, Ansell J. Quality assessment of anticoagulation dose management: Comparative evaluation of measures of time-in-therapeutic range. *J Thromb Thrombolysis.* (2003) 15:213–6. doi: 10.1023/B:THRO.0000011377.78585.63

18. Zhou XM, Zhuang W, Hu JG, Li JM, Yu JF, Jiang L. Low-dose anticoagulation in Chinese patients with mechanical heart valves. *Asian Cardiovasc Thorac Ann.* (2005) 13:341–4. doi: 10.1177/021849230501300410

19. Fihn SD, McDonell MB, Vermes D, Henikoff JG, Martin DC, Callahan CM, et al. A computerized intervention to improve timing of outpatient follow-up: A multicenter randomized trial in patients treated with warfarin. National Consortium of Anticoagulation Clinics. *J Gen Intern Med.* (1994) 9:131–9. doi: 10.1007/BF02600026

20. Connolly SJ, Pogue J, Eikelboom J, Flaker G, Commerford P, Franzosi MG, et al. Benefit of oral anticoagulant over antiplatelet therapy in atrial fibrillation depends on the quality of international normalized ratio control achieved by centers and countries as measured by time in therapeutic range. *Circulation.* (2008) 118:2029–37. doi: 10.1161/CIRCULATIONAHA.107.750000

21. Mueller S, Pfannkuche M, Breithardt G, Bauersachs R, Maywald U, Kohlmann T, et al. The quality of oral anticoagulation in general practice in patients with atrial fibrillation. *Eur J Intern Med.* (2014) 25:247–54. doi: 10.1016/j.ejim.2013.12.013

22. Lee A, Crowther M. Practical issues with vitamin K antagonists: Elevated INRs, low time-in-therapeutic range, and warfarin failure. *J Thromb Thrombolysis.* (2011) 31:249–58. doi: 10.1007/s11239-011-0555-z

23. Aspinall SL, Zhao X, Handler SM, Stone RA, Kosmoski JC, Libby EA, et al. The quality of warfarin prescribing and monitoring in Veterans Affairs nursing homes. *J Am Geriatr Soc.* (2010) 58:1475–80. doi: 10.1111/j.1532-5415.2010.02967.x

24. Morgan CL, McEwan P, Tukiendorf A, Robinson PA, Clemens A, Plumb JM. Warfarin treatment in patients with atrial fibrillation: Observing outcomes associated with varying levels of INR control. *Thromb Res.* (2009) 124:37–41. doi: 10.1016/j.thromres.2008.09.016

25. Zubaid M, Saad H, Ridha M, Nair KKM, Rashed W, Alhamdan R, et al. Quality of anticoagulation with warfarin across Kuwait. *Hellenic J Cardiol.* (2013) 54:102–6.

26. Hong KS, Kim YK, Bae HJ, Nam HS, Kwon SU, Bang OY, et al. Quality of anticoagulation with warfarin in Korean patients with atrial fibrillation and prior stroke: A multicenter retrospective observational study. *J Clin Neurol.* (2017) 13:273–80. doi: 10.3988/jcn.2017.13.3.273

27. Avarello I, Bianchi S, Toschi V, Zighetti ML, Faioni EM. Time in therapeutic range is lower in women than in men and is not explained by differences in age or comorbidity. *Thrombosis Res.* (2021) 203:18–21. doi: 10.1016/j.thromres.2021.04.011

28. Henderson JB, Iyer P, Coniglio AC, Katz JN, Chien C, Hollis IB, et al. Predictors of warfarin time in therapeutic range after continuous-flow left ventricular assist device. *Pharmacother J Hum Pharmacol Drug Ther.* (2019) 39:1030–5. doi: 10.1002/phar.2324

29. Apostolakis S, Sullivan RM, Olshansky B, Lip GYH. Factors affecting quality of anticoagulation control among patients with atrial fibrillation on warfarin: The SAMe-TTR score. *Chest.* (2013) 144:1555–63. doi: 10.1378/chest.13-0054

30. Ansell J, Caro JJ, Salas M, Dolor RJ, Corbett W, Hudnut A, et al. Quality of clinical documentation and anticoagulation control in patients with chronic nonvalvular atrial fibrillation in routine medical care. *Am J Med Qual.* (2007) 22:327–33. doi: 10.1177/1062860607303003

31. Gross CP, Vogel EW, Dhond AJ, Marple CB, Edwards RA, Hauch O, et al. Factors influencing physicians' reported use of anticoagulation therapy in nonvalvular atrial fibrillation: A cross-sectional survey. *Clin Ther.* (2003) 25:1750–64. doi: 10.1016/S0149-2918(03)80167-4

frontiers | Frontiers in Cardiovascular Medicine

TYPE Original Research
PUBLISHED 23 September 2022
DOI 10.3389/fcvm.2022.1004968

OPEN ACCESS

EDITED BY
Ruizheng Shi,
Central South University, China

REVIEWED BY
Yu Lu,
Shenzhen Technology University, China
Bijiao Ding,
Huaqiao University Affiliated Strait Hospital, China
Yucheng Song,
Central South University, China

*CORRESPONDENCE
Jianhuang Wu
jh.wu@siat.ac.cn

SPECIALTY SECTION
This article was submitted to Cardiovascular Imaging, a section of the journal Frontiers in Cardiovascular Medicine

RECEIVED 27 July 2022
ACCEPTED 06 September 2022
PUBLISHED 23 September 2022

CITATION
Wang H and Wu J (2022) A time-dependent offset field approach to simulating realistic interactions between beating hearts and surgical devices in virtual interventional radiology.
Front. Cardiovasc. Med. 9:1004968.
doi: 10.3389/fcvm.2022.1004968

A time-dependent offset field approach to simulating realistic interactions between beating hearts and surgical devices in virtual interventional radiology

Haoyu Wang[1,2] and Jianhuang Wu[1,2]*

[1]Shenzhen Institutes of Advanced Technology, Chinese Academy of Sciences, Shenzhen, China, [2]Shenzhen College of Advanced Technology, University of Chinese Academy of Sciences, Shenzhen, China

Endovascular interventional radiology (IR) is a minimally invasive procedure for the treatment of vascular diseases. This procedure requires physicians to be highly skilled at manipulating interventional devices under the guidance of two-dimensional X-ray imaging. By offering a non-error-sensitive and radiation-free environment, a virtual reality-based simulator provides a promising alternative for surgical skills training and surgery planning. Building a realistic and interactive simulator is a challenging task. To achieve better realism, this paper proposes a novel method of simulating the heartbeat for both standard and patient-specific anatomical data. A time-dependent offset field approach is proposed to efficiently and stably simulate the interactive behavior between the dynamic heart mesh and surgical devices. For medical imaging simulation, we propose a GPU-based linear depth subtraction method to approximate fluoroscopic images based on the attenuation of the X-ray. On this basis, a topology-based flow map method is proposed to simulate the propagation of the contrast medium in angiography. Experimental results show that the proposed algorithm can simulate heartbeat stably for meshes with varying geometrical shapes and complexities. In efficiency, the dynamic heart mesh can interact with surgical devices stably at 60 frames/s. Under the simulated fluoroscopic imaging effect, the injected contrast medium can realistically visualize both dynamic and static vessels. In a face validity by medical students and clinicians, the category of effectiveness score 8.35 out of 10 on average, demonstrating that our simulator is useful in surgical skills training and surgery planning.

KEYWORDS

virtual reality, interventional radiology, heartbeat simulation, angiography, skills training, surgery planning

Introduction

Background

In recent decades, endovascular procedures have gained increasing popularity because of their advantages over traditional open surgeries, such as minimum invasiveness, short hospital stays, and fewer complications. However, these procedures require physicians to be highly skilled at manipulating surgical devices under the guidance of two-dimensional X-ray imaging. In addition to achieving a complex understanding of three-dimensional anatomy from two-dimensional displays, physicians must spend years of practice acquiring good hand-eye coordination (1). Traditional training methods (e.g., apprenticeships on patients, using human cadavers or live animals, and employing phantoms) are risky, expensive, and restricted to limited morphological models (2). Moreover, exposure to radiation during these training processes harms trainees' health.

Interactive virtual reality-based simulators provide a promising solution that addresses all the above difficulties by offering a non-error-sensitive and radiation-free environment in which physicians can practice surgical skills repeatedly (3–5). Research (6) has shown that experiences in simulator training can increase medical students' enthusiasm for interventional radiology (IR). A recent study (7) demonstrated that patient-specific procedure rehearsal can effectively improve surgical performance and patient outcomes.

Challenges

Building a realistic interventional simulator for surgical skills training and preoperative rehearsal is a challenging task. Realism, real-time interaction, and the capability of processing patient-specific data are the essential features of such a simulator.

Heartbeat is the vital sign of a live person. Most simulators (8) proposed in recent decades use static polygonal meshes to represent the patient's circulatory system. The absence of heartbeat results in a lack of realism. However, real-time heartbeat simulation is a challenging task. Most research (9) on this subject focuses on the numerical analysis of hemodynamic and cardiac electrophysiology instead of real-time soft tissue deformation. Therefore, these simulation results cannot be used in interactive applications. Moreover, the heart meshes used in these works are crafted to preserve ventricles, atriums, and valves for complicated mathematical modeling. In contrast, the morphological details of the heart mesh in interventional simulators are limited by the quality of patient-specific computerized tomography (CT) images. Without extra artificial intervention, only the outer surface of the heart and its nearby coronary arteries can be reconstructed. Thus, most of the existing modeling methods cannot be adopted in real-time heartbeat simulation. Handcrafted animations are used in some simulators (10, 11) to achieve higher fidelity, but they are not applicable to patient-specific data. Some work (12) has used 4D (3D + time) CT images to create animated heart meshes. Although better realism is achieved, the access requirement for specific types of images limits this method's feasibility. As described, realistic and real-time heartbeat simulation for patient-specific data is a challenging but essential task.

The collision detection and response between the dynamic heart mesh and surgical devices is another challenging task (13). Unlike other interactive applications (e.g., video games), the primitive of collision detection in an IR simulator is the triangular facet that composes vascular meshes. On the one hand, the time variation of heart mesh vertices makes collision detection computationally intensive, although many optimization techniques (14) have been proposed to improve the efficiency and accuracy of continuous collision queries. On the other hand, the frequent change in boundary conditions makes it difficult to keep the simulation of the surgical devices stable.

The realism of medical imaging simulation is another criterion used to evaluate an IR simulator. Existing methods (15, 16) use volumetric rendering techniques to simulate X-ray imaging based on three-dimensional image data. Polygonal mesh-based methods (17) that utilize the programmable pipeline of a GPU are also proposed. In these methods, centerlines or hierarchical tree structures are created for vascular meshes to simulate digital subtraction angiography (DSA). With the assumption that all vascular meshes are static, these methods cannot properly handle a dynamic circulatory system involving beating heat meshes.

Our contributions

In this paper, a simplified heartbeat model is proposed to simulate real-time heartbeat for patient-specific data. The interactive behavior of surgical devices and dynamic heart meshes is simulated stably by the proposed time-dependent offset field approach. A linear depth subtraction algorithm is proposed and implemented in the GPU for the real-time simulation of X-ray imaging. Based on the vascular meshes' topological adjacency information, a blood flow map is generated to simulate the propagation of the contrast medium under virtual fluoroscopy. Experimental results demonstrate that the heartbeat can be simulated realistically and efficiently for heart models reconstructed from patient-specific data and that the simulated surgical devices interact with the dynamic heart meshes stably in real-time. Face validity by medical students and physicians indicates the feasibility of the proposed simulator in surgical skills training and procedure rehearsal.

Our contributions can be summarized as follows:

1) We propose an efficient and robust heartbeat simulation method for standard and patient-specific anatomical models to achieve higher fidelity in the IR simulator.
2) We propose a time-dependent offset field to simulate the interactive behavior of the dynamic heart mesh and surgical devices.
3) We propose a linear depth-based approach to simulate fluoroscopy in the GPU and a topology-based flow map method to simulate the propagation of contrast medium in DSA.

Related work

Much work on the development of virtual reality-based simulators has been done since Anderson et al. (18) first proposed their interventional simulator in 1996. Then, Wang et al. (19) proposed a simulator for percutaneous coronary revascularization procedures. They represented the vasculature with a centerline hierarchy model and simulated the behavior of surgical devices with the finite element method (FEM). Dawson et al. (10) also proposed a simulator, called ICTS, for interventional cardiology training. In this simulator, a multibody system is used to represent a catheter and guidewire. A polygonal model associated with the X-ray attenuation coefficient was used to simulate the fluoroscopic visual effect. In the simulator proposed by Cotin et al. (20) an incremental FEM is used to simulate the interaction between devices and the vascular model. An optimization strategy based on substructure decomposition is used to ensure real-time efficiency. In medical imaging simulation, a volume rendering method was proposed to approximate fluoroscopic imaging. Also, Korzeniowski et al. (21) proposed their interventional simulator in which a particle model (22) with adaptive radius was used to simulate the propagation of the contrast medium. Wang et al. (17) proposed a physics-based virtual reality simulator to simulate a guidewire and catheter. An RGB-encoded depth technique was used to approximate the X-ray imaging effect. In addition, they built a hierarchy tree of the vessels with centerline and radius information to simulate the propagation of the radiology contrast medium. Li et al. (23) built a personalized percutaneous coronary intervention simulator. For simulating heartbeat, myocardial fiber orientations are constructed to represent the cardiac dynamic characteristics. In an interventional electrocardiology training system proposed by Talbot et al. (12), 4D heart images were used to create an animated heart mesh, and a bounding volume hierarchy (BVH) proximity approach was proposed to ensure the efficiency and continuity of collision detection.

In addition to simulators proposed by research institutes and universities, there are some commercial interventional simulators (24). Mentice, Surgical Science (formerly Simbonix), and CAE have released commercial interventional simulators: the VIST series (25), ANGIO Mentor (26), and CathLabVR (11), respectively.

Most existing simulators use static polygonal meshes or hierarchical centerlines to represent the vasculature, limiting the realism of the simulation. Although some works (10, 11) use handcrafted animation created with computer-aided design software (Maya, Blender, etc.) to gain higher fidelity, this is not a feasible solution for patient-specific procedure rehearsal. Wu et al. (27) proposed a spatial distortion method to approximate the motion of the heart and the surgical devices inside. However, this method also distorts the heart's nearby anatomical models, resulting in severe artifacts. The behavior of surgical devices within animated heart meshes is simulated well in (12) based on a BVH that is updated in each simulation step. However, this simulation requires access to the patient's 4D heart images. Similarly, the heartbeat simulation in (23) also depends on the ECG and US data in addition to CT images. These methods bring extra constraints on the data source.

For medical imaging simulation, the volume rendering-based method proposed by Muniyandi et al. (15) approximates fluoroscopic images by tuning the parameters of the transfer function. Its efficiency drops greatly as the volume size increases. The X-ray simulation method proposed in (17) uses only polygonal meshes to generate essential information for creating fluoroscopic images. However, their DSA simulation algorithm is dependent on hierarchical vascular centerlines, the extraction of which from triangular meshes is another popular research subject (28).

In contrast to Dawson et al. (10) and Talbot et al. (12), the heartbeat simulation method proposed in this paper is built upon a simplified heartbeat model using triangular meshes. Without the requirement of having access to specific types of original images, our method provides better efficiency and flexibility for patient-specific procedural simulation. Instead of constantly updating the BVH (12), the surgical device behavior within the beating heart mesh is simulated with a novel time-dependent offset field method. The reasonable tradeoff between computational resources and memory space ensures the realism, efficiency, and robustness of our simulation. For X-ray imaging, our method is based on the linear depth of the triangular meshes. Realistic fluoroscopic images for both static and dynamic models are generated in real-time. Unlike (17, 21), the proposed angiography simulation method is based on the intrinsic topology information of triangular meshes. Without requirements for a centerline or tree structure representation of the vasculature, our method is more flexible for handling vascular meshes with various morphological features. Experiments and user evaluation results show that our simulator can simulate interventional procedures realistically in real time.

Methodology

As illustrated in Figure 1, the workflow of our simulator has two paths: one for surgical skills training and the other for procedure rehearsal. Each path is divided into two consecutive stages. The anatomical models are prepared at the pre-simulation stage, while the surgical procedures are simulated at the simulation stage.

Surgical skills training

A collection of clinical cases specialized for training certain types of interventional surgical skills are built. The case files include surgical devices, anatomical models, and optionally patient CT and/or magnetic resonance image (MRI). The simulator imports the digital resources of the selected training case to initiate the simulation. Note that, the CT/MRI images help trainees understand the anatomy's morphological features for educational purposes. These images are not necessary for the surgery simulation itself.

Procedure rehearsal

Instead of being imported directly from prebuilt training case files, the anatomical models used for patient-specific procedure rehearsal must be reconstructed from the patient's CT/MRI image data. The binary masks for the anatomy of interest are first segmented from the input raw images. Then, the segmentation results are used to reconstruct the anatomical triangular meshes. Before being imported for procedure simulation, the reconstructed meshes must be optimized to gain better performance. After selecting the proper surgical devices, physicians can start the patient-specific procedure simulation to rehearse the upcoming surgery.

In this section, we first describe the acquisition of anatomical models for patient-specific data (see section "Anatomical mesh acquisition"). Then, the methods for heartbeat simulation (see section "Heartbeat simulation"), surgical device simulation (see section "Surgical device simulation"), and fluoroscopic simulation (see Section "Fluoroscopy simulation") are described in sequence.

Anatomical mesh acquisition

The triangular meshes used in our simulator are generated from patient CT images. The process uses two consecutive steps: image segmentation and 3D reconstruction. As a complex task in medical analysis, medical segmentation takes original CT/MRI images and outputs volumetric binary images for the anatomy of interest. Many traditional and deep learning-based methods of medical image segmentation have been proposed over the last several decades (29). Based on our previous work (30, 31), we use a global context network to produce

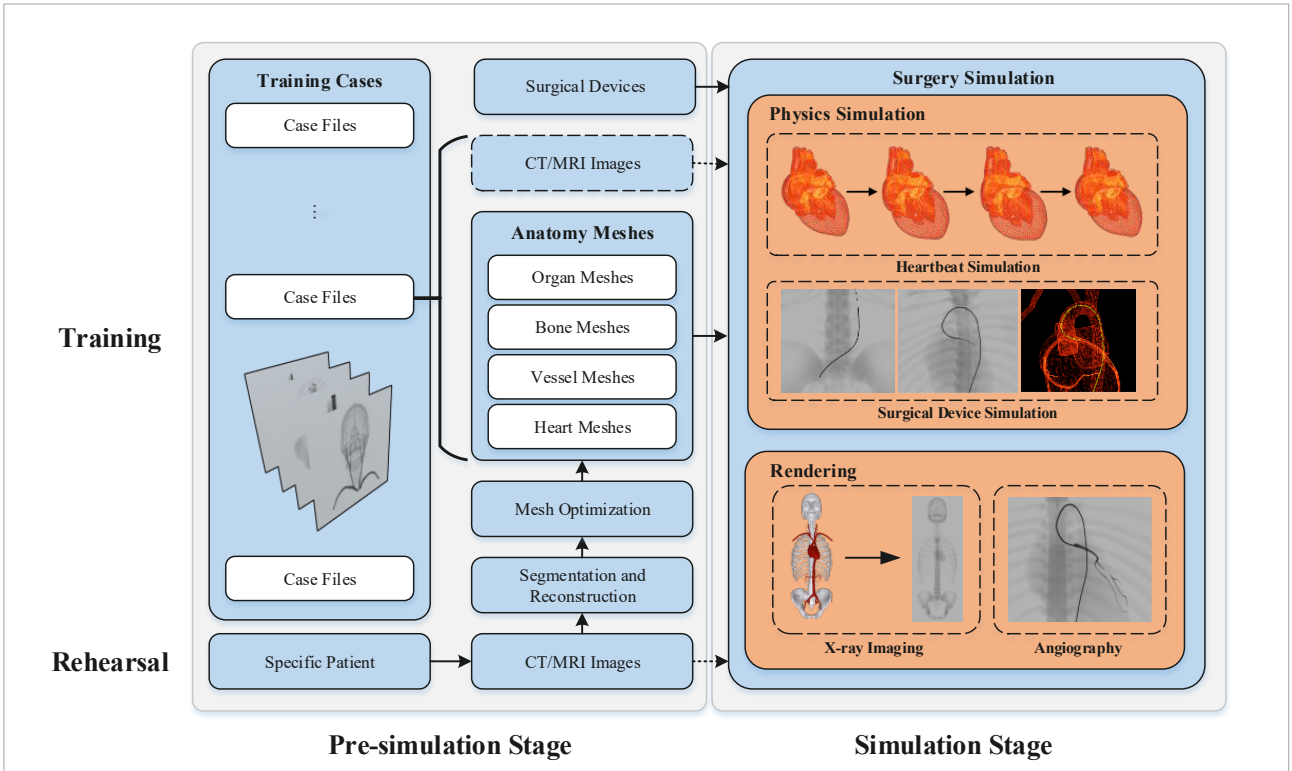

FIGURE 1
Workflow of our interventional simulator.

representative features of the target anatomy and aggregate the contextual information with two attention modules. With the deep learning-based method, the anatomy of interest can be effectively and efficiently segmented.

3D reconstruction takes the volumetric binary images generated in the previous step and creates triangular meshes. Research on 3D reconstruction from medical images has been a popular subject for decades (32, 33). Based on our previous work (34), an adaptive curvature-based method is used to reconstruct the vascular meshes.

Meshes reconstructed from volumetric binary images cannot be directly used for rendering and physics simulation in our simulator. Optimizations including smoothing, simplification, non-manifold edge fixing, and hole filling must be performed before the simulation starts. First, mesh smoothing methods are used to remove the stair artifacts induced by reconstruction algorithms such as the marching cube. Second, the original reconstructed mesh usually consists of an excessive number of facets, which leads to extra computational cost with little improvement in rendering realism and simulation accuracy. Simplification methods are used to reduce the number of facets while preserving the meshes' intrinsic geometrical details. Third, our DSA simulation algorithm (see Section "Fluoroscopy simulation") requires the mesh geometry to be a non-manifold to achieve fast and accurate flow map generation. Therefore, all non-manifold edges introduced at the reconstruction stage need to be fixed. Last, our X-ray imaging simulation method assumes that all rendered meshes are closed. Meshes with holes will cause rendering artifacts because their linear depth (thickness) cannot be calculated correctly.

Heartbeat simulation

As depicted in **Figure 2**, the heartbeat is simulated in three steps. Below, we elaborate on all the steps in details.

Step 1: Isolate the heart mesh

First, the reconstructed circulatory system is represented by one triangular mesh in which the heart and its biologically connected vessels (the aorta, pulmonary veins, etc.) are also linked topologically. Compared with the magnitude of the heartbeat, the movement of most arterial vessel walls (pulse) is too small to be visually perceived. Therefore, only the heart and its nearest vessel meshes are used for heartbeat simulation, and the rest of the vasculature is considered static in this paper. With this approximation, the mesh for heartbeat simulation is disconnected from the remaining vascular mesh and used as input for the subsequent algorithm, as shown in **Figure 2**.

Step 2: Simulate the heartbeat

The human heart consists of four chambers: two atria and two ventricles. The heart beats because of the contraction and relaxation of the heart muscle. The contraction makes the volume smaller, while the relaxation does the opposite. To approximate this phenomenon, an imaginary point is placed at the geometrical center of each heart chamber. A periodic force in the direction of this point is then exerted on the chamber mesh's vertices to simulate the volume change of this chamber.

Based on the work of Wang et al. (35), we use a simplified model of the heartbeat, two piecewise trigonometric functions, to describe the contraction and relaxation of the atrium and ventricle. A cardiac cycle is divided into eight deformation stages. For the atrium, the function is defined as:

$$\varphi_{\mathbf{Atrium}} = \begin{cases} \cos(\pi \cdot \mathbf{t}), \mathbf{t} \in [\mathbf{0}, \mathbf{1}) \\ \cos\left(\pi \cdot \mathbf{t}/7 + \frac{6}{7}\pi\right), \mathbf{t} \in [\mathbf{1}, \mathbf{8}) \end{cases}$$

For the ventricle, the function is defined as:

$$\varphi_{\mathbf{Ventricle}} = \begin{cases} \cos\left(\pi \cdot \mathbf{t}/5 + \frac{44}{25}\pi\right), \mathbf{t} \in [\mathbf{0}, \mathbf{1}) \\ \cos\left(\pi \cdot \mathbf{t}/3 - \frac{2}{5}\pi\right), \mathbf{t} \in [\mathbf{1}, \mathbf{4}) \\ \cos\left(\pi \cdot \mathbf{t}/5 + \frac{4}{25}\pi\right), \mathbf{t} \in [\mathbf{4}, \mathbf{8}) \end{cases}$$

The force exerted on the vertex of the chamber with index i is defined as:

$$\boldsymbol{F_i} = \boldsymbol{k}(|\boldsymbol{x_c} - \boldsymbol{x_i}|) \cdot \frac{\boldsymbol{x_c} - \boldsymbol{x_i}}{|\boldsymbol{x_c} - \boldsymbol{x_i}|} \cdot \boldsymbol{\varphi}$$

where $\mathbf{x_i}$ is the vertex position, $\mathbf{x_c}$ is the geometric center of the chamber, and k is the elastic coefficient. To obtain a smooth surface during deformation, we add two stretching constraints: the distance between adjacent vertices and the distance from a vertex's current position to its initial position (36). Additionally, volume conservation constraints are added to preserve the heart volume during deformation. Within the framework of position-based dynamics (PBD) (37), the stable shapes of the heart for a complete cardiac cycle can be calculated iteratively.

The experimental results (see section "Heartbeat simulation") demonstrate that the heartbeat can be simulated in real time for meshes within a limited number of vertices. Nevertheless, the simulation is computationally intensive, and its efficiency drops as the number of vertices increases. As another key component of a realistic IR simulator, the simulation of surgical devices also requires numerous computations. The finite CPU resources must be distributed properly to ensure the real-time efficiency of the whole simulation. The deformation of the heart repeats itself periodically. If the parameters of the simulation remain the same, it is not necessary to repeatedly calculate the shapes of the heart except in the first cardiac cycle. To achieve higher efficiency and reserve enough computational resources for the surgical device simulation, a time-dependent offset field is created to cache the simulation results of a complete cardiac cycle for rendering and subsequent simulation.

As illustrated in **Figure 3**, a list of heart meshes $(S_1, S_2, \ldots, S_M)$ is sampled from the simulation results for the first complete cardiac cycle. The first sample S_1 is selected as

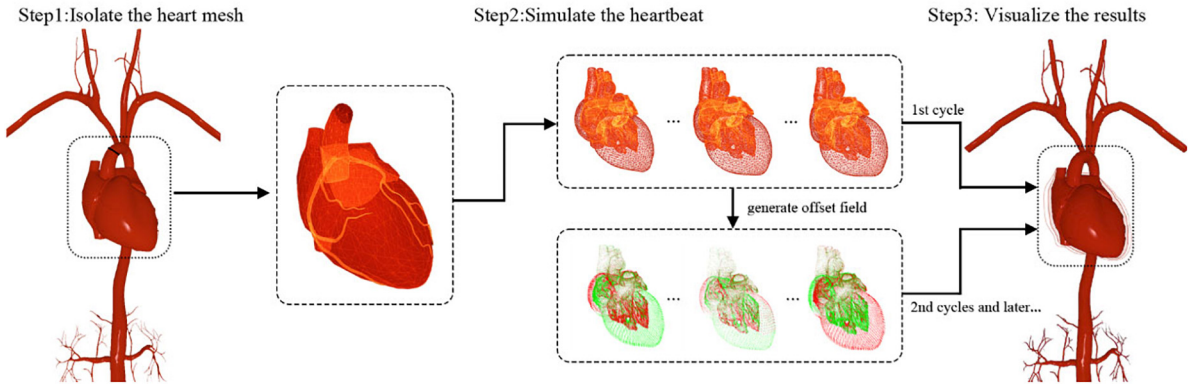

FIGURE 2
Heartbeat simulation and visualization.

the base mesh, whose vertex position is treated as the baseline for offset. For the ith vertex $\mathbf{v}_i^j$ of the jth sample mesh, the positional offset $\boldsymbol{\sigma}_i^j$ from its counterpart $\mathbf{v}_i^1$ in the baseline mesh can be calculated as $\boldsymbol{\sigma}_i^j = \mathbf{v}_i^j - \mathbf{v}_i^1$. The offset vectors are depicted with short colored lines in **Figure 3**. The vector in red is in the same direction as the normal of the vertex, indicating that the chamber's volume increases due to heart muscle relaxation. Conversely, the vector in green points in the opposite direction of the vertex normal, indicating a decrease in the chamber's volume caused by the contraction of the heart muscles. The periodic change of the heart chamber's volume results in a realistic heartbeat simulation. For a cardiac cycle, the direction and magnitude of the offset vectors change over time due to the deformation of the heart mesh, forming a time-dependent offset field in 3D space.

Step 3: Visualize the results

As depicted in **Figure 2**, the simulation results are visualized with different inputs for the first and subsequent cardiac cycles. In the first cycle, the deformed heart meshes are calculated and used to generate the time-dependent offset field. These meshes are uploaded to the GPU for visualization. Starting in the second cycle, the instantaneous offset vector for a vertex of the heart mesh can be fetched from the newly generated offset field with the vertex index i and a normalized time parameter $t \in (0, 1)$. By adding this offset vector to the position for every vertex of the base mesh, we can calculate the shape of the deformed heart at any instant of a cardiac cycle at a low computational cost. Moreover, the calculation can be further optimized by uploading the offset field to the GPU and adding offset vectors in parallel for each vertex.

As mentioned above, the offset field remains invariant unless the parameters of the heartbeat simulation change. Hence, for a cardiac cycle, the heart meshes are calculated once, and the results are cached by creating a time-dependent offset field. The subsequent heartbeat simulation and visualization run completely in the GPU, reserving sufficient computational resources in the CPU for surgical device simulation.

With this method, the heartbeat for any patient-specific data can be simulated realistically and efficiently. Note that, the magnitude and rate of the heartbeat can be changed by tuning the parameters to simulate the human body's reaction to stimulation in surgical procedures.

Surgical device simulation

One of the most important tasks in building an IR simulator is simulating the interactive behavior between the circulatory system and surgical devices. As explained in section "Anatomical mesh acquisition," we represent the circulatory system with triangular meshes that are suitable for rendering and collision detection. For different types of interventional devices, which in most cases are long, thin, and hollow, we model them as rigid rods linked by points $(\mathbf{p_0}, \mathbf{p_1}, \mathbf{p_2}, \ldots, \mathbf{p_n})$ that carry the discretized material properties (38). Based on Hook's law, we formulate the total energy of the device-circulatory system. By iteratively minimizing the total energy, we calculate the devices' equilibrium shape, which is represented as a list of 3D positions $(\mathbf{x_0}, \mathbf{x_1}, \mathbf{x_2}, \ldots, \mathbf{x}_n)$.

Instead of constantly performing collision detection, which is very time-consuming for an algorithm with $O(n^3)$ time complexity such as ours, we propose a deviation-feedback approach to update the external forces exerted on the device centerline points as in (39). With an adaptive feedback coefficient based on the centerline points' historical displacements, the simulation converges within fewer iterations, and the simulated device behaves stably in vascular models with complex morphological features.

In endovascular procedures, multiple interventional devices (guidewire, catheter, etc.) are usually manipulated in turn to reach certain places in the circulatory system. To represent

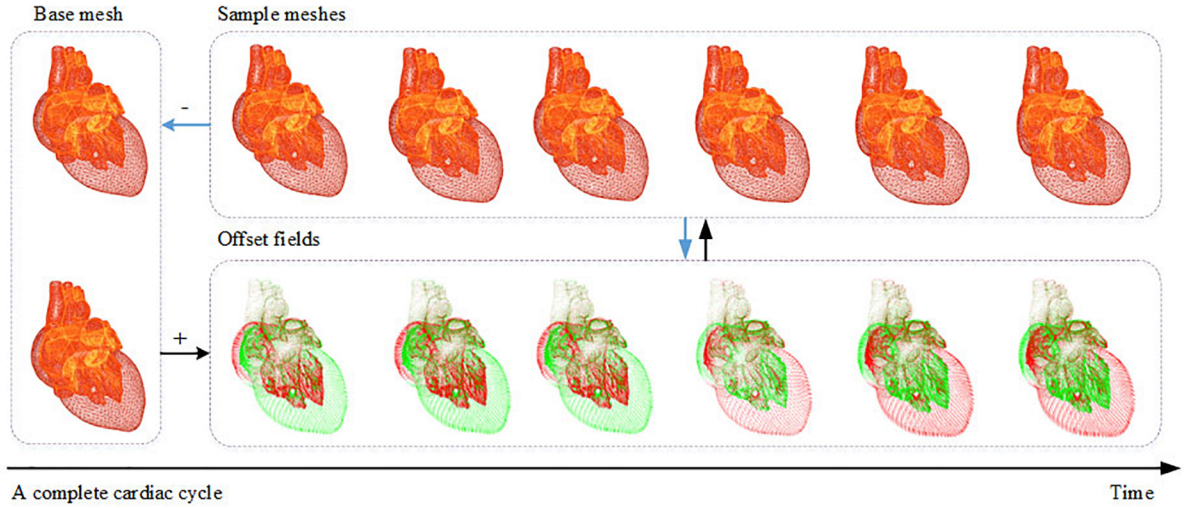

FIGURE 3
Generation of the time-dependent offset field.

nested interventional devices, we propose a shared-centerline model in which the centerline points are shared while their material properties are blended. With this model, the interaction between nested interventional devices is simulated by dynamically blending the material properties of the shared centerline points.

With the incorporation of the heartbeat, the circulatory system now comprises static vascular meshes and a dynamic heart mesh. When they are advanced into the heart area, the simulated interventional devices must interact with the dynamic mesh realistically and stably in real time. The shape of an interventional device is maintained when it collides with vessel walls. It is observed that the devices tend to move along with periodically moving vessel walls instead of bouncing back and forth inside the vascular tunnels of the beating heart mesh. Utilizing the time-dependent offset field, we propose a visual-deviation method to simulate the synchronous movements of surgical devices and the beating heart. The method is explained in Algorithm 1.

Simulation stage:
For each point $\boldsymbol{p_i}$ in device centerline D_p:
    Perform collision detection between $\boldsymbol{p_i}$ and the baseline mesh S_1 to obtain the spatial neighbor vertex index collection C_i of $\boldsymbol{p_i}$.
Calculate the stable shapes of the devices $(\boldsymbol{x_0}, \boldsymbol{x_1}, \boldsymbol{x_2}, ..., \boldsymbol{x}_n)$.
Visualization stage:
Obtain the normalized time parameter t of the heartbeat.
For each point $\boldsymbol{p_i}$ in the device centerline:
    For each vertex index j in C_i:
        Obtain the offset vector $\boldsymbol{\sigma_j}(t)$ for vertex $\boldsymbol{v_j}$ of mesh S_1 from the offset field at time t.
    Calculate the visual offset $\boldsymbol{\delta_i}(t) = \frac{1}{n}\sum_{j=1}^{n} \boldsymbol{\sigma_j}(t)$.
Calculate the new device centerline D_r by adding $(\boldsymbol{\delta_0}, \boldsymbol{\delta_1}, \boldsymbol{\delta_2}, ..., \boldsymbol{\delta_n})$ to $(\boldsymbol{x_0}, \boldsymbol{x_1}, \boldsymbol{x_2}, ..., \boldsymbol{x}_n)$.
Render D_r.

Algorithm 1. Simulation of the interaction between surgical devices and beating heart meshes.

When the simulation starts, the baseline mesh in the heartbeat simulation is used to perform collision detection and calculate the stable shape of the device centerline. Meanwhile, we can obtain the neighboring vertices of the heart mesh for each point $\mathbf{p_i}$ of the centerline. Thus far, the calculated device centerline is static. To make the devices move synchronously along with the beating heart, a time-dependent offset vector is added to every point of the centerline based on the progress of the heartbeat, as shown in Figure 4A.

For example, $\mathbf{x_i}$ is the stable position of point $\mathbf{p_i}$ on the centerline. There are n vertices of the mesh S_1 in the spatial neighborhood of $\mathbf{p_i}$, and their indices are $C_i = \{c_1, c_2 c_n\}$. The instantaneous offset vector $\boldsymbol{\sigma_j}(t)$ for the heart mesh vertex with index $j \in C_i$ at time t can be retrieved directly from the time-dependent offset field generated in the heartbeat simulation. The

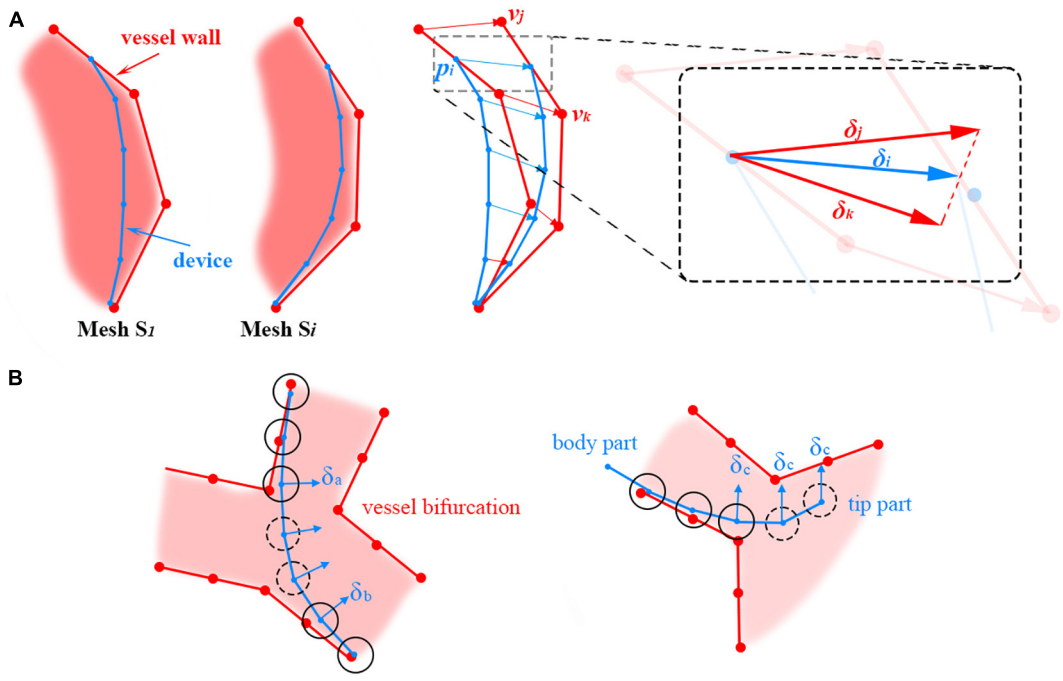

FIGURE 4
(A) Adding positional deviations to the device centerline to make it move along with the beating heart. **(B)** Offset vector calculation for centerline points (floating points) without the surrounding heart mesh vertices. The floating and non-floating points of the centerline are circled with dotted and solid lines, respectively.

average offset vector for the vertices in C_i is calculated and then added to $\mathbf{x_i}$ to visually deviate the centerline to synchronize the movement of the devices and the heartbeat.

In the simulation, there are centerline points that are not directly in collision with vessel walls. Thus, no heart mesh vertices can be found in their close neighborhoods, and their offset vectors cannot be directly calculated from the offset field. For brevity, these points are referred to as 'floating' points. Floating points are usually located on a sharp curve at vessel bifurcations and at the tip of the device; they are circled with dotted lines in **Figure 4B** left and right, respectively. Different methods are used to calculate the offset vectors of these floating points under these two circumstances. For floating points in the middle of the device centerline, the offset vectors are calculated by interpolating their adjacent non-floating points' offset vectors $\boldsymbol{\delta_a}$ and $\boldsymbol{\delta_b}$, as shown in **Figure 4B** left. Smooth transitions between the line segments separated by the floating points can be obtained in this way. For floating points at the tip of the device centerline, the offset vector $\boldsymbol{\delta_c}$ for the closest non-floating point is used directly, as shown in **Figure 4B** right.

In summary, the baseline mesh for heartbeat simulation is used for collision detection and surgical device centerline calculation. Utilizing the time-dependent offset field, the surgical device centerline is visually deviated to synchronously move with the beating heart, resulting in realistic, efficient, and stable simulation results for the interactive behavior between surgical devices and the dynamic heart mesh.

Fluoroscopy simulation

As an important part of IR procedures, fluoroscopy is a continuous X-ray imaging technique that shows the movement of a body part (e.g., heart) or the course that a medical instrument or dye (contrast medium) takes as it travels through the body (40). In this paper, we propose a geometry-based method to simulate X-ray imaging. On this basis, we propose a topology-based flow map method to simulate the propagation of the contrast medium under the fluoroscope.

X-ray imaging simulation

Based on the physics of X-ray imaging (41), an X-ray image shows the variations in transmission caused by structures in an object of varying thickness, density, or atomic composition. To approximate different anatomies' attenuation in X-ray imaging, we introduce a weighted thickness variable μ, which is defined as $\mu = sd$, where s and d are the weight and linear thickness of the anatomy, respectively.

The proposed X-ray imaging simulation method takes two render passes: one for creating the weighted thickness

texture for all anatomical models and the other for creating fluoroscopic images.

Pass 1: Create the thickness texture

In this pass, the linear thickness d of the rendered anatomy model is first calculated for each pixel by subtracting its front faces' linear depth from that of its back faces. The formula is defined as $d = z_{back} - z_{front}$, where z_{front} and z_{back} are the z components of the pixel's camera space position for the front and back faces, respectively. Then, the thickness is multiplied by the anatomy-specific weight value s. The weighted thicknesses for all rendered anatomies are summed, and the results are written to a rendered texture (target) in float format. In this way, the sum of the weighted thickness for any pixel can be read directly from the texture.

Pass 2: Create the fluoroscopic image

In this pass, the grayscale g for each pixel is calculated based on the attenuation formula, defined as

$$\mathbf{g} = \mathbf{e}^{-\mathbf{a}\sum\boldsymbol{\mu}}$$

where a is the uniform attenuation factor and $\sum\mu$ is the summed weighted thickness obtained from the texture created in the first render pass. By selecting proper values of the weight s for different anatomies, X-ray imaging can be simulated realistically at a very low cost.

Note that, the depth value in the camera space is used for the thickness calculation because the normalized depth value retrieved directly from the Z-buffer of the rendering pipeline is non-linear and suffers from precision problems. Because both the front and back faces are needed to calculate the thickness, all triangular meshes must be closed. Otherwise, there will be artifacts in the holes of the unclosed meshes.

Unlike existing image-based methods, the proposed algorithm for X-ray imaging simulation takes only triangular meshes as input and runs in parallel at the pixel stage of the rendering pipeline, ensuring real-time efficiency. Moreover, the vertices of the heart mesh are offset for heartbeat rendering at the vertex stage, the output of which can be used directly as input for the pixel stage to simulate X-ray imaging. The coherency of the pipeline means that our method works for both static and dynamic meshes.

Digital subtraction angiography simulation

Digital subtraction angiography is a fluoroscopic technique used extensively in IR for visualizing blood vessels. Contrast medium is injected into the vasculature through catheters, and the affected blood vessels are visually enhanced in dark gray. DSA is one of the most commonly used techniques in IR, and it is necessary to realistically simulate this procedure for building a simulator with high fidelity.

The contrast medium propagates downstream with the blood flow from the tip of the angiography catheter. Only the vasculature that the contrast medium flows through can be visualized. In this paper, a gradient-based region growing method is proposed to simulate this process with triangular meshes. The idea is to find the submesh that is affected by the contrast medium and render it progressively under the fluoroscope to approximate the propagation of the contrast medium. This method can be divided into three steps.

Step 1: Build the flow map of the arterial blood

To create the downstream vascular mesh visualized by the contrast medium, the direction of the blood flow must be calculated everywhere in the circulatory system. In this paper, an attribute called a 'sequence' is introduced for the triangular facets. The gradient of the sequence approximates the direction of the blood flow nearby. After the sequences for all facets are calculated, a blood flow map can be built for the triangular mesh.

As shown in **Figure 5**, a seed plane P is defined at the root of a vessel with two branches. The plane's normal $\mathbf{d}$ points in the same direction as the blood flow. By performing collision detection between P and the vascular mesh, we can obtain a looped triangle strip that intersects with the plane. Let us define this strip as $S_1 = \{f_0, f_1, ..., f_r\}$, where f_i is the triangle's index in the vascular mesh. In the direction of $\mathbf{d}$, we can obtain S_1's adjacent strip S_2, defined as $\{f_{r+1}, f_{r+2}, ..., f_s\}$. Based on the breadth-first search (BFS) algorithm, we can obtain a list of strips $\{S_1, S_2 S_N\}$, as shown in **Figures 5A–E**. For clarity, the adjacent layers of the strips are alternately colored cyan and blue. The strip's index is used as the value of the sequence for each facet of this strip. As shown in **Figure 5F**, the direction of the sequence's gradients is in accordance with that of the blood flow.

Step 2: Generate the contrast-enhanced vascular submesh

The contrast medium is injected into the vasculature and propagates with the blood flow to visualize the vessels downstream under fluoroscopy. After building the flow map of the blood in the first step, a sequence value is assigned to every facet of the vascular mesh. Let us define $\mathbf{x_b}$ as the first point of the catheter centerline's body part (distinguished from the intrinsically curved tip part). The closest facet of the vascular mesh to the point $\mathbf{x_b}$ is f_b. The direction of the sequence gradient of facet f_b is defined as $\mathbf{n_b}$. Starting from the seed plane defined by $\mathbf{x_b}$ and $\mathbf{n_b}$, a list of triangle strips is collected by the region growing in the direction of the sequence gradient. By merging all these strips, we obtain an ordered collection of facets that defines the contrast-medium-affected submesh of the vascular model. The order of the facets approximates the propagation of the contrast medium.

Step 3: Render the submesh progressively with a time-varying thickness weight

At the rendering stage, the sorted triangles are uploaded to the GPU and rendered incrementally over time. The

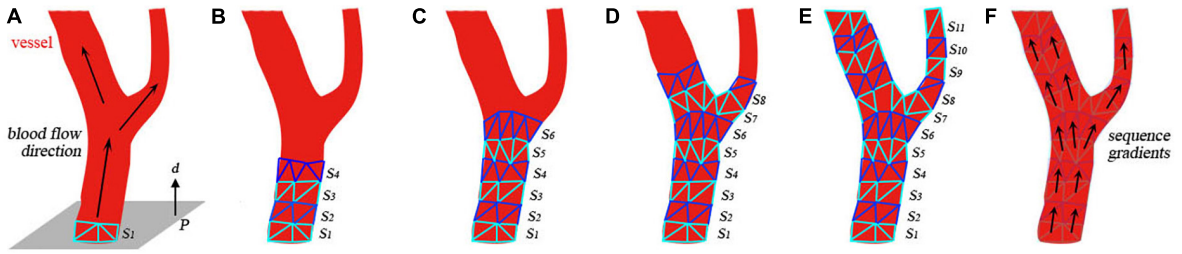

FIGURE 5
Generation of the submesh of the contrast-medium-affected vascular mesh. **(A)** Initial settings of the calculation. **(B–E)** Intermediate results of the calculation. **(F)** Visualization of the sequence gradients.

number of rendered facets over time n(t) is defined as follows:

$$\mathbf{n(t)} = \mathbf{v}(t - t_0)$$

where t_0 is defined as the moment when the contrast medium is injected and v is the number of facets rendered per second. To simulate the contrast medium's influence on X-rays, we use a higher value s_{angio} to replace the vessel's initial weight s_v for thickness calculation when the submesh is being rendered. As shown in Figure 6, the weight value jumps from s_v to s_{angio} at t_0. The weight value decreases over time to simulate the dilution of contrast medium in the blood.

Experiments and discussion

Experimental setup

The experiments described in this section were conducted in our homemade IR simulator which are composed of haptic feedback devices and a consumer-level laptop (CPU: Intel Core i5, RAM: 16 GB, GPU:NVIDIA GeForce MX450).

The vascular models are reconstructed from real patients' CT images. The interventional devices are the most commonly used types in daily interventional procedures. The intrinsic material properties of the devices are selected by trial and error offline. One unit for the vascular model in the coordinate system of the virtual world represents one millimeter in the real world.

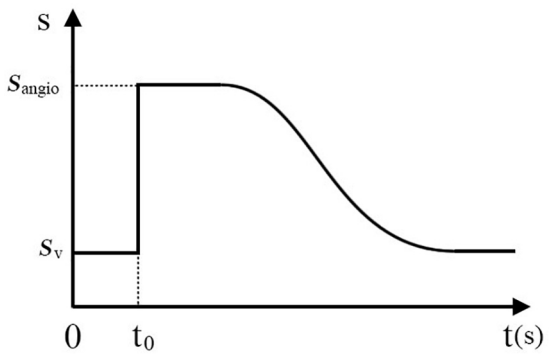

FIGURE 6
Variation in the weight value over time when the contrast medium is injected.

Heartbeat simulation

In this experiment, six different heart meshes are used as input to run the proposed heartbeat simulation algorithm. Meshes 1–4 are reconstructed from four different patients, while meshes 5 and 6 originate from the same patient but with different degrees of simplification (Table 1). As shown in Figure 7, eight samples are taken in the first cycle of the simulated heartbeat to generate the time-dependent offset fields for each heart mesh. To demonstrate the magnitudes of the simulated heartbeats and the geometrical variation between adjacent samples, we merge the silhouettes of the samples into one image, which is placed at the end of each row in Figure 7. Additionally, we record the frame rates of the simulation for the first and the later cycles of the heartbeat to validate the efficiency of our algorithm. Different elastic coefficients (see Section "Surgical device simulation") are used for meshes 4–6 to change the magnitude of the heartbeat to demonstrate the flexibility of our algorithm.

Figure 7 shows that there are no broken or flying vertices in the samples for any of the six meshes, indicating that our algorithm is stable for meshes with varying geometrical shapes and complexities. The shape variation between adjacent samples

TABLE 1 Configuration and results for input heart meshes.

Mesh	Vertex count	Face count	Elastic coefficient	1st cycle fps	2nd and later fps
1	27369	54566	1.0	35	60
2	29438	58880	1.0	32	60
3	81145	162498	1.0	24	60
4	44452	88727	1.0	28	60
5	177622	354876	1.5	10	60
6	710151	1419576	2.0	2	47

FIGURE 7
Simulation results for six sets of data.

increases from mesh 4 to 6, showing that we can simulate heartbeats with larger magnitudes by using larger values of the elastic coefficient. To simulate the heart rate change induced by stimulation, we can simply modify the rendering parameters instead of recalculating the heart meshes for a complete cycle (for detailed information, see the **Supplementary Video**).

With regard to efficiency, our algorithm can simulate the heartbeat at an interactive rate for meshes 1–4. The frame rate drops dramatically as the number of vertices increases from mesh 4 to 6. This is because the increase in the vertex number greatly slows the proposed algorithm by introducing additional constraints and the resulting computation. However, once the time-dependent offset field is built in the first cycle, the frame rate jumps to 60 frames per second (fps) for meshes 1–5. Even for mesh 6, the simulation achieves interactive rates. Because the heart mesh vertices are offset in parallel in the GPU, this method is less sensitive to a change in the number of vertices within a certain range. With this method, many of the computational resources of the CPU are saved for simulating the behavior of surgical devices, ensuring that the surgical procedure can be simulated in real time.

In summary, our method can simulate the heartbeat stably and realistically. By tuning the parameters, we can change the heart rate and the magnitude of the heartbeat. The incorporation of the simulated heartbeat builds a dynamic circulatory system, achieving higher realism for our simulator with little CPU cost.

Device simulation

The femoral artery is one of the most commonly used access points for physicians to start endovascular procedures. In this experiment, we navigate a catheter and guidewire from the femoral artery to three clinically typical target vessels to validate our device simulation algorithm. As shown in **Figure 8**, with proper manipulation, the guidewire is advanced from the femoral artery to the left and right renal artery branches. The results show that the simulated devices behave stably when advanced from trunk vessels with large diameters to subsequent narrow branches. Our simulation algorithm is robust enough to handle complex morphological situations (for detailed information, see the **Supplementary Video**).

As shown in **Figure 9**, we advance the devices to the left coronary artery, which is another important area in clinical practice. The catheter and guidewire must be manipulated in coordination to enter the left coronary artery. By comparing **Figures 9A,B**, we can see that the guidewire straightens the catheter's intrinsic curved part (circled in blue) while the

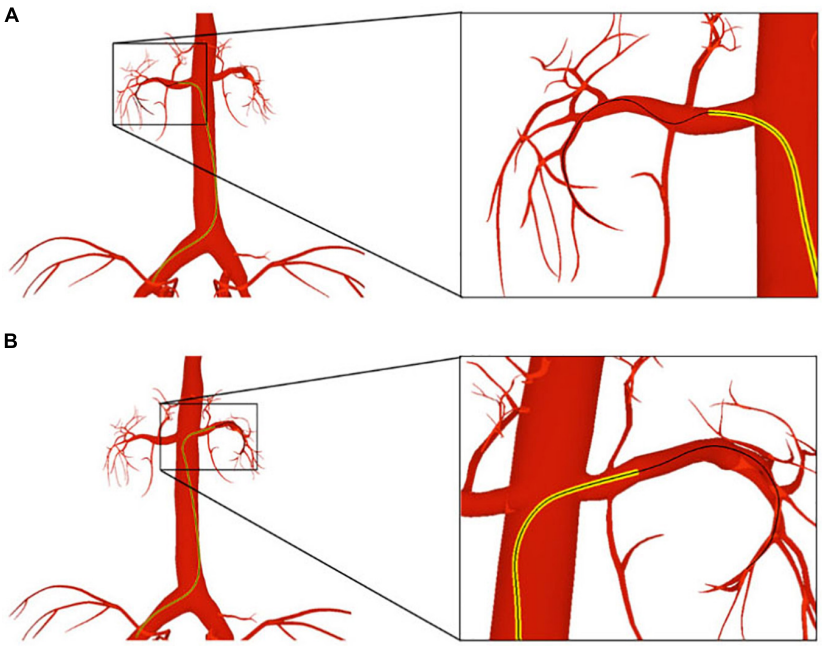

FIGURE 8
The catheter and guidewire are navigated from the femoral artery to the left **(A)** and right **(B)** renal artery branches. The catheter is displayed as a yellow tube, while the guidewire is represented as a black wire.

guidewire is advanced out of the catheter. This indicates that the existence of the guidewire makes the weighted property of the shared centerline more resistant to bending than the catheter itself. This validates the effectiveness of our shared centerline model. From another perspective, **Figure 9C** shows the devices' final shape when the guidewire reaches the target branch vessel, the diameter of which is ten times smaller than that of the aortic arch. The robustness of our algorithm is further proven.

When navigated into the cardiac region, the simulated devices move along with the beating heart in synchronization. Three samples are taken at different moments of a cardiac cycle, as shown in **Figures 9D–F**. To make the shape variation of the heart and devices more evident, we display the devices' centerlines and the hearts' silhouettes in **Figure 9G**. The device shape remains stable, and the relative distances to the colliding vessel walls remain visually unchanged. In addition, the frame rate remains at 60 fps while the simulated devices are interacting with the beating heart. The results demonstrate that our method can simulate the behavior of interventional devices realistically and stably under dynamic and static mesh circumstances in real time.

Fluoroscopy simulation

X-ray imaging simulation

In this experiment, a cardiac training case is imported into our simulator. The imported meshes contain a skeleton, vessel, and heart. The devices used in this procedure are a catheter and guidewire. The anatomy rendered in the Phong lighting model is displayed in **Figure 10A**. The corresponding simulated fluoroscopic image is shown in **Figure 10B**. We move the virtual camera closer to the devices and take a screenshot, which is shown in **Figure 10C**. Then, angiography is simulated, and the enhanced coronary artery vessels are displayed in **Figure 10D**.

The skeleton, vessels, and heart mesh can be clearly seen in **Figure 10A**, while only the skeleton can be identified in **Figure 10B**. This is because the skeleton's attenuation in X-ray is much higher than that of the vessels. Unlike human anatomy, surgical devices can be easily found under the fluoroscope because of their specialized materials. The catheter is a hollow tube device with a larger diameter than that of the guidewire, and it can be treated as solid. Thus, we can distinguish these devices by the width of the centerline in **Figure 10C**. After contrast medium is injected through the catheter, the affected vessel branches are visualized in a dark color under the fluoroscope, as shown in **Figure 10D**. The frame rate remains at 60 fps regardless of whether the fluoroscope effect is enabled. These results demonstrate that our algorithm can efficiently simulate the X-ray imaging effect of objects with varying properties by tuning the weight value s as explained in section "Fluoroscopy Simulation."

The coronary angiography simulation

In this experiment, we simulate the coronary angiography procedure. First, we create the flow map for a complex vascular

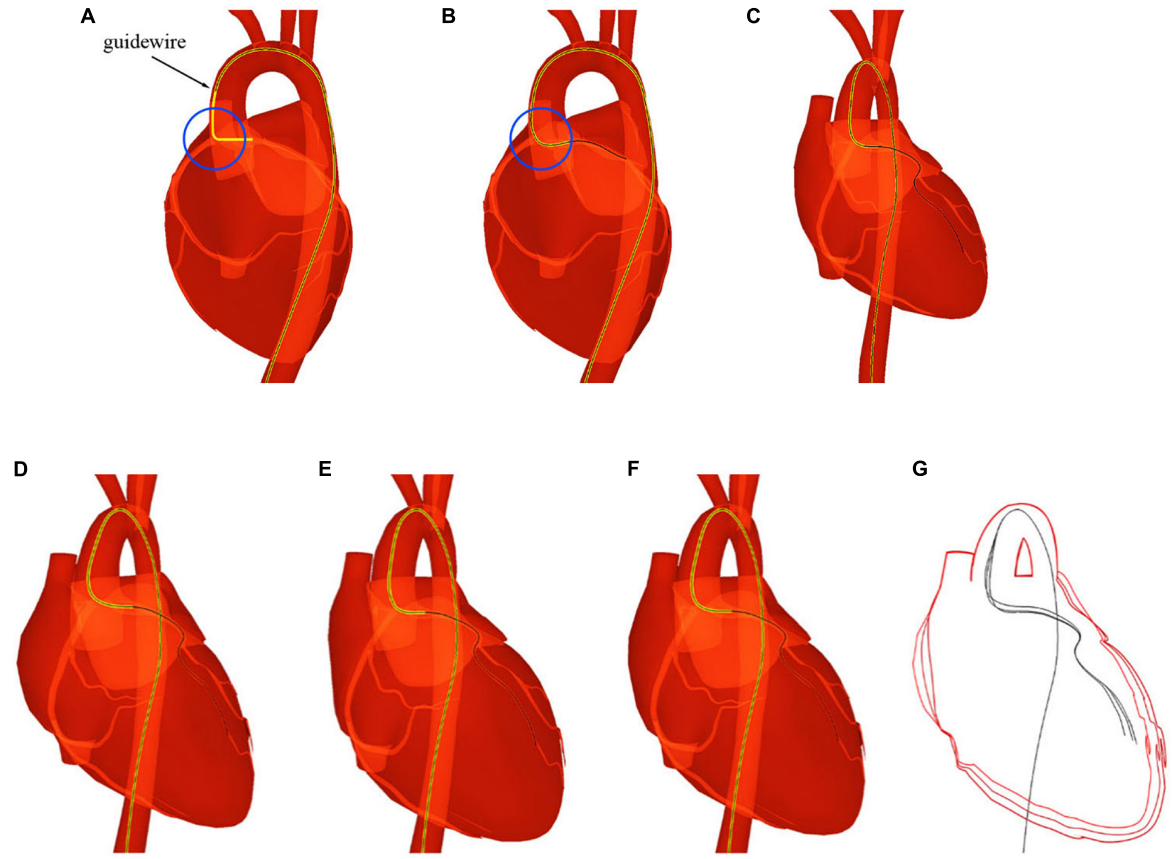

FIGURE 9
The catheter and guidewire reach the left coronary artery from the femoral artery. **(A)** Before the guidewire passes through the intrinsic curved part of the catheter. **(B)** After the guidewire passes through the intrinsic curved part of the catheter. **(C)** The guidewire reaches the terminal branch of the left coronary artery. **(D–F)** Screenshots taken at different moments of a cardiac cycle. **(G)** Shape variation of the heart and devices.

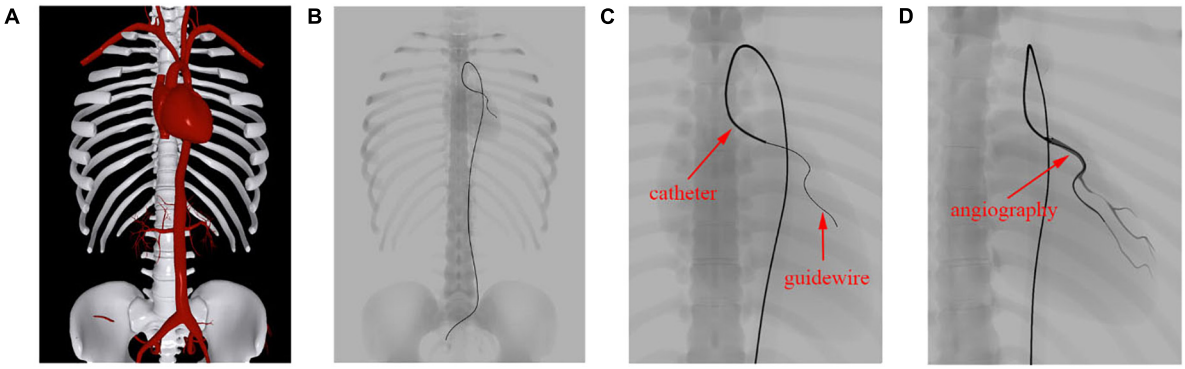

FIGURE 10
Simulation results of fluoroscope imaging. **(A)** Anatomy rendered in the Phong lighting model. **(B)** Anatomy and surgical devices under a simulated fluoroscope. **(C)** Zoomed view of the devices in the left coronary artery. **(D)** Contrast-enhanced coronary artery vessels.

system that includes the aorta, the carotid artery, the renal artery, and the femoral artery. By placing the seed plane at the beginning of the aorta, we calculate the value of the sequence for all triangles that compose the arterial vessels.

As shown in Figure 11, the gradients of the sequence are depicted with short lines colored from red to blue, indicating the facet's topological distance to the heart from close to far as well as the blood flow from the aorta to the branch vessels.

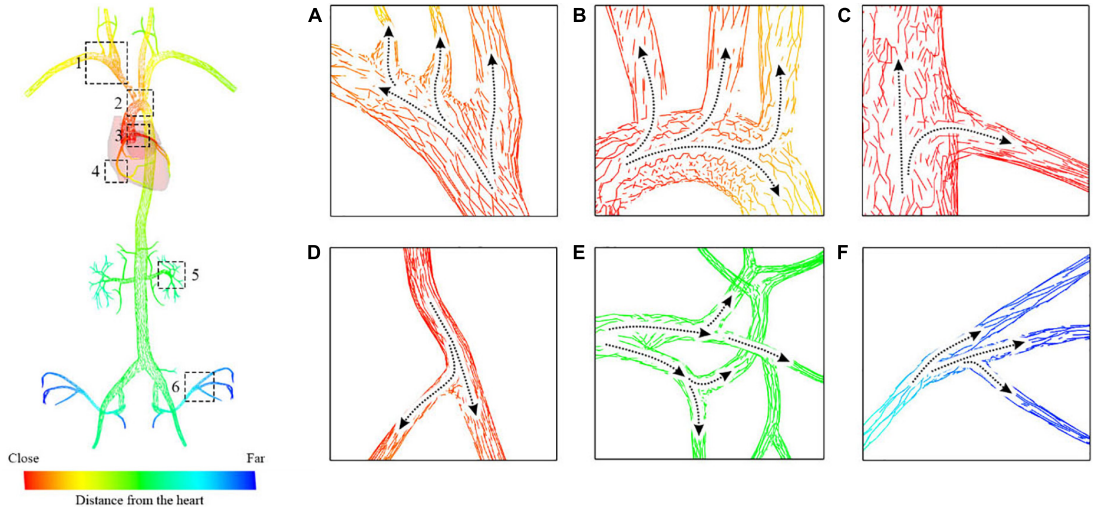

FIGURE 11
Blood flow map starting from the aorta to the carotid artery and the femoral artery. **(A)** Subclavian artery blood flow. **(B)** Aortic arch blood flow. **(C,D)** Coronary artery blood flow. **(E)** Renal artery blood. **(F)** Iliac artery flow.

In Figures 11A–F, there are lines pointing from the trunk to the branches at vessel bifurcations with various morphological features. This demonstrates that the gradient can help solve the propagation problem at the bifurcation of blood vessels without building hierarchical tree structures or extracting vascular centerlines.

The catheter is then navigated to the entrance of the left coronary artery, and the contrast medium is injected through the catheter to visualize the coronary vessels. The screenshots shown in Figure 12 are taken at different stages of the procedure, showing the life cycle of the contrast medium from injection to dilution (for detailed information, see the Supplementary Video).

The propagation of the contrast medium is progressive. It runs from the injection point to its downstream vessel branch in the direction of blood flow and dilutes in the blood over time. After the angiography catheter reaches the entrance of the left coronary artery, the contrast medium is injected through the catheter, as shown in Figure 12A. Then, a submesh of the coronary artery is generated progressively and rendered using our fluoroscopy simulation algorithm with a high weight value s_{angio}, as explained in section "Fluoroscopy simulation." Figures 12B–D) shows the simulation result of the contrast medium's propagation. As time passes, the contrast medium starts to dilute, and the color of the affected submesh begins to fade, as shown in Figures 12D–F). Note that, the coronary artery is also dynamic because it is a part of the heart.

Angioplasty simulation

In this experiment, we perform coronary angioplasty and stent placement for the heart. There are two blockages in the patient's left coronary artery. In this procedure, we navigate the catheter and guidewire into the left coronary artery and implant two stents to open the narrowed vessels. Screenshots of key moments of the procedure are shown in Figure 13.

In Figure 13A, the surgical devices reach the entrance of the left coronary artery. After the injection of the contrast medium, we can see two areas in which plaque blocks the blood flow of the visualized vessels. Balloon catheters are then advanced to the narrowed vessel to implant two stents consecutively from the far end to the near end of the vessel branch, as shown in Figures 13B,C. Contrast medium is injected again to visualize the coronary artery for observation of blood flow after the procedure, as shown in Figure 13D. Then, the surgical devices are pulled out of the coronary artery. The stents stay where they are placed and move along with the pumping heart, as shown in Figure 13E. The frame rate stays at 60 fps for the whole simulation time. The results demonstrate that our simulator can simulate complex endovascular procedures realistically in a dynamic circulatory system with real-time efficiency (for detailed information, see the Supplementary Video).

Face validity

To validate the effectiveness of our simulator, 24 participants with varying degrees of expertise in IR are recruited to evaluate our simulator. A questionnaire is designed for participants to grade our simulator in six respects: the virtual anatomical environment, device behavior, visualization, efficiency, robustness, and effectiveness. The criteria for the scores are as follows: 0–2 means strongly disagree; 3–5 means disagree; 6–8 means agree, and 9–10 means strongly agree. The

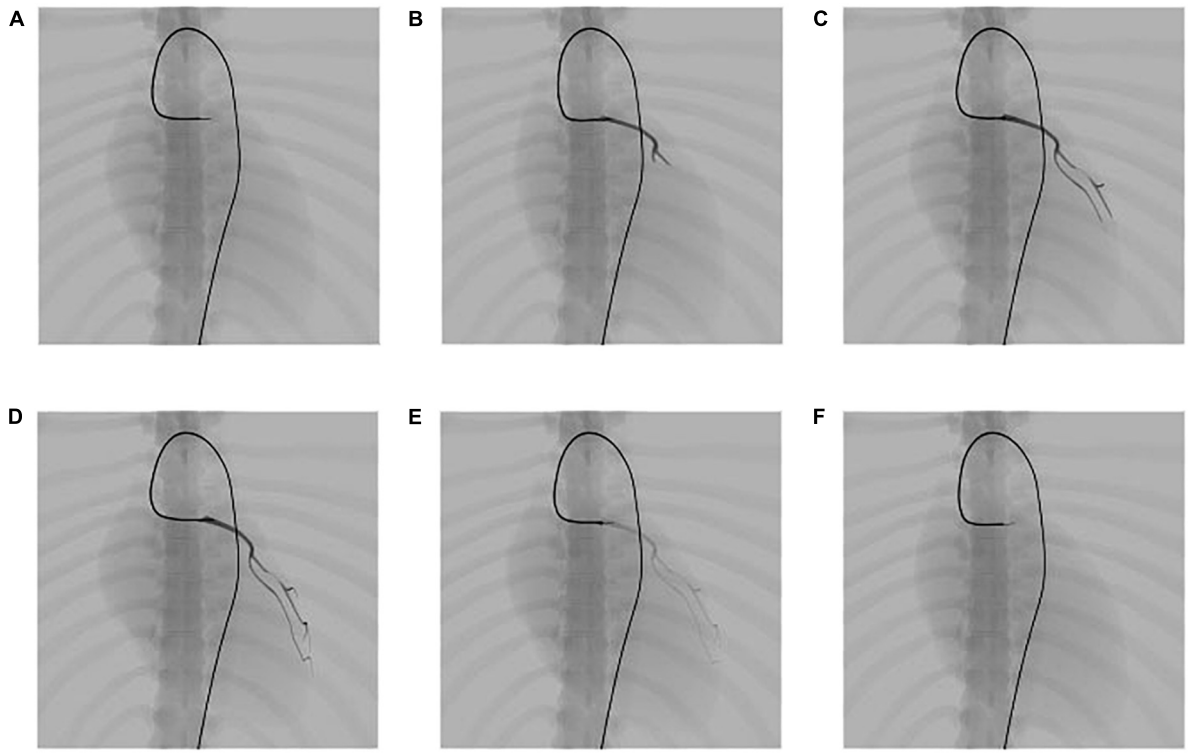

FIGURE 12
Simulation results of the propagation of contrast medium under fluoroscopy. **(A)** Angiography catheter reaches the entrance of the left coronary artery. **(B–D)** Propagation of the contrast medium and corresponding fluoroscopic images. **(E,F)** Dilution of the contrast medium and corresponding fluoroscopic images.

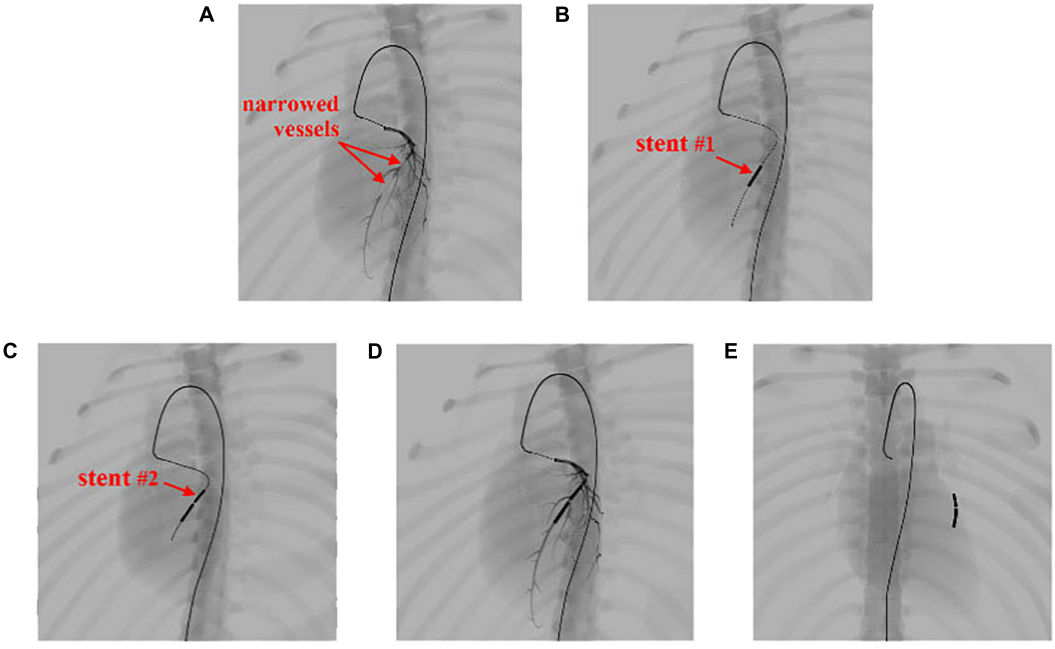

FIGURE 13
Simulation of the coronary artery stent implantation procedure. **(A)** Visualization of the narrowed vessels with simulated angiography. **(B,C)** Results of stent implantation for the two narrowed vessels. **(D)** Visualization of the post-operative results with simulated angiography. **(E)** The implanted stents stay within the coronary artery and move with the beating heart.

average score in each category is listed in the second column of Table 2.

In the first category, approximately 80% of the participants agree that the simulated heartbeat is realistic and its incorporation greatly increases the realism of our simulator. The other 20% of participants, who have more than 10 years of clinical experience, suggest that the heartbeat should not only be visually plausible but also be numerically accurate for further application in hydrodynamic analysis. Almost all participants give a high rating to the accuracy of our reconstructed vessels and skeletons after a thorough cross-reference with the original CT images.

The device behavior in our simulator obtains a high rating, especially in the interaction with vessel walls, bifurcation, and narrow branches. The average score of the device behavior inside the beating heart is not as high as the other scores because experienced participants expect to see how the devices interact with the blood flow pumped out of the heart. However, our simulator does not incorporate real-time blood flow simulation, which is another very challenging task. Nevertheless, good ratings are received in the device behavior category.

In the category of fluoroscopy simulation, more than 90% of the participants agreed that the results are realistic enough for training and surgery planning purposes. Approximately 5% of the participants suggest that more anatomical parts should be involved in visualization to enrich the simulated fluoroscopic images even if they might not be visually evident as skeletons and vessels affected by the contrast medium.

TABLE 2 Numerical metrics of the user evaluation.

Category	Score
(1) Virtual anatomical environment	
(1.1) The heartbeat is realistic.	8.3
(1.2) The reconstructed vessels are accurate.	9.6
(1.3) The reconstructed skeleton is accurate.	9.7
(2) Device behavior	
(2.1) Devices' interaction with vessel wall is realistic.	9.0
(2.2) Interaction between devices is realistic.	9.1
(2.3) Devices' interaction with the beating heart is realistic.	8.6
(2.4) Devices' behavior at vessel bifurcation is realistic.	8.9
(2.5) Devices' behavior at narrow branches is realistic.	9.6
(3) Visualization	
(3.1) Fluoroscopy effect is realistic.	8.7
(3.1.1) Anatomy under fluoroscope is realistic.	8.3
(3.1.2) Devices under fluoroscope are realistic.	9.4
(3.2) Propagation of contrast medium is realistic.	8.6
(4) Efficiency	
The simulation runs smoothly without lag.	9.8
(5) Robustness	
The simulation runs stably without crash or exception.	9.7
(6) Effectiveness	
(6.1) The simulator is useful for surgical skills training.	8.5
(6.2) The simulator is useful for surgery planning.	8.2

All participants agree that our simulator runs quickly and that no operational lag is detected in the whole procedure. In addition, no vital errors that can corrupt the simulation are found. The numerical metrics in Table 2 show that participants reached a consensus in terms of the stability of our simulator.

In summary, participants with less clinical experience give our simulator high rankings on average. They believe that our simulator is a very useful tool for training interventional skills because it is realistic, reusable, and free of radiation and ethical risks. In comparison, participants with more experience are more interested in the surgery planning capability of our simulator and set a much higher standard for us. Nevertheless, they agree that our simulator's ability to process and import patient-specific data for simulation can offer much help in making surgery plans.

Conclusion

In this paper, we propose a novel approach to simulating the heartbeat for building a realistic and interactive IR simulator. A simplified heartbeat model is used to formulate the driving force of the heartbeat. To achieve better efficiency, a time-dependent offset field is built to cache and reproduce the simulation results. The interaction between surgical devices and the beating heart is simulated realistically and stably with the proposed visual-deviation method. For X-ray imaging, a linear depth subtraction method is proposed to approximate the fluoroscopic images with an anatomy-specific weight value. For angiography simulation, a blood flow map and a gradient-based region growing method are used to generate the contrast-enhanced vascular meshes. A progressive rendering technique with a time-varying weight value is used to render these meshes for simulating the propagation of the contrast medium. To summarize, the proposed methods solve three challenging simulation problems which are the real-time heartbeat simulation for patient-specific data, the stable interaction between dynamical meshes and surgical devices, and the realistic medical visualization and angiography. Experimental results demonstrate that our approach is capable of realistically simulating the heartbeat and its interaction with surgical devices in real time. The simulation results of the angioplasty for the left coronary artery validate the realism and efficiency of the proposed methods for X-ray imaging and angiography simulation.

Despite the increase in the realism of our simulator, there are still some problems to solve for achieving better fidelity and functionality. Blood flow simulation is one of the most essential but challenging tasks to be accomplished. The real-time simulation of the blood flow and its interaction with surgical devices will not only achieve higher fidelity for the simulator,

but also provide a promising way to perform hydrodynamics analysis for procedures like aneurysm embolization. Computational modelling of the blood vessels (42, 43) can enable us to understand the blood dynamics while the guidewire is travelling through the vessel, which helps in the research of cardiovascular condition during treatment. However, most of the existing methods (e.g., computational fluid dynamics) suffer from performance issues and cannot be used for interactive simulation. Our future work will focus on finding solutions to achieve both numerical accuracy and real-time efficiency for blood flow simulation.

Data availability statement

The original contributions presented in this study are included in the article/**Supplementary material**, further inquiries can be directed to the corresponding author.

Ethics statement

Ethical review and approval was not required for this study in accordance with the local legislation and institutional requirements.

Author contributions

HW designed and conducted the experiments, analyzed the results, and wrote the manuscript. JW raised critical comments and edited the manuscript. Both authors contributed to the article approved the submitted version.

Funding

This work was supported in part by the Shenzhen Basic Research Program (No. JCYJ20180507182441903), National Natural Science Foundation of China (No. 61672510), and the Open Research Fund of Key Laboratory of Rehabilitation Technique of Fujian Province (No. KF2019001).

Conflict of interest

The authors declare that the research was conducted in the absence of any commercial or financial relationships that could be construed as a potential conflict of interest.

Publisher's note

All claims expressed in this article are solely those of the authors and do not necessarily represent those of their affiliated organizations, or those of the publisher, the editors and the reviewers. Any product that may be evaluated in this article, or claim that may be made by its manufacturer, is not guaranteed or endorsed by the publisher.

Supplementary material

The Supplementary Material for this article can be found online at: https://www.frontiersin.org/articles/10.3389/fcvm.2022.1004968/full#supplementary-material

References

1. Gallagher AG, Cates CU. Virtual reality training for the operating room and cardiac catheterisation laboratory. *Lancet.* (2004) 364:1538–40. doi: 10.1016/S0140-6736(04)17278-4

2. Mirza S, Athreya S. Review of simulation training in interventional radiology. *Acad Radiol.* (2018) 25:529–39. doi: 10.1016/j.acra.2017.10.009

3. Cao C, Cerfolio RJ. Virtual or augmented reality to enhance surgical education and surgical planning. *Thoracic Surg Clin.* (2019) 29:329–37. doi: 10.1016/j.thorsurg.2019.03.010

4. McGuire LS, Fuentes A, Alaraj A. Three-dimensional modeling in training, simulation, and surgical planning in open vascular and endovascular neurosurgery: a systematic review of the literature. *World Neurosurg.* (2021) 154:53–63. doi: 10.1016/j.wneu.2021.07.057

5. Bakhsh A, Martin GFJ, Bicknell CD, Pettengell C. An evaluation of the impact of high-fidelity endovascular simulation on surgeon stress and technical performance. *J Surg Educ.* (2019) 76:864–71. doi: 10.1016/j.jsurg.2018.10.015

6. Stoehr F, Schotten S, Pitton MD, Dueber C, Schmidt F, Hansen NL, et al. Endovascular simulation training: a tool to increase enthusiasm for interventional radiology among medical students. *Eur Radiol.* (2020) 30:4656–63. doi: 10.1007/s00330-019-06646-2

7. Ghazi A, Melnyk R, Farooq S, Bell A, Holler T, Saba P, et al. Validity of a patient-specific percutaneous nephrolithotomy (PCNL) simulated surgical rehearsal platform: impact on patient and surgical outcomes. *World J Urol.* (2022) 40:627–37. doi: 10.1007/s00345-021-03766-7

8. Sharei H, Alderliesten T, van den Dobbelsteen JJ, Dankelman J. Navigation of guidewires and catheters in the body during intervention procedures: a review of computer-based models. *J Med Imag.* (2018) 5:010902. doi: 10.1117/1.JMI.5.1.010902

9. Doost SN, Ghista D, Su B, Zhon L, Morsi YS. Heart blood flow simulation: a perspective review. *Biomed Eng Online.* (2016) 15:1–28. doi: 10.1186/s12938-016-0224-8

10. Dawson SL, Cotin S, Meglan D, Shaffer DW, Ferrell MA. Designing a computer-based simulator for interventional cardiology training. *Catheterization Cardiovasc Intervent.* (2000) 51:522–7. doi: 10.1002/1522-726X(200012)51:4<522::AID-CCD30>3.0.CO;2-7

11. CAE Inc. *CathlabVR.* (2022). Available online at: https://caehealthcare.com/surgical-simulation/cathlabvr/ (accessed July 11, 2022).

12. Talbot H, Spadoni F, Duriez C, Sermesant M, O'Neill M, Jaïs P, et al. Interactive training system for interventional electrocardiology procedures. *Med Image Anal.* (2017) 35:225–37. doi: 10.1016/j.media.2016.06.040

13. Tang M, Curtis S, Yoon S, Manocha D. ICCD: interactive continuous collision detection between deformable models using connectivity-based culling. *IEEE Trans. Visualizat Comput Graph.* (2009) 15:544–57. doi: 10.1109/TVCG.2009.12

14. Wang B, Ferguson Z, Schneider T, Jiang X, Attene M, Panozzo D. A Large-scale benchmark and an inclusion-based algorithm for continuous collision detection. *ACM Trans Graph (TOG).* (2021) 40:1–16. doi: 10.1145/3460775

15. Muniyandi M, Cotin S, Srinivasan M, Dawson S. Real-time PC based X-ray simulation for interventional radiology training. *Stud Health Technol Inform.* (2003) 94:233–9.

16. van Walsum T, Zuiderveld KJ, Chin-A-Woeng JWC, Eikelboom BC, Viergever MA. CT-based simulation of fluoroscopy and DSA for endovascular surgery training. *Proceedings of the CVRMed-MRCAS'97*. Berlin: Springer (1997). doi: 10.1007/BFb0029246

17. Wang F, Duratti L, Samur E, Spaelter U, Bleuler H. A computer-based real-time simulation of interventional radiology. *Proceedings of the 2007 29th Annual International Conference of the IEEE Engineering in Medicine and Biology Society*. Lyon: IEEE (2007). doi: 10.1109/IEMBS.2007.4352647

18. Anderson J, Brody W, Kriz CJ, Wang YP, Raghavan R, Viswanathan R. Da vinci: a vascular catheterization and interventional radiology–based training and patient pretreatment planning simulator. *J Vasc Intervent Radiol.* (1996) 1:373. doi: 10.1016/S1051-0443(96)70159-8

19. Wang Y, Chui C, Lim H, Cai Y, Mak K. Real-time interactive simulator for percutaneous coronary revascularization procedures. *Comput Aided Surg.* (1998) 3:211–27. doi: 10.1002/(SICI)1097-0150(1998)3:5<211::AID-IGS1>3.3.CO;2-Y

20. Duriez C, Cotin S, Lenoir J, Neumann P. New approaches to catheter navigation for interventional radiology simulation. *Comput Aided Surg.* (2006) 11:300–8. doi: 10.3109/10929080601090623

21. Korzeniowski P, White RJ, Bello F. VCSim3: a VR simulator for cardiovascular interventions. *Int J Comput Assist Radiol Surg.* (2018) 13:135–49. doi: 10.1007/s11548-017-1679-1

22. Wang Y. *Simulation of Blood Flow and Contrast Medium Propagation for a Vascular Interventional Radiology Simulator*. London: Imperial College London (2009).

23. Li S, Cui J, Hao A, Zhang S, Zhao Q. Design and evaluation of personalized percutaneous coronary intervention surgery simulation system. *IEEE Trans Visualizat Comput Graph.* (2021) 27:4150–60. doi: 10.1109/TVCG.2021.3106478

24. Voelker W. Computer simulation as training tool for coronary interventions. In: Lanzer P editor. *Catheter-Based Cardiovascular Interventions.* Berlin: Springer (2013). p. 187–200.

25. Mentice. *Vist-G7*. (2020). Available online at: https://www.mentice.com/vist-g7 (accessed July 11, 2022).

26. Surgical Science. *Angio-Mentor.* (2022). Available online at: https://simbionix.com/simulators/angio-mentor/ (accessed July 11, 2022).

27. Wu X, Allard J, Cotin S. Real-time modeling of vascular flow for angiography simulation. *Proceedings of the International Conference on Medical Image Computing and Computer-Assisted Intervention*. Berlin: Springer (2007).

28. Wei M, Wang Q, Li Y, Pang W-M, Liang L, Wang J, et al. Centerline extraction of vasculature mesh. *IEEE Access.* (2018) 6:10257–68. doi: 10.1109/ACCESS.2018.2802478

29. Moccia S, De Momi E, El Hadji S, Mattos LS. Blood vessel segmentation algorithms—review of methods, datasets and evaluation metrics. *Comput Methods Programs Biomed.* (2018) 158:71–91. doi: 10.1016/j.cmpb.2018.02.001

30. Ni J, Wu J, Tong J, Chen Z, Zhao J. GC-Net: global context network for medical image segmentation. *Comput Methods Programs Biomed.* (2020) 190:105121. doi: 10.1016/j.cmpb.2019.105121

31. Ni J, Wu J, Wang H, Tong J, Chen Z, Wong KKL, et al. Global channel attention networks for intracranial vessel segmentation. *Comput Biol Med.* (2020) 118:103639. doi: 10.1016/j.compbiomed.2020.103639

32. Zheng L, Li G, Sha J. The survey of medical image 3D reconstruction. *Proceedings of the Fifth International Conference on Photonics and Imaging in Biology and Medicine*. Bellingham, DC: SPIE (2007).

33. Khan U, Yasin A, Abid M, Shafi I, Khan SA. A methodological review of 3D reconstruction techniques in tomographic imaging. *J Med Syst.* (2018) 42:1–12. doi: 10.1007/s10916-018-1042-2

34. Wu J, Ma R, Ma X, Jia F, Hu Q. Curvature-dependent surface visualization of vascular structures. *Comput Med Imaging Graph.* (2010) 34:651–8. doi: 10.1016/j.compmedimag.2010.07.006

35. Wang Y, Xiong YS, Tan K, Guo G. Real-time heartbeat modeling based on a hybrid mass-spring model. *Comput Eng Sci.* (2008) 30:132–4.

36. Wang H, Wu J. A virtual reality based surgical skills training simulator for catheter ablation with real-time and robust interaction. *Virtual Real Intell Hardw.* (2021) 3:302–14. doi: 10.1016/j.vrih.2021.08.004

37. Müller M, Heidelberger B, Hennix M, Rafcliff J. Position based dynamics. *J Visual Commun Image Represent.* (2007) 18:109–18. doi: 10.1016/j.jvcir.2007.01.005

38. Wang H, Wu J, Wei M, Ma X. A robust and fast approach to simulating the behavior of guidewire in vascular interventional radiology. *Comput Med Imag Graph.* (2015) 40:160–9. doi: 10.1016/j.compmedimag.2014.10.006

39. Wang H, Wu J, Cai Y. An adaptive deviation-feedback approach for simulating multiple devices interaction in virtual interventional radiology. *Comput Aided Design.* (2019) 117:102738. doi: 10.1016/j.cad.2019.102738

40. Daly B, Templeton PA. Real-time CT fluoroscopy: evolution of an interventional tool. *Radiology.* (1999) 211:309–15. doi: 10.1148/radiology.211.2.r99ma51309

41. Carlsson CA, Carlsson GA. *Basic Physics of X-Ray Imaging.* Linköping: Linköping University Electronic Press (1973). p. 29.

42. Liu G, Wu J, Ghista DN, Huang W, Wong KKL. Hemodynamic characterization of transient blood flow in right coronary arteries with varying curvature and side-branch bifurcation angles. *Comput Biol Med.* (2015) 64:117–26.

43. Wong KKL, Thavornpattanapong P, Cheung SCP, Tu JY. Biomechanical investigation of pulsatile flow in a three-dimensional atherosclerotic carotid bifurcation model. *J Mech Med Biol.* (2012) 13:1–21.

frontiers | Frontiers in Cardiovascular Medicine

TYPE Original Research
PUBLISHED 19 October 2022
DOI 10.3389/fcvm.2022.1013031

OPEN ACCESS

EDITED BY
Ruizheng Shi,
Xiangya Hospital, Central South University, China

REVIEWED BY
Cong Lee,
Cardiovascular Medicine, Imaging Medicine, Medical Engineering, China
Jianshe Shi,
Huaqiao University Affiliated Strait Hospital, China

*CORRESPONDENCE
Yong Ni
sjwkny@163.com

†These authors have contributed equally to this work and share first authorship

SPECIALTY SECTION
This article was submitted to Cardiovascular Imaging, a section of the journal Frontiers in Cardiovascular Medicine

RECEIVED 06 August 2022
ACCEPTED 29 September 2022
PUBLISHED 19 October 2022

CITATION
Wang B, Liao X, Ni Y, Zhang L, Liang J, Wang J, Liu Y, Sun X, Ou Y, Wu Q, Shi L, Yang Z and Lan L (2022) High-resolution medical image reconstruction based on residual neural network for diagnosis of cerebral aneurysm.
Front. Cardiovasc. Med. 9:1013031.
doi: 10.3389/fcvm.2022.1013031

High-resolution medical image reconstruction based on residual neural network for diagnosis of cerebral aneurysm

Bo Wang†, Xin Liao†, Yong Ni*, Li Zhang, Jinxin Liang, Jiatang Wang, Yongmao Liu, Xianyue Sun, Yikuan Ou, Qinning Wu, Lei Shi, Zhixiong Yang and Lin Lan

Department of Neurosurgery, The Second Affiliated Hospital of Guizhou Medical University, Kaili, China

Objective: Cerebral aneurysms are classified as severe cerebrovascular diseases due to hidden and critical onset, which seriously threaten life and health. An effective strategy to control intracranial aneurysms is the regular diagnosis and timely treatment by CT angiography (CTA) imaging technology. However, unpredictable patient movements make it challenging to capture sub-millimeter-level ultra-high resolution images in a CTA scan. In order to improve the doctor's judgment, it is necessary to improve the clarity of the cerebral aneurysm medical image algorithm.

Methods: This paper mainly focuses on researching a three-dimensional medical image super-resolution algorithm applied to cerebral aneurysms. Although some scholars have proposed super-resolution reconstruction methods, there are problems such as poor effect and too much reconstruction time. Therefore, this paper designs a lightweight super-resolution network based on a residual neural network. The residual block structure removes the B.N. layer, which can effectively solve the gradient problem. Considering the high-resolution reconstruction needs to take the complete image as the research object and the fidelity of information, this paper selects the channel domain attention mechanism to improve the performance of the residual neural network.

Results: The new data set of cerebral aneurysms in this paper was obtained by CTA imaging technology of patients in the Department of neurosurgery, the second affiliated of Guizhou Medical University Hospital. The proposed model was evaluated from objective evaluation, model effect, model performance, and detection comparison. On the brain aneurysm data set, we tested the PSNR and SSIM values of 2 and 4 magnification factors, and the scores of our method were 33.01, 28.39, 33.06, and 28.41, respectively, which were better than those of the traditional SRCNN, ESPCN and FSRCNN. Subsequently, the model is applied to practice in this paper, and the effect, performance index and diagnosis of auxiliary doctors are obtained. The experimental results show that the high-resolution image reconstruction model based on the residual neural network designed in this paper plays a more influential role than other image classification methods. This method has higher robustness, accuracy and intuition.

Conclusion: With the wide application of CTA images in the clinical diagnosis of cerebral aneurysms and the increasing number of application samples, this method is expected to become an additional diagnostic tool that can effectively improve the diagnostic accuracy of cerebral aneurysms.

KEYWORDS

ResNet, CTA, brain aneurysm, medical image, super-resolution

Introduction

Brain aneurysms and hazards

Intracranial aneurysms are cerebral hemangioma-like protrusions caused by abnormal local blood vessel morphology changes. The etiology of aneurysms is not clear. Genetic factors include: the thickness of the cerebral artery wall being about 1 % thinner than that of other parts of the same diameter or so, and lack of surrounding tissue support, the blood flow is significant, especially at the bifurcation is more vulnerable to the impact of blood flow; acquired factors include infection, trauma, tumor and atherosclerosis; most of them are genetic factors (1). The formation mechanism of the intracranial aneurysm is the stress damage to blood flow to the arterial wall. Due to the change in blood flow, a part of the arterial wall protrudes outward, forming a permanent local expansion. The magnitude of the stress is usually related to the velocity and angle of the blood vessel. Intracranial aneurysms are classified as severe cerebrovascular diseases due to their insidious onset, complex pathogenesis and acute onset (2).

Aneurysmal subarachnoid hemorrhage (aSAH) has consistently ranked among the cerebrovascular diseases that seriously endanger human health due to its insidious onset and complex pathogenesis. According to incomplete statistics, the incidence of bleeding has also remained high, accounting for about 85%. The most common symptom of aSAH is sudden severe headache, often described as the most severe and severe headache of the lifetime, with vomiting, nausea, photophobia, neck stiffness, transient loss of consciousness, or focal neurological deficits, such as cranial nerve palsy (3). Fortunately, 2– 8 weeks before some aneurysms rupture, patients may have "warning" symptoms in advance. Some patients are self-reported to have very mild cold-like headaches or mild nausea and vomiting that lasted for several days. It is difficult to be associated with severe intracranial hemorrhage. If relevant examinations are carried out in this period for differential diagnosis and symptomatic and supportive treatment, the occurrence of fatal hemorrhage can be largely avoided.

At present, the clinical symptoms of SAH patients are mainly determined by the Hunt-Hess classification, Glasgow Coma Scale (GCS), World Federation of Neurological Surgeons (WFNS) and prognostic scores on admission for aneurysmal subarachnoid hemorrhage (prognosis on the admission of aneurysmal subarachnoid hemorrhage, PAASH) (4). This study used the Hunt-Hess classification according to the condition at the time of admission: grade I: asymptomatic, or mild headache, mild neck stiffness; grade II: moderate to severe headache, neck stiffness or cranial nerve palsy; grade III I: lethargy or confusion, mild focal neurological impairment; grade IV: coma, moderate to moderate hemiplegia; grade V: deep coma, cerebral rigidity, moribund state. Regardless of the typical clinical symptoms of the disease, once the tumor ruptures and bleeds, there is a high risk of death and disability. Therefore, early diagnosis and symptomatic surgical treatment can effectively prevent the recurrence of intracranial aneurysms and reduce the rebleeding of intracranial aneurysms, thereby further improving the survival rate and quality of life of patients (5).

CTA imaging technology

CTA is convenient, fast and straightforward to operate and can display the three-dimensional structure of cerebral blood vessels, which has a specific guiding role in detecting and detecting aneurysms (6). CTA can also observe and restore the internal conditions of blood vessels from different directions and angles, maximizing the accurate display of the three-dimensional anatomy of the aneurysm body, neck and parent artery from multiple angles and maximizing the natural restoration of multiple angles (7). The shape, size, and adjacent relationship of the tumor body provide the anatomical information of various aneurysms such as tumor wall calcification and intratumoral thrombus to the greatest extent accurately and display brain tissue lesions. The preservation of V.R. images of skull base provides essential reference information for clinical selection of surgical approach and provides help for the selection of surgical approach (8). The V.R. image is closer to the actual anatomical structure. It can display the diameter of the aneurysm, the width of the aneurysm, the shape of the aneurysm and the protruding direction of the aneurysm. Ninety-three percent of intracranial aneurysms occur in the circle of Willis and its branches, bifurcations and bends. CTA can display the course and variation of the circle of Willis and its branches, as well as the vertebral-basilar artery system

and the circle of Willis. It has obvious advantages in observing the blood supply of the intracranial arteries, the degree of collateral circulation opening, and comparing the blood vessels on both sides. CTA is a non-invasive examination technique that can effectively reduce the occurrence of vasospasm, plaque and thrombus shedding caused by invasive surgery (9).

High-resolution medical image reconstruction technology

In most digital imaging applications, images are often used and viewed by people, especially in the eyes of doctors, who prefer to choose high-quality, high-resolution images as diagnostic references (10). Improving the resolution of an image is a widely studied problem in computer vision. Its purpose is to generate high-resolution images from one or more low-resolution images. Super-resolution reconstruction (S.R.) algorithms aim to generate finer details than the sampling grid of a given imaging device by increasing the number of pixels per unit area in an image. S.R. is a well-known ill-posed inverse problem, recovering high-resolution images from low-resolution images (often affected by noise, motion blur, cerebral aneurysms, optical distortion, etc.) (11). S.R. techniques can be applied in many scenarios, where multiple frames of images of a single scene can be obtained (for example, a single camera can obtain multiple images of the same object), and various images of the scene can be obtained from many sources, such as multiple cameras from different Position captures a single scene. S.R. has applications in various fields, such as satellite imaging, remote sensing imaging, security and surveillance where it may be necessary to zoom in on specific points of interest in a scene (e.g., zoom in on criminal faces or license plate numbers), in computers that can improve pattern recognition performance The field of vision, as well as other fields such as facial image analysis, text image analysis, biometric recognition, fingerprint image enhancement, etc. S.R. is especially important in medical imaging, where more detailed image detail information is required, and high-resolution medical images can help doctors make correct diagnoses. For example, in computed tomography (C.T.) for diagnosis, the resulting low-resolution images have lower pixel density and provide minor detail due to various uncertainties, which significantly reduces the efficiency of doctor visits.

However, the imaging acquisition device or imaging acquisition process consisting of imaging sensors limits the resolution of the images. In theory, the higher the density of sensors in a digital imaging device, the higher-resolution images it is possible to produce. In fact, due to product cost considerations and the limitations of today's integrated circuits, increasing the number of sensors on a fixed area of a device is not an easy task. Post-processing methods such as super-resolution reconstruction can break through traditional physical limitations and improve image resolution. With the increase in human production and life, the demand for high-resolution images increases (12). With the rise of artificial intelligence technology and the rapid development of Graphics Processing Unit (GPU), deep learning to tap various complex image processing tasks has excellent potential and has become the favorite of many researchers. Deep learning mainly simulates human thinking and analysis by constructing deep neural networks, excavating potential laws between samples, extracting useful feature information, and assisting human beings in various data processing tasks.

In today's high incidence of various diseases such as cancer, high-resolution medical imaging technology is an essential basis for containing various information, which can accurately determine the location and direction of the disease for doctors to understand the disease more comprehensively assist doctors. Medication treatment. This paper uses deep learning technology to analyze various medical images in detail. The methods for super-resolution reconstruction of medical images in three different situations are discussed, effectively avoiding the defects of artificial extraction of data features in traditional methods. Compared with the hardware method, it has excellent advantages. To sum up, super-resolution techniques to improve the quality of medical images have significant research value for helping medical diagnosis (13).

Related work

Interpolation-based super-resolution reconstruction

Interpolation-based super-resolution reconstruction methods are implemented in the spatial domain, and most of the commonly used interpolation algorithms belong to non-uniform interpolation (14). The image after super-resolution reconstruction based on the interpolation algorithm is based on the most intuitive pixel information. The method is based on simple image prior information, so the image information used by this method is limited when we reconstruct the image. Generally, the magnification should not be too large, generally not more than twice the magnification. Otherwise, the reconstructed image will be prone to be over-smoothed at the edges or discontinuous points of the image. The nearest neighbor interpolation method, bilinear interpolation, and bicubic interpolation algorithms are the most commonly used interpolation algorithms. The following is a brief introduction to the three traditional interpolation algorithms.

The idea of this method is to restore the lost pixels by using the gray value of the known pixels around the point to be interpolated, calculate the pixels of the point to be found, and realize the upsampling and zooming operation of the image,

such as nearest-neighbor interpolation, bilinear interpolation method and bicubic interpolation (15).

However, due to the shortcomings of this kind of algorithm, such as being significantly affected by noise and artificial artifacts in reconstructed images, they are primarily used in situations where the resolution requirements of images are not exceptionally high.

Reconstruction-based super-resolution reconstruction

The theoretical basis of reconstruction-based methods is the degradation model of images. The reconstruction-based method uses the prior knowledge of the image as a constraint to realize the super-resolution reconstruction of the image, such as smoothing prior, reconstruction prior and so on. Standard reconstruction methods mainly include the iterative back-projection method, convex set projection method, and maximum a posteriori probability estimation (16). The reconstruction steps are shown in Figure 1.

The super-resolution reconstruction can be regarded as the inverse process of the image degradation process. The high-frequency information lost in the degradation process is added to the image reconstruction process. The image super-resolution reconstruction problem is finally transformed into the inverse solution of the image degradation model.

Different image acquisition devices often use different imaging technologies to acquire images. However, the acquired images usually have different degrees of degradation, affected by device accuracy and environmental factors. In order to reconstruct a super-resolution image from the degraded low-resolution image, the degradation process of the image needs to be modeled first. In the field of medical imaging studied in this paper, the main factors that cause the degradation of imaging quality are insufficient radiation dose, too low sampling frequency, sampling blur caused by patient motion, and equipment noise (17). Its degradation process can be approximated by Equation (1), and the corresponding mathematical model is:

$$\mathrm{I_{LR}} = \mathrm{G_{blur}}(\mathrm{I_{HR}}) \downarrow_{\mathrm{s}} + \mathrm{n}_{\sigma} \tag{1}$$

Among them, $I_{LR}$is the degraded low-resolution image, which I_{HR} is the original high-resolution image, which G_{blur} represents the blur function, usually Gaussian blur, which represents the $\downarrow_s$ downsampling method with a n_σ downsampling coefficient of, which represents additive noise.

Based on the above definition of the image degradation model, the super-resolution reconstruction algorithm can be defined as Equation (2):

$$\mathrm{I_{SR}} = \mathrm{F_s}(\mathrm{P}(\mathrm{I_{LR}})) \tag{2}$$

$P(\cdot)$ represents the preprocessing process for low-resolution images, such as upsampling, filtering, noise reduction, etc. In the algorithm designed in this paper, the preprocessing operation is directly removed, making the algorithm more concise; $F_s(\cdot)$ represents the upsampling coefficient. Rebuild the model for super-resolution.*s*.

Learning-based super-resolution reconstruction

The basic idea is to learn the mapping relationship between high-resolution and low-resolution images. The learning process is divided into training and guided reconstruction, based on dictionary learning and based on the neural network (18).

Compared with interpolation-based and reconstruction-based algorithms, learning-based algorithms are more in line with the current research trend of intellectual development. Learning-based super-resolution reconstruction algorithms used in medical images are mainly divided into general and deep learning algorithms.

SRCNN is the first attempt to apply deep learning to the field of super-resolution reconstruction. It is the first application of deep learning in this field. He is a deep learning method for single image super-resolution (S.R.) (19). End-to-end learning is achieved by directly learning the functional relationship between low-resolution and high-resolution images. In traditional sparse coding-based super-resolution reconstruction methods, for each component, each step requires a specific method to be processed separately, which implements a joint optimization of all neural network layers. Moreover, because the structure is relatively shallow, the structure is light, the speed of reconstruction efficiency is better than the traditional method, and the quality of the reconstructed image effect is also greatly improved.

For the input image, SRCNN first needs to preprocess the input L.R. image, explicitly using the bicubic interpolation algorithm (Bicubic) to enlarge the low-resolution (L.R.) image to the size of the target image (20). The image is then fed into the deep learning network. Because it is an early application, the entire network structure has only three layers of convolutional neural networks, as shown in Figure 2.

Specifically, according to the theoretical knowledge of sparse coding, the author divides the overall network architecture into three modules: the underlying feature extraction module, non-linear learning, and reconstruction module (20).

(1) Feature extraction and representation: extract a low-resolution image patch from the L.R. image Y, and use a high-dimensional vector to represent an image patch. These vectors are combined to form a set of low-resolution feature maps, the number of which is equal to the dimension of the vector.

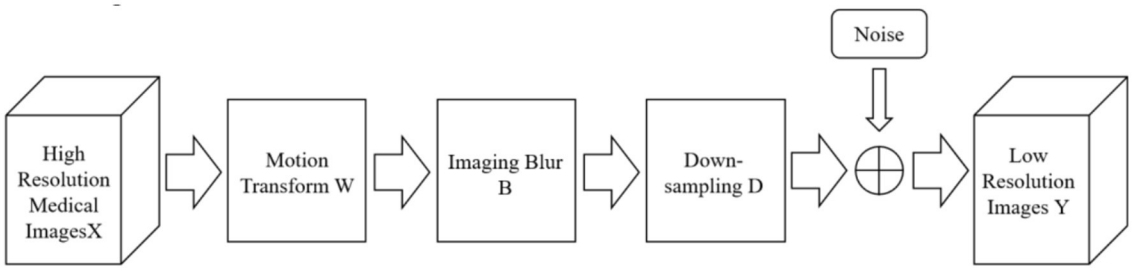

FIGURE 1
Reconstruction-based super-resolution reconstruction step diagram.

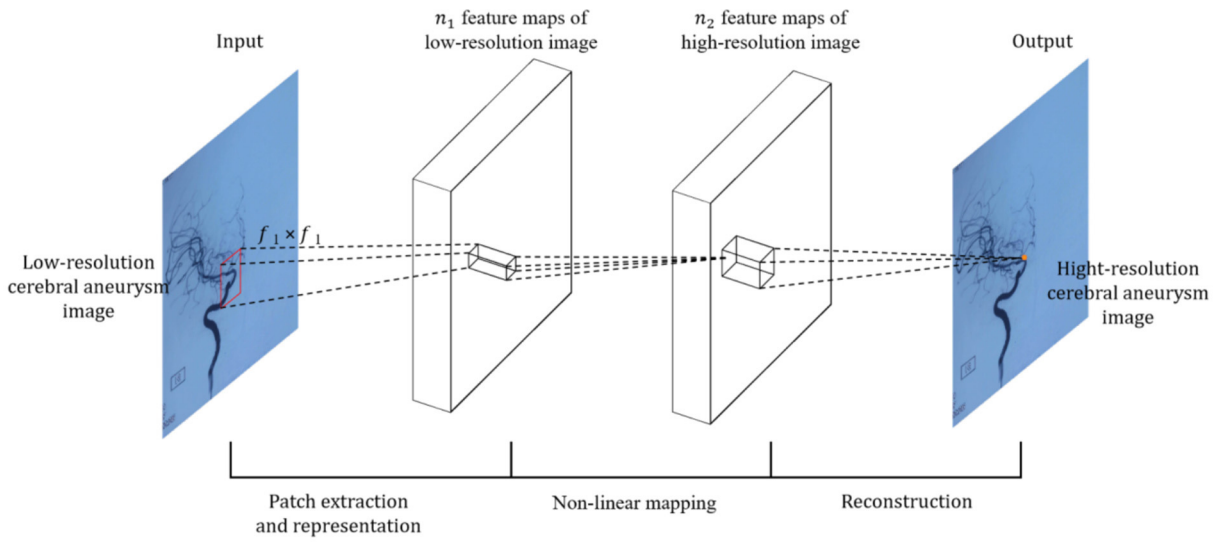

FIGURE 2
Schematic diagram of SRCNN neural network.

The operations of the first layer are expressed, as shown by Equation (3).

$$F_1(Y) = \max(0, W_1 \times Y + B_1) \quad (3)$$

where W_1 and B_1 represents the filter and offset, W_1 the size is, $c$is the number of channels in the input image, is the size of the n_1 filter, the number of filters, so the output n_1 feature map B_1 is one n_1-dimensional vector.

(2) Non-linear mapping: Non-linearly map each high-dimensional vector to another high-dimensional vector. The high-dimensional mapping vector obtained through the mapping relationship can represent a high-resolution image block. These vectors are combined to form a feature map, and the operation of the second layer is expressed, as shown in Equation (4).

$$F_2(Y) = \max(0, W_2 \times F_1(Y) + B_2) \quad (4)$$

where W_2 dimension is, B_2 is one n_2-dimensional vector. F_2 Represents the output n_2 dimensional high-resolution image patch that will be used for reconstruction.

(3) Reconstruction: The high-resolution image patches are aggregated together to reconstruct the final high-resolution image, similar to the original high-resolution image. The last convolutional layer produces the final high-resolution image, defined as, as shown in Equation (5):

$$F(Y) = W_3 \times F_2(Y) + B_3 \quad (5)$$

where W_3 dimension is, B_3 is one c-dimensional vector.

The related literature shows that, compared with the state-of-the-art learning-based methods, the SRCNN model has a

TABLE 1 The usage of the dataset selected for the experiment.

	Total	Training group $n = 300$	Test group $n = 100$	Proportion
An unruptured cerebral aneurysm (positive)	400	240	80	8
Normal (negative)	100	60	20	2

simple structure, high robustness, provides high accuracy, and restores images of high quality, indicating that convolutional neural networks can be applied to image classification involving computer vision for object recognition. The SRCNN method proposed by the authors learns the end-to-end mapping between low-resolution and high-resolution images with little additional pre-and post-processing other than optimization.

Materials and methods

Dataset

A total of 865 patients with unruptured saccular aneurysm (positive cerebral aneurysm) and 120 normal subjects without aneurysm who underwent routine physical examination (physical examination) or visited a doctor from January 2013 to May 2022 at Department of neurosurgery, the second affiliated of Guizhou Medical University Hospital were retrospectively collected (cerebral aneurysm negative) CTA image. After screening by inclusion and exclusion criteria, 500 subjects were included in the study, including 400 cerebral aneurysms positive and 100 cerebral aneurysms negative. The CTA dataset was randomly divided into a training group ($n = 300$, including 240 cerebral aneurysm positive cases and 60 cerebral aneurysm negative cases) and a testing group ($n = 100$, including 80 cerebral aneurysm positive cases and 20 cerebral aneurysm negative cases) according to the number of subjects. The ratio is 8:2.

See Table 1 for details.

The development of diagnostic criteria for a cerebral aneurysm is divided into "gold standard" and "silver standard" (21):

① The "gold standard" refers to the diagnosis of cerebral aneurysm patients by DSA;
② "Silver standard" refers to some patients whom DSA has not confirmed. Two radiologists with more than 5 years of experience review the original and reconstructed images, imaging reports and clinical history, and successive examinations (including CTA and MRA) to determine the most likely label for the diagnostic criteria. In the event of disagreement, a third deputy chief physician assists, and three radiologists vote to determine the presence of an aneurysm.

Inclusion criteria:

(1) Unruptured saccular aneurysm;
(2) No history of surgical clipping or coil embolization.

Exclusion criteria:

(1) subarachnoid hemorrhage;
(2) Severe stenosis of the cerebral atherosclerotic lumen;
(3) Poor image quality with noticeable artifacts;
(4) Other lesions in the brain, such as a tumor, intracranial hematoma, arteriovenous malformation, etc.

ResNet architecture and model training

From a theoretical point of view, the deeper the network, the more sufficient the features extracted by the network, and the more favorable it is for image reconstruction (22). However, blindly increasing the depth will cause the gradient to disappear and the gradient to explore. In backpropagation, the gradient needs to be calculated; according to the chain derivation rule, a series of gradients are multiplied and then added. The obtained partial derivative updates the weight, and the update Equation (6) of the weight is as follows (23):

$$w = w - \alpha \frac{\partial loss}{\partial w} \tag{6}$$

Where α is the learning rate. When the number of network layers is deepened, and the value of the gradient is <1, it can be seen from Equation 6 that the multiplication of multiple values <1 causes $\frac{\partial loss}{\partial}$ the value to approach 0. At this time, the shallow weights of the network cannot be updated, resulting in insufficient training of the network; that is, the gradient disappears; on the contrary, if the value of the gradient is >1, the multiplication of multiple values >1 will result *in* $\partial loss/\partial w$ in an infinite value, resulting in the weight of It cannot be calculated, that is, the gradient explosion phenomenon occurs (24).

The idea of residuals can effectively solve the above gradient problem. The residual structure allows the network to not degenerate with depth by stacking identity mapping layers on an external network (25). The residual block structure consists of a convolutional layer-batch normalization layer and an activation function layer, as shown in Figure 3. The residual structure introduces a fast connection based on the original network, and x is used as the input. After convolution transformation, the output $H(x)$becomes, at that time, which can ensure that the network forms an identity mapping; at that time, the network was regular. $F(x) \neq 0$ Iterating, the weights are updated accordingly.

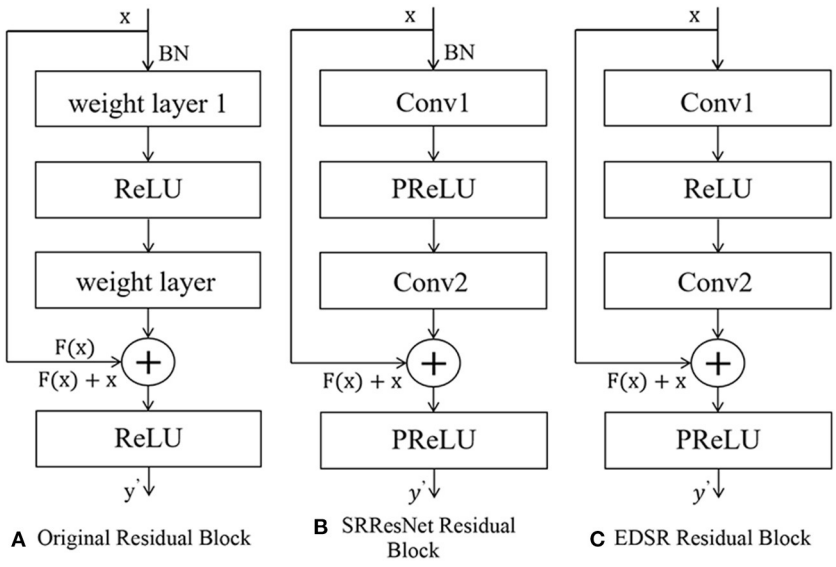

FIGURE 3
The structure of residual net. **(A)** Original residual block. **(B)** SRResNet residual block. **(C)** EDSR residual block.

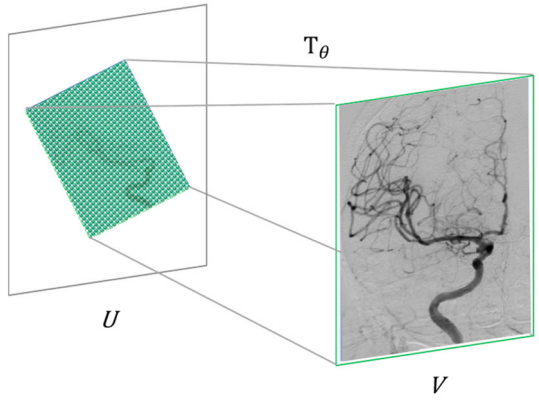

FIGURE 4
Schematic diagram of the attention mechanism in the spatial domain.

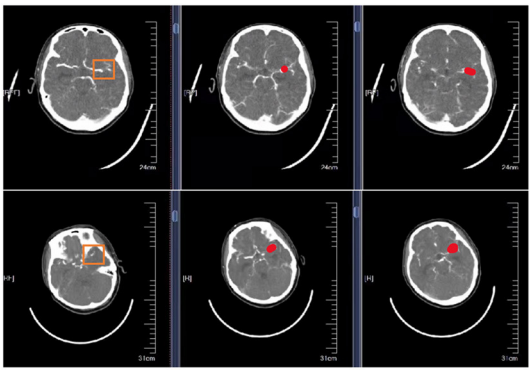

FIGURE 5
Schematic representation of correctly segmented cerebral aneurysms at different locations. The first column is the original CTA image. The second column is the result of physician annotation. The third column is the result of physician detection after high-resolution image reconstruction.

The generation part of SRGAN, SRResNet, uses 16 residual blocks to cascade to complete feature extraction. The structure of residual blocks is shown in Figures 2–5B. Each residual block contains two 3 × 3 convolutional layers. After layering, the B.N. layer and the PReLU activation function layer are connected to realize the fusion of low-frequency and high-frequency features. The reconstruction part can obtain a feature map containing rich, detailed information (26).

The EDSR model fine-tunes and improves the interior of the residual structure, and removes the B.N. layer, as shown in Figures 2–5C. The B.N. layer was initially used for high-level computer vision problems such as classification tasks, which can effectively implement the process of regular training and avoid overfitting (27). B.N. plays a significant role in classification tasks because image classification does not need to preserve image contrast and can use structural information to complete classification (28). The B.N. layer returns the mean value to 0 and the variance to 1. Although the absolute difference of pixels is ignored, it does not affect the classification task. For image super-resolution reconstruction, the B.N. layer will change the original contrast of the image

and normalize the image's color distribution, which affects the reconstruction quality.

To sum up, removing the residual block structure of the B.N. layer has the following advantages. First, it can reduce memory usage and thus speed up the running time; the limit of normalization to 1 meets the requirements of the image in terms of color, contrast, and brightness.

Self-attention mechanism

The attention mechanism is another effective means to improve the performance of neural networks (29). Its principle is mainly based on the attention distribution method of the human brain when processing signals. When the brain receives external signals, it tends to focus on what it is interested in to achieve efficient information extraction. In recent years, researchers have achieved many results by applying attention mechanisms to natural language processing, speech recognition, and image recognition (30).

In computer vision, the specific implementation of attention mechanisms is mainly divided into two categories: spatial domain and channel domain. The spatial domain attention mechanism refers to focusing the computational resources of the network on the spatial locations of interest in the image (31). Firstly, the spatial transformation network obtained by training T_θ extracts the area that needs attention from the input image U and, at the same time, uses the learned perspective transformation matrix to adjust it to a more easily discernible shape, thereby realizing computing resources. Reasonable distribution in the input image. The spatial domain attention mechanism can improve image recognition accuracy to a certain extent. In the super-resolution problem studied in this paper, it is usually necessary to take the complete image as the research object. For the fidelity of information, the image is generally not perspective. In transformation, we adopt the channel domain attention mechanism in this paper, as shown in Figure 4.

The principle of the channel domain attention mechanism is straightforward. A natural image usually consists of three channels of RGB or YCbCr. The importance of information in each channel must be unequal (32). The brain will focus on the information of specific channels, and relatively the remaining channels are ignored. Similarly, in the output feature map of the convolutional layer, the features of different channels are extracted by different convolution kernels, and their importance is obviously different, so they should be treated differently. Based on the above considerations, Hu et al. proposed the S.E. module (Squeeze-and-Excitation module) to simulate the channel attention mechanism (33). In the S.E. module, $W \times H$ the feature map with the size and number of channels as C is used as input. First, the squeeze operation is performed on each channel of the feature map, as shown in Equation (7):

$$z_e = F_{sq}(u_e) = \frac{1}{W \times H} \sum_{i=1}^{H} \sum_{j=1}^{W} u_e(i, j) \tag{7}$$

The squeezing function $F_{sq}(\cdot)$ does a global average pooling operation, encoding the spatial features on each channel into a global feature.

The squeeze operation yields a global description feature, followed by an excitation operation to learn the importance of different channel features. In the S.E. module, this operation is implemented by two fully connected layers, and the specific operation process is shown in Equation (8):

$$s = F_{ex}(z) = \sigma(W_2 \times \mathrm{ReLU}(W_1 \times z)) \tag{8}$$

where $\sigma(\cdot)$ represents the sigmoid activation function; $ReLU(\cdot)$ represents the ReLU activation function; W_1 and W_2 represents the weight coefficients of the two fully connected layers, respectively, r is a dimension reduction coefficient, so the first fully connected layer also plays a role in dimension reduction. Then the second fully connected layer, the connection layer restores the original dimensionality, which ensures that the entire S.E. module has only a small number of parameters.

Finally, the channel attention assignment is completed by assigning the learned activation value as a weight to each channel on the original feature map.

Performance evaluation indicator

Image Quality Assessment (IQA) for the reconstructed image is also an essential field in super-resolution reconstruction technology (34). In order to make the reconstructed image or video as close to the actual H.R. image as possible, a reasonable image or video quality evaluation index is required. Generally speaking, the image quality criterion usually includes subjective and objective evaluations. The two indicators are described in detail below.

Subjective evaluation criteria

The subjective evaluation method is a method in which the observer subjectively evaluates the quality of the reconstructed image and gives the corresponding score through the analysis of people's eyes (35). Commonly used methods include the mean subjective score (Mean Opinion Score, MOS) or the mean subjective score difference (Differential Mean Opinion Score, DMOS). The MOS method is proposed by the SRGAN paper and has a good evaluation effect. Generally, the test images are directly handed over to the testers, and the images are scored according to their personal feelings. The scores are divided into five grades, corresponding to 1–5 points. The better the effect,

the higher the score, which can be expressed by the following Equation (9):

$$MOS = \frac{\sum_{i=1}^{N} R_i}{N} \quad (9)$$

Where R represents the score, N represents the number of people tested, and the average is taken. It can be seen from the Equation that the higher the mos score, the better. For the subjective evaluation of reconstructed images, people are the main body. It is more in line with human subjective visual perception and more in line with the fact that people are often the foremost observers of images. However, this method also has shortcomings. First, the evaluation standard depends on the person, and there is no mathematical principle as the basis for evaluation. Therefore, many repeated experiments are often carried out. Secondly, the subjective evaluation relies on human vision and is also affected by the surrounding environment. Influence, such as light, angle, etc., has certain limitations, so the experimental environment. Therefore, it takes a long time, and many workforce and financial resources are invested. The difficulty of operation is relatively great. Therefore, this subjective evaluation method using MOS is rarely used. More is to observe through the human eye or zoom in on a particular area and then observe and compare. Therefore, the objective evaluation method is the mainstream of the current evaluation method.

Objective evaluation criteria

The method of objectively evaluating the quality of the reconstructed image generally uses a mathematical model to give a specific quantitative value, which is separated from the judgment of human subjective consciousness and has a specific mathematical theoretical basis. It starts from an objective mathematical model, separates from the judgment of people's subjective consciousness, and defines the standard through mathematical function Equations (36). The reconstructed images to be evaluated have the same evaluation criteria, and there is no difference in subjective evaluation criteria. So it has always been the focus of IQA research. Objective IQA methods are divided into three categories: full-reference methods that use reference images for evaluation, such as peak signal-to-noise ratio (PSNR) (37). Pixel-wise loss for PSNR calculation, and MSE in addition to that. Both calculations are essentially the same. PSN calculates the ratio through 1og. The larger the value, the better, indicating better reconstruction quality. The smaller the MSE, the better. In addition, there is structural similarity (Structure Similarity, SSIM). Based on the partial reference method of extracting feature comparison, the focus and difficulty of partial image reference are to find suitable feature information; no reference method without a reference image (i.e., blind IQA), such as mean, standard deviation, etc.

(1) Mean Square Error (MSE), the Equation is shown in Equation (10).

$$MSE = \frac{1}{M \times N} \sum_{i=1}^{M} \sum_{j=1}^{N} \left(f^{'}(i,j) - f(i,j)\right)^2 \quad (10)$$

It represents the expectation of the sum of squared losses per pixel between the reconstructed image and the actual H.R. image. $f^{'}$ *Where* $F(i,j)$ and $f(i,j)$ represents the image to be evaluated and the original image, respectively, M, N represents the length and width of the image, respectively. MSE, in terms of super-resolution, is the expected value of the square of the difference between the pixel estimated value and the actual image pixel value. The smaller the MSE value, indicating that it is closer to each pixel of the image and the reconstruction quality is better. The restoration degree is good; the information loss is slightly closer to the HE image.

(2) Peak-Signal to Noise Ratio (PSNR) (38), as the name implies, calculates a ratio. Because of the similarities between PSNR and MSE in some aspects. We can think of it as the logarithmic representation of MSE. Define Equation (11) as follows:

$$PSNR = 10 \frac{Maxvalue^2}{MSE} = 10 \frac{2^{bits} - 1}{MSE} \quad (11)$$

The larger the PSNR value, the better the quality of the reconstructed image. The *Maxvalue*value is 255 because the pixels in the image are stored quantized in the computer; each pixel occupies 8 bits, and the computer is binary, so calculate 2 to the eighth power and subtract one to get 255. The algorithm is simple, and the inspection speed is fast. However, based on the error between the corresponding pixel points, the presented difference value is not proportional to the subjective human feeling. However, the pure pursuit of the point-to-point loss between pixels ignores human beings' main body of visual evaluation.

Experiments and analysis

Experimental details

The operating system used in this experiment is the Ubuntu 16.06 operating system based on the Linux system. The deep learning framework that implements the neural network is Tensorflow, version 2.0. The programming language is Python3.6, and the graphics card is 1080Ti. The compilation environment is pycharm and juypter notebook. There are also some shared third-party libraries, such as Open CVnumpy and so on.

The deep learning model optimization algorithm adopts the Adam optimization algorithm. Adamy optimization algorithm

is one of the most popular optimization algorithms out there. The learning rate can be adjusted adaptively. The learning rate of each training has a fixed range, and the parameter changes are relatively small. The advantage of Adagrad is that it is suitable for dealing with sparse gradients but not suitable for dealing with non-stationary targets. The Adam optimization algorithm has improved this point. Excellent results are achieved very quickly. The Equation is shown in Equations (12)–(16) (39, 40):

$$m_t = \beta_1 m_{t-1} + (1-\beta_1) g_t \quad (12)$$

$$v_t = \beta_2 v_{t-1} + (1-\beta_2) g_t^2 \quad (13)$$

$$\widehat{m_t} = \frac{m_t}{1-\beta_1^t} \quad (14)$$

$$\widehat{v_t} = \frac{v_t}{1-\beta_2^t} \quad (15)$$

$$\theta_{t+1} = \theta_t - \frac{\eta}{\widehat{v_t}+\varepsilon}\widehat{m_t} \quad (16)$$

Specific parameters use the default parameters; The learning rate is a 1×10^{-4} value $\varepsilon$to 10^{-8} prevent the divisor from being 0. The data is trained after data augmentation. Because of the need to initialize the weights of the neural network. We use the He initialization strategy to initialize the network. The mathematical form is shown in Equation (17):

$$W \sim N(0, \sqrt{\frac{2}{n_1}}) \quad (17)$$

Where N represents the uniform distribution and $n_1$represents the first layer of the neural network, through this initialization method, the initial weight can be prevented from being too large or too small. It prevents the network from having gradient dispersion (gradient disappearance) and other difficult-to-train problems during training.

Experimental metrics and results

Objective evaluation

In the following, we compare and analyze our proposed algorithm and other super-resolution algorithms from an objective evaluation method. We use two evaluation indicators as an objective evaluation method: peak signal-to-noise ratio and structural similarity. PSNR and SSIM measure the reconstructed E image, and the larger the value, the better. The specific calculation method and meaning are described in the fourth subsection of paper 2. I will not go into details here.

For the test set, we divided it into two parts, corresponding to abdominal gastric adenocarcinoma images and abdominal esophageal cancer C.T. images, respectively. Under the 2× magnification factor and 4× magnification factor, the PSNR and SSIM corresponding to the test set are counted. The corresponding average value is taken as the final objective result of the test set. The experimental results are shown in Tables 2, 3 below.

According to the above two tables, the objective evaluation indicators PSNR and SSIM show the worst effect of bicubic interpolation, which is also in line with our subjective visual evaluation. The super-resolution C.T. images reconstructed by the SRCNN, ESPCN, and FSRCNN models are on the C.T. image test set. Compared with the traditional interpolation algorithm, it has been dramatically improved. At the same time, our proposed deep learning model has achieved the corresponding improvement based on the former. The PSNR is improved by about 5 dB compared with the traditional bicubic interpolation algorithm and about 1 dB compared with the previous deep learning model. On the SSIM indicator, it is about 0.1–0.3 higher than other S.R. models. At the same time, in terms of horizontal comparison, the PSNR and SSIM of the image enlarged by 2. times are better than the C.T. image reconstructed by 4 times. Explain that small magnifications of images are better for training during reconstruction. If the magnification factor is too significant, the reconstruction effect will be worse because of the increased information to be learned.

Therefore, summarizing the above subjective evaluation methods and objective evaluation indicators and comparing them with the traditional double interpolation algorithm and the classic deep learning S.B. model fully demonstrates the superiority of our proposed algorithm for super-resolution reconstruction on abdominal C.T. medical images, sex and effectiveness.

Residual network model effect

① The 3D U3-Net model missed 36 aneurysms, including 22 in ICA, 4 in MCA, 7 in ACA, 2 in PCA, and 1 in B.A. The diameters of missed aneurysms ranged from 2.20 to 5.38 mm. ② 37 false-positive aneurysms, 9 from cerebral aneurysm-negative subjects and 28 from cerebral aneurysm-positive subjects, of which 13 were located in the ICA, 12 were located in orbit, 4 were located in the ethmoid sinus, and 6 were located in the neck Veins, 1 in the ACA and 1 in the left FCA. ③ The model found two newly missed aneurysms, one in the left MCA and one in the left VA (40).

Are shown in Figure 5 schematic illustration of correctly classified aneurysms at different locations.

Residual network model performance

The diagnostic sensitivity of the 3D U2-Net model for aneurysms with diameters >3 mm was 85.9% (171/199), which was higher than that for aneurysms <3 mm in diameter (23/36, 63.7%). The difference was statistically significant. Significance ($P = 0.001 < 0.05$). The diagnostic sensitivity of the 3D U-Net model in different locations of the aneurysm (anterior

TABLE 2 PSNR experimental data.

Data set	Scale	Bicubic	SRCNN	ESPN	FSRCNN	Our method
Brain aneurysm CTA imaging	2	28.54	30.65	32.01	31.91	33.01
Brain aneurysm CTA imaging	4	24.55	25.52	26.93	26.69	28.39

TABLE 3 SSIM experimental data.

Data set	Scale	Bicubic	SRCNN	ESPN	FSRCNN	Our method
Brain aneurysm CTA imaging	2	0.9400	0.9301	0.9324	0.9341	0.9521
Brain aneurysm CTA imaging	4	0.8653	0.8801	0.9023	0.8879	0.9138

TABLE 4 Model checking performance.

Parameters	Test set
Number of examiners	268
Number of aneurysms	235
Sensitivity	82.7% (194/235)
Positive predictive value	82.3% (194/236)
Specificity	86.0% (43/50)
Aneurysm size	Sensitivity
<3 mm	64.7% (23/36)
3–7 mm	80.2% (95/118)
>7 mm	93.3% (76/81)
Aneurysm location	
ICE	82.8% (130/157)
MCA	70.3% (19/27)
ACA	74.3% (29/39)
PCA	40.0% (2/5)
BA	91.6% (11/12)
VA	100% (3/3)

circulation and posterior circulation), different field strengths (1.5 and 3.0 T), and different imaging equipment (Philips, Siemens, GE) had no statistically significant difference ($P > 0.05$), see Table 4 for details.

Comparison of aneurysm detection

The 3D U2-Net model is compared with the indicators detected by radiologists of different seniority, as shown in Table 5. 3DU-Net model detected a total of 236 aneurysms, Physician 1 and Physician 2 217 and 225 were detected, respectively. The sensitivities of the three groups were Physician 1 <3D U2-Net model < Physician 2, and the difference was not statistically significant (Physician 1 vs. model, $P = 1.000$; Physician 2 vs. model, $P = 0.170$), diagnostic specificity and positive predictive value were Physician 2 > Physician 1 > 3DU3-Net model, the false positive rate of 3D TU-Net model was 0.14 cases/case, which was higher than that of Physician 1 (0.07 cases/case) and Physician 2 (0.06 cases/case). The performance of the three groups in different aneurysm sizes, locations, field strengths and the sensitivity of imaging equipment are shown in Table 5.

Discussion

Review of the experimental procedure

This paper is mainly based on the multi-scale joint convolutional neural network proposed in Section Materials and methods. In order to stack more networks and enhance the flow of feature information between networks, a residual network is introduced. Besides, in the existing research, most S.R. models on medical images use one-shot reconstruction and generalize the problem of poor image reconstruction quality for prominent magnification factors. Considering that it becomes challenging to reconstruct the image due to the increased loss of information under prominent magnification factors, a multi-level output network is introduced to achieve progressive reconstruction, and our framework has a certain flexibility to obtain intermediate-level outputs; it is realized that the same network can be reconstructed with different multiples. Experiments are carried out on abdominal C.T. medical images. Experiments are carried out on CTA medical images of the brain. The experimental results show that the improved network proposed by us can enhance the quality of the reconstructed images under large magnification and achieve better results than the bicubic interpolation algorithm and the ESPCN algorithm. Moreover, CTA images of cerebral aneurysms verify that our model has good generality and generalization.

Comparison with other studies

According to the above two tables, the objective evaluation indicators PSNR and SSIM show the worst effect of bicubic

TABLE 5 Comparison of physician detection and model-assisted physician detection results.

Diagnosis technique	Check out(s)	Missed/misdiagnosed (pcs)	Sensitivity (%)	Positive predictive value (%)	Specificity (%)	False-positive rate (pieces/example)
Physician 1	217	37, 19	84.3	91.2	90.0%	0.07
Model aided	236	36, 37	84.7	84.3	88.0%	0.14

interpolation, which is also in line with our subjective visual evaluation. The super-resolution C.T. images reconstructed by the SRCNN, ESPCN, and FSRCNN models are on the C.T. image test set. Compared with the traditional interpolation algorithm, it has been dramatically improved. At the same time, our proposed deep learning model has achieved the corresponding improvement based on the former. The PSNR is improved by about 5 dB compared with the traditional bicubic interpolation algorithm and about 1 dB compared with the previous deep learning model. On the SSIM indicator, it is about 0.1–0.3 higher than other S.R. models. At the same time, in terms of horizontal comparison, the PSNR and SSIM of the image enlarged by 2. times are better than the C.T. image reconstructed by 4 times. Explain that small magnifications of images are better for training during reconstruction. If the magnification factor is too significant, the reconstruction effect will be worse because of the increased information to be learned.

Therefore, summarizing the above subjective evaluation methods and objective evaluation indicators and comparing them with the traditional double interpolation algorithm and the classic deep learning S.B. model fully demonstrates the superiority of our proposed algorithm for super-resolution reconstruction on abdominal C.T. medical images, sex and effectiveness.

Innovations

Based on the field of medical images, this paper focuses on the super-resolution reconstruction technology of medical images, from the traditional super-resolution reconstruction technology—based on interpolation, based on sparse dictionaries and other methods, and is composed of deep learning widely used in various fields. The convolutional neural network, one of the units, is introduced, focusing on the deep learning-based super-resolution reconstruction of several typical S.B. models, SRCNN, ESPCN, etc. Given the shortcomings of the traditional deep learning S-up model in super-resolution medical image reconstruction, a summary is made, corresponding improvements are made in response to the problems, and two deep learning models are proposed for abdominal C.T. medical images. Super-resolution reconstruction. The innovation points of this study are summarized as follows:

(1) In the existing research, most deep learning models based on medical image super-resolution reconstruction use a single-scale convolution kernel to build the network, ignoring the difference in the information contained in images of different scales and feelings wild information. In order to fully extract multiple different scale information, we propose a multi-scale joint convolutional neural network for super-resolution reconstruction in the field of C.T. medical images.
(2) Introduce local residual learning to form a multi-scale joint residual block, which is used as the basic unit to avoid the gradient disappearance and gradient explosion problems caused by the deepening of the network layer. In addition, both SRCNN, ESPCN and other networks perform single-multiple L.R. image reconstruction and cannot perform L.R. image reconstruction output with multiple magnifications simultaneously, poor quality. Therefore, in response to this problem, the idea of upsampling the Laplacian pyramid network is introduced, and a multi-level output network is constructed to achieve the same network, which can output multiple magnified images simultaneously. It realizes multi-level magnification and step-by-step reconstruction and enhances the quality of reconstructed images under prominent magnification factors.

Research significance

Through the results of this study, it can be found that the deep learning CAD system based on 3D U-Net has the following advantages in the detection of cerebral aneurysms: First, it helps physicians to perform an initial screening of diseases, which can effectively assist radiologists in reducing work intensity and improving work efficiency; Second, the accuracy of identifying cerebral aneurysm is equivalent to that of a radiology resident, and the "human-machine integration" mode in clinical applications can significantly improve the accuracy of diagnosis; third, the standardized process of a CAD system can ensure the objectiveness of diagnostic results stability, repeatability, and the ability to learn and improve from feedback continuously. Note that extreme learning deep neural networks (41) can be implemented for the high-resolution medical image reconstruction of cerebral aneurysm in the future. The three dimensional visualization framework (38) in

monitoring of cerebral aneurysm can be enhanced based on such advanced spatial models.

Conclusion

Our study is a retrospective analysis. In order to further verify the clinical application value of ResNet in the detection of cerebral aneurysms, we next plan to conduct a prospective study based on multi-center clinical data. Moreover, our algorithm uses only CTA source images and no MIP images and using both source and MIP images may show better performance in detecting intracranial aneurysms. Finally, the algorithm was only developed for cystic unruptured aneurysms, and its performance in other types of aneurysms has not been studied. Fourth, the training dataset does not contain enough specific regions and sizes data. More unusual locations and small aneurysms should be added to the training process to improve the algorithm further.

Data availability statement

The raw data supporting the conclusions of this article will be made available by the authors, without undue reservation.

Ethics statement

Ethical review and approval was not required for the study on human participants in accordance with the local legislation and institutional requirements. Written informed consent for participation was not required for this study in accordance with the national legislation and the institutional requirements. Written informed consent was obtained from the individual(s) for the publication of any potentially identifiable images or data included in this article.

Author contributions

All authors listed have made a substantial, direct, and intellectual contribution to the work and approved it for publication.

Conflict of interest

The authors declare that the research was conducted in the absence of any commercial or financial relationships that could be construed as a potential conflict of interest.

Publisher's note

All claims expressed in this article are solely those of the authors and do not necessarily represent those of their affiliated organizations, or those of the publisher, the editors and the reviewers. Any product that may be evaluated in this article, or claim that may be made by its manufacturer, is not guaranteed or endorsed by the publisher.

References

1. Hassan T, Tamimi A. Successful endovascular management of brain aneurysms presenting with mass effect and cranial nerve palsy. *Neurosurg Rev*. (2013) 36:87–97. doi: 10.1007/s10143-012-0404-3

2. Quilici L, Boccardi E. *Endovascular Treatment of Brain Aneurysms*. New York, NY: Springer (2015). doi: 10.1007/978-1-4614-9212-2_6-1

3. Sanai N, Zador Z, Lawton MT. Bypass surgery for complex brain aneurysms: an assessment of intracranial-intracranial bypass. *Neurosurgery*. (2009) 65:670–83. doi: 10.1227/01.NEU.0000348557.11968.F1

4. DeAngelis LM. Brain tumors. *New Engl J Med*. (2001) 344:114–23. doi: 10.1056/NEJM200101113440207

5. Black PML. Brain tumors. *New Engl J Med*. (1991) 324:1555–64. doi: 10.1056/NEJM199105303242205

6. Acharya BS, Actis M, Aghajani T, Agnetta G, Aguilar J, Aharonian F, et al. Introducing the CTA concept. *Astroparticle Phys*. (2013) 43:3–18. doi: 10.1016/j.astropartphys.2013.01.007

7. Wong K.K.L., Fortino G. and Abbott D., Deep learning-based cardiovascular image diagnosis: a promising challenge. *Fut Gen Comput Syst*. (2020) 110:802–11. doi: 10.1016/j.future.2019.09.047

8. Sheng J, Tang P, Li H, Ma L, Hu J, Xu T, et al. Application value of CTA combined with digital technology in the design of anterolateral thigh flap in repairing operative defect of the head, neck and maxillofacial tumor resection. *J Clin Otorhinolaryngol Head Neck Surg*. (2021) 35:992–7. doi: 10.13201/j.issn.2096-7993.2021.11.007

9. Nakao T, Miura Y, Furuichi K, Yasukawa M. Cellulose Triacetate (CTA) Hollow-Fiber (H.F.) membranes for sustainable seawater desalination: a review. *Membranes*. (2021) 11:183. doi: 10.3390/membranes11030183

10. Liu G, Wu J, Ghista DN, Huang W, Wong KKL. Hemodynamic characterization of transient blood flow in right coronary arteries with varying curvature and side-branch bifurcation angles. *Comput Biol Med*. (2015) 64:117–26. doi: 10.1016/j.compbiomed.2015.06.009

11. Yadlapati R, Kahrilas PJ, Fox MR, Bredenoord AJ, Gyawali CP, Roman S, et al. Esophageal motility disorders on high-resolution manometry: Chicago classification version 4.0©. *Neurogastroenterol Motility*. (2021) 33:e14058. doi: 10.1111/nmo.14053

12. Peirlinck M, Costabal FS, Yao J, Guccione JM, Tripathy S, Wang Y, et al. Precision medicine in human heart modeling. *Biomech Model Mechanobiol*. (2021) 20:803–31. doi: 10.1007/s10237-021-01421-z

13. Sherwood KR, Tran J, Günther OP, Lan J, Aiyegbusi O, Liwski R, et al. Genome Canada precision medicine strategy for structured national implementation of epitope matching in renal transplantation. *Hum Immunol*. (2022) 83:264–9. doi: 10.1016/j.humimm.2022.01.002

14. Zhao M, Wei Y, Wong KKL. A Generative Adversarial Network technique for high-quality superresolution reconstruction of cardiac magnetic resonance images. *Magn Reson Imaging*. (2022) 85:153–60. doi: 10.1016/j.mri.2021.10.033

15. Zhang M, Sun X, Zhu Q, Zheng G. A survey of hyperspectral image super-resolution technology. In: *2021 IEEE International Geoscience and Remote Sensing Symposium IGARSS*. Brussels: IEEE (2021). p. 4476–9. doi: 10.1109/IGARSS47720.2021.9554409

16. Gardiner BS, Wong KKL, Joldes GR, Rich AJ, Tan CW, Burgess AW, et al. Discrete element framework for modeling extracellular matrix, deformable cells and subcellular components. *PLoS Comput Biol.* (2015) 11:e1004544. doi: 10.1371/journal.pcbi.1004544

17. Yue HH, Qin SJ. Reconstruction-based fault identification using a combined index. *Indus Eng Chem Res.* (2001) 40:4403–14. doi: 10.1021/ie000141+

18. Gajjar PP, Joshi MV. New learning-based super-resolution: use of DWT and IGMRF prior. *IEEE Trans Image Process.* (2010) 19:1201–13. doi: 10.1109/TIP.2010.2041408

19. Wang D, Fong S, Wong RK, Mohammed S, Fiaidhi J, Wong KKL. Robust High-dimensional bioinformatics data streams mining by ODR-ioVFDT. *Sci Rep.* (2017) 7:43167. doi: 10.1038/srep43167

20. Ren H, El-Khamy M, Lee J. CT-SRCNN: cascade trained and trimmed deep convolutional neural networks for super image resolution. In: *2018 IEEE Winter Conference on Applications of Computer Vision (WACV)*. Lake Tahoe, NV: IEEE (2018). p. 1423–31. doi: 10.1109/WACV.2018.00160

21. Filannino M, Di Bari M. Gold standard vs. silver standard: the case of dependency parsing for Italian. In: *2016 Proc. CLiC.* (2016). p. 288. doi: 10.4000/books.aaccademia.1475

22. Wang M, Zhang X, Niu X, Wang F, Zhang X. Scene classification of high-resolution remotely sensed image based on ResNet. *J Geovisualiz Spatial Anal.* (2019) 3:1–9. doi: 10.1007/s41651-019-0039-9

23. Ding L, Zheng K, Lin D, Chen Y, Liu B, Li J, et al. MP-ResNet: Multipath residual network for the semantic segmentation of high-resolution PolSAR images. *IEEE Geosci Remote Sensing Lett.* (2021) 19:1–5. doi: 10.1109/LGRS.2021.3079925

24. Lu Z, Jiang X, Kot A. Deep coupled resnet for low-resolution face recognition. *IEEE Signal Process Lett.* (2018) 25:526–30. doi: 10.1109/LSP.2018.2810121

25. Wei L, Wan S, Guo J, Wong KKL. Novel hierarchical selected ensemble classifier with bioinformatics application. *Artif Intell Med.* (2017) 83:82–90. doi: 10.1016/j.artmed.2017.02.005

26. Zhou Q, Zhu W, Li F, Yuan M, Zheng L, Liu X. Transfer learning of the ResNet-18 and DenseNet-121 model used to diagnose intracranial hemorrhage in C.T. scanning. *Curr Pharm Design*. (2022) 28:287–95. doi: 10.2174/1381612827666211213143357

27. Reed R, Dericquebourg E, Canals R, Hafiane A. Transformer neural network for weed and crop classification of high-resolution UAV images. *Remote Sensing.* (2022) 14:592. doi: 10.3390/rs14030592

28. Ayyachamy S, Alex V, Khaled M, Krishnamurthi G. Medical image retrieval using Resnet-18. In: *Medical Imaging 2019: Imaging Informatics for Healthcare, Research, and Applications*. San Diego, CA: International Society for Optics and Photonics (2019).

29. Cui B, Li Y, Chen M, Zhang Z. Fine-tune BERT with sparse self-attention mechanism. In: *Proceedings of the 2019 Conference on Empirical Methods in Natural Language Processing and the 9th International Joint Conference on Natural Language Processing (EMNLP-IJCNLP).* Hong Kong (2019). p. 3548–53. doi: 10.18653/v1/D19-1361

30. Alboucai I. *Optimizations on ResNet Using a Self-Attention Mechanism*. Ann Arbor, MI: The Cooper Union for the Advancement of Science and Art (2021).

31. Pedro R, Oliveira AL. Assessing the impact of attention and self-attention mechanisms on the classification of skin lesions. In: *2022 International Joint Conference on Neural Networks (IJCNN).* Padua: IEEE (2022). p. 1–8. doi: 10.1109/IJCNN55064.2022.9892274

32. Rao A, Park J, Woo S, Lee JY, Aalami O. Studying the effects of self-attention for medical image analysis. In: *Proceedings of the IEEE/CVF International Conference on Computer Vision.* (2021). p. 3416–25. doi: 10.1109/ICCVW54120.2021.00381

33. Hoogi A, Wilcox B, Gupta Y, Rubin DL. Self-attention capsule networks for object classification. *arXiv preprint arXiv:1904.12483*. (2019). doi: 10.48550/arXiv.1904.12483

34. Zhai G, Min X. Perceptual image quality assessment: a survey. *Sci China Inform Sci.* (2020) 63:1–52. doi: 10.1007/s11432-019-2757-1

35. Vardaxis N G, Bard D, Persson Waye K. Review of acoustic comfort evaluation in dwellings—part I: associations of acoustic field data to subjective responses from building surveys. *Build Acoust.* (2018) 25:151–70. doi: 10.1177/1351010X18762687

36. Vaira LA, Deiana G, Fois AG, Pirina P, Madeddu G, De Vito A, et al. Objective evaluation of anosmia and ageusia in COVID-19 patients: single-center experience on 72 cases. *Head Neck*. (2020) 42:1252–8. doi: 10.1002/hed.26204

37. Tirkolaee EB, Mardani A, Dashtian Z, Soltani M, Weber GW. A novel hybrid method using fuzzy decision making and multi-objective programming for sustainable-reliable supplier selection in two-echelon supply chain design. *J Clean Prod.* (2020) 250:119517. doi: 10.1016/j.jclepro.2019.119517

38. Zhao C, Lv J, Du S. Geometrical deviation modeling and monitoring of 3D surface based on multi-output gaussian process. *Measurement*. (2022) 199:111569. doi: 10.1016/j.measurement.2022.111569

39. James IKM, Ismail AR, Nisa SQ. Adam optimization algorithm for the broad and deep neural network. *Knowl Eng Data Sci.* (2019) 2:41–6. doi: 10.17977/um018v2i12019p41-46

40. Liang G, Zheng L. A transfer learning method with deep residual network for pediatric pneumonia diagnosis. *Comput Methods Programs Biomed.* (2020) 187:104964. doi: 10.1016/j.cmpb.2019.06.023

41. Tang Z, Wang S, Chai X, Cao S, Ouyang T, Li Y. Auto-encoder-extreme learning machine model for boiler NOx emission concentration prediction. *Energy*. (2022) 256:124552. doi: 10.1016/j.energy.2022.124552

frontiers | Frontiers in Cardiovascular Medicine

TYPE Original Research
PUBLISHED 26 October 2022
DOI 10.3389/fcvm.2022.1012450

OPEN ACCESS

EDITED BY
Ruizheng Shi,
Central South University, China

REVIEWED BY
Defu Qiu,
China University of Mining and Technology, China
Weiwei Yu,
Northwestern Polytechnical University, China
Xiliang Zhu,
Zhengzhou University, China

*CORRESPONDENCE
Yi Wang
wangyi@fjmu.edu.cn
Jing Huang
star19871010@163.com

†These authors have contributed equally to this work and share first authorship

SPECIALTY SECTION
This article was submitted to Cardiovascular Imaging, a section of the journal Frontiers in Cardiovascular Medicine

RECEIVED 05 August 2022
ACCEPTED 06 October 2022
PUBLISHED 26 October 2022

CITATION
Li Y, Liu Z, Lai Q, Li S, Guo Y, Wang Y, Dai Z and Huang J (2022) ESA-UNet for assisted diagnosis of cardiac magnetic resonance image based on the semantic segmentation of the heart. *Front. Cardiovasc. Med.* 9:1012450. doi: 10.3389/fcvm.2022.1012450

ESA-UNet for assisted diagnosis of cardiac magnetic resonance image based on the semantic segmentation of the heart

Yuanzhe Li[1†], Zhiqiang Liu[2†], Qingquan Lai[1], Shuting Li[1], Yifan Guo[3], Yi Wang[1*], Zhangsheng Dai[4] and Jing Huang[1*]

[1]Department of CT/MRI, The Second Affiliated Hospital of Fujian Medical University, Quanzhou, China, [2]Medical Imaging Department, Guangzhou Twelfth People's Hospital, Guangzhou, China, [3]Department of Radiology, The First Affiliated Hospital of Zhejiang Chinese Medical University (Zhejiang Provincial Hospital of Traditional Chinese Medicine), Hangzhou, China, [4]Department of Orthopaedic Surgery, The Second Affiliated Hospital of Fujian Medical University, Quanzhou, China

Background: Cardiovascular diseases have become the number one disease affecting human health in today's society. In the diagnosis of cardiac diseases, magnetic resonance image (MRI) technology is the most widely used one. However, in clinical diagnosis, the analysis of MRI relies on manual work, which is laborious and time-consuming, and also easily influenced by the subjective experience of doctors.

Methods: In this article, we propose an artificial intelligence-aided diagnosis system for cardiac MRI with image segmentation as the main component to assist in the diagnosis of cardiovascular diseases. We first performed adequate pre-processing of MRI. The pre-processing steps include the detection of regions of interest of cardiac MRI data, as well as data normalization and data enhancement, and then we input the images after data pre-processing into the deep learning network module of ESA-Unet for the identification of the aorta in order to obtain preliminary segmentation results, and finally, the boundaries of the segmentation results are further optimized using conditional random fields. For ROI detection, we first use standard deviation filters for filtering to find regions in the heart cycle image sequence where pixel intensity varies strongly with time and then use Canny edge detection and Hough transform techniques to find the region of interest containing the heart. The ESA-Unet proposed in this article, moreover, is jointly designed with a self-attentive mechanism and multi-scale jump connection based on convolutional networks.

Results: The experimental dataset used in this article is from the Department of CT/MRI at the Second Affiliated Hospital of Fujian Medical University. Experiments compare other convolution-based methods, such as UNet, FCN, FPN, and PSPNet, and the results show that our model achieves the best results on Acc, Pr, ReCall, DSC, and IoU metrics. After comparative analysis, the experimental results show that the ESA-UNet network segmentation model designed in this article has higher accuracy, intuitiveness, and more application value than traditional image segmentation algorithms.

Conclusion: With the continuous application of nuclear magnetic resonance technology in clinical diagnosis, the method in this article is expected to become a tool that can effectively improve the efficiency of doctors' diagnoses.

KEYWORDS

cardiovascular disease, artificial intelligence, image segmentation, ESA-UNet, conditional random field

Introduction

Cardiovascular disease has become the number one killer that affects human health in today's society (1). According to domestic statistics, the number of deaths caused by cardiovascular disease has accounted for more than 40% of the total number of deaths from the disease, ranking at the forefront in the composition of deaths, higher than other diseases such as tumors. Research on cardiac diagnosis has always been a research hotspot. With the development of digital imaging technology and the continuous improvement of image segmentation technology (2, 3), medical imaging has become more and more widely used in clinical diagnosis and has become the primary basis for doctors' diagnosis and treatment. Among them, magnetic resonance imaging (MRI) is the most widely used one in the diagnosis of heart disease. Cardiac MRI can provide clearer information on cardiac structure, myocardial motion, and histological features.

Although MRI technology plays an important role in the diagnosis of heart disease, medical imaging itself is complex and requires extremely high accuracy of results. At present, the analysis of medical images is mainly completed by experienced doctors. Since automatic segmentation and diagnosis cannot meet clinical needs, they can only be used as auxiliary supplements. However, the workload required for manual analysis by radiologists is large and time-consuming and is affected by the subjective experience, environment, and working status of different radiologists, and the results vary from person to person. The sketched results are not 100% reproducible. In recent years, with the rapid development of artificial intelligence and deep learning, the use of computer-aided diagnosis and treatment can significantly improve the efficiency of diagnosis. Classification and semantic segmentation are commonly used, in which semantic segmentation can not only diagnose the type of disease but also point out the location of the disease, which is an effective auxiliary means for intelligent diagnosis. Computer technology can be harnessed to locate and segment the region of interest (ROI) in the medical image, identify the pixel points in the ROI area, and obtain the characteristic parameters of the ROI, to provide reliable reference information for the subsequent analysis of the disease and evaluation of treatment, and assist doctors to carry out diagnosis and treatment. Medical image segmentation is a key step in medical image processing and is crucial for the next step of diagnosis and treatment (4).

At present, there are many segmentation methods widely used at home and abroad. The traditional segmentation methods include edge-based image segmentation, region-based image segmentation, and image segmentation combined with specific theories, etc. (5–8). Zhang et al. (9) proposed a medical image clustering and segmentation algorithm, which uses a dictionary as the clustering center of clustering segmentation, and determines the cluster attribution through sparse representation to achieve medical image segmentation.

In recent years, deep learning algorithms have shown powerful capabilities in image processing, especially the convolutional network model for medical image segmentation is better than traditional segmentation algorithms. M.R. Avendi et al. (10) used a convolutional neural network to locate the left ventricular region of the heart from cardiac MRI, and then used a stack auto-encoding algorithm model to outline the initial shape of the left ventricle. Long et al. (11) proposed a fully convolutional neural network segmentation method, which uses transposed convolution to restore the feature map to the original image size to achieve pixel-level segmentation, and then realize the entire image segmentation. Nasresfahani et al. (12) extracted the ROI region in the image processing stage and used a fully convolutional neural network to segment the left ventricle.

Although convolutional networks have achieved promising results in MRI segmentation tasks, they lack efficiency in capturing global contextual information due to the inherent limitations of convolutions. This results in large differences in texture, shape, and size of segmented hearts from patient to patient. For two pixels that are far apart, many layers of convolution are often needed to achieve, but too deep can easily affect the training effect.

For this reason, the self-attention mechanism based on CNN features is proposed to solve this problem (13, 14). The attention mechanism was first proposed by Vaswani et al. (15) to solve the problem of machine translation. The attention mechanism can adjust the learned weights to make important features more weighted. Wang et al. (16) introduced the attention mechanism into computer vision for the first time and adjusted the weights

of feature maps by calculating the correlation between pixels. Subsequently, attention mechanisms have been widely used in the field of medical images. Li et al. (17) designed an attention-based nested UNet model to segment liver tumor images. The network proposes an attention gate module, which can aggregate the encoder and upsampled information while adjusting the weights. Fan et al. (18) proposed a network Inf-Net for segmenting CT images of COVID-19. The network utilizes a set of implicit reverse attention modules and explicit edge attention guidance to establish the relationship between regions and boundaries. Liu et al. (19) designed a CANet network based on an attention conditional random field to segment gliomas, where attention can regulate the amount of information flowing between different features. Dou et al. (20) designed a segmentation network with deep attention module convolution kernels to segment fetal cortical plates.

The attention mechanism can obtain long-range feature information and adjust the weight of feature points by aggregating the correlation information of global feature points. Although the attention mechanism has significantly improved the recognition accuracy of the model, attention mechanism has the problems of high time complexity, slow training speed, and many weight parameters. To ensure rich semantic information, the semantic segmentation network usually uses large-sized feature maps, which causes the time complexity of the model to be too high. To solve the problem of time complexity brought by the attention mechanism, tensor decomposition can well reduce the time complexity of the attention mechanism. Tensor decomposition is widely used in computer vision acceleration. According to tensor decomposition theory (21), high-rank tensors can be decomposed into linear combinations of low-rank tensors. Lebedev et al. (22) proposed a method for accelerating convolutional layers in large convolutional networks based on CP tensor decomposition. The method first decomposes a high-rank tensor of four-dimensional convolution kernels into multiple rank tensors and then uses a rank-one convolution kernel to speed up network training. Wu et al. (23) decomposed the weight matrix of the fully connected layer into a Kronecker product of multiple sub-tensors to approximate the fully connected layer while reducing the parameters in the neural network. Sun et al. (24) designed a tensor decomposition method for network optimization. This method realizes the compression of the model by using the characteristic that the weight tensors between each layer of the network contain the same or independent components, and decomposes the sequence of the coupling tensors on the shared network structure.

Chen et al. (25) proposed RecoNet, a three-dimensional contextual feature representation semantic segmentation model. The model achieves the approximation of a high-rank tensor by the linear combination of low-rank sub-tensor features, which significantly reduces the computational complexity of the model compared to the original feature map. The above methods usually replace a high-rank tensor with multiple low-rank tensors. Tensor decomposition can decompose the original tensor with high computational complexity into a set of low-rank sub-tensors. By calculating the low-rank sub-tensor, the parameter quantity of the network model can be reduced and the network can be accelerated at the same time. Although the tensor decomposition method can improve the compression rate of the model, the recognition efficiency of the model will decrease when the model compression rate is high. To alleviate the problem of low recognition efficiency caused by tensor decomposition, this article uses a shared structure in the network to improve the performance of the model.

Based on the above analysis, this article proposes a deep learning-based cardiac MRI segmentation scheme. We first performed pre-processing of the unsegmented MRI, including the region of interest detection (ROI), data normalization, and data enhancement of the cardiac MRI data. ROI detection is based on Canny edge detection, and ROI detection is performed by using the Hough transform for the detection of circles to narrow down the segmentation region. We then artificially augment the experimental dataset using multiple data augmentation means. For the semantic segmentation network, we introduce a self-attention module in the traditional convolutional network structure. We propose ESA-UNet, a U-shaped semantic segmentation network, which is embedded with a low-rank tensor self-attention structure. ESA-UNet uses an encoding-decoding structure to realize the fusion of feature information of different scales. To obtain richer semantic information and reduce the complexity of the self-attention model, this article designs a low-rank tensor self-attention reconstruction module, decomposes high-rank tensors into low-rank tensors, and uses low-rank tensors to construct the Self-attention feature maps, and then aggregate multiple low-rank self-attention maps to generate high-rank self-attention feature maps. For the network segmentation results, we performed a further optimization of tumor boundaries using conditional random fields. We conduct a full experimental analysis of the ACDC dataset, and the results show that our proposed segmentation method outperforms other methods. This method will play an extremely important role in the diagnosis, treatment, and prognosis of heart disease.

Method

Datasets

In this article, the Department of CT/MRI at the Second Affiliated Hospital of Fujian Medical University collects cardiac MRIs from 150 different patients. The dataset includes 100 training samples and 50 testing samples. Each training sample contains expert manual segmentation and annotation results of the right atrium, left atrium, and aorta at end-diastole (ED) and

end-systole (ES). The MRI data for each patient consisted of 28 to 40 frames of a series of short-axis image slices of the entire cardiac cycle from the bottom to the top of the left ventricle. The spatial resolution of each slice averages 235–263 voxels.

Pre-processing

To ensure the segmentation effect of the segmentation network, we first perform sufficient pre-processing on the MRI. The pre-processing steps include region of interest detection (ROI), data normalization, and data enhancement for cardiac MRI data.

Region of interest detection is divided into two steps: filtering and edge detection. The filtering operation uses a standard deviation filter to find regions of the cardiac cycle image sequence where the pixel intensity varies strongly over time. Edge detection uses Canny edge detection (26) and the Hough transform technique (27) to find the region of interest containing the heart.

The Canny edge detection consists of the following four steps.

Remove noise in the image *via* a gaussian smoothing filter

In the process of image edge detection, the edge and noise of the image are difficult to distinguish, and the edge detection algorithm alone cannot eliminate the influence of noise on the edge detection process and results, so the original image needs to be preprocessed. Common filtering methods in image pre-processing include mean filtering, median filtering, and Gaussian filtering. Compared with mean filtering and median filtering, Gaussian filtering can well preserve the grayscale distribution in the image when smoothing the image.

Calculate image gradient strength and orientation

The basic idea of Canny's algorithm is to find the position of the strongest gray intensity change in an image, that is, the gradient direction. The gradient of each pixel in the smoothed image is calculated by the Sobel operator. First, the following convolution arrays S_x and S_y are used to obtain the gradients G_x and G_y of the original image A along the horizontal (x) and vertical (y) directions, respectively:

$$G_x = S_x * A = \begin{bmatrix} -1 & 0 & +1 \\ -2 & 0 & +2 \\ -1 & 0 & +1 \end{bmatrix} * A \tag{1}$$

$$G_y = S_y * A = \begin{bmatrix} -1 & -2 & -1 \\ 0 & 0 & 0 \\ +1 & +2 & +1 \end{bmatrix} * A \tag{2}$$

Then use the following equation to find the gradient magnitude of each pixel:

$$G = \sqrt{G_x^2 + G_y^2} \tag{3}$$

A large gradient metric value G will be obtained in places with drastic changes (at the boundary), but these boundaries are usually very thick, and it is difficult to demarcate the real position of the boundary. To demarcate the boundary, the direction information of the gradient is also required:

$$\theta = \arctan\left(\frac{G_x}{G_y}\right) \tag{4}$$

A non-maximum suppression technique is applied to eliminate edge false detections

Each pixel's gradient direction was set to one of the following values: (0°, 45°, 90°, 135°, 180°, 225°, 270°, and 315°). We judge whether it is an edge by comparing the gradient strength of the pixel and the two pixels in the positive and negative gradient directions. If the gradient strength of the pixel is the largest, it will be retained, and it will be regarded as an edge. This way we will get one of the brightest thin lines at the border, and the edges of the image will be noticeably thinner.

A double threshold is applied to decide possible edges

The technique of double threshold is applied in the Canny algorithm, that is, an upper threshold T1 and a lower threshold T2 are set. If the gradient value of the pixel point exceeds T1, it is called a strong edge, and the one in between is called a weak edge, otherwise, it is not an edge. The larger the T1, the more severe the gradient change in strong edge pixels. Canny recommends setting T1:T2 to 2:1.

Segmentation network model

The ESA-Unet proposed in this article is shown in Figure 1. The network mainly consists of three parts: encoder, decoder, and low-rank self-attention reconstruction module. ESA-UNet jointly designs a self-attention mechanism and multi-scale skip connections based on a convolutional network, which effectively makes up for the problem that convolution is difficult to model long sequences. This ensures that the global context in cardiac MRI is not completely ignored, effectively enhancing the functionality and robustness of the traditional U-shaped architecture. ES-UNet network consists of three parts: decoder, encoder, and self-attention module.

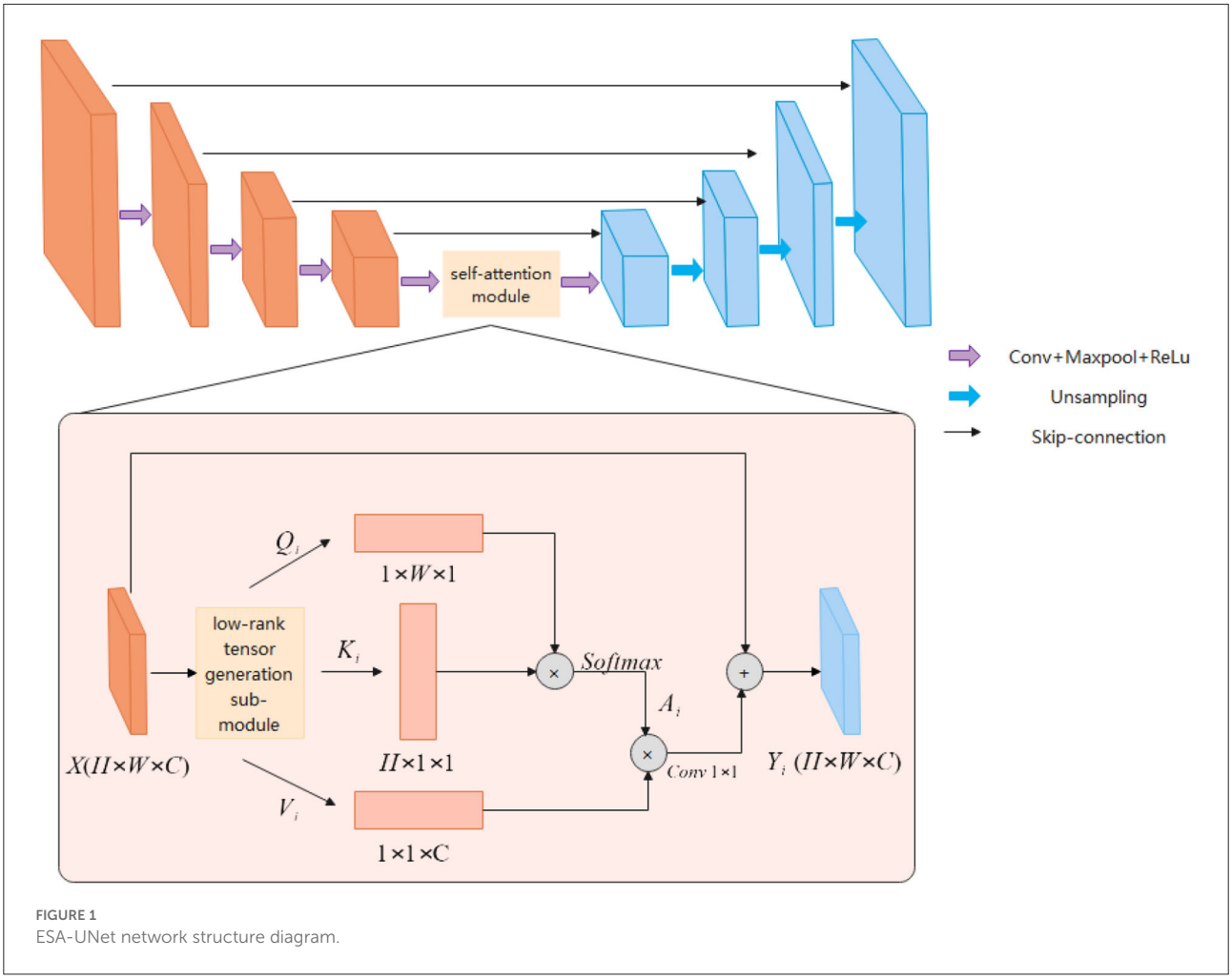

FIGURE 1
ESA-UNet network structure diagram.

Encoder

The encoder is a structure used to extract image features. The encoder uses a five-layer residual connected downsampling layer to obtain multi-scale feature information of five different levels of the image. The low-level features are mainly used to obtain the detailed features and position information of the image, and the high-level features are abstract semantic features information. Each downsampling layer consists of two consecutive 3 × 3 convolutional layers, a RELU activation function, and a 2 × 2 max-pooling layer. And the downsampling is connected in a residual structure. The residual structure can obtain richer semantic information by extending the depth of the network.

Decoder

The main function of the decoder is to gather feature information at different levels. The decoder first uses a cascaded upsampling layer to restore the image resolution to the original size of $H \times W$, and finally uses a 1 × 1 convolutional layer. Decrease the number of channels to get the final segmentation map. Each of these upsampling layers consists of a 2 × 2 Up-Conv, a 3 × 3 convolutional layer, and a RELU layer. We still maintain the U-shaped structure of UNet and concatenate the features extracted in the encoder with the upsampled feature map to fuse the feature information of different levels. This can effectively avoid the loss of low-level information, such as organ shape and boundary.

Low-rank tensor self-attention module

The attention module is used to obtain richer contextual information. Although the convolutional structure can expand the receptive field and extract rich information by stacking more layers, the deeper convolutional layer structure is not good for global information to obtain. The attention module can adjust the global information, and each point in the image will calculate the correlation with other points. The correlation information obtained through the attention feature map adjusts the pixel weights in the picture, the weights belonging to the same other points will be aggregated, and the pixel point information of

different categories will be suppressed to highlight the important parts of the picture. The attention mechanism can obtain rich semantic information, but the amount of computation will be relatively large. The low-rank tensor self-attention reconstruction module LRSAR Block proposed in this article can well solve the computationally complex problem.

The low-rank tensor self-attention module includes three parts: low-rank tensor generation sub-module, low-rank self-attention sub-module, and high-rank tensor reconstruction sub-module.

Low-rank tensor generation sub-module

The low-rank tensor generation sub-module can perform high-rank tensor decomposition along the width, height, and channel dimensions. According to the CP tensor decomposition theory, a high-rank tensor can be decomposed into a linear combination of multiple-rank tensors. A rank tensor can be composed of the outer product of three one-dimensional vectors. According to the definition of a rank tensor, the author decomposes the high-rank tensor along the width, height, and channel dimensions to generate multiple one-dimensional

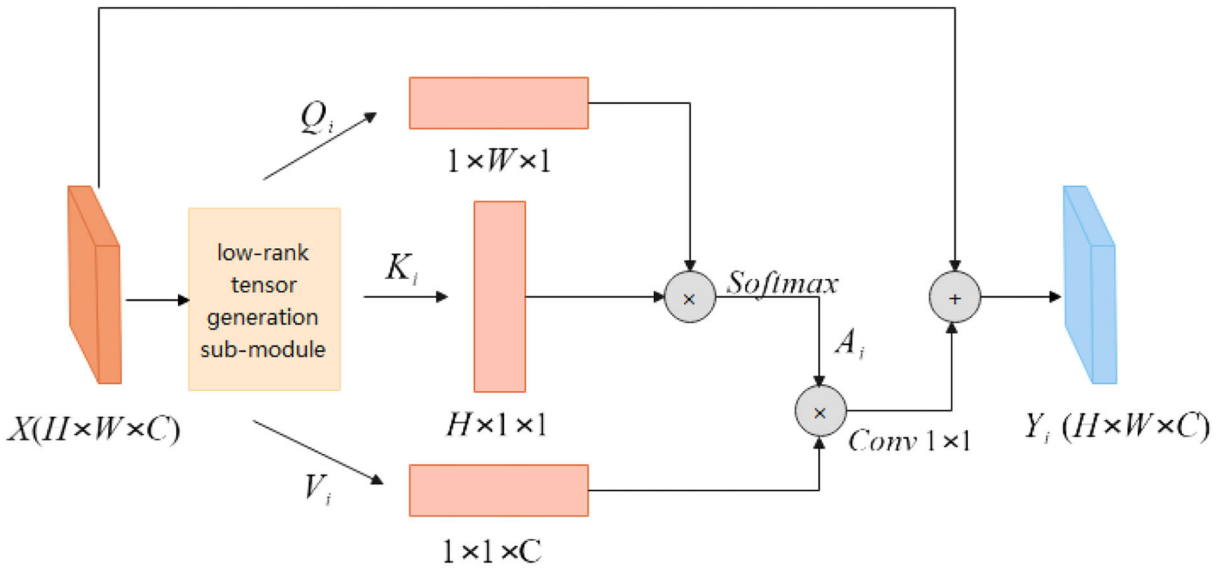

FIGURE 2
Low-rank self-attention sub-module.

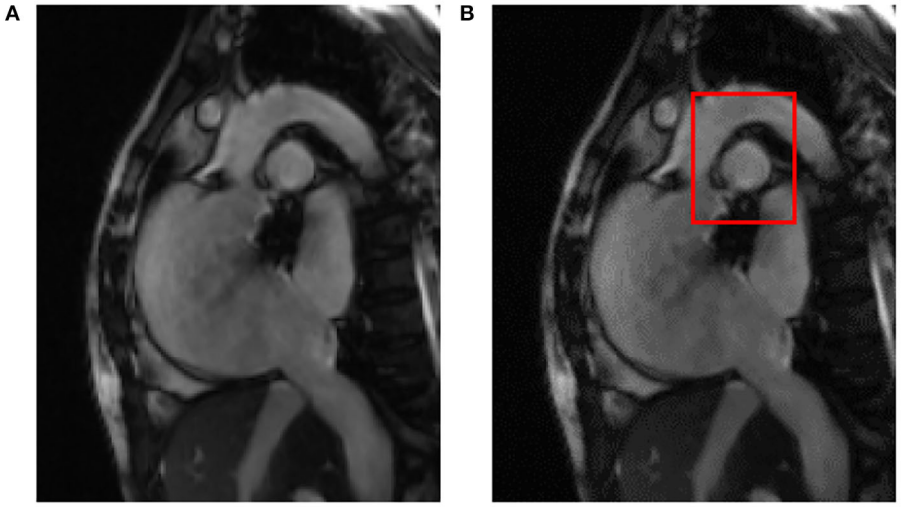

FIGURE 3
ROI detection results based on **(A)** the original image and **(B)** the detected target area.

vectors. These one-dimensional vectors are input into the low-rank tensor self-attention sub-module to generate a rank tensor. The high-rank tensor extracted by the coding layer is input into three low-rank tensor generation modules to extract the low-rank tensor feature information. The high-rank tensor is input to the low-rank tensor generation module multiple times to generate multiple different low-rank tensor features. That is, the high-rank tensor feature X is input to the low-rank tensor generation sub-module s times, which will generate s different low-rank tensor features. The low-rank tensor decomposed along the same dimension has the same network structure, but different parameter information.

The feature map X will be input to the low-rank tensor generation sub-module multiple times along the three dimensions of height, width, and channel to generate different feature vectors $(\mathbf{Q}_1, \mathbf{K}_1, \mathbf{V}_1)$, $(\mathbf{Q}_2, \mathbf{K}_2, \mathbf{V}_2) \ldots (\mathbf{Q}_i, \mathbf{K}_i, \mathbf{V}_i)$, $(\mathbf{Q}_s, \mathbf{K}_s, \mathbf{V}_s)$.$\mathbf{Q}_i, \mathbf{K}_i$ and $\mathbf{V}_i$ represent the one-dimensional vectors generated by decomposition along with the height, width, and channel dimensions, respectively, and represents the number of one-dimensional vectors generated along a certain dimension. Equations (6–8) Represent Q_i, K_i and V_i, respectively. These low-rank feature vectors are passed through the low-rank self-attention module to generate different low-rank self-attention sub-feature maps$\mathbf{Y}_1, \mathbf{Y}_2, \ldots, \mathbf{Y}_i, \ldots, \mathbf{Y}_s$. Each low-rank tensor generation sub-module consists of global average pooling (GAP), fully connected layer (FC), and sigmoid activation function, and generates a one-dimensional feature vector for self-attention feature maps. The principle of global average pooling is to first slice the high-rank tensor along a certain dimension and perform global average pooling for each slice matrix. Through global average pooling, each element in each vector aggregates the corresponding slice matrix information. The fully connected layer can realize the aggregation of all element information by any element in the vector. The sigmoid activation function can enhance the nonlinear fitting ability of the network, and map the feature information to the range of 0–1, highlighting the important feature information in the feature vector. The low-rank tensor generation module in the literature (28) uses the convolution structure, and this article replaces the convolution with the FC layer. Each feature point in the FC layer will be aggregated with other feature information, while the single-layer convolutional structure can only aggregate local feature information. The FC layer parameter information of different low-rank tensor features is different. Although the FC layer will increase the number of parameters, the feature dimension of the last layer of the encoding layer is relatively low, and the number of parameters will not increase much.

$$\mathbf{Q}_i = \left(q_1, q_2, \cdots, q_m, \cdots, q_H\right), i = 1, 2, \cdots, s; m = 1, 2, \cdots, H \quad (5)$$

$$\mathbf{K}_i = \left(k_1, k_2, \cdots, k_n, \cdots, k_W\right), i = 1, 2, \cdots, s; n = 1, 2, \cdots, W \quad (6)$$

$$\mathbf{V}_i = \left(v_1, v_2, \cdots, v_l, \cdots, v_C\right), i = 1, 2, \cdots, s; l = 1, 2, \cdots, C \quad (7)$$

Low-rank self-attention sub-module

As shown in Figure 2, the feature map $\mathbf{X} \in \mathbf{R}^{H \times W \times C}$ is first input into the low-rank tensor generation sub-module to generate multiple different low-rank tensors $\mathbf{Q}_i, \mathbf{K}_i$ and $\mathbf{V}_i$. The height feature $\mathbf{Q}_i$ is multiplied by the width feature $\mathbf{K}_i$ to obtain the spatial similarity matrix $\mathbf{A}_i \in \mathbf{R}^{H \times W \times 1}$, which is activated by the Softmax layer. The specific calculation process is shown in equation (9). Equation (10) is a more detailed explanation of the feature similarity matrix $\mathbf{A}_i$, a_{mn} represents each point on the spatial similarity matrix, q_m and k_n, respectively, represent the width feature information, and height feature information. The obtained spatial attention feature map $\mathbf{A}_i$ has no correlation information between channels, and feature $\mathbf{V}_i$ aggregates the information between channels. The attention feature map $\mathbf{A}_i$ is multiplied by the channel attention information $\mathbf{V}_i$ to

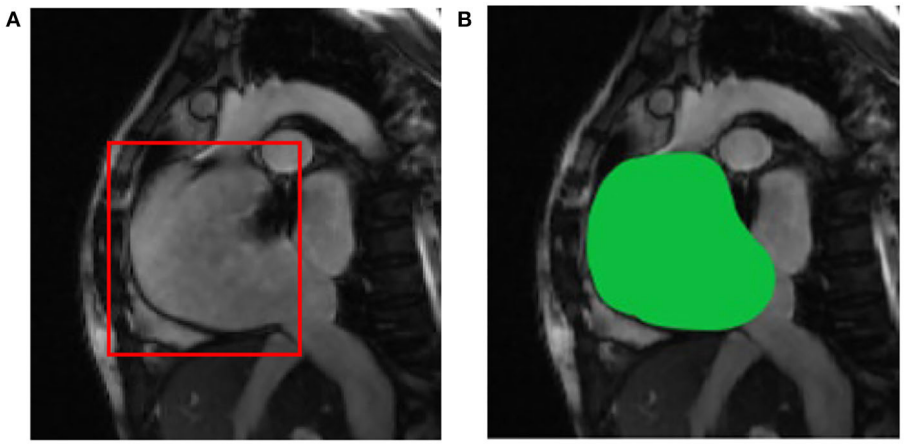

FIGURE 4
ROI detection and segmentation results based on **(A)** the original two-chamber image; and **(B)** the right atrium image after ROI detection.

obtain three-dimensional attention information. The calculation process is shown in Equation (11). The input feature map X is added to the attention feature to obtain long-range semantic information features and the feature map $\mathbf{Y}_i$ is obtained.

$$\mathbf{A}_i = \text{softmax}\left(\mathbf{Q}_i \times \mathbf{K}_i\right) \tag{8}$$

$$a_{mn} = \frac{\exp\left(q_m k_n\right)}{\sum_{m=1}^{W} \exp\left(q_m k_n\right)} \tag{9}$$

$$\mathbf{Y}_i = \mathbf{X} + \text{Conv1} \times 1\left(\mathbf{A}_i \times \mathbf{V}_i\right) \tag{10}$$

The self-attention module non-local block calculates the correlation between any two points in the image when calculating the similarity of pixels. For the feature map X, the time complexity of the self-attention module is $O(H \times W \times H \times W)$, while the LRSAR block only needs to calculate the outer product of two vectors, and the time complexity is $O(H \times W)$, lower degree. Compared with the self-attention module, the LRSAR-Net proposed in this article has lower time complexity and faster speed.

High-rank tensor reconstruction sub-module

According to tensor decomposition theory, high-order tensors can be decomposed into linear combinations of multiple rank-one tensors. The feature map X passes through the low-rank self-attention module to generate multiple rank-one attention feature maps $\mathbf{Y}_i$, and $\mathbf{Y}_i$ only contains low-level semantic information. The rank-one attention feature map $\mathbf{Y}_i$ is generated by different parameters low-rank tensor generation modules, so the feature information contained in different rank-one attention feature maps is different. The authors introduce a learnable weight parameter λ_i before each rank-one attention feature map $\mathbf{Y}_i$, which is adjusted with training. Each low-rank self-attention feature map is multiplied by the corresponding weight parameter λ_i, and then combined into a high-rank self-attention tensor Y. The tensor reconstruction method is shown in Equation(12). The high-rank attention feature map Y contains rich semantic information, realizes the aggregation of global feature information, and reduces the computational cost of self-attention feature maps. In this experiment, to balance the

TABLE 1 Results of different method models on the cardiac MRI.

Model	Pr	Re	F1	IOU	DSC
FCN-16s	0.902	0.862	0.880	0.804	0.839
FCN-8s	0.921	0.853	0.881	0.820	0.856
PSPNet	0.836	0.868	0.852	0.752	0.850
MSFCN	0.861	0.916	0.886	0.821	0.854
MSRN	0.873	0.925	0.898	0.833	0.867
FPN	0.904	0.904	0.909	0.832	0.868
UNet	0.902	0.904	0.903	0.857	0.872
Our(ESA-Unet)	0.919	0.939	0.928	0.888	0.903
Our(ESA-Unet + preprocessing)	0.925	0.936	0.930	0.898	0.906
Our(ESA-Unet + preprocessing + CRF)	0.944	0.929	0.935	0.899	0.915

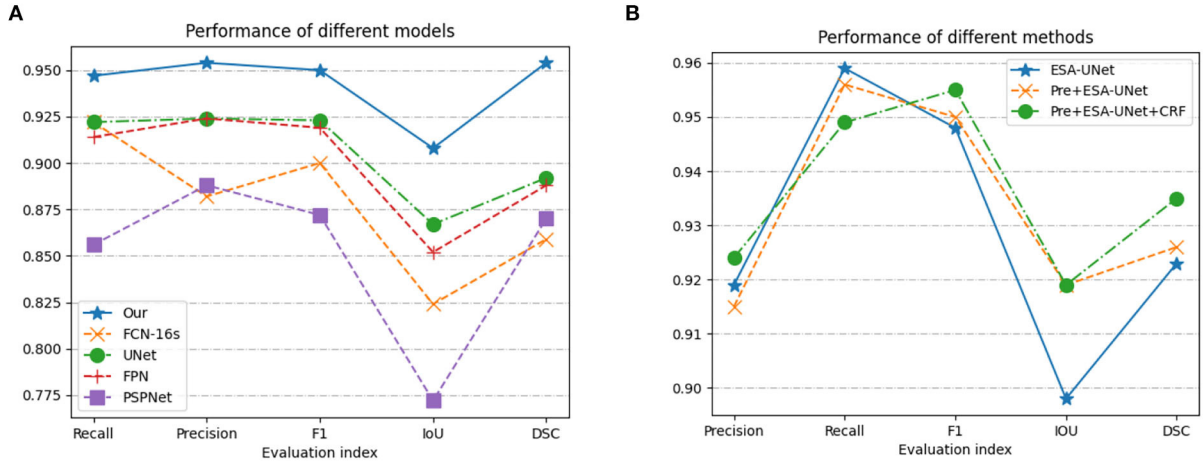

FIGURE 5
Performance based on **(A)** model methods on different indicators; and **(B)** three methods combination proposed.

complexity of the model and the amount of computation, s is set to 4.

$$\mathbf{Y} = \sum_i^n \lambda_i \mathbf{Y}_i \tag{11}$$

Conditional random fields optimize segmentation boundaries

After network segmentation, we use a conditional random field (CRF) to further optimize the segmentation boundary.

For the probability map U after the output of the neural network, we can use the following equation to describe the predicted value of each pixel. $X = \{x_1, x_2, \ldots, x_n\}$ represents each pixel feature point on the probability map, $Y = \{y_1, y_2, y_3, \ldots, y_n\}$ represents each point according to its texture, gray value, and other attributes and surrounding The label for the probability prediction of the point.

$$P(y|x) = \frac{1}{Z(x)} exp\left(\sum_{i\epsilon U}\sum_{j\in U(x_i)} T_{i,j}(y_j, y_i, x_i, i) + \sum_{i\epsilon U} S_i(y_i, x_i)\right) \tag{12}$$

Among them, $U(x_i)$ represents the points around x_i, ,$T_{i,j}$ is the function of the feature transfer between the i-th point and the surrounding points, S_i is the state feature function about the

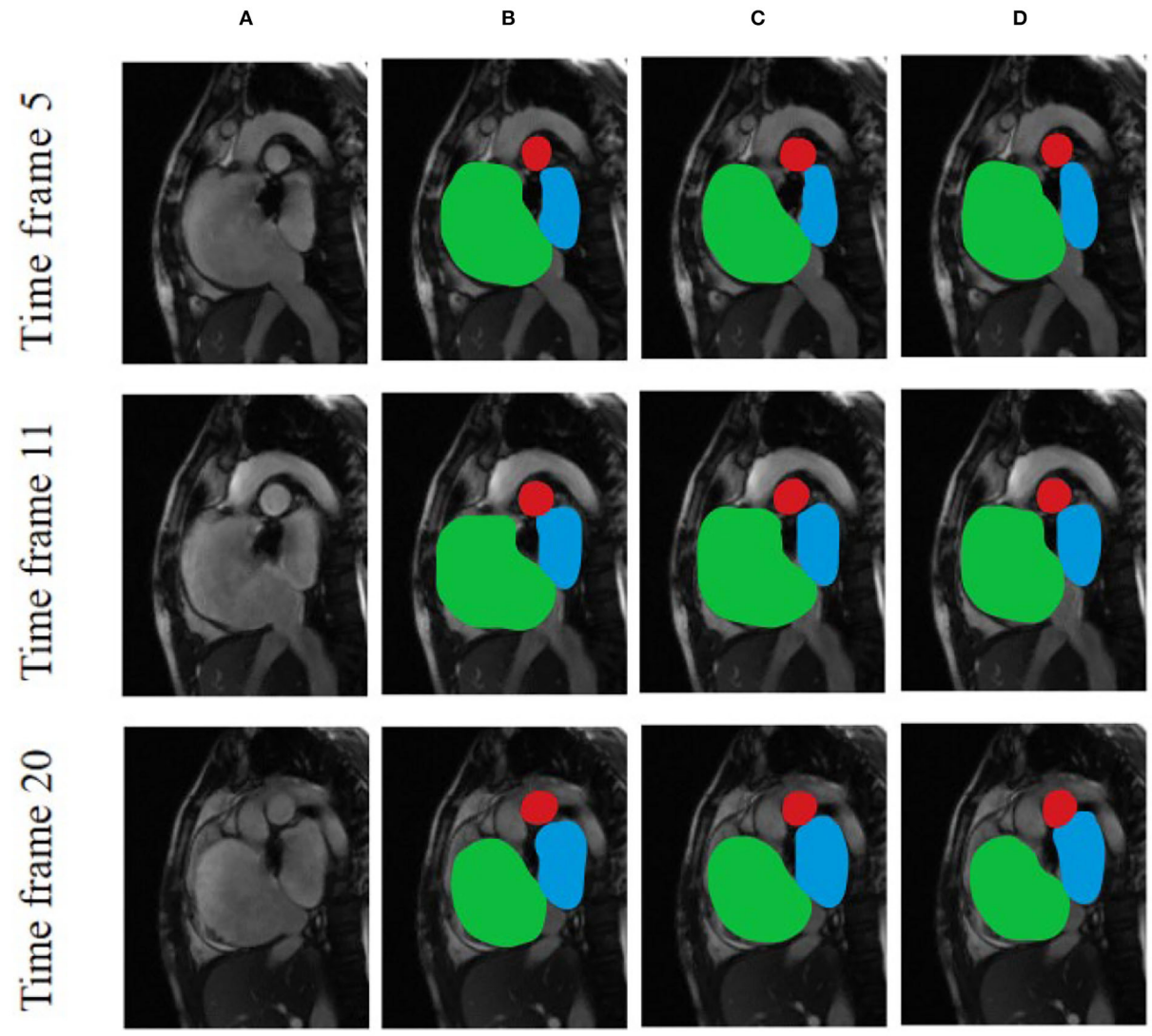

FIGURE 6
Comparison of the effects of different segmentation models using various cardiac MRI slices based on **(A)** Original and unprocessed images; **(B)** ESA-UNet; **(C)** UNET; and **(D)** FCN.

i-th point, and $Z(x)$ is the normalization function:

$$Z(x) = \sum_{y \epsilon Y} P(y|x) \tag{13}$$

Evaluation metrics for segmentation results

The evaluation indicators for segmentation results in semantic segmentation problems include accuracy (Acc), precision (Pre), recall (Re), F1 score (F1), intersection of union (IoU), and dice similarity coefficient (DSC) (29, 30). Calculating these evaluation metrics requires the use of four commonly used metrics for prediction results, namely the true positive (TP), false positive (FP), true negative (TN), and false negative (FN). The true negative mainly refers to the situation that the model predicts that the pixels belong to the background area and are consistent with the actual gold standard. False negatives mainly refer to the situation that the model predicts that the pixels belong to the background area, but are opposite to the actual gold standard.

$$\begin{aligned} \mathrm{Acc} &= \frac{\mathrm{TP}+\mathrm{TN}}{\mathrm{TP}+\mathrm{TN}+\mathrm{FP}+\mathrm{FN}} \\ \mathrm{Pre} &= \frac{\mathrm{TP}}{\mathrm{TP}+\mathrm{FP}} \\ \mathrm{Re} &= \frac{\mathrm{TP}}{\mathrm{TP}+\mathrm{FN}} \end{aligned} \tag{14}$$

$$\begin{aligned} \mathrm{F1} &= \frac{2^{*}\mathrm{Pre}^{*}\mathrm{Re}}{\mathrm{Pre}+\mathrm{Re}} \\ \mathrm{IOU} &= \frac{\mathrm{I}_1 \cap \mathrm{I}_2}{\mathrm{I}_1 \cup \mathrm{I}_2} \\ \mathrm{DSC} &= \frac{2^{*}\left|\mathrm{I}_1 \cap \mathrm{I}_2\right|}{\left|\mathrm{I}_1\right|+\left|\mathrm{I}_2\right|} \end{aligned}$$

Results and discussion

ROI detection results

After reading the original cardiac MRI data, after the pre-processing step including ROI detection, the results are shown in Figure 3, where Figure 3A is the input of the original cardiac MRI data and Figure 3B is the aorta as the center after ROI detection A gray mask of the ROI containing the aorta is drawn.

After image data standardization and data enhancement processing, according to the ROI area center and area radius obtained by ROI detection, the image data are cropped into a 128 × 128 block with the ROI center, i.e., the aorta as the center, as the input of the deep learning segmentation network. Compared with the raw cardiac MRI slice data with an average spatial resolution of 235–263 voxels per slice as input directly, the GPU memory size occupied by the same model training is reduced from more than 10 GB to less than 6GB. The results of ROI detection and segmentation are shown in Figure 4. In Figure 4A is the input image and Figure 4B is the 128 × 128 image after ROI.

Image segmentation results

We have fully experimented with our method with a variety of excellent convolution-based methods (31–36). From the data in Table 1, we can see that our model performs well in all indicators. On the important indicators Iou and DSC, our model achieves 0.899 and 0.915, respectively. It can also be seen from Figure 5 that pre-processing can improve the IoU indicator to 0.898. Conditional random fields can improve the IoU indicator to 0.915. As can be seen from the data, both pre-processing and conditional random fields can facilitate segmentation.

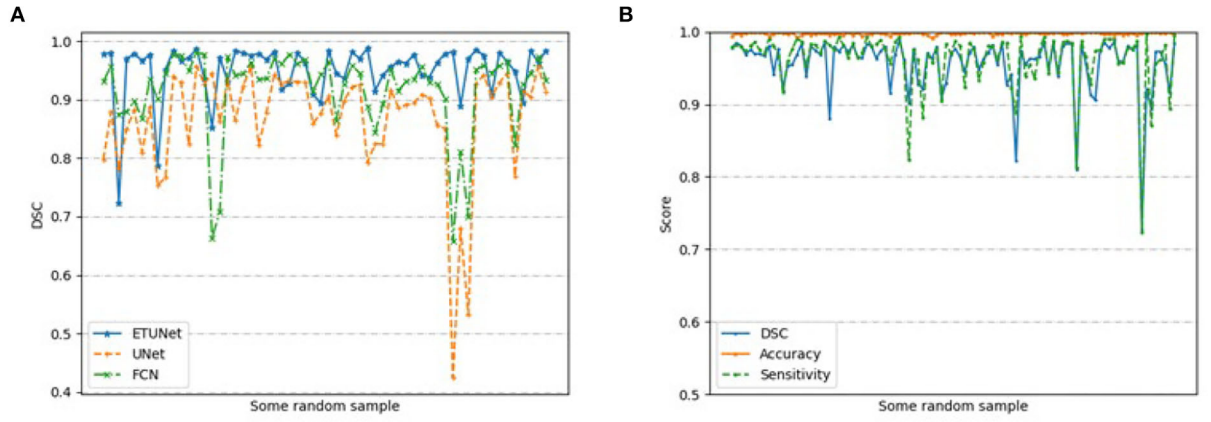

FIGURE 7
Performance based on **(A)** different models on randomly selected samples; and **(B)** our segmentation model on 200 randomly selected samples.

Figure 6 compares the segmentation effects of different segmentation models on cardiac MRI. Figure 7 shows the performance of different models on different metrics on some specific datasets. As can be seen from the segmentation effect in Figure 6, the segmentation effect of ESA-UNet is better than that of other pure convolutions, and the segmentation results are more robust. Especially when segmenting small target areas such as the red part, other models perform very unstable, but our model can still segment accurately. Figure 7 shows the performance comparison between different models on some characteristic data samples. We can find that our method is more robust in terms of various indicators, and it is not easy to produce samples with poor segmentation results. However, the segmentation results of other methods are more volatile and prone to poorly segmented samples (37, 38).

Conclusion

In this article, we propose a set of solutions for assisting cardiac MRI diagnosis based on semantic segmentation technology. We first preprocessed the input MRI data, we first filtered using a standard deviation filter to find regions of the cardiac cycle image sequence where pixel intensity varied strongly with time and then used Canny edge detection and Hough transform techniques to find regions containing the heart area of interest. Then, the image is input into the ESA-Unet model network, and the preliminary segmentation results are obtained through the encoder, self-attention module, and decoder; finally, we use the conditional random field to reprocess the segmented image to optimize its segmentation boundary. The results show that our method has a good segmentation effect, which facilitates the diagnosis of clinical cardiovascular diseases and improves the efficiency and accuracy of diagnosis.

In future, we will continue to improve the experiment in combination with clinical practice and try to introduce implicit feature information such as texture to optimize the error of complex segmentation boundaries and further improve the segmentation accuracy.

Data availability statement

The original contributions presented in the study are included in the article/supplementary material, further inquiries can be directed to the corresponding author/s.

Ethics statement

The studies involving human participants were reviewed and approved by the Second Affiliated Hospital of Fujian Medical University. The patients/participants provided their written informed consent to participate in this study.

Author contributions

YW, QL, SL, and ZL were responsible for the integrity of the data analysis. YL oversaw manuscript drafting and study design. YW and JH oversaw data interpretation. All authors contributed to the article and approved the submitted version.

Funding

This work was sponsored by Fujian Provincial Health Technology Project (2020CXA045 and 2021QNA038).

Acknowledgments

The deep learning-based segmentation model in this research is generated using the Deep Red AI Toolbox [http://www.deepredsys.com].

Conflict of interest

The authors declare that the research was conducted in the absence of any commercial or financial relationships that could be construed as a potential conflict of interest.

Publisher's note

All claims expressed in this article are solely those of the authors and do not necessarily represent those of their affiliated organizations, or those of the publisher, the editors and the reviewers. Any product that may be evaluated in this article, or claim that may be made by its manufacturer, is not guaranteed or endorsed by the publisher.

References

1. Hu SS, Kong LZ, Gao RL, Zhu ML, Wen WA, Wang YJ, et al. Outline of the report on cardiovascular disease in China, 2010. *Biomed Environ Sci.* (2012) 25:251–6.

2. He J, Chen S. A new two-step automatic medical image segmentation scheme. *Elect Sci Technol.* (2016) 29:85–7. doi: 10.16180/j.cnki.issn1007-7820.2016.07.025

3. Hong L, Han JD, Fang Y. A review of active contour model in medical image segmentation. *Sci Technol Eng.* (2018) 18:161–7. doi: 10.3969/j.issn.1671-1815.2018.16.025

4. An FP, Liu J. Medical image segmentation algorithm based on multilayer boundary perception-self attention deep learning model. *Multimedia Tools Appl.* (2021) 80:15017–39. doi: 10.1007/s11042-021-10515-w

5. Lee C, Huh S, Ketter TA, Unser M. Unsupervised connectivity-based thresholding segmentation of midsagittal brain MR images. *Comput Biol Med.* (1998) 28:309–38. doi: 10.1016/S0010-4825(98)00013-4

6. Wang L, Ma Y, Zhan K, Ma Y. Automatic left ventricle segmentation in cardiac MRI via level set and fuzzy C-means 2015 in *2nd International Conference on Recent Advances in Engineering and Computational Sciences (RAECS)*. IEEE (2015), p. 1–6.

7. Luo G, Sun G, Wang K. A novel left ventricular volumes prediction method based on deep learning network in cardiac MRI in *2016 Computing in Cardiology Conference (CinC)*. IEEE (2016), p. 89–92.

8. Gupta A, Von Kurowski L, Singh A, Geiger D, Liang CC. Cardiac MR image segmentation using deformable models in *Proceedings of Computers in Cardiology Conference*. IEEE (1993), p. 747–50.

9. Picard RW. Future affective technology for autism and emotion communication. *Philos Trans Royal Soc B Biol Sci.* (2009) 364:3575–84. doi: 10.1098/rstb.2009.0143

10. Avendi MR, Kheradvar A, Jafarkhani H. A combined deep-learning and deformable-model approach to fully automatic segmentation of the left ventricle in cardiac MRI. *Med Image Anal.* (2016) 30:108–19. doi: 10.1016/j.media.2016.01.005

11. Long JE, Darrell T. Fully convolutional networks for semantic segmentation 2015 in *IEEE Conference on Computer Vision and Pattern Recognition (CVPR). IEEE.* (2015).

12. Nasr-Esfahani M, Mohrekesh M, Akbari M, Soroushmehr SR, Nasr-Esfahani E, Karimi N, et al. Left ventricle segmentation in cardiac MR images using fully convolutional network in *2018 40th Annual International Conference of the IEEE Engineering in Medicine and Biology Society (EMBC)*. IEEE (2018).

13. Schlemper J, Oktay O, Schaap M, Heinrich M, Kainz B, Glocker B, et al. (2019). Attention gated networks: Learning to leverage salient regions in medical images. *Med. Image Anal.* 53, 197–207. doi: 10.1016/j.media.2019.01.012

14. Leo M, Furnari A, Medioni GG, Trivedi M, Farinella GM. Deep learning for assistive computer vision in *Proceedings of the European Conference on Computer Vision (ECCV) Workshops.* (2018).

15. Yin W, Lu P, Zhao Z, Peng X. Yes, "attention is all you need", for exemplar based colorization in *Proceedings of the 29th ACM International Conference on Multimedia.* (2021), p. 2243–51.

16. Wang C, Bai X, Zhou L, Zhou J. Hyperspectral image classification based on non-local neural networks in *IGARSS 2019-2019 IEEE International Geoscience and Remote Sensing Symposium*. IEEE (2019).

17. Li C, Tan Y, Chen W, Luo X, He Y, Gao Y, et al. ANU-Net: attention-based nested U-net to exploit full resolution features for medical image segmentation. *Comput Graph.* (2020) 90:11–20. doi: 10.1016/j.cag.2020.05.003

18. Fan DP, Zhou T, Ji GP, Zhou Y, Chen G, Fu H, et al. Inf-net: automatic COVID-19 lung infection segmentation from ct images. *IEEE Trans Med Imag.* (2020) 39:2626–37. doi: 10.1109/TMI.2020.2996645

19. Liu Z, Tong L, Chen L, Zhou F, Jiang Z, Zhang Q, et al. CANet: context aware network for brain glioma segmentation. *IEEE Trans Med Imag.* (2021) 40:1763–77. doi: 10.1109/TMI.2021.3065918

20. Dou H, Karimi D, Rollins CK, Ortinau CM, Vasung L, Velasco-Annis C, et al. A deep attentive convolutional neural network for automatic cortical plate segmentation in fetal MRI. *IEEE Trans Med Imag.* (2020) 40:1123–33. doi: 10.1109/TMI.2020.3046579

21. Kolda TG, Bader BW. Tensor decompositions and applications. *SIAM Rev.* (2009) 51:455–500. doi: 10.1137/07070111X

22. Lebedev V, Ganin Y, Rakhuba M, Oseledets I, Lempitsky V. Speeding-up convolutional neural networks using fine-tuned cp-decomposition. *arXiv preprint arXiv:1412.6553i* (2014).

23. Wu JN. Compression of fully-connected layer in neural network by kronecker product in *2016 Eighth International Conference on Advanced Computational Intelligence (ICACI) 2016*. IEEE (2016), p. 173–9.

24. Sun W, Chen S, Huang L, So HC, Xie M. Deep convolutional neural network compression via coupled tensor decomposition. *IEEE J Selected Topics Sig Process.* (2020) 15:603–16. doi: 10.1109/JSTSP.2020.3038227

25. Chen W, Zhu X, Sun R, He J, Li R, Shen X, et al. Tensor low-rank reconstruction for semantic segmentation in *European Conference on Computer Vision*, Cham (2020), p. 52–69.

26. Canny J. A computational approach to edge detection. *IEEE Tran Pattern Anal Machine Int.* (1986) 6:679–98. doi: 10.1109/TPAMI.1986.4767851

27. Duda RO, Hart PE. Use of the Hough transformation to detect lines and curves in pictures. *Commun ACM.* (1972) 15:11–5. doi: 10.1145/361237.361242

28. Milletari F, Navab N, Ahmadi SA. V-net: Fully convolutional neural networks for volumetric medical image segmentation in *2016 Fourth International Conference on 3D Vision (3DV)*, IEEE (2016), p. 565-71. doi: 10.1109/3DV.2016.79

29. Anuar N, Sultan ABM. Validate conference paper using dice coefficient. *Comput Info Sci.* (2010) 3:13. doi: 10.5539/cis.v3n3p139

30. Isensee F, Jäger PF, Kohl SA, Petersen J, Maier-Hein KH. Automated design of deep learning methods for biomedical image segmentation. *arXiv preprint arXiv:08128* (2019).

31. Long J, Shelhamer E, Darrell T. Fully convolutional networks for semantic segmentation in *Proceedings of the IEEE Conference on Computer Vision and Pattern Recognition*. (2015), p. 3431–40.

32. Zhao H, Shi J, Qi X, Wang X, Jia J. Pyramid scene parsing network in *Proceedings of the IEEE Conference on Computer Vision and Pattern Recognition.* (2017), p. 2881–90.

33. Lin, TY, Dollár P, GirshickR, He K, Hariharan B, et al. Feature pyramid networks for object detection in *Proceedings of the IEEE Conference on Computer Vision and Pattern Recognition.* (2017), p. 2117–25.

34. Huang L, Xia W, Zhang B, Qiu B, Gao X. MSFCN-multiple supervised fully convolutional networks for the osteosarcoma segmentation of CT images. *Comput Methods Prog Biomed.* (2017) 143:67–74. doi: 10.1016/j.cmpb.2017.02.013

35. Zhang R, Huang L, Xia W, Zhang B, Qiu B, Gao X, et al. Multiple supervised residual network for osteosarcoma segmentation in CT images. *Comput Med Imag Graph.* (2018) 63:1–8.

36. Ronneberger O, Fischer P, Brox T. U-net: Convolutional networks for biomedical image segmentation in *International Conference on Medical Image Computing and Computer-Assisted Intervention*, Cham (2015), p. 234–41.

37. Chicco D, Jurman G. The advantages of the Matthews correlation coefficient (MCC) over F1 score and accuracy in binary classification evaluation. *BMC Genom.* (2020) 21:1–13. doi: 10.1186/s12864-019-6413-7

38. Cheadl, C, Vawter MP, Freed WJ, Becker KG. Analysis of microarray data using Z score transformation. *J. Mol. Diag.* (2003) 5:73-81. doi: 10.1016/S1525-1578(10)60455-2

frontiers | Frontiers in Cardiovascular Medicine

TYPE Original Research
PUBLISHED 24 November 2022
DOI 10.3389/fcvm.2022.1011916

OPEN ACCESS

EDITED BY
Ruizheng Shi,
Xiangya Hospital, Central South University, China

REVIEWED BY
Yu Lu,
Shenzhen Technology University, China
Bijiao Ding,
Huaqiao University Affiliated Strait Hospital, China

*CORRESPONDENCE
Yuan-Zhe Li
ctmr@fjmu.edu.cn
Yin-Hui Huang
251045413@qq.com

†These authors have contributed equally to this work

SPECIALTY SECTION
This article was submitted to Cardiovascular Imaging, a section of the journal Frontiers in Cardiovascular Medicine

RECEIVED 04 August 2022
ACCEPTED 04 November 2022
PUBLISHED 24 November 2022

CITATION
Wang Y, Li S-T, Huang J, Lai Q-Q, Guo Y-F, Huang Y-H and Li Y-Z (2022) Cardiac MRI segmentation of the atria based on UU-NET.
Front. Cardiovasc. Med. 9:1011916.
doi: 10.3389/fcvm.2022.1011916

Cardiac MRI segmentation of the atria based on UU-NET

Yi Wang[1†], Shu-Ting Li[1†], Jing Huang[1], Qing-Quan Lai[1], Yi-Fan Guo[2], Yin-Hui Huang[3*] and Yuan-Zhe Li[1*]

[1]Department of CT/MRI, The Second Affiliated Hospital of Fujian Medical University, Quanzhou, China, [2]Department of Radiology, The First Affiliated Hospital of Zhejiang Chinese Medical University (Zhejiang Provincial Hospital of Traditional Chinese Medicine), Hangzhou, China, [3]Department of Neurology, Jinjiang Municipal Hospital, Quanzhou, China

Background and objective: In today's society, people's work pressure, coupled with irregular diet, lack of exercise and other bad lifestyle, resulting in frequent cardiovascular diseases. Medical imaging has made great progress in modern society, among which the role of MRI in cardiovascular field is self-evident. Based on this research background, how to process cardiac MRI quickly and accurately by computer has been extensively discussed. By comparing and analyzing several traditional image segmentation and deep learning image segmentation, this paper proposes the left and right atria segmentation algorithm of cardiac MRI based on UU-NET network.

Methods: In this paper, an atrial segmentation algorithm for cardiac MRI images in UU-NET network is proposed. Firstly, U-shaped upper and lower sampling modules are constructed by using residual theory, which are used as encoders and decoders of the model. Then, the modules are interconnected to form multiple paths from input to output to increase the information transmission capacity of the model.

Results: The segmentation method based on UU-NET network has achieved good results proposed in this paper, compared with the current mainstream image segmentation algorithm results have been improved to a certain extent. Through the analysis of the experimental results, the image segmentation algorithm based on UU-NET network on the data set, its performance in the verification set and online set is higher than other grid models. The DSC in the verification set is 96.7%, and the DSC in the online set is 96.7%, which is nearly one percentage point higher than the deconvolution neural network model. The hausdorff distance (HD) is 1.2 mm. Compared with other deep learning models, it is significantly improved (about 3 mm error is reduced), and the time is 0.4 min.

Conclusion: The segmentation algorithm based on UU-NET improves the segmentation accuracy obviously compared with other segmentation models. Our technique will be able to help diagnose and treat cardiac complications.

KEYWORDS

cardiac MRI, deep deconvolution neural network, UU-NET, image segmentation, edge detection segmentation, threshold segmentation

Introduction

Recently, the worldwide prevalence of cardiovascular disease also gradually rise, according to world health organization in 2019 chart "cardiovascular disease risk, according to the world heart vascular disease prevalence in the rising trend, number of cases to exceed 500 million, 17.9 million people die each year from cardiovascular disease, first in all kinds of diseases (1). The public should pay attention to the prevention and treatment of cardiovascular diseases (2). Generally applied in clinical practice, for the diagnosis of cardiovascular disease, doctors usually only by observing the patients with cardiac image two-dimensional image of the fault, and according to the experience of the clinical cases of his past give treatment, the diagnosis for the dependence of subjective experience is bigger, and has led to bigger misjudgment. In addition, in some cases, to save resources and time, methods such as improving mri speed, imaging time, or spatial resolution are often adopted, but in such cases, a large amount of additional data is generated, which greatly reduces the efficiency of doctors to read images (3).

Medical image segmentation is to mark or extract a specific part of a medical image and apply it to other medical tasks. Therefore, the segmentation performance of medical images directly affects the development of other related technologies, such as three-dimensional reconstruction of human organs, registration of human parts, and localization of diseased or necrotic tissues. However, the development of medical image segmentation technology is also limited by many aspects. First, there are many kinds of imaging principles of medical image, and the quality of imaging is greatly affected by acquisition equipment and environment, that is, it is easy to be interfered by various noises. Therefore, it is difficult to generate a universal segmentation technique for all medical images. Secondly, according to the biological characteristics of human beings, the anatomical structure of each organ in human body is extremely complex, and there are significant differences between different ages of the same individual and individuals, which further increases the difficulty of segmentation (4). However, if medical image segmentation can be completed quickly and accurately, it will effectively improve the application of relevant imaging technology in clinical medicine.

The current development of computer field has added a possibility for the development of medical image segmentation. In 2012, artificial intelligence (AI), which focuses on computing power and deep learning, became the core technology of the next era (5). As an important branch of artificial intelligence technology, computer vision is developing very fast. In the 2015 ImageNet image recognition contest (6), computer recognition accuracy surpassed that of humans for the first time. Therefore, if the computer can be used to pre-process medical images to increase the efficiency of doctors or directly diagnose related diseases, it will be beneficial to improve the level of medical treatment.

Magnetic resonance (MRI) is a common heart imaging technique. In the early stage of the development of imaging technology, MRI has a slow imaging speed and is not suitable for the acquisition of cardiac images that require high imaging speed and resolution. However, with the development of medical image imaging technology, cardiac MRI has been able to obtain cardiac motion images by means of time-sharing acquisition in multiple cardiac systolic and diastolic cycles. MRI is the use of hydrogen atoms in the magnetic field in the human body to release energy information sampling technology, unlike conventional CT, MRI without ionizing radiation damage, imaging at the same time to be able to reflect the high contrast between different blood groups, is helpful to obtain clear heart anatomy structure (7). Therefore, MRI is recognized as the gold standard for evaluating cardiac function. Therefore, the image segmentation technology in this paper will be based on MRI imaging.

The left atrium is directly connected with the left ventricle and pulmonary veins. Its basic functions include channel function, contraction function and reserve function. Channel function refers to the early and middle stage of left ventricular diastole, when the left atrium sends blood from the pulmonary vein to the left ventricle. Systolic function refers to the active contraction of left atrial myocardium to provide blood for the left ventricle. Reserve function means that the systole of the left ventricle acts as a vessel for storing blood. In addition, the atrial structure directly maintains human atrial fibrillation (8), and the main reason for the poor clinical performance of atrial fibrillation is the lack of a deeper understanding of the underlying atrial anatomical structure (9). Therefore, understanding the atrial morphology and changes of patients with atrial fibrillation has certain reference value for understanding the clinical treatment of atrial fibrillation.

Manual segmentation of the left atrium by a medical expert does guarantee high accuracy, but it can take a lot of time for the expert to annotate an individual's data. The boring and long-term nature of labeling images will often lead to fluctuations in the state of labeling images and affect the accuracy of labeling, that is, the accuracy level is subjective. The scarcity of medical experts also leads to the lack of widespread application of left atrial segmentation. Therefore, it is necessary to adopt the means of computer field to solve this problem.

However, there are many schemes for ventricular image segmentation based on machine learning, such as deep belief network (DBN) (10), stack autocoding (SAE) (11), deep autoencoder (DAE) (12) and other technologies. However, these researches mainly focus on neuroimage analysis and have little effect on ventricular image segmentation. Using random forest

method (13) and constrained Boltzmann machine (14) will lead to high computational complexity and unstable results. Therefore, the above methods have great limitations in the segmentation of ventricular images.

To solve this problem, we design a local image segmentation method based on U-NET. Based on the full convolutional neural network and the combination of deconvolution technology and deconvolution technology, a dual cavity scan image segmentation based on U-NET network is realized. At the same time, in order to avoid excessive model parameters, the number of convolutional filters is appropriately set according to the characteristics of MRI and the needs of the segmentation task. Experimental results show that the segmentation method of U-NET atrial image has better effect compared with several existing classification methods.

Methodology

Region growing

The basic idea of regional growth is that regions to be segmented have the same or similar properties within the region and different properties outside the region (15). The specific implementation steps are as follows:

1. Select a seed pixel for each region to be segmented.
2. All pixels in the field of the region where the seed pixel is located are judged according to certain growth criteria. If there are pixels that meet the growth criteria, all the pixels will be absorbed into the region where the seed pixels are, and the second step will be performed again.
3. When there is no pixel satisfying the growth criterion in the field of a region, the region no longer expands, that is to say, the region has grown.

For the specific segmentation process, please refer to Figure 1, that is, select the growth cycle until the end of all growth.

It should be pointed out that the growth or similarity standard usually set is related to the characteristics of the image itself, usually, the difference between gray scale and gray scale is within a critical value. This paper uses a threshold of 25.

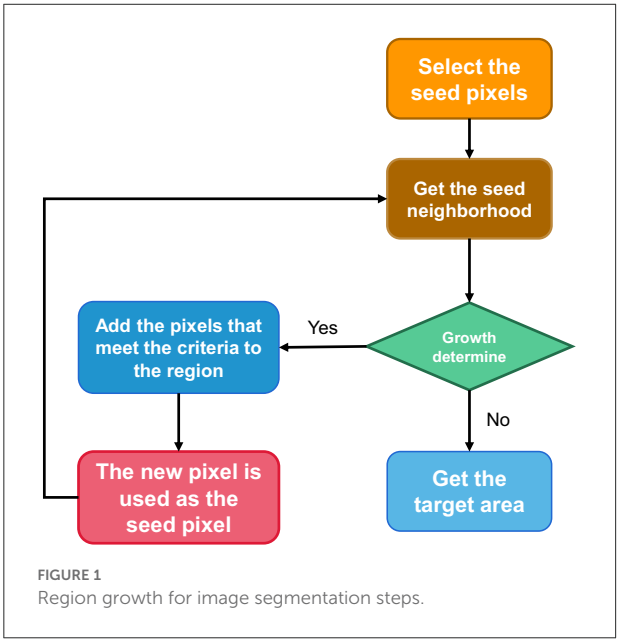

FIGURE 1
Region growth for image segmentation steps.

Threshold segmentation method

Threshold segmentation

Threshold method were the first to be applied to achieve a segmentation method of image segmentation (16), the key technique of the threshold segmentation method is: according to the statistics of the whole image grayscale characteristics, according to the gray level range and the number of the gray value for that one or more of the image threshold value, then one by one traverse each gray value of the image, and each gray level values and threshold values After comparison, classify according to the final comparison results or preset rules, and divide each pixel within different threshold ranges into different categories in order to achieve segmentation. Figure 2 shows the general steps of the threshold segmentation method for image segmentation, among which there are many methods to determine the threshold.

The limitations method of threshold

Maximum interclass variance method

The maximum inter-class variance, also known as the algorithm, was proposed by The Japanese scholar Otsu. It is an algorithm for image binary segmentation threshold. The basic idea of threshold determination is that the threshold should be able to maximize the feature difference between the target and the background (17).

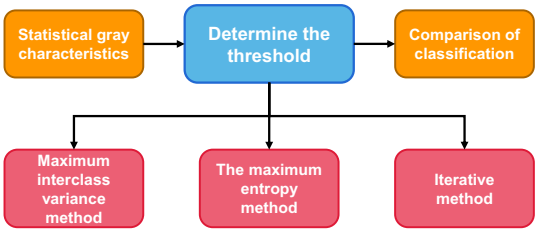

FIGURE 2
Steps of threshold segmentation method.

Variance is a statistical measure of the uniformity of distribution. Therefore, the segmentation that maximizes the variance between classes means the smallest misclassification probability.

If T is regarded as the segmentation threshold of target and background, the proportion of foreground (target) region to image is denoted as w_0, and the average gray level is u_0. The proportion of background region to the image is denoted as w_1, the average gray level is u_1, the total average gray level of the image is U, and the variance of foreground and background image g(T) is as follows:

$$u = w_0 \times u_0 + w_1 \times u_1 \quad (1)$$

$$g(T) = w_0 \times (u_0 - u)^2 + w_1 \times (u_1 - u)^2 \quad (2)$$

Since under this method, the image is only treated as foreground and background overlay, there are

$$w_0 + w_1 = 1 \quad (3)$$

Equations (1)–(3) can be obtained simultaneously

$$g(T) = w_0 \times w_1 \times (u_0 - u_1)^2 \quad (4)$$

To ensure that g(T) is the largest, T is selected as the desired. Notice that this formula w_0 is symmetric about w_1, so w_0 can be set as the partition less than the threshold value, that is, the foreground represents the region s_0 occupied by all gray values in the image S less than the threshold value. u_0 represents the average gray level of s_0 region.

$$w_0 = \frac{s_0}{s} \quad (5)$$

$$u_0 = \frac{\sum s_0}{s_0} \quad (6)$$

Here, s_1 is the same as u_1. And then one obtains g(T) as a function of T and then you invert the maximum value of T for g of T.

Threshold iteration method

The main idea of threshold iteration method is that the mean sum of two parts A and B after image segmentation basically remains stable (18). In other words, with the iteration, the final convergence value of [mean(A)+mean(B)]/2 is taken as the segmentation threshold. The specific method is as follows:

(1) Select an initial threshold T;
(2) The given image is divided into two groups of images by threshold T, denoted as R1 and R2;
(3) Calculate the mean values of R1 and R2 μ1 and μ2;
(4) Select a new threshold T, and T= (μ1 + μ2) /2;
(5) Repeat steps (2) to (4) until the difference of T for two consecutive times is less than a preset value.

On this basis, in the case that the target region is equal to the background region, the initial threshold T is set as the average gray value of the overall image, so as to accelerate the convergence rate. In the case of large difference between target and background area, the initial threshold T is set as the intermediate value between the maximum gray scale and the minimum gray scale. The default values depend on the image size, grayscale distribution, and calculation time required, but are generally small and accurate. Its construction is shown in Figure 3.

The maximum entropy method

The principle of image maximum entropy threshold segmentation: make the selected threshold to segment the target area and background area of image gray statistics of the two parts of the maximum information (19).

The area whose gray value is ≤T is S0, and the rest of the image is S1. Let PI represent the probability of gray value being I, and PT represent the sum of gray value probabilities from 0 to T. H (S) represents the information entropy of the region.

$$P_T = \sum_{i=0}^{T} p_i \quad (7)$$

$$H(S_0) = -\sum_{i=0}^{T} \frac{p_i}{P_T} \ln \frac{p_i}{P_T} \quad (8)$$

$$H(S_1) = -\sum_{i=T+1}^{T} \frac{p_i}{1 - P_T} \ln \frac{p_i}{1 - P_T} \quad (9)$$

By traversing the gray value, T that maximized H(S0)+H(S1) was found.

The difficulty of threshold segmentation

The difficulties of threshold segmentation are as follows: (1) Before image segmentation, the number of regions generated by image segmentation cannot be determined; (2) Determination of threshold value, because the determination of threshold value directly affects the accuracy of segmentation and the correctness of description analysis of the segmented image.

UU-NET network

UU-NET

In 2015, Ronneberger et al. trained the U-NET model based on convolutional neural network with a small number of training samples and won the ISBI Cell Tracking Challenge. The network is called U-NET because it is shaped like the letter "U". Subsequently, U-NET network obtained excellent segmentation results in medical images of the heart.

The U-NET model consists of a downsampling encoder and an upsampling decoder, as shown in Figure 4. The structure

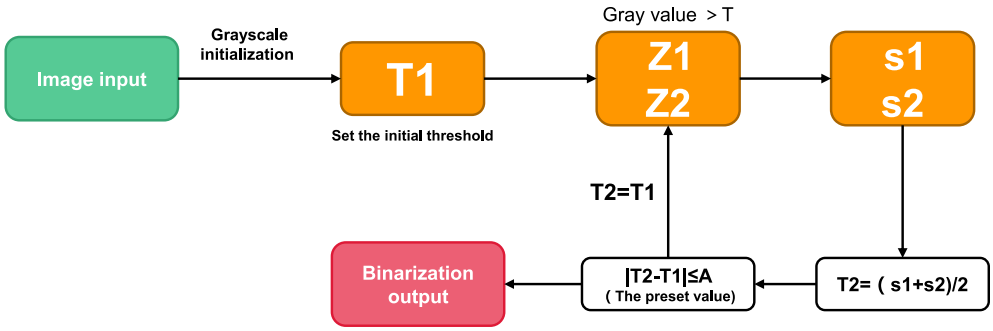

FIGURE 3
Program flow chart of threshold iteration method.

is simple and easy to understand. The contraction process of the model is the down-sampling process. The author extracts features through multiple 3*3 convolution layers and uses the maximum pooling of 2*2 for down-sampling (20). In the expansion process of the model, that is, the upsampling process, the feature graph of the previous stage is firstly upsampled, and then the feature graph of the contraction process is splice and further refined by jumping connection. Finally, the channel number mapping of the feature map is scaled down to the segmented category number through the 1*1 convolution layer. U-net has been widely used in the field of medical image segmentation because of its simple structure, easy transformation and adjustment, and its high ability of obtaining context information and precise positioning.

Data preprocessing and data amplification

Data standardization

Due to the differences of acquisition equipment and conditions in various research institutions, there are differences in brightness and contrast of cardiac MRI images. The essence of neural networks is to learn by distributing data. If there is a big difference between the training data and the experimental data, the generalization ability of the model will be greatly weakened. To solve this problem, it is often required to normalize the input data.

On this basis, cardiac short-axis MRI was processed to obtain a normalized data with 0 pixel mean, 1. On this basis, a normalization algorithm based on maximum normalization is proposed.

$$x = \frac{x - x_{mean}}{x_{\max} - x_{min}} \tag{10}$$

Where x_{mean} represents the average value of the required data, x_{max} represents the maximum value of the required data, and x_{min} represents the minimum value of the required data.

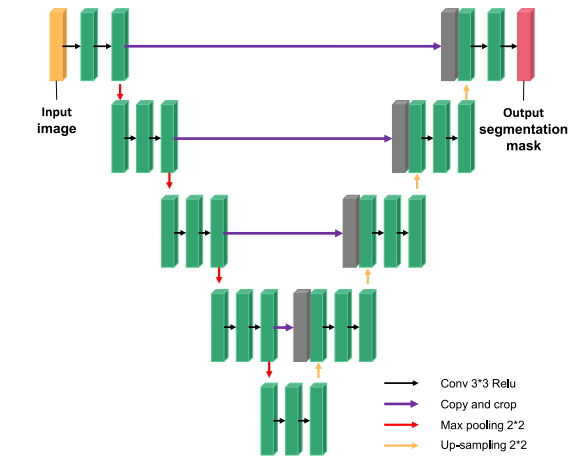

FIGURE 4
U-NET network model.

Data enhancement

However, due to the high cost of image acquisition, social ethical privacy and high human cost of professionals, many medical image research based on deep learning cannot obtain enough data for training or verification. However, in the case of small samples, there is the problem of over-fitting. The data intensification methods used in this paper include −0.2–0.2 random scale, −5 to +5% random direction shearing, −5 to +5% contrast correction, etc.

UU-NET model structure

Based on the improvement of U-NET model, this paper designs a UU-NET model which is more suitable for medical image segmentation. In this paper, u-shaped upper and lower sampling modules are constructed by using residual theory, which are used as encoders and decoders of the model. Then, the modules are interconnected to form multiple paths from input

to output to increase the information transmission capability of the model.

Residual module

The depth of neural network largely determines image classification and computer vision tasks. Theoretically, the higher the depth of the network, the better its fitting effect. But that's not true. This is because with the increase of network depth, the gradient will gradually weaken, thus affecting the segmentation of the network. In this paper, we use ResNet to delay gradient extinction in network propagation.

The mathematical principle of ResNet is as follows: Assume that the mapping of input X to output Y is H, that is, $Y = H(X)$; After input X passes through multiple nonlinear layers, the result Y satisfies another mapping as F, that is, $Y = F(X)$, where $F(X) = H(X) - x$ between F and H satisfies. Thus, the original mapping H is represented as $F(X) + X$. In the feedforward neural network, the required mapping H can be realized through the connection mode of "layer hopping," as shown in Column B in Figures 2, 3. The UU-NET model in this paper uses this residual idea to construct convolution blocks in U-NET as shown in Figure 5. The essence is to replace ordinary convolution modules with residual convolution modules and apply batch regularization rules to model training.

Sampling module

By connecting the intermediate result of the former U-NET decoder to the latter U-NET encoder through Addition, the latter can be supplemented with additional information on the feature graph of each scale. At the same time, this method can construct multiple paths to transmit information, and each path is equivalent to an FCN variant. Therefore, it has the potential to capture more complex features and produce higher accuracy. Similarly, in order to construct multiple paths, this paper constructs two types of U-NET modules, which are respectively used for the outer U-shaped encoder (column A and decoder in Figure 6 and column B in Figure 6 for the design of UU-NET model.

Overall model structure

Through the construction of two types of U-NET modules, referred to as external U encoder module and external U decoder module, the UU-NET model is designed. The "hop layer" in the U-NET module is connected by Concatenation. The smallest feature graph in the outer U encoder module will be the input of the lower outer U encoder module. U decoder module and external U encoder module on the size of the corresponding figure for Addition (Addition) operation, namely "U" encoder module and the intermediate results produced by decoding part of the "U" decoder module coding and some intermediate results, so the latter on the characteristics of various scale chart to get the additional information added, at the same time, Added multiple paths from input to output. Compared with LadderNet, this paper not only uses the residual convolution

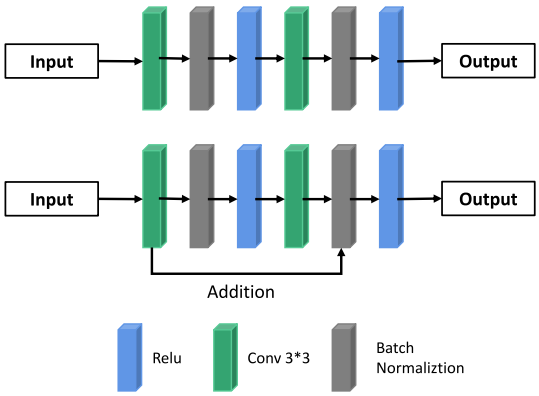

FIGURE 5
Ordinary convolution block and residual convolution block.

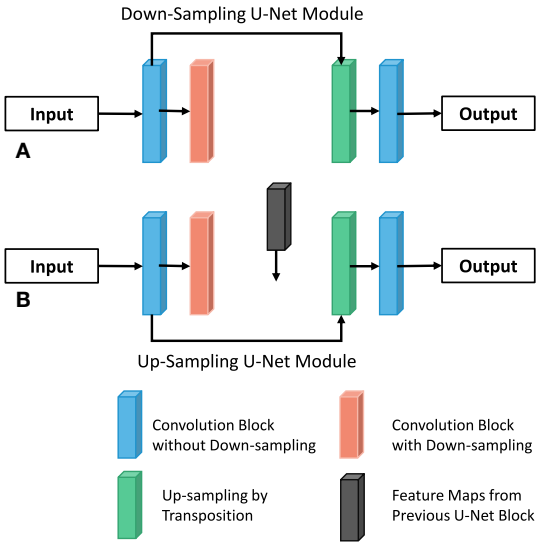

FIGURE 6
Modules of two UU-NET models. **(A)** Down-Sampling. **(B)** Up-Sampling of the U-Net module.

block to increase the depth of the outer U-shaped structure, but also constructs more information transmission paths through the double-layer structure, that is, more FCN variants are added. As shown in Figure 7, the outer layer of the normal U-Net model is connected by residual convolution blocks, thus forming a double-layer U model. It is equivalent to regard each neural network of U-NET model as a U-NET model.

Deconvolution neural network

Deep deconvolution network is a supervised learning method, which includes training stage and test stage (as shown

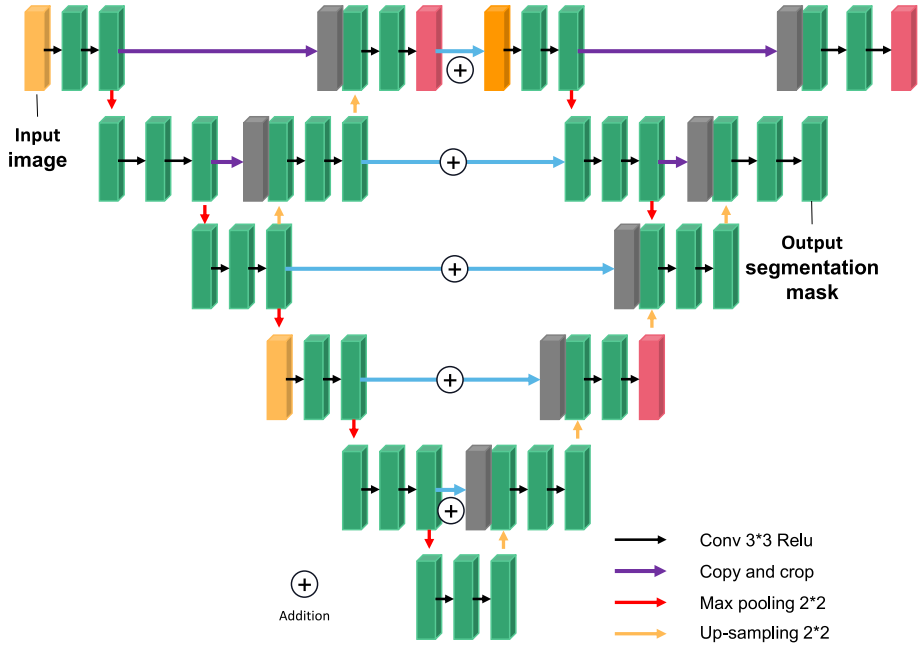

FIGURE 7
Overall structure of UU-NET network.

in Figure 8). Ten times in the training phase, this paper uses the method of cross validation, the magnetic resonance image segmentation and manual real image as the training sample input of neural network, through the forward and reverse transmission, iteratively weight training network model, and with the other five patients image of the sample as the validation sample, for training the model provide supervision and guidance. Finally, a Softmax classifier was trained and Dice loss function was optimized to obtain the classification probability map of the whole image. In the test stage, the test image is input into the trained network model after contrast adjustment processing, and the final test image segmentation result is obtained through a forward propagation calculation.

Structure and parameters of deconvolution networks

Figure 9 shows the network architecture referenced here. In order to facilitate network input, all input images are uniformly divided into 3 × 2,244 × 224 pixels. In convolutional networks, we use a similar structure to FCN, and replace all the final connection layers with a convolutional layer. The convolutional network model includes five convolution layers, five maximum layers and two convolution layers. The convolution method is an overlapping method, that is, one or two successive convolution layers are placed behind each convolution layer. In the network, all convolution kernels are small Windows 3 × 3 and 1 step long. In order to keep the size of the feature graph consistent before and after the convolution operation, a numerical value "0" of 1 is added to the edge of the input feature graph. Overlapping convolutional layer can not only improve the depth of the network, learn the parameters of the network, but also effectively prevent over-fitting.

In the deconvolution network part, the mirror structure of the convolutional network is used to reconstruct the input object. Therefore, multilayer deconvolution can also obtain different morphological details like convolutional networks. In the convolutional network model, low-level features can reflect the overall roughness of the target, such as target position and rough shape, while higher-level features have classification characteristics and contain the details of the target.

Dice depletion layer

The image is trained into the network, and then the software mapping layer is used to get the classification map with the same resolution as the initial input, so as to reflect the possibility that each pixel point is the foreground or background. On this basis, the loss function is optimized by using the classification method based on actual tags, so as to obtain the final weight of the convolutional network. In the learning process, due to the strong learning characteristics of the network, the usual loss function tends to fall into local minimization, resulting in the detection of future regions. In order to improve the response curve after classification, a new target loss function D was established by Dice similarity coefficient, which made

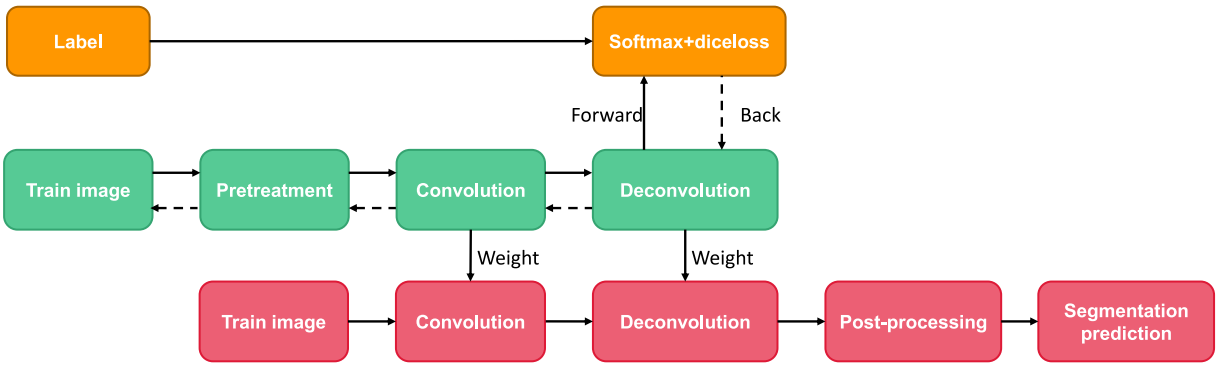

FIGURE 8
Deconvolution neural network framework used in this paper.

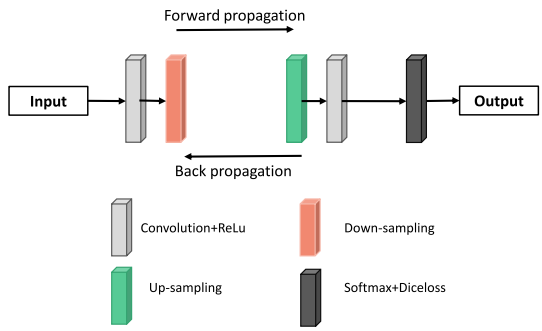

FIGURE 9
Structure diagram of deconvolution network.

the predicted response curve and the actual segmentation result have the maximum similarity.

$$D = \frac{2\sum_i^N p_i g_i}{\sum_i^N p_i^2 + \sum_i^N g_i^2} \tag{11}$$

Where, p_i and g_i represent the value of the ith pixel in the prediction graph and the real segmentation graph, respectively. We take the derivative of this

$$\frac{\partial D}{\partial p_i} = 2\left[\frac{g_i\left(\sum_i^N p_i^2 + \sum_i^N g_i^2\right) - 2p_i\left(\sum_i^N p_i g_i\right)}{\left(\sum_i^N p_i^2 + \sum_i^N g_i^2\right)^2}\right] \tag{12}$$

The partial derivative is used for parameter updating in back propagation. Experimental results show that Dice loss function has better performance than ordinary loss function.

Evaluation standard

Parameters of the standard

On this basis, DSC and Hausdorff distance (HD) were used to evaluate the two methods quantitatively. DSC algorithm performs similarity analysis in the range of two contour lines. The point set within the range of two contour lines represented by A and B is defined as follows

$$DSC(A,B) = \frac{2|A \cap B|}{|A| + |B|} \tag{13}$$

HD reflects the maximum difference between the two contour point sets and is defined as

$$HD(A,B) = max(h(A,B), h(B,A)) \tag{14}$$

Among them

$$h(A,B) = \max_{a_i \varepsilon A} \min_{b_i \varepsilon B} ||a_i - b_i|| \tag{15}$$

$$||a_i - b_j|| = \sqrt{\left(x_{a_i} - x_{b_j}\right)^2 + \left(y_{a_i} - y_{b_j}\right)^2} \tag{16}$$

Smaller HD values mean higher segmentation accuracy.

Results

The experimental analysis

A total of 150 patients were enrolled in the Department of CT/MRI at the Second Affiliated Hospital of Fujian Medical University, 8 to 15 groups for each. Each sequence consisted of a 20-frame cardiac cycle, consisting of 15,000 artificially segmented images, 12,000 images as training samples, and 3,000 images as experimental samples. From the initial reading of cardiac MRI data, to the normalization described in the previous, to the normalization and data enhancement of

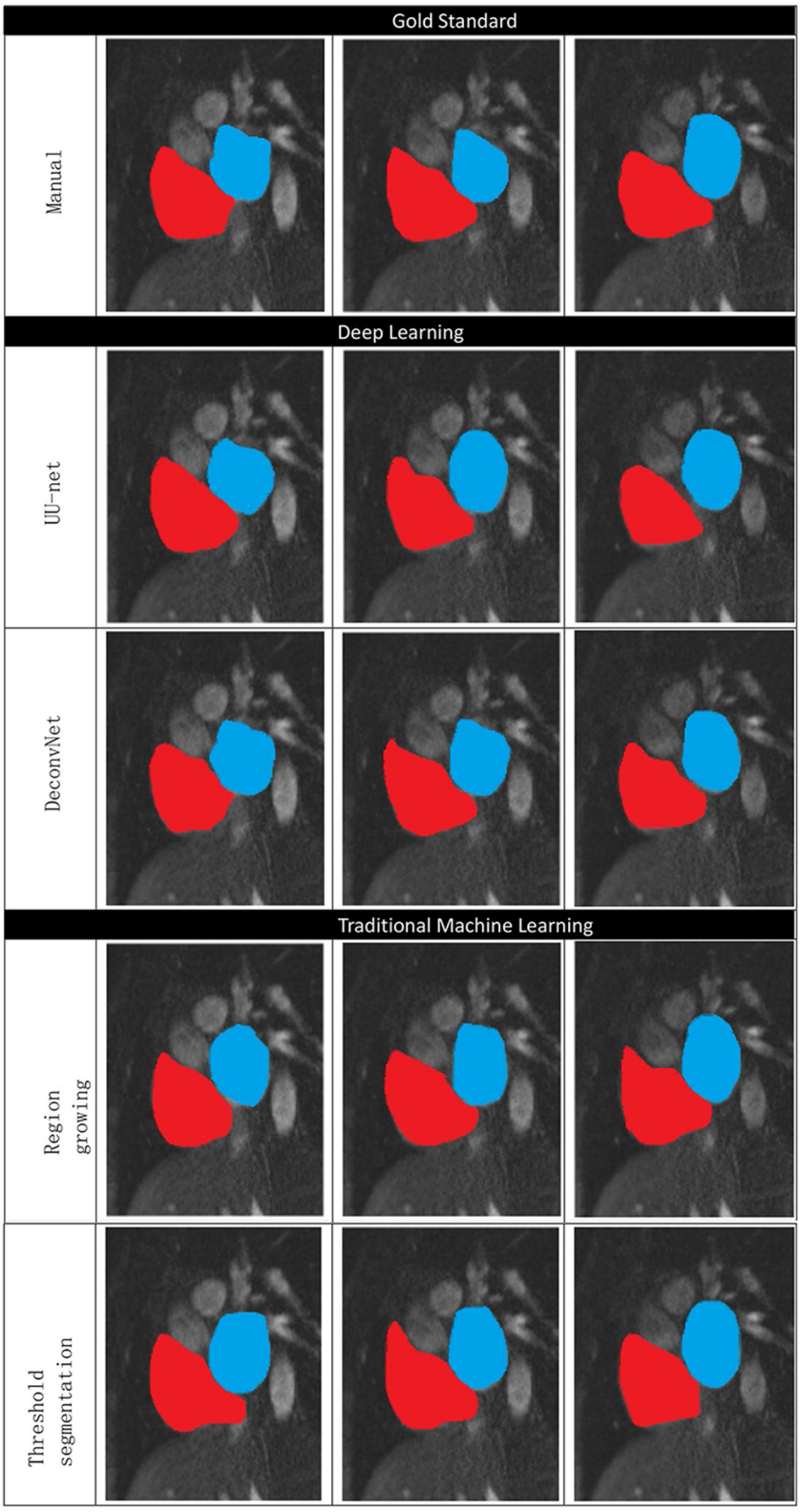

FIGURE 10
Comparison of traditional methods, deep learning, and manual segmentation in atrial segmentation.

TABLE 1 Result data of each method on validation set.

Methods	DSC/%	HD/mm	Time/min
Region growing	83.4	9.3	4
Threshold segmentation	86.7	8.5	6
Deconvolution neural network	95.8	5.5	1.4
UU-NET	96.7	1.3	0.4

image data, and then, according to the ROI area center and ROI detection results, the image data were divided into 128 × 128 pieces, clustered in the ROI center, namely the left ventricle, and input to the ROI center, namely the left ventricle. Compared with the original cardiac MRI slice with average spatial resolution of 235–263 voxel/slice, the GPU storage capacity was reduced from more than 10 GB to <6 GB by using the same model for training. This method uses ROI to extract 128 × 128 images and reduces unnecessary information while maintaining the left exterior shape.

The segmentation results of region growing image differ greatly when the gray difference threshold is different. When the threshold was small, the whole myocardium could not be separated. When the threshold is large, other surrounding tissues are incorrectly separated. However, the determination of threshold depends on the determination in advance, so it cannot adapt to the changeable conditions of cardiac MR images.

Since other tissues outside the myocardium are similar to the myocardium in gray scale, threshold segmentation method only uses gray level to determine whether pixels belong to segmentation target, without utilizing relevant spatial information. Therefore, tissues near the myocardium with similar gray scale are often segmented together. Threshold method is not effective in ventricular segmentation of cardiac MRI.

The deep learning image segmentation method is relatively ideal, but the deconvolution neural network is sometimes over-sharpened.

Figure 10 shows the manual segmentation and traditional image segmentation methods (region growth, threshold segmentation) and deep learning image segmentation method (UU-NET, deconvolution neural network), where red is right atrium (RA) and blue is left atrium (LA).

The experimental results

Table 1 lists the performance of the relevant methods mentioned in this article. As can be seen from the table, deep learning image segmentation algorithm has obvious advantages over traditional methods, while DSC obtained by the algorithm in this paper is slightly higher than deconvolution neural network, which means that the image segmentation completed in this paper is more accurate in atrial coverage. At the same time, it has obvious advantages in HD, which means that the set of contour points in this paper is closer to the standard, that is, the probability of sharpening is lower. At the same time, we should also realize that the processing time of computer-aided calculation is far shorter than that of manual segmentation (15–20 min) by professional doctors, which indicates that the application of deep learning in image segmentation is a general trend.

Discussion

Segmentation of medical image is an important and difficult problem in clinical diagnosis (21). Accurate segmentation, identification and analysis can be used for qualitative and quantitative analysis of target organs and tissues in clinical practice, improve the accuracy and reliability of diagnosis, and indirectly improve the survival of patients (22). MRI has been widely used in the diagnosis and evaluation of many important diseases including cardiovascular diseases (23). It is widely used. In order to solve the problem of ventricular segmentation in MRI, a new deep deconvolution neural network is used for segmentation, and good results are obtained in the experiment. However, on the basis of in-depth analysis of deep learning technology, existing problems are found and possible directions for further research are proposed:

1. Reliable data sets. First, due to the high cost, there are relatively few relevant data sets that can be used for deep learning modeling. Although common data expansion means can be used to expand, the expansion cannot reflect the sample distribution in the real world, which may have hidden dangers for clinical use. Second, there is no unified standard, because the equipment of different research institutions is not consistent, the data quality, code, scale and so on are not consistent.
2. Expand the application scope. The current application scope of the model in this paper is 2D cardiac MRI, which can be considered for segmentation of other medical images, such as CT, ultrasound and X-ray. Segmentation of medical images of other parts, such as head, neck, chest, etc. The 3D heart model was segmented. In order to better present relevant information to doctors from multiple fields.
3. Improve noise resistance. Because of the particularity of medical image acquisition, shadow and noise are common phenomena. There is still room to improve the noise resistance of the model used in this paper. The subsequent optimization may be carried out by adopting a more suitable preprocessing method and a more accurate loss function.

4. Stereotypes. The types of training sets are also different, which leads to poor generalization performance of the models. Increasing the diversity of data is key to solving this problem. However, one is the lack of credible data in the above data, and the other is that some cases are very rare in the history of human medicine.

Because of the complexity of medical images and gradient fuzzy boundaries, need more high resolution information, after join operations directly from the encoder to the decoder with height on the high-resolution information can provide the division with the fine features, such as gradient, and in view of the left ventricle segmentation data sets have labeled images is small in the segmentation problem such as low precision, learning difficulties, Deep learning in medicine has a long way to go (24–26).

Conclusion

The segmentation task of atrial image is realized by using the latest deep learning technology. In order to achieve pixel-by-pixel segmentation of images, this paper proposes an embedded UU-NET model with dual U structure, which is used to segment the left atrium of MRI data preprocessed by subjective screening, data amplification and image enhancement. Experimental verification shows that this design method improves the segmentation accuracy of left and right atrial in MRI. The experimental results show that the segmentation accuracy of UU-NET model has exceeded that of partial deep learning method. Further improvements will be made under the guidance of experts.

Data availability statement

The original contributions presented in the study are included in the article/supplementary material, further inquiries can be directed to the corresponding author/s.

Ethics statement

The studies involving human participants were reviewed and approved by the Second Affiliated Hospital of Fujian Medical University. The patients/participants provided their written informed consent to participate in this study.

Author contributions

Study design: YW and S-TL. Data interpretation: JH and Q-QL. Manuscript production and takes responsibility for the integrity of the data analysis: YW and Y-ZL. All authors contributed to the article and approved the submitted version.

Acknowledgments

The deep learning based segmentation model in this research is generated using the Deep Red AI Toolbox (http://www.deepredsys.com).

Conflict of interest

The authors declare that the research was conducted in the absence of any commercial or financial relationships that could be construed as a potential conflict of interest.

Publisher's note

All claims expressed in this article are solely those of the authors and do not necessarily represent those of their affiliated organizations, or those of the publisher, the editors and the reviewers. Any product that may be evaluated in this article, or claim that may be made by its manufacturer, is not guaranteed or endorsed by the publisher.

References

1. Knaul FM, Farmer PE, Krakauer EL, De Lima L, Bhadelia A, Kwete XJ, et al. Alleviating the access abyss in palliative care and pain relief-an imperative of universal health coverage: the Lancet Commission report. *Lancet* (2018) 391:1391–454. doi: 10.1016/S0140-6736(17)32513-8

2. Galarza-Delgado DA, Colunga-Pedraza IJ, Azpiri-Lopez JR, Guajardo-Jauregui N, Rodriguez-Romero AB, et al. Statin indication according to the 2019 World Health Organization cardiovascular disease risk charts and carotid ultrasound in Mexican mestizo rheumatoid arthritis patients. *Adv Rheumatol.* (2022) 62:6. doi: 10.1186/s42358-022-00235-6

3. Karimi D, Salcudean SE. Reducing the hausdorff distance in medical image segmentation with convolutional neural networks. *IEEE Trans Med Imaging.* (2020) 39:499–513. doi: 10.1109/TMI.2019.2930068

4. Audebert N, Boulch A, Le Saux B, Lefèvre S. Distance transform regression for spatially-aware deep semantic segmentation. *Comp Vision Image Understand.* (2019) 39:499–513. doi: 10.1016/j.cviu.2019.102809

5. Morid MA, Borjali A, Del Fiol G, A. scoping review of transfer learning research on medical image analysis using ImageNet. *Comput Biol Med.* (2021) 128:104115. doi: 10.1016/j.compbiomed.2020.104115

6. Zhou T, Ruan S, Canu S, A. review: deep learning for medical image segmentation using multi-modality fusion. *Array.* (2019) 3:100004. doi: 10.1016/j.array.2019.100004

7. Wijesurendra RS, Casadei B. Heart (British Cardiac Society) Mechanisms of atrial fibrillation. *Heart.* (2019) 105:1860–7. doi: 10.1136/heartjnl-2018-314267

8. Delgado V, Di Biase L, Leung M, Romero J, Tops LF, Casadei B, et al. Structure and function of the left atrium and left atrial appendage: AF and stroke implications. *J Am Coll Cardiol.* (2017) 70:3157–72. doi: 10.1016/j.jacc.2017.10.063

9. Dangi S, Linte CA, Yaniv Z, A. distance map regularized CNN for cardiac cine MR image segmentation. *Med Phys.* (2019) 46:5637–51. doi: 10.1002/mp.13853

10. Bansal A, Pandey MK, Yamada S. Zr-DBN labeled cardiopoietic stem cells proficient for heart failure. *Nucl Med Biol.* (2020) 90:23–30. doi: 10.1016/j.nucmedbio.2020.09.001

11. Li J, Li X, He D, Qu Y, A. novel method for early gear pitting fault diagnosis using stacked SAE and GBRBM. *Sensors.* (2019) 19:758. doi: 10.3390/s19040758

12. Larrazabal AJ, Martinez C, Glocker B, Ferrante E. Post-DAE: Anatomically plausible segmentation via post-processing with denoising autoencoders. *IEEE Trans Med Imaging.* (2020) 39:3813–20. doi: 10.1109/TMI.2020.3005297

13. Yang L, Wu H, Jin X, Zheng P, Hu S, Xu X, et al. Study of cardiovascular disease prediction model based on random forest in eastern China. *Sci Rep.* (2020) 10:5245. doi: 10.1038/s41598-020-62133-5

14. Wu J, Mazur TR, Ruan S, Lian C, Daniel N, Lashmett H, et al. A deep Boltzmann machine-driven level set method for heart motion tracking using cine MRI images. *Med Image Anal.* (2018) 47:68–80. doi: 10.1016/j.media.2018.03.015

15. Biratu ES, Schwenker F, Debelee TG, Kebede SR, Negera WG, Molla HT. Enhanced region growing for brain tumor MR image segmentation. *J Imaging.* (2021) 7:22. doi: 10.3390/jimaging7020022

16. Tamal M. Intensity threshold based solid tumour segmentation method for positron emission tomography (PET) images: a review. *Heliyon.* (2020) 6:e05267. doi: 10.1016/j.heliyon.2020.e05267

17. Liu X, Yin G, Shao J, Wang X. Learning to predict layout-to-image conditional convolutions for semantic image synthesis. *Adv Neu Inform Process Sys.* (2019) 5:32.

18. Han S, Carass A, He Y, Prince JL. NeuroImage Automatic cerebellum anatomical parcellation using U-Net with locally constrained optimization. *Neuroimage.* (2020) 218:116819. doi: 10.1016/j.neuroimage.2020.116819

19. Isola P, Zhu JY, Zhou TH, et al. Proceedings of the IEEE conference on computer vision and pattern recognition. *Image-to-Image Translat Cond Adv Networks.* (2017) 5:632. doi: 10.1109/CVPR.2017.632

20. Ding H, Jiang X, Liu AQ. Boundary-aware feature propagation for scene segmentation. In *Proceedings of the IEEE/CVF International Conference on Computer Vision*. (2019) (p. 6819-6829). doi: 10.1109/ICCV.2019.00692

21. Zhao M, Wei Y, Lu Y, Wong KK. A novel U-Net approach to segment the cardiac chamber in magnetic resonance images with ghost artifacts. *Comput Methods Programs Biomed.* (2020) 196:105623. doi: 10.1016/j.cmpb.2020.105623

22. Zhu X, Wei Y, Lu Y, Zhao M, Yang K, Wu S, et al. Comparative analysis of active contour and convolutional neural network in rapid left-ventricle volume quantification using echocardiographic imaging. *Comp Meth Program Biomed.* (2020) 199:105914. doi: 10.1016/j.cmpb.2020.105914

23. Zhao M, Wei Y, Wong KK. A generative adversarial network technique for high-quality super-resolution reconstruction of cardiac magnetic resonance images. *Magn Reson Imaging.* (2022) 85:153–60. doi: 10.1016/j.mri.2021.10.033

24. Gunderman R. Deep questioning and deep learning. *Acad Radiol.* (2012) 19:489–90. doi: 10.1016/j.acra.2011.12.018

25. Lindner T, Debus H, Fiehler J. Virtual non-contrast enhanced magnetic resonance imaging (VNC-MRI). *Magn Reson Imaging.* (2021) 81:67–74. doi: 10.1016/j.mri.2021.06.004

26. Caliva F, Iriondo C, Martinez AM, Majumdar S, Pedoia V. Distance map loss penalty term for semantic segmentation. *arXiv preprint arXiv.* (2019) 3:190803679.

frontiers | Frontiers in Cardiovascular Medicine

TYPE Original Research
PUBLISHED 29 November 2022
DOI 10.3389/fcvm.2022.1018048

OPEN ACCESS

EDITED BY
Ruizheng Shi,
Central South University, China

REVIEWED BY
Ronak Soni,
Jack Stephens Heart Institute, United States
Defu Qiu,
China University of Mining and Technology, China

*CORRESPONDENCE
Junping Tian
tianjp506@163.com

SPECIALTY SECTION
This article was submitted to General Cardiovascular Medicine, a section of the journal Frontiers in Cardiovascular Medicine

RECEIVED 12 August 2022
ACCEPTED 15 November 2022
PUBLISHED 29 November 2022

CITATION
Wang H, Wang R and Tian J (2022) Association of admission serum calcium level with left ventricular dysfunction in patients with acute coronary syndrome.
Front. Cardiovasc. Med. 9:1018048.
doi: 10.3389/fcvm.2022.1018048

Association of admission serum calcium level with left ventricular dysfunction in patients with acute coronary syndrome

Hong Wang[1], Rongrong Wang[2,3] and Junping Tian[3]*

[1]Department of Endocrinology, Aerospace Center Hospital, Beijing, China, [2]Department of Rheumatology, Aerospace Center Hospital, Beijing, China, [3]Department of Cardiovascular Medicine, Beijing Tiantan Hospital, Capital Medical University, Beijing, China

Background: The relationship between serum calcium and left ventricular function in patients with acute coronary syndrome (ACS) has not been explored. Our aim was to investigate the correlation of admission serum calcium with left ventricular dysfunction in ACS patients.

Methods: In this cross-sectional study, 658 ACS patients who were admitted in the Department of Cardiovascular Disease from June 1st, 2019 to December 31st, 2019 were enrolled in the present study. Serum calcium and B-type natriuretic peptide (BNP) were measured at admission. Left ventricular ejection fraction (LVEF) was assessed using echocardiography. The correlation between admission serum calcium and left ventricular dysfunction was analyzed.

Results: When stratified by serum calcium quartiles calculated from all patients, patients with lower serum calcium quartile showed a markedly higher BNP and lower LVEF ($P < 0.05$). Patients with LVEF$\leq$ 50% showed a significantly lower serum calcium and higher BNP compared to those with LVEF$>$ 50% ($P < 0.05$). Admission serum calcium was positively correlated with LVEF ($P < 0.01$) but negatively correlated with BNP ($P < 0.01$). Multivariate logistic regression analysis showed that lower serum calcium (adjusted OR: 0.720, 95% CI: 0.519–0.997, $P = 0.048$) was independently associated with BNP $\geq$ 300 pg/ml in ACS patients. Using LVEF as a dependent variable, no significant correlation between low serum calcium and left ventricular systolic dysfunction was found in ACS patients.

Conclusions: In patients with ACS, admission serum calcium was positively correlated with LVEF and negatively with BNP. Lower admission serum calcium was an independent risk factor for elevated BNP.

KEYWORDS

acute coronary syndrome, serum calcium, left ventricular dysfunction, left ventricular ejection fraction, B-type natriuretic peptide

Introduction

Cardiovascular disease is the major cause of death globally (1, 2). Acute coronary syndrome (ACS) represents a severe type of atherosclerotic cardiovascular disease. Studies reported that about 30–50% of ACS patients had left ventricular systolic dysfunction (3–5) which was an important determinant of poor outcome (3, 6, 7).

Serum calcium is a common monitored clinical biomarker. Calcium plays a critical role in excitation, contraction and relaxation of the myocardium (8, 9). Both clinical electrophysiology studies and preclinical experiments demonstrated that abnormal intracellular calcium concentration was a key biomarker of heart failure with preserved ejection fraction (10–12). Previous studies indicated that high level of serum calcium concentration was independently associated with heart failure (10–12). However, Wang et al. (13) found that low serum calcium was associated with left ventricular systolic dysfunction in patients with coronary artery disease (CAD).

The relationship between serum calcium and left ventricular function in ACS patients has not been investigated. Therefore, our aim was to explore the correlation between admission serum calcium and left ventricular dysfunction in ACS patients.

Methods

Study participants

Patients with ACS who were admitted to the Department of Cardiovascular Disease, Beijing Tiantan Hospital, Capital Medical University from June 1st, 2019 to December 31st, 2019 were screened. The ACS included unstable angina pectoris, acute ST-segment elevation myocardial infarction (STEMI) and non-ST-segment elevation myocardial infarction (non-STEMI) (14). The inclusion criteria were as follows: (1) age > 18 years; (2) ACS was confirmed by coronary angiography; (3) complete information of echocardiographic examination; (4) signed informed consent form. Patients with any of the following conditions were excluded: preexisting cardiomyopathy, endocarditis, severe valvular heart disease, cerebrovascular disease, liver dysfunction, chronic renal insufficiency, acute infection, known malignancies, thyroid diseases, parathyroid disorders, mal-absorption, bone disease, systemic immune disease, hemorrhagic diathesis or coagulation disorders. In total, 658 ACS patients were eligible for the study. The study was performed according to the Declaration of Helsinki and approved by the ethical committee of Beijing Tiantan hospital. Written informed consents were obtained from all patients or their legal representatives.

Demographic and clinical data

Clinical data including height, weight, body mass index, blood pressure, heart rate, and Global Registry of Acute Coronary Events (GRACE) risk score were collected at admission. Medical history, history of smoking and drinking were also collected upon admission. GRACE score was calculated based on the following eight indexes: age, heart rate, systolic blood pressure, blood creatinine concentration, Killip classification, prehospital cardiac arrest, ST-segment deviation on electrocardiography, and cardiac enzyme elevation.

Biochemical measurements

Fasting blood samples were obtained from the peripheral veins on the first morning after admission. Levels of serum calcium, phosphate, albumin, serum lipid, serum glucose and creatinine were measured by the Hitachi LABOSPECT 008 automatic biochemical analyzer (Hitachi Corporation, Japan). Glycosylated hemoglobin A1c (HbA1c), C-reactive protein (CRP), and B-type natriuretic peptide (BNP) were determined using routine methods. Abnormal elevated BNP was defined as ≥300 pg/ml (15–17). The troponin I (TnI), and creatine kinase isoenzymes MB (CK-MB) levels were also measured using the Architect system (Abbott Diagnostics).

Coronary angiography

Coronary angiography was carried out *via* the radial or femoral artery approach according to the standard Judkins technique in ACS patients. CAD was defined as having a single or multiple coronary artery stenosis with at least 50% diameter reduction according to the American College of Cardiology/American Heart Association lesion classification (18). Based on the results of coronary angiography, CAD severity was estimated by the number of coronary artery lesions and classified as three groups: single-vessel disease, double-vessel disease, triple-vessel disease. And left main lesion was equivalent to triple-vessel disease (19).

Left ventricular systolic function assessment

Echocardiography was performed with a Vivid 7 Dimension equipped with a multifrequency transducer (GE Healthcare, Vingmed, Norway) within 24 h after admission. Left ventricular systolic function was evaluated by left ventricular ejection fraction (LVEF). LVEF was measured using the Simpson's method based on two-dimensional echocardiography in all patients. Low LVEF was defined as LVEF ≤ 50% (20, 21).

Statistical analysis

Normality of the distribution of the studied variables was assessed by normal probability plots and one-sample Kolmogorov–Smirnov test. Continuous variables were presented as mean ± standard deviation (SD) or median (interquartile range), as appropriate. Differences in normally distributed variables were determined by independent-samples *t*-test or one-way ANOVA, while the non-parametric Mann-Whitney *U*-test or Kruskal-Wallis test was used for the variables not normally distributed. Categorical variables were given as ratio or percentage. The Chi-square test was applied for categorical variables. Pearson correlation was performed to determine the association between serum calcium and left ventricular function. Multivariate logistic regression analyses were used to examine the relationship between left ventricular dysfunction based on BNP ≥ 300 pg/ml or LVEF ≤ 50% and related factors, after adjustment for potential confounders, including age, gender, biochemical parameters and GRACE score. The odds ratio (OR) and 95% confidence interval (95% CI) were reported separately. A two-tailed *P*-value < 0.05 was considered as statistically significant difference.

The data were analyzed with SPSS version 26 (SPSS for Windows, IBM Corp., USA).

Results

Comparisons of clinical characteristics of ACS patients according to serum calcium quartiles

In total, 658 ACS patients were included, with a mean age of 62.0 ± 10.1 years, (range: 23–85 years). Four hundred and seventy-seven participants (72.5%) were males. The average serum calcium level was 2.27 ± 0.10 mmol/l. The average LVEF was 60.7 ± 6.8% and the proportion of LVEF ≤50 was 9.3%.

All patients were divided into four groups according to serum calcium quartiles: Quartile 1 (serum calcium level ≤ 2.19 mmol/L), Quartile 2 (2.20–2.25 mmol/L), Quartile 3 (2.26–2.32 mmol/L), and Quartile 4 (≥2.33 mmol/L). The biochemical indexes and clinical data of ACS patients in the different groups were shown in Table 1. When stratified by serum calcium quartiles, the mean age, proportion of acute myocardial infarction, troponin I at admission, BNP and GRACE score were significantly higher in Quartile 1 group as compared with Quartile 3 group and Quartile 4 group ($P < 0.01$). At the same time, the patients in Quartile 2 group were older than those in Quartile 4 group and also had higher troponin I at admission, BNP and GRACE score than those in Quartile 3 group and Quartile 4 group ($P < 0.05$). However, patients in Quartile 1 group showed an obviously lower LVEF than those in Quartile 3 group and Quartile 4 group ($P < 0.01$). A lower triglycerides and total cholesterol were found in Quartile 1 group than those in Quartile 4 group ($P < 0.01$). And body mass index was also lower in Quartile 1 group than that in Quartile 2 group and Quartile 3 group ($P < 0.01$). With increasing serum calcium, serum albumin and serum phosphorus showed a significant increase ($P < 0.05$). No differences in gender, previous history, blood pressure, creatinine or number of coronary artery lesions were observed among four groups.

Comparisons of clinical characteristics of ACS patients according to LVEF

The ACS patients were categorized into two groups according to LVEF, with one group of ACS patients with lower LVEF (LVEF ≤ 50%, $n = 61$) and one group with higher LVEF (LVEF > 50%, $n = 597$). Seen from Table 2, the male, smoking, proportion of acute myocardial infarction, heart rate, troponin I at admission, creatinine, BNP, and GRACE score were obviously higher in lower LVEF group than in higher LVEF group ($P < 0.05$). As compared to those with higher LVEF, the patients with lower LVEF had a significantly decreased serum albumin, serum calcium and phosphorus ($P < 0.05$). The age, blood pressure, serum lipid, or number of coronary artery lesions didn't differ between both groups.

Correlations of serum calcium with left ventricular function in ACS patients

In Table 3, Pearson correlation analysis found that admission serum calcium level showed a significantly positive correlation with hemoglobin, serum albumin, serum glucose, serum uric acid, serum phosphorus, triglycerides, total cholesterol, low density lipoprotein cholesterol, and LVEF ($P < 0.05$). And serum calcium was significantly and negatively associated with age, BNP, troponin I at admission, and GRACE score ($P < 0.001$).

Multivariate logistic regression in ACS patients

In multivariate logistic regression analysis, BNP was defined as 1 when BNP ≥ 300 pg/ml, and BNP was defined as 0 when BNP < 300 pg/ml. LVEF was considered as 1 when LVEF ≤ 50%, and LVEF was considered as 0 when LVEF > 50%. Male was defined as 1 while female was as 0. Multivariate backward stepwise logistic regression analysis was used to explore the independent factors associated with BNP ≥ 300 pg/ml or LVEF ≤ 50%.

TABLE 1 Comparisons of clinical characteristics of ACS patients according to serum calcium quartiles.

Variables	Total	Quartile 1 (≤2.19)	Quartile 2 (2.20–2.25)	Quartile 3 (2.26–2.32)	Quartile 4 (≥2.33)	*P*-value
Number	658	146	154	193	165	–
Age (years)	62.0 ± 10.1	64.7 ± 9.0	63.1 ± 9.5	61.1 ± 9.8*	59.7 ± 11.3*#	**<0.001**
Gender (male/female)	477/181	114/32	104/50	146/47	113/52	0.090
BMI (kg/m^2)	25.55 ± 2.81	24.96 ± 2.58	25.81 ± 2.86*	25.86 ± 2.97*	25.47 ± 2.68	**0.016**
Previous history						
Coronary artery disease (%)	275 (41.8)	60 (41.1)	61 (39.6)	83 (43.0)	71 (43.0)	0.908
Hypertension (%)	456 (69.3)	93 (63.7)	108 (70.1)	135 (69.9)	120 (72.7)	0.369
Diabetes (%)	256 (38.9)	53 (36.3)	61 (39.6)	74 (38.3)	68 (41.2)	0.839
Stroke (%)	73 (11.1)	15 (10.3)	21 (13.6)	19 (9.8)	18 (10.9)	0.701
Smoking (%)	378 (57.4)	85 (58.2)	84 (54.5)	115 (59.6)	94 (57.0)	0.815
Drinking (%)	310 (47.1)	68 (46.6)	66 (42.9)	97 (50.3)	79 (47.9)	0.585
Diagnosis						**0.003**
AMI (%)	142 (21.6)	47 (32.2)	34 (22.1)	34 (17.6)*	27 (16.4)*	
Unstable angina pectoris (%)	516 (78.4)	99 (67.8)	120 (77.9)	159 (82.4)	138 (83.6)	
Systolic BP (mmHg)	128.9 ± 17.1	126.8 ± 19.2	129.7 ± 16.6	129.7 ± 16.7	128.9 ± 15.9	0.389
Diastolic BP (mmHg)	77.2 ± 10.6	77.1 ± 10.9	77.0 ± 10.5	76.9 ± 10.4	77.7 ± 10.8	0.908
Heart rate (beats per min)	71.7 ± 9.3	71.8 ± 9.9	71.0 ± 8.6	71.6 ± 9.2	72.4 ± 9.5	0.594
Troponin I at admission (ng/mL)	0.005 (0.002, 0.066)	0.011 (0.003, 0.876)	0.008 (0.002, 0.087)	0.004 (0.002, 0.018)*^	0.004 (0.001, 0.018)*#	**<0.001**
Hemoglobin (g/L)	140.9 ± 15.5	138.1 ± 16.9	141.3 ± 15.5	141.1 ± 14.5	142.5 ± 15.3	0.083
Serum albumin (g/L)	40.3 ± 3.0	38.1 ± 2.8*	39.6 ± 2.3#	40.5 ± 2.3&	42.5 ± 2.7	**<0.001**
Serum calcium (mmol/L)	2.27 ± 0.10	2.13 ± 0.05*	2.23 ± 0.02#	2.29 ± 0.02&	2.39 ± 0.06	**<0.001**
Serum phosphorus (mmol/L)	1.13 ± 0.19	1.05 ± 0.20*	1.11 ± 0.17	1.16 ± 0.18^	1.18 ± 0.17#	**<0.001**
Serum glucose (mmol/L)	4.91 (4.34, 6.04)	4.75 (4.26, 5.76)	4.89 (4.37, 6.16)	4.98 (4.36, 5.96)	5.08 (4.40, 6.53)	0.123
Triglycerides (mmol/L)	1.46 (1.04, 2.01)	1.33 (0.95, 1.86)	1.41 (1.01, 1.92)	1.48 (1.04, 1.97)	1.64 (1.22, 2.24)*#	**0.001**
Total cholesterol (mmol/L)	3.89 ± 0.96	3.75 ± 0.84	3.80 ± 0.93	3.89 ± 0.96	4.08 ± 1.07*#	**0.013**
LDL-C (mmol/L)	2.43 ± 0.89	2.34 ± 0.76	2.39 ± 0.86	2.41 ± 0.91	2.56 ± 1.00	0.157
HDL-C (mmol/L)	1.01 ± 0.25	1.01 ± 0.28	0.97 ± 0.20	1.03 ± 0.27	1.03 ± 0.25	0.125
Serum uric acid (μmol/L)	349.6 ± 86.0	333.4 ± 78.8	350.0 ± 88.3	353.4 ± 77.5	359.3 ± 97.5	0.053
Creatinine (μmol/L)	68.1 ± 17.1	69.6 ± 20.5	67.5 ± 15.7	68.5 ± 16.6	66.9 ± 15.5	0.527
Glycosylated hemoglobin A1C (%)	6.72 ± 1.38	6.50 ± 1.15	6.70 ± 1.32	6.84 ± 1.46	6.79 ± 1.50	0.136
BNP (pg/mL)	45.0 (22.9, 115.7)	69.3 (32.0, 193.2)	48.5 (25.8, 136.6)	39.4 (18.6, 90.5)*^	36.7 (16.4, 80.2)*#	**<0.001**
LVEF (%)	60.7 ± 6.8	59.2 ± 7.0	60.5 ± 7.4	61.5 ± 6.6*	61.3 ± 5.9*	**0.012**
GRACE score	113.6 ± 23.6	121.0 ± 25.2	116.6 ± 21.0#	109.6 ± 23.3*	108.9 ± 22.9*	**<0.001**
Number of coronary artery lesions	2 (1, 3)	2 (1, 2)	2 (1, 3)	2 (1, 3)	2 (1, 3)	0.562

BMI, body mass index; AMI, acute myocardial infarction; BP, blood pressure; LDL-C, low density lipoprotein cholesterol; HDL-C, high density lipoprotein cholesterol; BNP, B-type natriuretic peptide; LVEF, left ventricular ejection fraction; GRACE, Global Registry of Acute Coronary Events.
*Q1 vs. Q2, Q1 vs. Q3, Q1 vs. Q4, $P < 0.01$.
#Q2 vs. Q3, Q2 vs. Q4, $P < 0.01$.
^Q2 vs. Q3, $P < 0.05$.
&Q3 vs. Q4, $P < 0.01$.
The bold values indicate statistical differences.

In model 1, age, gender and serum calcium quartile were used as the independent variables. The data in Table 4 exhibited that age (OR: 1.049, 95% CI: 1.016–1.083, $P = 0.003$) and lower serum calcium quartile (OR: 0.569, 95% CI: 0.429–0.754, $P < 0.001$) were independently associated with BNP ≥ 300 pg/ml after adjustment for potential confounding factors in ACS patients. In contrast, male (OR: 2.640, 95% CI: 1.228–5.678, $P = 0.013$) and lower serum calcium quartile (OR: 0.796, 95% CI: 0.623–1.016, $P = 0.066$) correlated with LVEF ≤ 50%.

In model 2, serum phosphorus, serum albumin, creatinine and GRACE score were also included in addition to those used in model 1. Multivariate backward stepwise logistic regression

TABLE 2 Comparisons of clinical characteristics of ACS patients according to LVEF.

Variables	Lower LVEF group (≤50%)	Higher LVEF group (>50%)	*P*-value
No.	61	597	
Age (years)	61.3 ± 11.5	62.1 ± 10.0	0.569
Gender (male/female)	53/8	424/173	**0.008**
BMI (kg/m^2)	25.42 ± 2.96	25.56 ± 2.79	0.709
Previous history			
Coronary artery disease (%)	31 (50.8)	244 (40.9)	0.133
Hypertension (%)	38 (62.3)	418 (70.0)	0.213
Diabetes (%)	27 (44.3)	229 (38.4)	0.368
Stroke (%)	10 (16.4)	63 (10.6)	0.167
Smoking (%)	47 (77.0)	331 (55.4)	**0.001**
Drinking (%)	36 (59.0)	274 (45.9)	0.051
Diagnosis			**<0.001**
AMI (%)	35 (57.4)	107 (17.9)	
Unstable angina pectoris (%)	26 (42.6)	490 (82.1)	
Systolic BP (mmHg)	126.2 ± 21.2	129.1 ± 16.6	0.301
Diastolic BP (mmHg)	77.5 ± 13.3	77.1 ± 10.3	0.817
Heart rate (beats per min)	75.7 ± 14.3	71.3 ± 8.5	**0.022**
Troponin I at admission (ng/mL)	0.076 (0.012, 16.914)	0.004 (0.002, 0.040)	**<0.001**
Hemoglobin (g/L)	141.7 ± 19.1	140.8 ± 15.1	0.728
Serum albumin (g/L)	39.4 ± 3.2	40.3 ± 2.9	**0.021**
Serum calcium (mmol/L)	2.24 ± 0.10	2.27 ± 0.10	**0.043**
Serum phosphorus (mmol/L)	1.08 ± 0.21	1.13 ± 0.19	**0.028**
Serum glucose (mmol/L)	5.30 (4.32, 6.74)	4.89 (4.35, 5.98)	0.181
Triglycerides (mmol/L)	1.30 (1.01, 1.95)	1.46 (1.05, 2.02)	0.413
Total cholesterol (mmol/L)	4.00 ± 1.05	3.88 ± 0.96	0.347
LDL-C (mmol/L)	2.55 ± 0.95	2.42 ± 0.89	0.272
HDL-C (mmol/L)	1.02 ± 0.27	1.01 ± 0.25	0.900
Serum uric acid (μmol/L)	365.2 ± 85.6	348.0 ± 86.0	0.137
Creatinine (μmol/L)	72.2 ± 15.9	67.7 ± 17.1	**0.049**
Glycosylated hemoglobin A1C (%)	6.98 ± 1.58	6.69 ± 1.36	0.123
BNP (pg/mL)	147.8 (37.6, 354.4)	42.8(21.6, 100.4)	**<0.001**
GRACE score	128.9 ± 29.5	112.0 ± 22.4	**<0.001**
LVEF (%)	44.3 ± 6.1	62.4 ± 4.1	**<0.001**
Number of coronary artery lesions	2 (1, 3)	2 (1, 3)	0.185

BMI, body mass index; AMI, acute myocardial infarction; BP, blood pressure; LDL-C, low density lipoprotein cholesterol; HDL-C, high density lipoprotein cholesterol; BNP, B-type natriuretic peptide; LVEF, left ventricular ejection fraction; GRACE, Global Registry of Acute Coronary Events.
The bold values indicate statistical differences.

showed that lower serum calcium quartile (OR: 0.720, 95% CI: 0.519–0.997, $P = 0.048$), lower serum albumin (OR: 0.901, 95% CI: 0.802–1.012, $P = 0.080$), increased creatinine (OR: 1.020, 95% CI: 1.005–1.035, $P = 0.010$) and GRACE score (OR: 1.042, 95% CI: 1.027–1.057, $P < 0.001$) were independently correlated with BNP ≥ 300 pg/ml after adjusting for other potential confounders in ACS patients. When LVEF was used as the dependent variable, male (OR: 2.469, 95% CI: 1.095–5.565, $P = 0.029$), age (OR: 0.931, 95% CI: 0.900–0.965, $P < 0.001$) and increased GRACE score (OR: 1.050, 95% CI: 1.035–1.056, $P < 0.001$) were independently associated with LVEF ≤ 50%.

Discussion

The present study analyzed the correlation between the level of admission serum calcium and left ventricular dysfunction in ACS patients. Admission serum calcium was positively correlated with LVEF and negatively correlated with BNP. Low

TABLE 3 Correlations of serum calcium in ACS patients.

Variables	*r*-value	*P*-value	Variables	*r*-value	*P*-value
Age (years)	−0.186	**<0.001**	Creatinine (μmol/L)	−0.053	0.176
BMI (kg/m^2)	0.065	0.097	Triglycerides (mmol/L)	0.149	**<0.001**
Systolic BP (mmHg)	0.063	0.106	Total cholesterol (mmol/L)	0.131	**0.001**
Diastolic BP (mmHg)	0.036	0.358	LDL-C (mmol/L)	0.092	**0.019**
Hemoglobin (g/L)	0.101	**0.010**	HDL-C (mmol/L)	0.067	0.084
Serum albumin (g/L)	0.592	**<0.001**	BNP (pg/mL)	−0.155	**<0.001**
Serum glucose (mmol/L)	0.089	**0.023**	Troponin I at admission (ng/mL)	−0.171	**<0.001**
Serum uric acid (μmol/L)	0.104	**0.008**	LVEF (%)	0.115	**0.003**
Serum phosphorus (mmol/L)	0.264	**<0.001**	GRACE score	−0.230	**<0.001**

BMI, body mass index; BP, blood pressure; LDL-C, low density lipoprotein cholesterol; HDL-C, high density lipoprotein cholesterol; BNP, B-type natriuretic peptide; LVEF, left ventricular ejection fraction; GRACE, Global Registry of Acute Coronary Events.
The bold values indicate statistical differences.

TABLE 4 Backward stepwise multivariate logistic regression in ACS patients.

Variables	BNP				LVEF			
	β	OR	95% CI	*P*-value	β	OR	95% CI	*P*-value
Model 1								
Age (years)	0.048	1.049	1.016–1.083	**0.003**				0.824
Gender				0.213	0.971	2.640	1.228–5.678	**0.013**
Serum calcium quartile	−0.564	0.569	0.429–0.754	**<0.001**	−0.228	0.796	0.623–1.016	0.066
Model 2								
Age (years)				0.388	−0.071	0.931	0.900–0.965	**<0.001**
Gender				0.956	0.904	2.469	1.095–5.565	**0.029**
Serum calcium quartile	−0.329	0.720	0.519–0.997	**0.048**				0.402
Serum albumin (g/L)	−0.104	0.901	0.802–1.012	0.080				0.578
Creatinine (μmol/L)	0.020	1.020	1.005–1.035	**0.010**				0.943
Serum phosphorus (mmol/L)				0.120				0.780
GRACE score	0.041	1.042	1.027–1.057	**<0.001**	0.049	1.050	1.035–1.066	**<0.001**

In Model 1, age, gender and serum calcium quartile were used as the independent variables.
In Model 2, age, gender, serum calcium quartile, serum phosphorus, serum albumin, creatinine and GRACE score were included as the independent variables.
The bold values indicate statistical differences.

level of serum calcium was independently associated with BNP ≥ 300 pg/ml after adjusting for other potential confounders. No significant association between low level of serum calcium and left ventricular systolic dysfunction was detected.

Previous studies investigated the correlation between serum calcium and left ventricular function and found that patients with low concentration of serum calcium were more likely to have LVEF <50% (22). And patient with established heart failure presented low level of serum calcium concentration (13, 23). Wang et al. (13) suggested that low serum calcium was independently associated with left ventricular systolic dysfunction in CAD patients with and without acute myocardial infarction. Batra and Agarwal (24) observed severe hypocalcemia and increased BNP in a patient with hypocalcemic cardiomyopathy and severe heart failure. Our results were consistent with these previous findings.

Other studies, on the contrary, showed different results. Li et al. (11) indicated that an increase in serum calcium concentration was correlated with an increased risk of heart failure with preserved ejection fraction in patients with type 2 diabetes mellitus. Additionally, Lutsey et al. (10) also demonstrated that baseline high serum calcium was independently correlated with greater risk of incident heart failure in this population-based cohort.

Many reasons may contribute to these different observations. It is well-known that serum calcium is affected by many factors, such as diseases, drugs and measurement techniques. In aforementioned studies, patients with diabetes mellitus or communities population from the Atherosclerosis Risk in Communities (ARIC) cohort were recruited. But severely ill patients or patients with history of LVEF < 50% were excluded. In contrast, ACS patients who were severely ill or in

emergency condition were enrolled in our study. Additionally, albumin-adjusted serum calcium concentration was used in the previous study while admission serum calcium was measured in this study. By multivariate logistic regression analysis, low serum calcium was independently correlated with elevated BNP after adjustment for potential confounding factors such as age, serum albumin, and so on in ACS patients.

BNP and LVEF are objective indexes for assessment of left ventricular function (17, 25). To the best of our knowledge, this is the first study to evaluate the association between the level of admission serum calcium and left ventricular function in ACS patients. We demonstrated that low serum calcium quartile was independently associated with elevated BNP and serum calcium level was positively correlated with LVEF. However, no significant association of serum calcium with left ventricular systolic dysfunction was observed. The potential reason includes the small number of patients with LVEF $\leq$ 50%. Meanwhile, we noticed that serum calcium level was no longer correlated with the LVEF $\leq$ 50% when adjusted by GRACE score. Killip classification is used to stratify patients according to the severity of their post-myocardial infarction heart failure and included in the calculation of GRACE score, which may cause the futile correlation. By contrast, GRACE score was not included in the regression model in Wang et al.'s study (13).

The possible mechanism of the correlation between serum calcium and left ventricular dysfunction is unclear. Serum calcium ions play a vital role in many metabolic and regulatory processes associated with cardiovascular disease, such as platelet adhesion and aggregation, blood coagulation, enzymatic activity, myocardial excitation, contraction and relaxation (8, 9). In view of the roles of serum calcium in myocardial excitation-contraction coupling and cardiac electrophysiologic effect, abnormalities of serum calcium may cause disarrangement of calcium homeostasis in the cytoplasm of cardiomyocytes and lead to myocardial dysfunction (22). On the other side, hypocalcemia reduces renal sodium excretion (26), thus contributes to fluid overload and decreased myocardial contractility, as demonstrated by decreased left ventricular work index (9, 27). In addition, decreased serum calcium was correlated with various common cardiovascular risk profiles, such as hypertension, dyslipidemia, and so on (8).

This study had some limitations. First, it was a single-center, observational study, whether similar results are obtained in other patient categories remains to be investigated. Second, the current study included a relatively small number of patients with LVEF $\leq$ 50%. Third, recent studies (28, 29) found that high curvatures and branching of coronary arteries were associated with the risk of development of atherosclerosis and plaque formation, however, coronary curvatures and branching were not considered in our study. ACS patients with non-obstructive coronary artery were not included. Fourth, serum calcium measurement was performed on a single occasion after admission. Serum calcium levels might vary over time, therefore a longitudinal study is required. Finally, the pathophysiologic mechanism of the association between hypocalcaemia and left ventricular dysfunction was not investigated in the present study. However, with the explorative results generated from this study, a further study will be conducted.

In summary, admission serum calcium was positively correlated with LVEF and negatively with BNP in ACS patients. Low admission serum calcium was an independent biomarker for elevated BNP.

Data availability statement

The raw data supporting the conclusions of this article will be made available by the authors, without undue reservation.

Ethics statement

The studies involving human participants were reviewed and approved by the Ethical Committee of Beijing Tiantan Hospital. The patients/participants provided their written informed consent to participate in this study.

Author contributions

HW contributed to assembly of data, performed data analysis and interpretation, and wrote the manuscript. RW carried out the studies, collected and analyzed data, and participated in manuscript writing. JT conceived and designed this study, provided administrative support, collected and analyzed data, and wrote the manuscript. All authors have read and approved the final manuscript.

Funding

This work was supported by the Basic and Clinical Research Collaboration Programme (15JL55), Capital Medical University.

Acknowledgments

The authors thank all the staff in Department of Cardiovascular Medicine, Beijing Tiantan Hospital, Capital Medical University for their generous supports in this study.

Conflict of interest

The authors declare that the research was conducted in the absence of any commercial or financial relationships that could be construed as a potential conflict of interest.

Publisher's note

References

1. Zhao D, Liu J, Wang M, Zhang X, Zhou M. Epidemiology of cardiovascular disease in China: current features and implications. *Nat Rev Cardiol.* (2019) 16:203–12. doi: 10.1038/s41569-018-0119-4

2. Mahmood SS, Levy D, Vasan RS, Wang TJ. The Framingham Heart Study and the epidemiology of cardiovascular disease: a historical perspective. *Lancet.* (2014) 383:999–1008. doi: 10.1016/S0140-6736(13)61752-3

3. Yahud E, Tzuman O, Fink N, Goldenberg I, Goldkorn R, Peled Y, et al. Trends in long-term prognosis according to left ventricular ejection fraction after acute coronary syndrome. *J Cardiol.* (2020) 76:303–8. doi: 10.1016/j.jjcc.2020.03.012

4. Kwok CS, Bachmann MO, Mamas MA, Stirling S, Shepstone L, Myint PK, Zaman MJ. Effect of age on the prognostic value of left ventricular function in patients with acute coronary syndrome: a prospective registry study. *Eur Heart J Acute Cardiovasc Care.* (2017) 6:191–8. doi: 10.1177/2048872615623038

5. HananiaG, CambouJP, Guéret P, Vaur L, Blanchard D, Lablanche JM, et al. USIC 2000 Investigators. Management and in-hospital outcome of patients with acute myocardial infarction admitted to intensive care units at the turn of the century: results from the French nationwide USIC 2000 registry. *Heart.* (2004) 90:1404–10. doi: 10.1136/hrt.2003.025460

6. Lopez-Jimenez F, Goraya TY, Hellermann JP, Jacobsen SJ, Reeder GS, Weston SA, et al. Measurement of ejection fraction after myocardial infarction in the population. *Chest.* (2004) 125:397–403. doi: 10.1378/chest.125.2.397

7. Khaled S, Matahen R. Cardiovascular risk factors profile in patients with acute coronary syndrome with particular reference to left ventricular ejection fraction. *Indian Heart J.* (2018) 70:45–9. doi: 10.1016/j.ihj.2017.05.019

8. Zhang C, Cao B, Huang X, Gu J, Xia M, Yang X, et al. Association between serum calcium and first incident acute myocardial infarction: a cross-sectional study. *Iran J Public Health.* (2020) 49:1278–88. doi: 10.18502/ijph.v49i7.3581

9. Yan S, Liu XJ, Peng Y, Xia TL, Liu W, Tsauo JY, et al. Admission serum calcium levels improve the grace risk score prediction of hospital mortality in patients with acute coronary syndrome. *Clin Cardiol.* (2016) 39:516–23. doi: 10.1002/clc.22557

10. Lutsey PL, Alonso A, Michos ED, Loehr LR, Astor BC, Coresh J, Folsom AR. Serum magnesium, phosphorus, and calcium are associated with risk of incident heart failure: the Atherosclerosis Risk in Communities (ARIC) Study. *Am J Clin Nutr.* (2014) 100:756–64. doi: 10.3945/ajcn.114.085167

11. Li J, Wu N, Dai W, Jiang L, Li Y, Li S, Wen Z. Association of serum calcium and heart failure with preserved ejection fraction in patients with type 2 diabetes. *Cardiovasc Diabetol.* (2016) 15:140. doi: 10.1186/s12933-016-0458-6

12. Cubbon RM, Thomas CH, Drozd M, Gierula J, Jamil HA, Byrom R, et al. Calcium, phosphate and calcium phosphate product are markers of outcome in patients with chronic heart failure. *J Nephrol.* (2015) 28:209–15. doi: 10.1007/s40620-014-0075-y

13. Wang Y, Ma H, Hao X, Yang J, Chen Q, Lu L, et al. Low serum calcium is associated with left ventricular systolic dysfunction in a Chinese population with coronary artery disease. *Sci Rep.* (2016) 6:22283. doi: 10.1038/srep22283

14. Kimura K, Kimura T, Ishihara M, Nakagawa Y, Nakao K, Miyauchi K, et al. Japanese Circulation Society Joint Working Group. JCS 2018 guideline on diagnosis and treatment of acute coronary syndrome. *Circ J.* (2019) 83:1085–96. doi: 10.1253/circj.CJ-19-0133

15. Yamauchi Y, Fujita SI, Shibata K, Morita H, Ito T, Sohmiya K, et al. Is serum uric acid independently associated with left ventricular mass index, ejection fraction, and B-type natriuretic peptide among female and male cardiac patients? *Int Heart J.* (2017) 58:562–9. doi: 10.1536/ihj.16-359

16. Berman J, Lee L, Monga R, Ye K, Sprayregen S, Haramati LB. Clearing the congestion: chest radiography and BNP to rule-out congestive heart failure. *J Thorac Imaging.* (2021) 1–5. doi: 10.1097/RTI.0000000000000625

17. Logeart D, Saudubray C, Beyne P, Thabut G, Ennezat PV, Chavelas C, et al. Comparative value of Doppler echocardiography and B-type natriuretic peptide assay in the etiologic diagnosis of acute dyspnea. *J Am Coll Cardiol.* (2002) 40:1794–800. doi: 10.1016/S0735-1097(02)02482-8

18. Douglas PS, Patel MR, Bailey SR Dai D, Kaltenbach L, Brindis RG, et al. Hospital variability in the rate of finding obstructive coronary artery disease at elective, diagnostic coronary angiography. *J Am Coll Cardiol.* (2011) 58:801–9. doi: 10.1016/j.jacc.2011.05.019

19. Perumalsamy S, Wan Ahmad WA, Zaman Huri H. Single Nucleotide Polymorphism rs17173608 in the Chemerin Encoding Gene: is it a predictor of insulin resistance and severity of coronary artery disease in non-obese type 2 diabetes? *Healthcare.* (2021) 9:623. doi: 10.3390/healthcare9060623

20. Albert J, Lezius S, Störk S, Morbach C, Güder G, Frantz S, et al. Trajectories of left ventricular ejection fraction after acute decompensation for systolic heart failure: concomitant echocardiographic and systemic changes, predictors, and impact on clinical outcomes. *J Am Heart Assoc.* (2021) 10:e017822. doi: 10.1161/JAHA.120.017822

21. Spitzer E, Pavo N, Abdelghani M, Beitzke D, Ren B, García-Ruiz V, et al. Assessment of left ventricular ejection fraction with late-systolic and mid-diastolic cardiac phases using multi-slice computed tomography. *Radiography.* (2018) 24:e85–90. doi: 10.1016/j.radi.2018.04.007

22. Su W, Zhu JG, Zhao XQ, Chen H, Li WP Li HW. Altered serum calcium homeostasis independently predicts mortality in patients with acute coronary syndrome: a retrospective observational cohort study. *BMJ Open.* (2021) 11:e049957. doi: 10.1136/bmjopen-2021-049957

23. Jensen AC, Polcwiartek C, Søgaard P, Mortensen RN, Davidsen L, Aldahl M, et al. The association between serum calcium levels and short-term mortality in patients with chronic heart failure. *Am J Med.* (2019) 132:200–8. doi: 10.1016/j.amjmed.2018.10.006

24. Batra CM, Agarwal R. Hypocalcemic cardiomyopathy and pseudohypoparathyroidism due to severe vitamin D deficiency. *J Assoc Phys India.* (2016) 64:74–6.

25. Wong KK, Wang D, Ko JK, Mazumdar J, Le TT, Ghista D. Computational medical imaging and hemodynamics framework for functional analysis and assessment of cardiovascular structures. *Biomed Eng Online.* (2017) 16:35. doi: 10.1186/s12938-017-0326-y

26. Levine SN, Rheams CN. Hypocalcemic heart failure. *Am J Med.* (1985) 78:1033–5. doi: 10.1016/0002-9343(85)90228-1

27. Hurley K, Baggs D. Hypocalcemic cardiac failure in the emergency department. *J Emerg Med.* (2005) 28:155–9. doi: 10.1016/j.jemermed.2004.06.014

28. Wong KKL, Wu J, Liu G, Huang W, Ghista DN. Coronary arteries hemodynamics: effect of arterial geometry on hemodynamic parameters causing atherosclerosis. *Med Biol Eng Comput.* (2020) 58:1831–43. doi: 10.1007/s11517-020-02185-x

29. Liu G, Wu J, Ghista DN, Huang W, Wong KK. Hemodynamic characterization of transient blood flow in right coronary arteries with varying curvature and side-branch bifurcation angles. *Comput Biol Med.* (2015) 64:117–26. doi: 10.1016/j.compbiomed.2015.06.009

frontiers | Frontiers in Cardiovascular Medicine

TYPE Review
PUBLISHED 15 December 2022
DOI 10.3389/fcvm.2022.1019053

OPEN ACCESS

EDITED BY
Junjie Xiao,
Shanghai University, China

REVIEWED BY
Soumyajit Mandal,
Brookhaven National Laboratory (DOE), United States
Lijian Gao,
Chinese Academy of Medical Sciences and Peking Union Medical College, China
Tak Kwan,
Lenox Hill Hospital, United States

*CORRESPONDENCE
Gaojun Cai
cgj982@126.com

SPECIALTY SECTION
This article was submitted to General Cardiovascular Medicine, a section of the journal Frontiers in Cardiovascular Medicine

RECEIVED 14 August 2022
ACCEPTED 22 November 2022
PUBLISHED 15 December 2022

CITATION
Chen T, Yu X, Song R, Li L and Cai G (2022) Application of ultrasound in cardiovascular intervention *via* the distal radial artery approach: New wine in old bottles?
Front. Cardiovasc. Med. 9:1019053.
doi: 10.3389/fcvm.2022.1019053

Application of ultrasound in cardiovascular intervention *via* the distal radial artery approach: New wine in old bottles?

Tao Chen[1], Xiaolong Yu[2], Ruixiao Song[2], Lamei Li[1] and Gaojun Cai[1]*

[1]Changzhou Key Laboratory of Molecular Diagnostics and Precision Cancer Medicine, Department of Cardiology, Wujin Institute of Molecular Diagnostics and Precision Cancer Medicine of Jiangsu University, Wujin Hospital Affiliated with Jiangsu University, The Wujin Clinical College of Xuzhou Medical University, Changzhou, Jiangsu, China, [2]Department of Ultrasonics, Wujin Hospital Affiliated with Jiangsu University, The Wujin Clinical College of Xuzhou Medical University, Changzhou, Jiangsu, China

The distal radial artery (DRA) approach has emerged as a new approach in cardiovascular intervention. In recent years, ultrasound has been widely used in cardiovascular intervention *via* the DRA approach. This article systematically discusses the progress of ultrasound in the preoperative vascular assessment, intraoperative guided puncture and postoperative observation of complications *via* the DRA approach.

KEYWORDS

ultrasound, distal radial artery, distal radial artery approach, cardiovascular intervention, vascular assessment

Introduction

The distal radial artery (DRA) approach has emerged as a new approach in cardiovascular interventions in recent years (1). Compared with the conventional radial artery (CRA) approach, the distal transradial approach (dTRA) dramatically reduces the risk of bleeding and radial artery occlusion (RAO) and offers higher operator and patient comfort (2–5). Although there is no discernible difference between the two techniques in terms of puncture success rate and other characteristics (6), there is a noticeable learning curve for dTRA puncture, with a longer puncture time than the transradial artery approach (TRA) (4, 7).

According to previous studies, puncture of the radial artery under ultrasound guidance can increase cannulation success rates and decrease the risk of haematoma at the puncture site (8–10). Ultrasound is also of high value in cardiovascular interventions

Abbreviations: DRA, distal radial artery; CRA, conventional radial artery; dTRA, distal transradial approach; RAO, radial artery occlusion; TRA, transradial artery approach; AS, anatomical snuffbox; BMI, body mass index; PSV, peak systolic velocity.

performed *via* the dTRA, which can not only improve the success of puncture and catheterization (11–13) and shorten the time of dTRA puncture and catheterization (14) but also monitor vascular access-related problems. In light of the contemporary literature, we systematically evaluated the value of ultrasound in the perioperative period of cardiovascular interventions performed *via* the dTRA.

Ultrasound examination methods

Ultrasound images of the anatomical snuffbox

The DRA is divided into the anatomical snuffbox (AS) and the Hegu acupoint by the tendon of the extensor pollicis longus (15). The AS is a triangular depression on the dorsum of the hand near the root of the thumb, with the abductor pollicis longus and extensor pollicis brevis on the outside and the extensor pollicis longus on the inside, the radial styloid process on the lower border, and the trapezium and scaphoid bones at the base (16). The AS contains the DRA, cephalic vein, and superficial branches of the radial nerve (16).

The vessel presents a hyperechoic anterior and posterior wall on two-dimensional ultrasound imaging in the long-axis view as well as a long, black, anechoic train-track structure in the middle and an anechoic oval structure in the short-axis view. The superficial branch of the radial nerve is located near the extensor pollicis longus, which presents with small striated structures with hypoechoic and hyperechoic lines alternating on the long-axis view and honeycomb-like structures with a mixture of hypoechoic and hyperechoic lines and annular hyperechoic wrapping on the short-axis view. Similar to the radial nerve, the image of the tendon displays a striatal-like structure along the long axis and a compact, fibrillar highly echogenic elliptical structure along the short axis with a terminal attachment to the bone. The bone cortical surface shows a strong echogenic signal with a posterior acoustic shadow (17) (**Figure 1**).

Ultrasound operation in the anatomical snuffbox

When the ultrasound examination is performed in the AS, the patient's hand is placed in a relaxed position, as in holding a wine glass, to fully expose the AS region. After applying the proper amount of ultrasound coupling agent, the thumb, index finger, and middle finger of the operator are used to secure the ultrasound probe, with the little finger touching the patient's forearm as a support point (**Figure 2**). As the DRA is usually superficial, excessive pressure is likely to cause measurement errors; thus, the ultrasound probe is placed lightly perpendicular to the skin until it contacts the coupling agent. A high-frequency (6–18 MHz) linear probe is usually chosen, and its size is appropriate to place in the narrow AS region (18).

Ultrasound-guided arterial puncture method

Ultrasound guidance can significantly improve the success rate of radial artery puncture (11). The basic methods for performing ultrasound-guided arterial puncture include the long-axis in-plane method, the short-axis out-of-plane method, the oblique axis in-plane method, and dynamic needle tip positioning (19, 20). In the long-axis in-plane method, the long-axis of the ultrasound probe is parallel to the longitudinal axis of the vessel, which appears as a tubular hypoechoic structure on imaging. During vascular puncture, the needle is inserted at 15°–30° to the skin with the tip parallel to the long axis of the vessel. The short-axis out-of-plane method involves placing the ultrasound probe perpendicular to the direction of the vessel, which then appears as a circular hypoechoic structure on imaging. The puncture needle is also inserted at 15°–30° to the skin with the tip perpendicular to the short-axis of the vessel. The oblique in-plane method is based on the short-axis out-of-plane method with an additional 45° clockwise rotation of the probe; the resulting vascular image is an elliptical hypoechoic structure. Dynamic needle tip positioning involves seeing the highlighted needle tip on the ultrasound image, holding the puncture needle still and translating the probe proximally until the tip disappears, followed by holding the ultrasound probe still and advancing the puncture needle until the tip reappears in the center of the vessel (**Figure 3**). Meta-analyses have revealed no significant difference among the various puncture guidance techniques for increasing radial artery puncture success rates (21, 22). Until now, there have been no studies on whether various ultrasonography manoeuvres are helpful in increasing the success rate of puncture *via* the dTRA.

Application of ultrasound in distal radial artery interventions

Measurement of the vascular diameter before surgery, puncture guidance during catheterization, and evaluation of complications related to puncture after surgery are of high clinical value. Currently, there are a large number of studies on the use of ultrasound for cardiovascular intervention *via* the DRA. We systematically searched the relevant literature in the PubMed database using the keywords "distal radial artery, distal radial approach, distal radial access, distal transradial artery, distal transradial approach, distal transradial access" and "ultrasound, ultrasound-guided, ultrasonography, duplex ultrasound" (last search date 2022.07.10), combined with a manual search of the references of the retrieved articles. A total

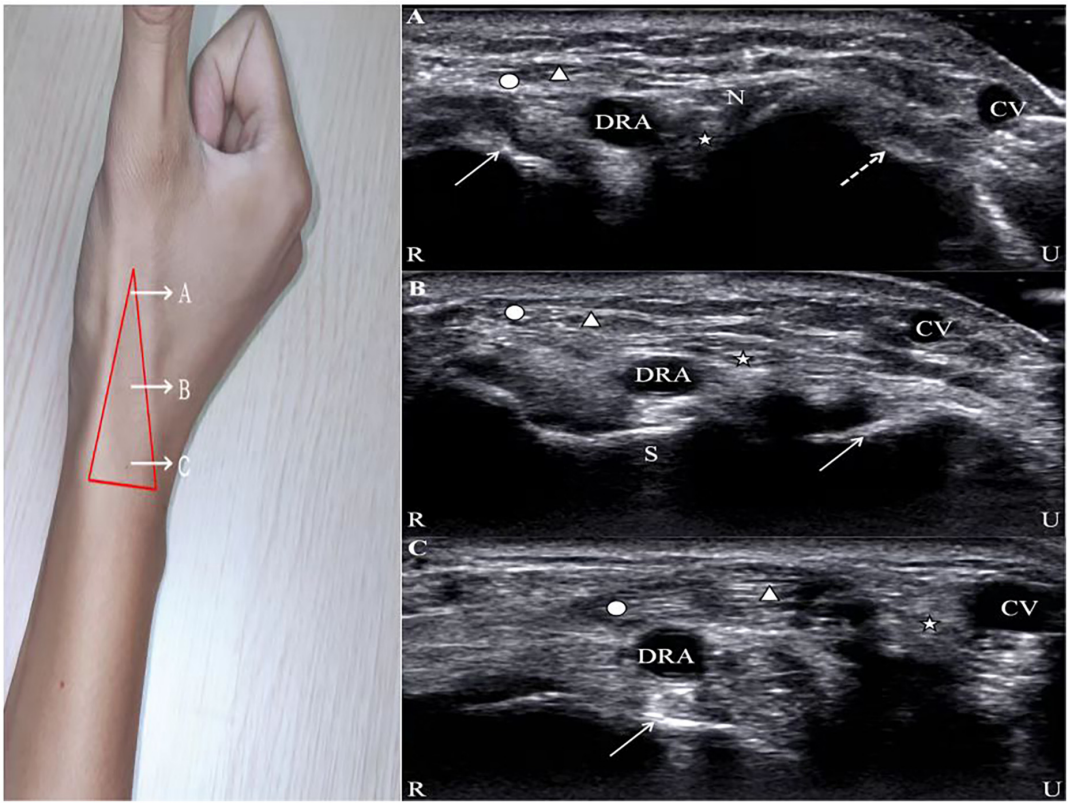

FIGURE 1
Ultrasound images of the AS. Circle, abductor pollicis longus; Triangle, extensor pollicis brevis; Star, extensor pollicis longus; DRA, distal radial artery; CV, cephalic vein; R, radial; U, ulnar. **(A)** N, radial nerve; solid line arrow, first metacarpal bone; dotted line arrow, second metacarpal bone. **(B)** S, scaphoid; solid line arrow, lunate. **(C)** Solid line arrow, radial styloid process.

of 3,581 articles were initially retrieved. Based on the titles and abstracts and removing duplicate articles, a total of 22 studies were ultimately enrolled (2, 6, 12, 13, 23–40), with thirteen studies from Asia, five from Europe, two from North America, and two from South America. The sample sizes ranged from 42 to 2,775 cases. The study types included two randomized controlled studies, six prospective cohort studies, one cross-sectional study, and thirteen retrospective studies (**Table 1**).

Preoperative measurement of vessel diameter

The results of a meta-analysis showed that the size of the outer diameter of the vascular sheath was positively correlated with the incidence of RAO (41), and mismatch between the sheath and vessel diameter increased the incidence of RAO. To reduce the risk of vascular injury, an increasing number of studies have focused on the preoperative assessment of the DRA diameter (2, 6, 12, 13, 23–40). Selection of suitable sheaths according to the diameter of the DRA appeared to reduce vascular damage (24). Although computed tomography or angiography can accurately measure vessel diameter (42–44), radiation and contrast agents are required and expensive. In contrast, ultrasound is a convenient and non-invasive method for evaluating vessel diameter (**Figure 4**).

Distal radial artery diameter and the influencing factors

As shown in **Table 1**, the diameter of the DRA varied greatly in various studies, which may be related to race, characteristics of the research objects, measurement location, diameter definition, demographic morphological characteristics, etc. (24, 25, 28–30, 37). As reported by Yu WW et al., the DRA diameter was 1.71 ± 0.50 mm in a Chinese population (25), but 2.40 ± 0.50 mm according to data from Mexico (37). The largest DRA diameter measured to date is 2.99 ± 0.60 mm in Japan (30) from a study that excluded subjects with a vessel diameter < 2.0 mm. In another Japanese population, Naito T et al. showed a DRA diameter of 2.02 ± 0.44 mm (29). According to Meo D et al., the diameter of the DRA was significantly larger in men than in women (34). Additionally, for the DRA, differences in vessel diameters measured inside and outside the AS have been found. The diameter was smaller at the Hegu acupoint than

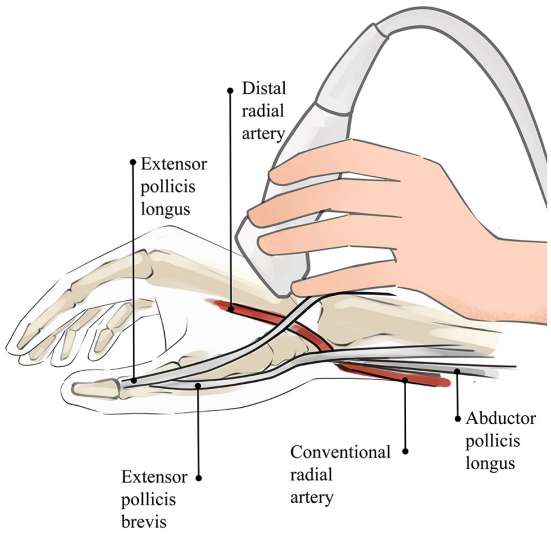

FIGURE 2
Sketch of ultrasound technique of AS. The operator's little finger touches the patient's forearm as a support point, which prevents the blood vessel from being affected by external forces.

at the AS (28). In addition, the methods used to measure the vessel diameter were different. In most studies, the definition of vessel diameter was the media to media distance (25, 27, 29), while the distance from the outer membrane to the outer membrane was used in other studies (24, 32). For example, Norimatsu K found the diameter of the DRA, defined as the distance from the outer membrane to the outer membrane, to be 2.6 ± 0.5 mm, which was larger than the results of other studies (24). A similar result was obtained in a Korean population (32).

The DRA is the continuation of the CRA on the back of the hand. Does the diameter of the CRA affect the diameter of the DRA? With the exception of one Canadian study (44), the majority of studies discovered a correlation between DRA and CRA diameters, with a ratio of almost 80% (24, 29, 33). Norimatsu K et al. highlighted a strong positive correlation ($r = 0.66$, $P < 0.0001$) between the DRA diameter to the CRA diameter, and the ratio of the DRA to CRA diameter was 0.8 ± 0.1 (24). Naito T et al. also found a strong correlation between the DRA and CRA diameters (29). In a large-sample Korean study, the DRA/CRA ratio was similar to the previous results on both sides (33). However, in another study, the DRA diameter was 2.10 ± 0.40 mm, and the CRA diameter was 2.60 ± 0.40 mm, which were not significantly correlated ($r = 0.053$, $P = 0.641$) (27). The diameter of the DRA was even larger than that of the CRA in 6.6–8% of patients (29, 34), considering vascular variation. Most studies have suggested that the CRA diameter affects the DRA diameter.

Sex may be a factor influencing DRA diameter, with studies from Asia, Europe, and the Americas showing that the DRA diameters in females are significantly smaller than those in males (23, 26, 31, 33, 34, 40). However, Norimatsu K et al. found that although the DRA diameter in women was smaller than that in men, the difference was not significant (men: 2.6 mm, women:

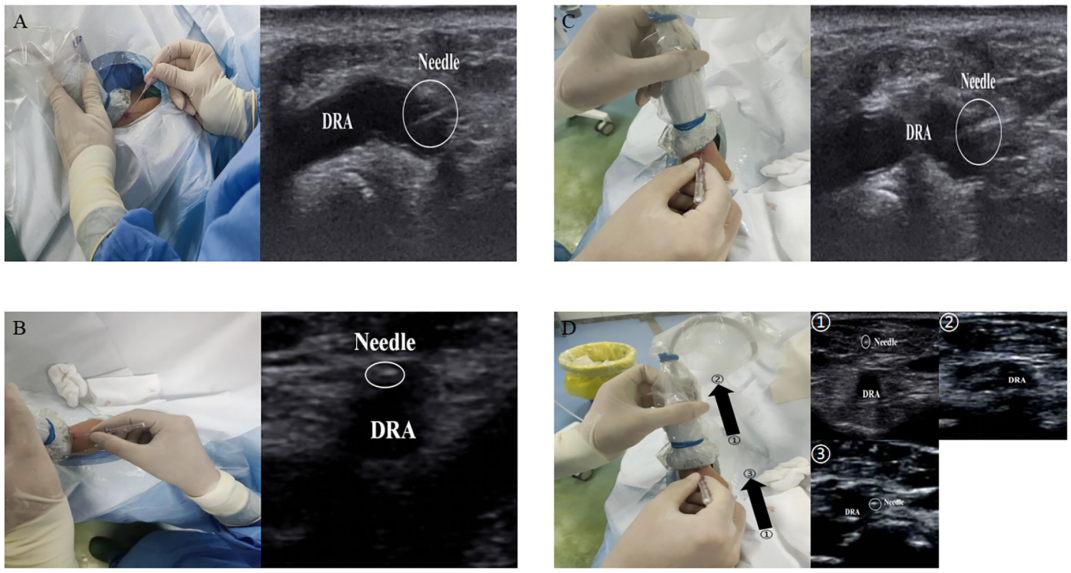

FIGURE 3
Ultrasound guided puncture. **(A)** The long-axis in-plane method; **(B)** the short-axis out-of-plane method; **(C)** the oblique axis in-plane method; **(D)** the dynamic needle tip positioning. ①, seeing the highlighted needle tip; ②, holding the puncture needle still and translating the probe proximally until the tip disappears; ③, followed by holding the ultrasound probe still and advancing the puncture needle until the tip reappears in the center of the vessel.

TABLE 1 DRA diameter and the influencing factors.

References	Country	Study design	Number (*n*)	Ultrasound machine model	Probe type	Probe frequency	Diameter definition	Diameter of distal radial artery (mm)	Influencing factors
Kaledin et al. (38)	Russia	Prospective	2,775	NA	NA	NA	Media to media	2.4*	NA
Kim et al. (31)	Korea	Retrospective	117	NA	NA	NA	Media to media	2.65 ± 0.46 men 2.40 ± 0.53 women	Gender
Lee et al. (32)	Korea	Prospective	151	NA	NA	NA	Adventitia to adventitia	2.41 ± 0.50 L 2.36 ± 0.49 R	NA
Babunashvili (39)	Russia	Retrospective	1631	NA	NA	NA	Media to media	2.13 ± 0.33	NA
Flores (40)	America	Retrospective	200	NA	NA	NA	Media to media	2.4 men# 2.1 women#	NA
Norimatsu et al. (24)	Japan	Retrospective	142	NA	NA	NA	Adventitia to adventitia	2.60 ± 0.50	Weight, CRA, BMI
Yu et al. (25)	China	Retrospective	92	Philips, iE33	Philips L11-3	NA	Media to media	1.70 ± 0.50 L 1.71 ± 0.50 R	NA
Mizuguchi et al. (28)	Japan	Retrospective	228	Boston scientific corporation	Linear probe	11 MHz	Media to media	2.40 ± 0.50 AS 2.30 ± 0.50 Hegu	NA
Naito et al. (29)	Japan	Retrospective	120	Philips, CX50	Linear probe	12–13 MHz	Media to media	2.02 ± 0.44	NA
Wang et al. (6)	China	Retrospective	620	NA	NA	NA	Media to media	2.20 ± 0.50	NA
Hadjivassiliou et al. (12)	Canada	Retrospective	287	NA	NA	NA	Media to media	2.34 ± 0.36	NA
Kawamura et al. (30)	Japan	Retrospective	50	NA	NA	NA	Media to media	2.99 ± 0.60	NA
Meo et al. (34)	Italy	Cross-sectional	700	Esaote MyLab two, Genova	Linear probe	10 MHz	Media to media	1.99 ± 0.47	Gender, BMI
Koury et al. (35)	Brazil	Prospective	42	NA	NA	NA	Media to media	2.31 ± 0.44	NA
Achim et al. (2)	Romania	Prospective	1240	NA	Linear probe	7.5 MHz	Media to media	2.30 ± 0.20	NA
Lee et al. (33)	Korea	Retrospective	1162	Vivid E95/Philips EPIQ7	11L-D/L12-3 linear probe	4.5–12 MHz /3–12 MHz	Media to media	2.35 ± 0.45 L 2.31 ± 0.43 R	Gender, BMI, BSA
Eid-Lidt et al. (37)	Mexico	Randomized	140	L741	SonoScapeE2	16–4 MHz	Media to media	2.40 ± 0.50	NA
Ghose et al. (13)	India	Prospective	108	NA	Philips, M2540 A	NA	Media to media	2.25 ± 0.34	NA
Deora et al. (23)	India	Prospective	1004	Philips, EPIC 7C	NA	8–11 MHz	Media to media	2.23 ± 0.39	Height, weight, gender
Li et al. (26)	China	Retrospective	246	NA	Philips, EPIQ 7C/IE33	NA	Media to media	2.05 ± 0.41	Gender
Xiong et al. (27)	China	Randomized	81	Wisonic, China	Linear probe	4–15 MHz	Media to media	2.10 ± 0.40	Weight
Horák et al. (36)	Czech Republic	Retrospective	115	GE Vivid S6	Linear 9L transducer	2.4–10.0 MHz	Media to media	2.31 ± 0.47	NA

*median values; #mean; L, Left; R, Right; NA, non-available; CRA, conventional radial artery; BMI, body mass index; BSA, body surface area; AS, anatomical snuffbox; Hegu, Hegu acupoint.

10.3389/fcvm.2022.1019053

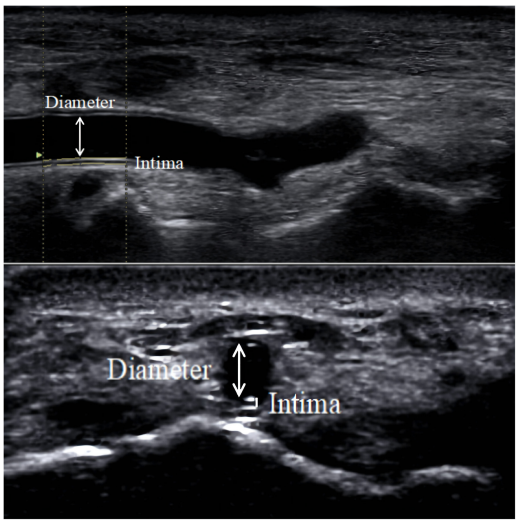

FIGURE 4
DRA diameter. The diameter measured in the figure is the distance from the media to the media.

2.5 mm, $P = 0.08$) (24). A similar conclusion was also obtained in a study by Horák D et al. (Men: 2.32 mm, Women: 2.25 mm, $P = 0.27$) (36). Despite the conflicting findings, generally, the DRA diameter is larger in men than in women.

The demographic and morphological characteristics of the patients may also influence the diameter of the DRA. Studies have shown that patients with diabetes or hypertension have smaller DRA diameters (2.18 ± 0.41 mm for hypertension, 2.26 ± 0.38 mm for non-hypertension, $P < 0.001$; 2.18 ± 0.44 mm for diabetes, 2.26 ± 0.38 mm for non-diabetes, $P = 0.004$) (23). In 2019, Japanese scholars found a positive correlation between body mass index (BMI) and DRA diameter ($r = 0.228$, $P = 0.007$) (24). Subsequently, a study by Meo D et al. found that subjects with BMI > 30 kg/m^2 had larger vessel diameters than those with BMI < 30 kg/m^2 (2.20 ± 0.50 mm vs. 1.97 ± 0.52 mm, $P < 0.001$) (34). Lee WJ et al. showed that low BMI and low body surface area were strong independent predictors of DRA diameter < 2.3 mm (33). In addition, DRA diameter was also reported to be positively correlated with both height and weight (23, 24, 27). In contrast, Naito T et al. discovered no correlation between DRA diameter and patient parameters such height, weight, and BMI (29). In conclusion, demographic and morphological characteristics such as body surface area and the presence of diabetes or hypertension can affect DRA diameter. Due to differences in study design and measurement methods, whether other patient parameters have an effect on DRA diameter has yet to be verified.

Effect of endovascular diameter on intraoperative selection of vascular sheath

Sheath placement may cause damage to the DRA (24). Hadjivassiliou A et al. concluded that different types of sheaths can be safely placed within different sized DRA (1.8–2.8 mm in diameter) (12). However, a retrospective study reported that an artery/sheath ratio > 1.0 was least damaging to the vessel during coronary intervention *via* the DRA (29). With conventional sheaths (Super Sheath^{TM}), the percentages of artery/sheath ratios ≥ 1.0 were 94, 77, 55, and 34% for 4 Fr (1.88 mm), 5 Fr (2.2 mm), 6 Fr (2.5 m), and 7 Fr (2.84 mm), respectively. In contrast, when using a slender sheath (Glidesheath Slender®), the percentages of artery/sheath ratios ≥ 1.0 were 81, 63, and 39% for 5 Fr (2.13 mm), 6 Fr (2.46 mm), and 7 Fr (2.79 mm), respectively (24). Only 57.6% of patients were suitable for placement of a 5 Fr catheter sheath (2.3 mm), and 35.1% were suitable for placement of a 6 Fr catheter sheath (2.7 mm) in Korean patients (32). This is similar to results obtained in European countries (34). The use of preoperative ultrasound to examine vessel size is an important guide for the selection of sheaths, and the use of slender or sheathless techniques may reduce vascular-related complications (33, 45).

Postoperative diameter change

The cannulation procedure may cause changes in the DRA vessel diameter (28, 30). Mizuguchi Y et al. used ultrasound to measure the DRA diameter before and after the procedure and observed a dynamic change in vessel diameter, which was 2.40 ± 0.50 mm before the operation, expanded significantly to 2.70 ± 0.50 mm 1 day after the operation and returned to 2.50 ± 0.50 mm 1 month after the operation (28). Similar vascular changes were observed in another study (30).

Operation guidance

Ultrasound guidance increases the success rate of distal radial artery puncture

Traditionally, interventionalists utilize palpation to identify the puncture site when performing radial artery puncture. However, pulse palpation in the DRA can be challenging and difficult in some conditions. For example, pulsation is weak in patients with multiple punctures, patients suffering from shock or peripheral vascular disease, and patients with RAO, who have only 70% arterial pressure on average at the distal remnant of the occluded radial artery (46). Additionally, in patients with small vessel diameters, it is difficult to identify the course of the blood vessels. These conditions make the patient prone to puncture failure. However, if ultrasound is used, successful puncture of the DRA may be obtained with ultrasound guidance even if the pulse is weak or the vessel diameter is small (47). Ultrasound-guided DRA cannulation can be used not only for coronary interventions but also for abdominopelvic and neurological interventions (35, 48). This visualization of the puncture not only increases the success rate but also reduces the complications, especially for precise or emergency interventions.

In recent years, an increasing number of studies have explored the relationship between ultrasound guidance and puncture success rate (11–13). Although in a small sample retrospective cohort study, the puncture success rate was similar between ultrasound-guided and palpation methods (49). In general, the success rate of ultrasound-guided puncture is higher than that of conventional dTRA puncture (11). A study that included 108 individuals demonstrated a high success rate from ultrasound-guided puncture (96.3%) as well as a reduced incidence of DRA spasm (13). As reported by Hadjivassiliou A et al., the puncture success rate in the left DRA reached 100% under ultrasound guidance (12). Possible biases in the conclusions were generally due to the small sample size, and the majority of research still favours ultrasound guidance to increase puncture success. Nevertheless, Tsigkas G et al. emphasized that although ultrasound guidance could improve the success rate of puncture, it might increase the procedure time and cost, and it was not advocated as a routine operation (3). Moreover, ultrasound guidance has a high value in the reverse recanalization of the proximal RAO *via* the DRA (50). In RAO patients, the radial artery in the AS circulates through the reverse lateral branch of the palmar arch. The palpation becomes weak or disappears, but blood flow signals are still visible under high-frequency ultrasound. Ultrasound guidance may significantly increase the puncture success rate (50, 51).

Ultrasound guidance reduces operation complications

During puncture, ultrasound can be used to identify the anatomical structures around the blood vessels and

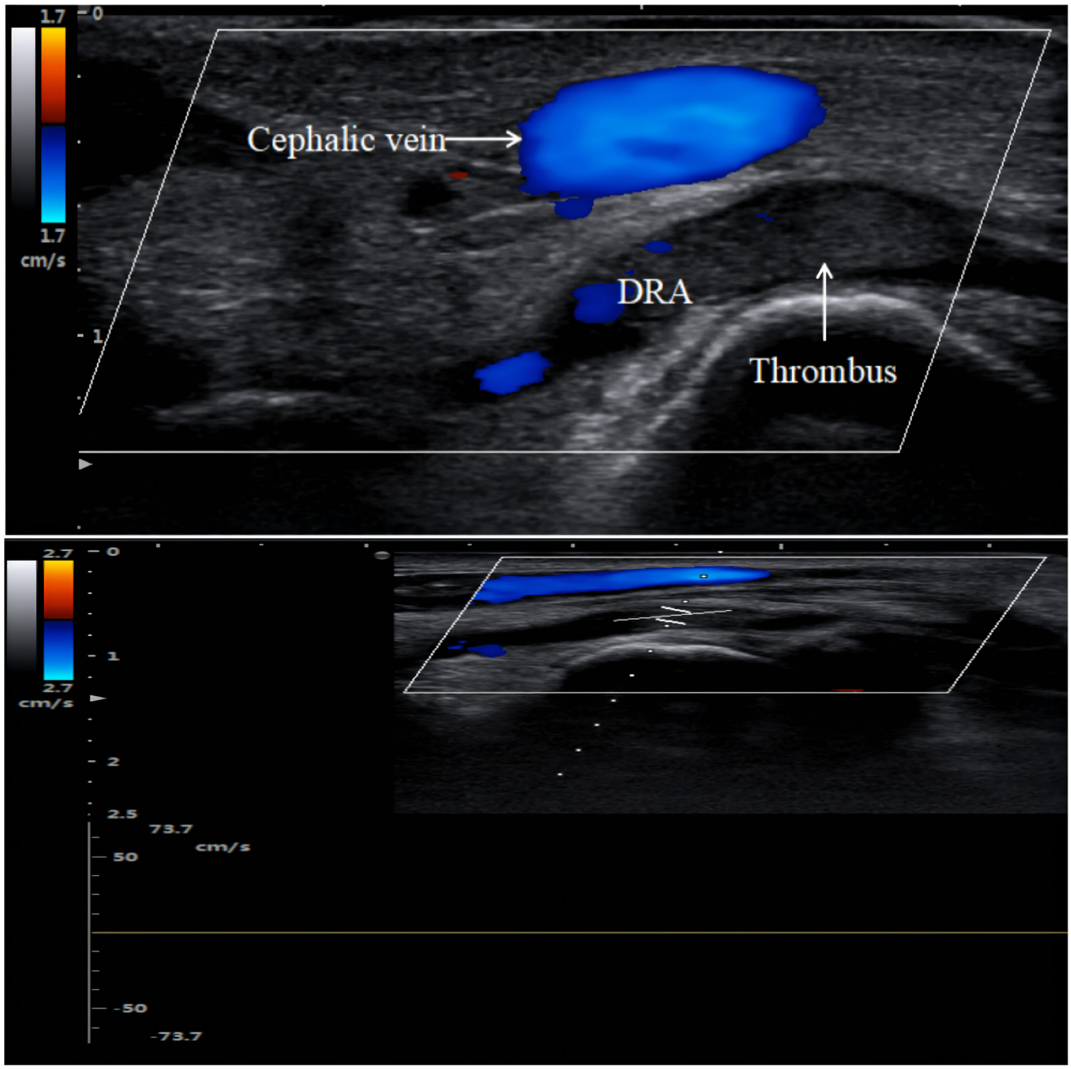

FIGURE 5
Distal radial artery occlusion. Thrombus is hypoechoic on color Doppler imaging. There is no blood flow spectrum waveform curve on pulse wave Doppler imaging.

avoid damage to normal tissue as much as possible (40). Rapid resolution of the arteriovenous system by means of a "compressibility test" with a probe showed pulsation of the artery, which did not collapse completely under pressure, and the vein was easily deflated completely. Ultrasound can also identify shallow radial nerves to avoid potential nerve damage (18). However, previous studies have also found no significant difference in vascular access-related complications (haematoma and neuropathy) with or without ultrasound guidance (11).

Evaluation of complications

Radial artery occlusion is a common complication of TRA interventions in clinical practice. The incidence of RAO after the TRA has been reported to range from 2.5 to 8.4%, which is higher than that after the dTRA (0–5%) (4, 45). In the past, some methods, such as palpation, the reverse Allen test, and the reverse Barbeau test, were typically used to determine the presence of RAO (52, 53). Due to the reverse blood supply of the collateral circulation and the fact that most patients with RAO are asymptomatic, only a small percentage of patients show hand ischaemia (54). The methods listed above for detecting RAO have the potential for false negatives, which can easily lead to missing a diagnosis of RAO. However, the absence of a blood flow signal in the occluded radial artery can be observed by ultrasound (**Figure 5**), which can greatly reduce the rate of underdiagnosis of RAO (6, 36). Complications such as distal radial artery occlusion, haematoma, bleeding, arteriovenous fistula, pseudoaneurysm, infection, and entrapment are equally common after coronary intervention *via* the dTRA (38, 55, 56). In recent years, the incidence of distal radial artery occlusion after dTRA intervention has been reported to range from 0.12 to 5.2% (28, 38–40, 57). In 2014, Kaledin A et al. reported a 2.2% incidence of RAO in 1,009 patients after dTRA, with 0.1% occlusion in the forearm, 1.8% in the AS, and 0.3% in both the forearm and AS (38). Subsequently, Mizuguchi Y et al. showed that the incidence of distal radial artery occlusion was 3.5% (8 cases/228 cases) in a Japanese population (28).

In addition, ultrasound follow-up revealed thrombus autolysis after acute RAO. The incidence of RAO was 8.4% at 24 h after intervention *via* CRA and decreased to 5.6% after 30 days, with a recanalization rate as high as 33.3% (37). In a meta-analysis, the incidence of RAO was 7.7% for the TRA at 24 h postoperatively and decreased to 5.8% at 30 days (41). Ultrasound can be performed repeatedly and has unique advantages in determining whether the radial artery is recanalized at follow-up.

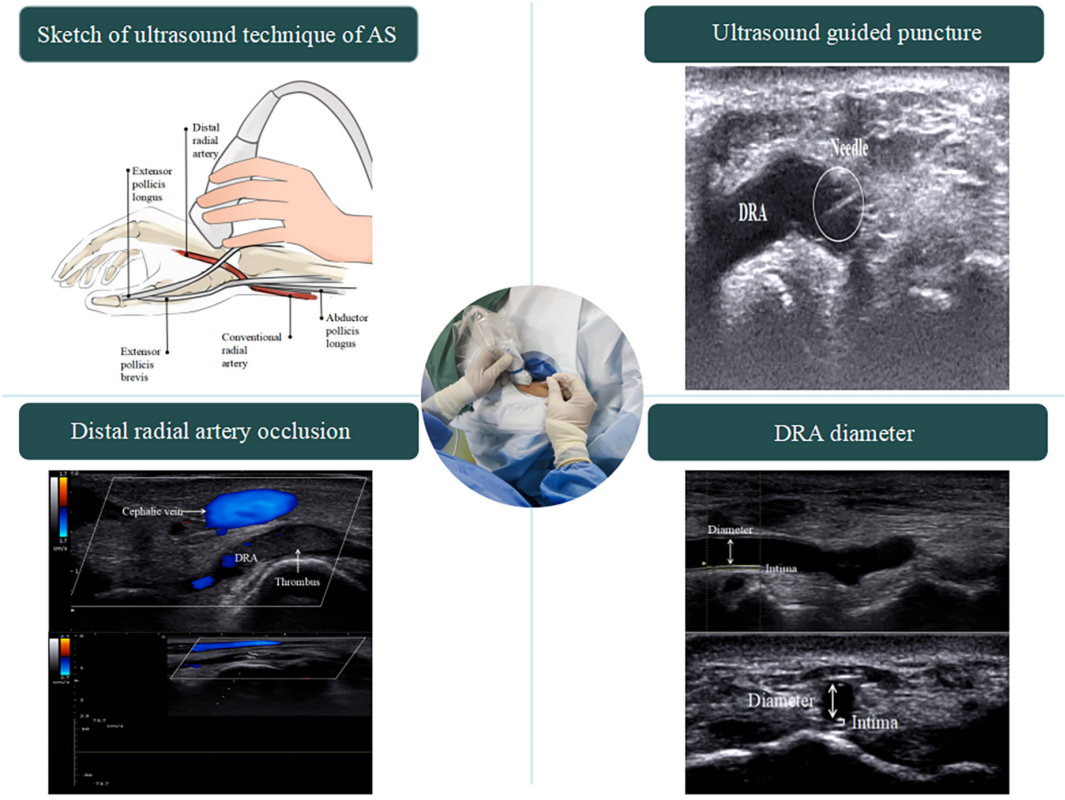

FIGURE 6
Central illustration.

Although the radial artery was not occluded in some patients after transradial catheterization, intravascular ultrasound revealed thickening of the CRA intima (intima-media thickness > 0.4 mm), resulting in stenosis (58). Intimal changes after radial artery cannulation were observed by optical coherence tomography, which also revealed postoperative CRA intimal thickening (59), and a significant increase in CRA intimal volume was still seen at the 9-month postoperative follow-up (60). Despite the fact that optical coherence tomography and intravascular ultrasound are more reliable at detecting endovascular injury, they are also more invasive and expensive, involve limited exploration of the vessels and should not be utilized as standard diagnostics. In addition to being non-invasive, ultrasound also offers an infinite range of detection and can be utilized as part of a standard postoperative assessment of the vessel intima (61, 62). Thus, ultrasound plays a major role in detecting the histopathological morphology and structure of radial artery vessels.

Furthermore, ultrasound can measure radial artery haemodynamic changes before and after the operation. Peak systolic velocity (PSV) in the radial artery was measured using ultrasound at different times after surgery. The preoperative PSV was 59.6 cm/s, which significantly increased to 63.1 cm/s half an hour later and decreased back to 57.3 cm/s 7 days after the operation (63). A study simulating RAO demonstrated that the PSV in the forearm radial artery and the radio-dorsal digital artery of the thumb were significantly reduced in the presence of RAO at the wrist level (forearm radial artery: 24 ± 13% of baseline, $P = 0.001$; digital artery of the thumb: 68 ± 8% of baseline, $P = 0.001$); however, the PSV in the forearm radial artery and the digital artery of the thumb were essentially unchanged when RAO was performed at the AS level (forearm radial artery: 93 ± 2% of baseline, $P = 0.65$; digital artery of the thumb: 95 ± 2% of baseline, $P = 0.71$) (64).

Ultrasound also helps to improve the efficiency of treatment for postoperative complications. For postoperative abnormal bulges near the puncture site that are difficult to identify on routine physical examination, such as haematomas, arteriovenous fistulas, or pseudoaneurysms, ultrasound can clarify the diagnosis. In patients with arteriovenous fistulas, ultrasound can probe the vascular breach for applying precise compression bandaging treatment to reduce patient pain (55, 65). Additionally, patients with pseudoaneurysms can be treated not only with ultrasound-guided compression bandaging (56, 66) but also with ultrasound-guided injection of thrombin (67).

Limitations

Interventional methods *via* DRA are only now emerging. The application of ultrasound has been recommended by some scholars (**Figure 6**). However, due to the special anatomical location of the AS, such as the abundant bony structures and the narrow range (15), it is not easy for the ultrasound probe to fully contact the examination site, which increases the difficulty of ultrasound examination. Moreover, unskilled operators require a learning curve (7), which may prolong the procedure time. Therefore, ultrasound guidance is difficult to apply in high-volume centers. The main disadvantage of ultrasound is the lack of a uniform definition and resolution of the machine or the measurement technique, which will influence the measurement results. To adapt to the anatomical characteristics of the AS, a smaller probe needs to be designed to achieve flexible exploration of the target vessels.

In conclusion, ultrasound has certain clinical application value in the process of DRA intervention. In the near future, as medical technology continues to be improved, the application of ultrasound in the interventional treatment of DRA may become more widespread.

Author contributions

GC conceived and designed the article. XY and RS reviewed the ultrasound diagnosis. LL analyzed the data. TC collected the literature and wrote the manuscript. All authors contributed to the article and approved the submitted version.

Funding

This study was supported by Changzhou Science & Technology Program (No. CE20225003).

Acknowledgments

We thank Jianmin Wang for his support.

Conflict of interest

The authors declare that the research was conducted in the absence of any commercial or financial relationships that could be construed as a potential conflict of interest.

Publisher's note

References

1. Kiemeneij F. Left distal transradial access in the anatomical snuffbox for coronary angiography (ldTRA) and interventions (ldTRI). *EuroIntervention.* (2017) 13:851–7. doi: 10.4244/EIJ-D-17-00079

2. Achim A, Kákonyi K, Jambrik Z, Nagy F, Tóth J, Sasi V, et al. Distal radial artery access for coronary and peripheral procedures: a multicenter experience. *J Clin Med.* (2021) 10:5974. doi: 10.3390/jcm10245974

3. Tsigkas G, Papageorgiou A, Moulias A, Kalogeropoulos A, Papageorgopoulou C, Apostolos A, et al. Distal or traditional transradial access site for coronary procedures: a single-center, randomized study. *JACC Cardiovasc Interv.* (2022) 15:22–32. doi: 10.1016/j.jcin.2021.09.037

4. Liang C, Han Q, Jia Y, Fan C, Qin G. Distal transradial access in anatomical snuffbox for coronary angiography and intervention: an updated meta-analysis. *J Interv Cardiol.* (2021) 2021:7099044. doi: 10.1155/2021/7099044

5. Cai G, Huang H, Li F, Shi G, Yu X, Yu L. Distal transradial access: a review of the feasibility and safety in cardiovascular angiography and intervention. *BMC Cardiovasc Disord.* (2020) 20:356. doi: 10.1186/s12872-020-01625-8

6. Wang H, Peng W, Liu Y, Ma G, Wang D, Su B, et al. A comparison of the clinical effects and safety between the distal radial artery and the classic radial artery approaches in percutaneous coronary intervention. *Ann Palliat Med.* (2020) 9:2568–74. doi: 10.21037/apm-19-479

7. Roh J, Kim Y, Lee O, Im E, Cho D, Choi D, et al. The learning curve of the distal radial access for coronary intervention. *Sci Rep.* (2021) 11:13217. doi: 10.1038/s41598-021-92742-7

8. Moussa Pacha H, Alahdab F, Al-Khadra Y, Idris A, Rabbat F, Darmoch F, et al. Ultrasound-guided versus palpation-guided radial artery catheterization in adult population: a systematic review and meta-analysis of randomized controlled trials. *Am Heart J.* (2018) 204:1–8. doi: 10.1016/j.ahj.2018.06.007

9. Tang L, Wang F, Li Y, Zhao L, Xi H, Guo Z, et al. Ultrasound guidance for radial artery catheterization: an updated meta-analysis of randomized controlled trials. *PLoS One.* (2014) 9:e111527. doi: 10.1371/journal.pone.0111527

10. Zhao W, Peng H, Li H, Yi Y, Ma Y, He Y, et al. Effects of ultrasound-guided techniques for radial arterial catheterization: a meta-analysis of randomized controlled trials. *Am J Emerg Med.* (2021) 46:1–9. doi: 10.1016/j.ajem.2020.04.064

11. Mori S, Hirano K, Yamawaki M, Kobayashi N, Sakamoto Y, Tsutsumi M, et al. A comparative analysis between ultrasound-guided and conventional distal transradial access for coronary angiography and intervention. *J Interv Cardiol.* (2020) 2020:7342732. doi: 10.1155/2020/7342732

12. Hadjivassiliou A, Cardarelli-Leite L, Jalal S, Chung J, Liu D, Ho S, et al. Left distal transradial access (ldTRA): a comparative assessment of conventional and distal radial artery size. *Cardiovasc Intervent Radiol.* (2020) 43:850–7. doi: 10.1007/s00270-020-02485-7

13. Ghose T, Kachru R, Dey J, Khan W, Sud R, Jabeen S, et al. Safety and feasibility of ultrasound-guided access for coronary interventions through distal left radial route. *J Interv Cardiol.* (2022) 2022:2141524. doi: 10.1155/2022/2141524

14. Mhanna M, Beran A, Nazir S, Al-Abdouh A, Barbarawi M, Sajdeya O, et al. Outcomes of distal versus conventional transradial access for coronary angiography and intervention: an updated systematic review and meta-analysis. *Int J Cardiol.* (2021) 344:47–53. doi: 10.1016/j.ijcard.2021.10.003

15. Chinese Expert Consensus Group for Percutaneous Coronary Intervention through the Distal Transradial Artery Access; Thumb Club. Chinese expert consensus on percutaneous coronary intervention through distal transradial artery access. *Cardiol Plus.* (2020) 5:175–85. doi: 10.4103/2470-7511.305423

16. Cerda A, del Sol M. Anatomical snuffbox and it clinical significance. a literature review. *Int J Morphol.* (2015) 33:1355–60. doi: 10.1016/j.math.2014.05.007

17. Borges Á, Souza S. Anatomy of the nerves, vessels, and muscular compartments of the forearm, as revealed by high-resolution ultrasound. Part 1: overall structure and forearm compartments. *Radiol Bras.* (2021) 54:388–97. doi: 10.1590/0100-3984.2021.0030

18. Hadjivassiliou A, Kiemeneij F, Nathan S, Klass D. Ultrasound-guided access to the distal radial artery at the anatomical snuffbox for catheter-based vascular interventions: a technical guide. *EuroIntervention.* (2021) 16:1342–8. doi: 10.4244/EIJ-D-19-00555

19. Clemmesen L, Knudsen L, Sloth E, Bendtsen T. Dynamic needle tip positioning - ultrasound guidance for peripheral vascular access. A randomized, controlled and blinded study in phantoms performed by ultrasound novices. *Ultraschall Med.* (2012) 33:E321–5. doi: 10.1055/s-0032-1312824

20. Phelan M, Hagerty D. The oblique view: an alternative approach for ultrasound-guided central line placement. *J Emerg Med.* (2009) 37:403–8. doi: 10.1016/j.jemermed.2008.02.061

21. Shi J, Shen J, Xiang Z, Liu X, Lu T, Tao X. Dynamic needle tip positioning versus palpation and ultrasound for arteriovenous puncture: a meta-analysis. *Ultrasound Med Biol.* (2021) 47:2233–42. doi: 10.1016/j.ultrasmedbio.2021.04.001

22. Wang H, Wang J, Chen W. Ultrasound-guided short-axis out-of-plane vs. long-axis in-plane technique for radial artery catheterization: an updated meta-analysis of randomized controlled trials. *Eur Rev Med Pharmacol Sci.* (2022) 26:1914–22. doi: 10.26355/eurrev_202203_28337

23. Deora S, Sharma S, Choudhary R, Kaushik A, Garg P, Khera P, et al. Assessment and comparison of distal radial artery diameter in anatomical snuff box with conventional radial artery before coronary catheterization. *Indian Heart J.* (2022) 74:322–6. doi: 10.1016/j.ihj.2022.06.007

24. Norimatsu K, Kusumoto T, Yoshimoto K, Tsukamoto M, Kuwano T, Nishikawa H, et al. Importance of measurement of the diameter of the distal radial artery in a distal radial approach from the anatomical snuffbox before coronary catheterization. *Heart Vessels.* (2019) 34:1615–20. doi: 10.1007/s00380-019-01404-2

25. Yu W, Hu P, Wang S, Yao L, Wang H, Dou L, et al. Distal radial artery access in the anatomical snuffbox for coronary angiography and intervention: a single center experience. *Medicine.* (2020) 99:e18330. doi: 10.1097/MD.0000000000018330

26. Li S, Li J, Liu L, Liu W, Yang H, Feng C. Analysis of the risk factors related to the success rate of distal transradial artery access in patients with coronary heart disease. *Risk Manag Healthc Policy.* (2022) 15:657–63. doi: 10.2147/RMHP.S357780

27. Xiong J, Hui K, Xu M, Zhou J, Zhang J, Duan M. Distal radial artery as an alternative approach to forearm radial artery for perioperative blood pressure monitoring: a randomized, controlled, noninferiority trial. *BMC Anesthesiol.* (2022) 22:67. doi: 10.1186/s12871-022-01609-5

28. Mizuguchi Y, Izumikawa T, Hashimoto S, Yamada T, Taniguchi N, Nakajima S, et al. Efficacy and safety of the distal transradial approach in coronary angiography and percutaneous coronary intervention: a Japanese multicenter experience. *Cardiovasc Interv Ther.* (2020) 35:162–7. doi: 10.1007/s12928-019-00590-0

29. Naito T, Sawaoka T, Sasaki K, Iida K, Sakuraba S, Yokohama K, et al. Evaluation of the diameter of the distal radial artery at the anatomical snuff box using ultrasound in Japanese patients. *Cardiovasc Interv Ther.* (2019) 34:312–6. doi: 10.1007/s12928-018-00567-5

30. Kawamura Y, Yoshimachi F, Nakamura N, Yamamoto Y, Kudo T, Ikari Y. Impact of dedicated hemostasis device for distal radial arterial access with an adequate hemostasis protocol on radial arterial observation by ultrasound. *Cardiovasc Interv Ther.* (2021) 36:104–10. doi: 10.1007/s12928-020-00656-4

31. Kim Y, Ahn Y, Kim M, Sim D, Hong Y, Kim J, et al. Gender differences in the distal radial artery diameter for the snuffbox approach. *Cardiol J.* (2018) 25:639–41. doi: 10.5603/CJ.2018.0128

32. Lee J, Park S, Son J, Ahn S, Lee S. Real-world experience of the left distal transradial approach for coronary angiography and percutaneous coronary intervention: a prospective observational study (LeDRA). *EuroIntervention.* (2018) 14:e995–1003. doi: 10.4244/EIJ-D-18-00635

33. Lee J, Son J, Go T, Kang D, Lee S, Kim S, et al. Reference diameter and characteristics of the distal radial artery based on ultrasonographic assessment. *Korean J Intern Med.* (2022) 37:109–18. doi: 10.3904/kjim.2020.685

34. Meo D, Falsaperla D, Modica A, Calcagno M, Libra F, Desiderio C, et al. Proximal and distal radial artery approaches for endovascular percutaneous procedures: anatomical suitability by ultrasound evaluation. *Radiol Med.* (2021) 126:630–5. doi: 10.1007/s11547-020-01299-4

35. Koury A Jr, Monsignore L, de Castro-Afonso L, Abud D. Safety of ultrasound-guided distal radial artery access for abdominopelvic transarterial interventions: a prospective study. *Diagn Interv Radiol.* (2020) 26:570–4. doi: 10.5152/dir.2020.19543

36. Horák D, Bernat I, Jirouš Š, Slezák D, Rokyta R. Distal radial access and postprocedural ultrasound evaluation of proximal and distal radial artery. *Cardiovasc Interv Ther.* (2022) 37:710–6. doi: 10.1007/s12928-022-00857-z

37. Eid-Lidt G, Rivera Rodríguez A, Jimenez Castellanos J, Farjat Pasos J, Estrada López K, Gaspar J. Distal radial artery approach to prevent radial artery occlusion trial. *JACC Cardiovasc Interv.* (2021) 14:378–85. doi: 10.1016/j.jcin.2020.10.013

38. Kaledin A, Kochanov I, Seletskii S, Arkharov I, Burak T, Kozlov K. Peculiarities of arterial access in endovascular surgery in elderly patients. *Adv Gerontol.* (2014) 27:115–9.

39. Babunashvili A. Novel distal transradial approach for coronary and peripheral interventions. *J Am Coll Cardiol.* (2018) 72(Suppl. 13):B323.

40. Flores E. Making the right move: use of the distal radial artery access in the hand for coronary angiography and percutaneous coronary interventions. *Cath Lab Digest.* (2018) 26:16–25.

41. Rashid M, Kwok C, Pancholy S, Chugh S, Kedev S, Bernat I, et al. Radial artery occlusion after transradial interventions: a systematic review and meta-analysis. *J Am Heart Assoc.* (2016) 5:e002686. doi: 10.1161/JAHA.115.002686

42. Vefalı V, Sarıçam E. The comparison of traditional radial access and novel distal radial access for cardiac catheterization. *Cardiovasc Revasc Med.* (2020) 21:496–500. doi: 10.1016/j.carrev.2019.07.001

43. Kim Y, Ahn Y, Kim I, Lee D, Kim M, Sim D, et al. Feasibility of coronary angiography and percutaneous coronary intervention via left snuffbox approach. *Korean Circ J.* (2018) 48:1120–30. doi: 10.4070/kcj.2018.0181

44. Valsecchi O, Vassileva A, Cereda A, Canova P, Satogami K, Fiocca L, et al. Early clinical experience with right and left distal transradial access in the anatomical snuffbox in 52 consecutive patients. *J Invasive Cardiol.* (2018) 30:218–23.

45. Aminian A, Sgueglia G, Wiemer M, Kefer J, Gasparini G, Ruzsa Z, et al. Distal versus conventional radial access for coronary angiography and intervention: the DISCO RADIAL trial. *JACC Cardiovasc Interv.* (2022) 15:1191–201. doi: 10.1016/j.jcin.2022.04.032

46. Pancholy S, Coppola J, Patel T, Roke-Thomas M. Prevention of radial artery occlusion-patent hemostasis evaluation trial (PROPHET study): a randomized comparison of traditional versus patency documented hemostasis after transradial catheterization. *Catheter Cardiovasc Interv.* (2008) 72:335–40. doi: 10.1002/ccd.21639

47. Lee S, Yoon W, Bae D, Kim M, Kim S, Bae J. Early experience with ultrasound guided distal trans-radial access in the anatomical snuffbox in coronary angiography and intervention. *Circulation.* (2018) 138(Suppl. 1):A17406–17406.

48. Pons R, Caamaño I, Chirife O, Aja L, Aixut S, de Miquel M. Transradial access for diagnostic angiography and interventional neuroradiology procedures: a four-year single-center experience. *Interv Neuroradiol.* (2020) 26:506–13. doi: 10.1177/1591019920925711

49. Maitra S, Ray B, Bhattacharjee S, Baidya D, Dhua D, Batra R. Distal radial arterial cannulation in adult patients: a retrospective cohort study. *Saudi J Anaesth.* (2019) 13:60–2. doi: 10.4103/sja.SJA_700_18

50. Shi G, Li F, Zhang L, Gong C, Xue S, Song Y, et al. Retrograde recanalization of occluded radial artery: a single-centre experience and literature review. *J Endovasc Ther.* (2022) 29:755–62. doi: 10.1177/15266028211067732

51. Alkhawam H, Windish S, Abo-Salem E. Distal radial artery access among cases with radial artery occlusion for primary percutaneous intervention. *Future Cardiol.* (2019) 15:169–73. doi: 10.2217/fca-2018-0057

52. Kotowycz M, Dzavík V. Radial artery patency after transradial catheterization. *Circ Cardiovasc Interv.* (2012) 5:127–33. doi: 10.1161/CIRCINTERVENTIONS.111.965871

53. Rao S, Tremmel J, Gilchrist I, Shah P, Gulati R, Shroff A, et al. Best practices for transradial angiography and intervention: a consensus statement from the society for cardiovascular angiography and intervention's transradial working group. *Catheter Cardiovasc Interv.* (2014) 83:228–36. doi: 10.1002/ccd.25209

54. Ayan M, Smer A, Azzouz M, Abuzaid A, Mooss A. Hand ischemia after transradial coronary angiography: resulting in right ring finger amputation. *Cardiovasc Revasc Med.* (2015) 16:367–9. doi: 10.1016/j.carrev.2015.06.002

55. Shah S, Kiemeneij F, Khuddus M. Distal arteriovenous fistula formation after percutaneous coronary intervention: an old complication of a new access site. *Catheter Cardiovasc Interv.* (2021) 97:278–81. doi: 10.1002/ccd.28772

56. Mizuguchi Y, Yamada T, Taniguchi N, Nakajima S, Hata T, Takahashi A. Pseudoaneurysm formation after cardiac catheterization using the distal transradial approach. *J Invasive Cardiol.* (2019) 31:E257.

57. Roghani-Dehkordi F, Hashemifard O, Sadeghi M, Mansouri R, Akbarzadeh M, Dehghani A, et al. Distal accesses in the hand (two novel techniques) for percutaneous coronary angiography and intervention. *ARYA Atheroscler.* (2018) 14:95–100. doi: 10.22122/arya.v14i2.1743

58. Wakeyama T, Ogawa H, Iwami T, Tanaka M, Harada N, Hiratsuka A, et al. Distal radial arterial hypertrophy after transradial intervention: a serial intravascular ultrasound study. *J Cardiol.* (2018) 72:501–5. doi: 10.1016/j.jjcc.2018.05.008

59. Di Vito L, Porto I, Burzotta F, Trani C, Pirozzolo G, Niccoli G, et al. Radial artery intima-media ratio predicts presence of coronary thin-cap fibroatheroma: a frequency domain-optical coherence tomography study. *Int J Cardiol.* (2013) 168:1917–22. doi: 10.1016/j.ijcard.2012.12.082

60. Kala P, Kanovsky J, Novakova T, Miklik R, Bocek O, Poloczek M, et al. Radial artery neointimal hyperplasia after transradial PCI-Serial optical coherence tomography volumetric study. *PLoS One.* (2017) 12:e0185404. doi: 10.1371/journal.pone.0185404

61. Stegemann E, Sansone R, Stegemann B, Kelm M, Heiss C. Validation of high-resolution ultrasound measurements of intima-media thickness of the radial artery for the assessment of structural remodeling. *Angiology.* (2015) 66:574–7. doi: 10.1177/0003319714544699

62. Zhang B, Zhou Y, Du J, Yang S, Wang Z, Shen H, et al. Comparison of very-high-frequency ultrasound assessment of radial arterial wall layers after first and repeated transradial coronary procedures. *J Geriatr Cardiol.* (2017) 14:245–53. doi: 10.11909/j.issn.1671-5411.2017.04.003

63. Liu L, Zhou H, Tang H, Zhou Q. Evaluation of radial and ulnar artery blood flow after radial artery decannulation using colour doppler ultrasound. *BMC Anesthesiol.* (2021) 21:312. doi: 10.1186/s12871-021-01538-9

64. Sgueglia G, Santoliquido A, Gaspardone A, Di Giorgio A. First results of the distal radial access doppler study. *JACC Cardiovasc Imaging.* (2021) 14:1281–3. doi: 10.1016/j.jcmg.2020.11.023

65. Koziński Ł, Dąbrowska-Kugacka A, Orzalkiewicz Z. Successful management of arteriovenous fistula after coronary catheterization via the snuffbox approach. *Cardiol J.* (2020) 27:200–1. doi: 10.5603/CJ.2020.0043

66. Gitto M, Brizzi S, Cozzi O, Gohar A, Maurina M, Spada P, et al. Radial artery pseudoaneurysm complicating distal transradial access for chronic total occlusion recanalization. *Cardiovasc Revasc Med.* (2022) 40:279–81. doi: 10.1016/j.carrev.2022.02.019

67. Budassi S, Zivelonghi C, De Roover D, Scott B, Agostoni P. Distal radial pseudoaneurysm after chronic total occlusion percutaneous coronary intervention resolved by percutaneous thrombin injection. *Cardiovasc Revasc Med.* (2020) 21:134–7. doi: 10.1016/j.carrev.2020.05.018

frontiers | Frontiers in Cardiovascular Medicine

TYPE Original Research
PUBLISHED 03 February 2023
DOI 10.3389/fcvm.2022.981333

OPEN ACCESS

EDITED BY
Pietro Enea Lazzerini,
University of Siena, Italy

REVIEWED BY
Scott Levick,
West Virginia University, United States
Giovanna Gallo,
Sapienza University of Rome, Italy

*CORRESPONDENCE
Philipp Hillmeister
✉ p.hillmeister@klinikum-brandenburg.de
Ivo Buschmann
✉ i.buschmann@klinikum-brandenburg.de

†These authors have contributed equally to this work

SPECIALTY SECTION
This article was submitted to General Cardiovascular Medicine, a section of the journal Frontiers in Cardiovascular Medicine

RECEIVED 29 June 2022
ACCEPTED 09 November 2022
PUBLISHED 03 February 2023

CITATION
Li K, Kratzmann V, Dai M, Gatzke N, Rocic P, Bramlage P, Grisk O, Lubomirov LT, Hoffmeister M, Lauxmann MA, Ritter O, Buschmann E, Bader M, Persson AB, Buschmann I and Hillmeister P (2023) Angiotensin receptor-neprilysin inhibitor improves coronary collateral perfusion.
Front. Cardiovasc. Med. 9:981333.
doi: 10.3389/fcvm.2022.981333

Angiotensin receptor-neprilysin inhibitor improves coronary collateral perfusion

Kangbo Li[1,2,3†], Victoria Kratzmann[1†], Mengjun Dai[1,2], Nora Gatzke[1], Petra Rocic[4], Peter Bramlage[5], Olaf Grisk[6], Lubomir T. Lubomirov[6], Meike Hoffmeister[7,8], Martin A. Lauxmann[7], Oliver Ritter[8,9], Eva Buschmann[10], Michael Bader[2,3,11,12], Anja Bondke Persson[2], Ivo Buschmann[1,8*] and Philipp Hillmeister[1,8*]

[1]Department for Angiology, Center for Internal Medicine I, Deutsches Angiologie Zentrum Brandenburg - Berlin, University Clinic Brandenburg, Brandenburg Medical School Theodor Fontane, Brandenburg an der Havel, Germany, [2]Charité – Universitätsmedizin Berlin, Corporate Member of Freie Universität Berlin and Humboldt-Universität zu Berlin, Berlin, Germany, [3]Max Delbrück Center for Molecular Medicine in the Helmholtz Association, Berlin, Germany, [4]Department of Physiology and Pharmacology, College of Osteopathic Medicine, Sam Houston State University, Huntsville, TX, United States, [5]Institute for Pharmacology and Preventive Medicine, Cloppenburg, Germany, [6]Institute of Physiology, Brandenburg Medical School Theodor Fontane, Neuruppin, Germany, [7]Institute of Biochemistry, Brandenburg Medical School Theodor Fontane, Brandenburg an der Havel, Germany, [8]Faculty of Health Sciences Brandenburg, Joint Faculty of the Brandenburg University of Technology Cottbus – Senftenberg, The Brandenburg Medical School Theodor Fontane, University of Potsdam, Brandenburg an der Havel, Germany, [9]Department for Cardiology, Center for Internal Medicine I, University Clinic Brandenburg, Brandenburg Medical School Theodor Fontane, Brandenburg an der Havel, Germany, [10]Department of Cardiology, University Clinic Graz, Graz, Austria, [11]German Center for Cardiovascular Research, Partner Site Berlin, Berlin, Germany, [12]Institute for Biology, University of Lübeck, Lübeck, Germany

Background: We investigated the pleiotropic effects of an angiotensin receptor-neprilysin inhibitor (ARNi) on collateral-dependent myocardial perfusion in a rat model of coronary arteriogenesis, and performed comprehensive analyses to uncover the underlying molecular mechanisms.

Methods: A rat model of coronary arteriogenesis was established by implanting an inflatable occluder on the left anterior descending coronary artery followed by a 7-day repetitive occlusion procedure (ROP). Coronary collateral perfusion was measured by using a myocardial particle infusion technique. The putative ARNi-induced pro-arteriogenic effects were further investigated and compared with an angiotensin-converting enzyme inhibitor (ACEi). Expression of the membrane receptors and key enzymes in the natriuretic peptide system (NPS), renin-angiotensin-aldosterone system (RAAS) and kallikrein-kinin system (KKS) were analyzed by quantitative polymerase chain reaction (qPCR) and immunoblot assay, respectively. Protein levels of pro-arteriogenic cytokines were measured by enzyme-linked immunosorbent assay, and mitochondrial DNA copy number was assessed by qPCR due to their roles in arteriogenesis. Furthermore, murine heart endothelial cells (MHEC5-T) were treated with a neprilysin inhibitor (NEPi)

alone, or in combination with bradykinin receptor antagonists. MHEC5-T proliferation was analyzed by colorimetric assay.

Results: The *in vivo* study showed that ARNis markedly improved coronary collateral perfusion, regulated the gene expression of KKS, and increased the concentrations of relevant pro-arteriogenic cytokines. The *in vitro* study demonstrated that NEPis significantly promoted MHEC5-T proliferation, which was diminished by bradykinin receptor antagonists.

Conclusion: ARNis improve coronary collateral perfusion and exert pro-arteriogenic effects *via* the bradykinin receptor signaling pathway.

KEYWORDS

angiotensin receptor-neprilysin inhibitor, angiotensin-converting enzyme inhibitor, kallikrein-kinin system, heart failure, myocardial infarction, coronary collateral perfusion, arteriogenesis

Introduction

Heart failure (HF) is a major negative prognostic factor in patients after myocardial infarction (MI). Despite this, efforts to improve myocardial repair have not been translated into clinical therapies. Post-MI HF remains a leading cause of morbidity and mortality worldwide, and is marked by a sharply rising prevalence in the Western population over age of 75 years (1). Recently, an angiotensin receptor-neprilysin inhibitor (ARNi) was approved as a first-in-class drug for the treatment of HF in both Europe and the U.S., representing a new milestone in pharmaceutical treatment for HF (2). ARNi is a sodium supramolecular complex of a neprilysin inhibitor (NEPi) (i.e., Sacubitril) and an angiotensin receptor blocker (ARB) (i.e., Valsartan) at a 1:1 ratio. Neprilysin (NEP), also known as neutral endopeptidase, enzymatically degrades natriuretic peptides (NPs), which includes atrial natriuretic peptide (ANP), B-type natriuretic peptide (BNP), and C-type natriuretic peptide (CNP). The natriuretic peptide system (NPS) plays a key role in cardiovascular homeostasis by regulating a wide spectrum of physiological processes, such as natriuresis and vasodilation. Therefore, NEPis are used clinically to counteract the defects of NPS during the pathological process of HF (3). However, because NEP also depletes angiotensin I (Ang I) and angiotensin II (Ang II), the NEPi (Sacubitril) is combined with the ARB (Valsartan) to further reduce the Ang II-induced vasoconstriction (4). Hence, the pharmacological mechanisms of ARNis are based on augmentation of NPS and inhibition of renin-angiotensin-aldosterone system (RAAS), thereby countering the damage caused by sustained neurohormonal overactivation of RAAS and sympathetic nervous system (SNS) in chronic HF (5).

Yet, the cardiovascular hormone regulation modulated by ARNis is not limited to NPS and RAAS. Since NEP cleaves a wide range of peptides such as bradykinin (BK) and kallidin (KD), the kallikrein-kinin system (KKS) is also involved in the hormonal regulation by ARNi (**Figure 1**). KKS is a key proteolytic system regulating vascular permeability, blood pressure and collateral blood flow (6). KKS exerts its biological functions by stimulating two G protein-coupled receptors (GPCRs): bradykinin receptor 1 (BDKRB1) and bradykinin receptor 2 (BDKRB2). Notably, our group was the first to demonstrate that arteriogenesis is modulated by bradykinin receptor signaling (7). Here, arteriogenesis is defined as the remodeling and outgrowth of pre-existing collateral arteries following stenosis or occlusion. More specifically, arteriogenesis is an adaptive response that a small collateral arteriole (native collateral) converts into a larger conduit artery, thereby restoring the nutritive blood flow to ischemic area (8). Therefore, arteriogenesis is regarded as the most effective compensatory mechanism to prevent cardiovascular ischemia (9).

For decades, clinicians and scientists have focused on therapeutic arteriogenesis by investigating the pleiotropic roles of new or classical medications in this context (10). Indeed, our latest study verified that cerebral arteriogenesis can be therapeutically stimulated by an angiotensin-converting enzyme inhibitor (ACEi) through the bradykinin receptor signaling pathway (11). As the cornerstones in cardiovascular disease management, ACEis cause inhibition of angiotensin-converting enzyme (ACE, also known as kininase II). ACE not only converts Ang I to Ang II, but also degrades BK and bradykinin-(1-8) (BK1-8). Therefore, inhibition of ACE accumulates BK and BK1-8, which in turn activate the bradykinin receptors directly or indirectly (12). Interestingly, because NEP is a major kininase like ACE, it is speculated that NEPis can stabilize and activate bradykinin receptors like ACEis, thereby exerting further cardiovascular protective effects. Therefore, in

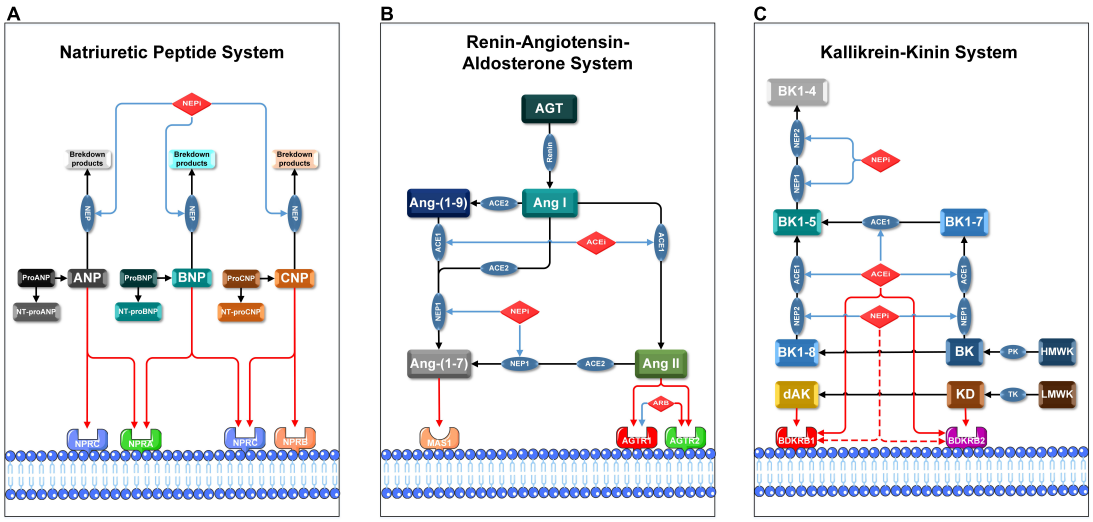

FIGURE 1
Pharmacological mechanisms of ARNis and ACEis in NPS, RAAS, and KKS. Blue lines indicate inhibitory or blocking effects, red lines indicate activating or stimulating effects, and red dashed lines indicate the hypothetical activating effects of NEPis on bradykinin receptors. AGT: angiotensinogen, Ang-(1-7): angiotensin-(1-7), Ang-(1-9): angiotensin-(1-9), BK1-4: bradykinin-(1-4), BK1-5: bradykinin-(1-5), BK1-7: bradykinin-(1-7), BK1-8: bradykinin-(1-8), dAK: des-Arg10-kallidin, HMWK: high-molecular-weight kininogen, LMWK: low-molecular-weight kininogen, NT-proANP: N-Terminal proANP, NT-proBNP: N-Terminal proBNP, NT-proCNP: N-Terminal proCNP, PK: plasma kallikrein, TK: tissue kallikrein. **(A)** Membrane receptors in NPS are NPRA, NPRB, and NPRC; key enzymes in NPS are NEP1 and NEP2. Precursor molecules of pro-ANP, pro-BNP, and pro-CNP break up into active ligands (ANP, BNP, and CNP) and corresponding inactive amino-terminal fragments (NT-proANP, NT-proBNP, and NT-proCNP), respectively. **(B)** Membrane receptors in RAAS are AGTR1, AGTR2, MAS1 proto-oncogene (MAS1); key enzymes in RAAS are ACE1 and ACE2. ACE1 converts Ang I to Ang II and subsequently activates AGTR1 and AGTR2. Either NEP1 or ACE2 converts Ang I or Ang II to Ang-(1-7), which then activates MAS1. **(C)** Membrane receptors in KKS are BDKRB1 and BDKRB2, both ACE1 and NEPs are involved in degradation of BK and KD in multiple steps. BK is cleaved by PK from HMWK, while KD is cleaved by TK from LMWK. BK and KD are the ligands of BDKRB2. BK and KD can be converted to BK1-8 and dAK, respectively. BK1-8 and dAK are the ligands of BDKRB1.

our current study, we hypothesized that coronary arteriogenesis can be therapeutically enhanced beyond its natural time course by administration of ARNis, and the putative ARNi-induced pro-arteriogenic effects are based on activation of bradykinin receptors.

To investigate the role of ARNis on coronary collateralization, a suitable animal model is needed. By conducting a repetitive occlusion procedure on the left anterior descending artery (LAD), a rat model of coronary arteriogenesis has been established successfully (**Figure 2**) (13). The current study consists of three sub-projects. (1) First, we investigated the effects of ARNis on coronary arteriogenesis by assessing collateral-dependent myocardial perfusion in a rat model. Since the ARNi is a dual-acting complex composed of a NEPi and an ARB, the effects of the ARB (Valsartan) were also investigated. (2) Second, to uncover the underlying molecular mechanism of ARNi-induced coronary arteriogenesis, we analyzed mRNA and protein expression levels of the relevant membrane receptors and key enzymes, concentrations of pro-arteriogenic cytokines and mitochondrial DNA copy number. Since ACEi-induced cerebral arteriogenesis was characterized in our recent study (11), an ACEi (Ramipril) was also investigated for coronary arteriogenesis for comparison. (3) Finally, we investigated the role of the NEPi (Sacubitril) on murine endothelial cells (ECs) proliferation, and functionally validated whether the putative NEPi-induced pro-arteriogenic effects were modulated by the bradykinin signaling pathway *in vitro*.

Materials and methods

Surgical protocol

Male Sprague-Dawley rats (300–350 g) were sedated by using ketamine (75 mg/kg; i.p.) (Wirtschaftsgenossenschaft deutscher Tierärzte eG) and xylazine (5 mg/kg; i.p.) (Bayer AG) before endotracheal intubation. Endotracheal general anesthesia was maintained during surgery by using isoflurane (1.2% in 95% O_2/5% CO_2) (CP-Pharma Handelsgesellschaft mbH).

Left-sided thoracotomy was performed to expose the rat heart. The so called "occluder" consists of a latex balloon (a micro-pneumatic snare mounted within an umbrella sheath) and a catheter, the former part was implanted on the heart wall. In brief, a 5-0 Prolene suture was tied around the proximal LAD when the latex balloon was inflated with 0.6 ml of air. The latex balloon was connected to the catheter, which was protected by a stainless steel coil and externalized between the rat's scapulae, and finally connected to an air pump machine

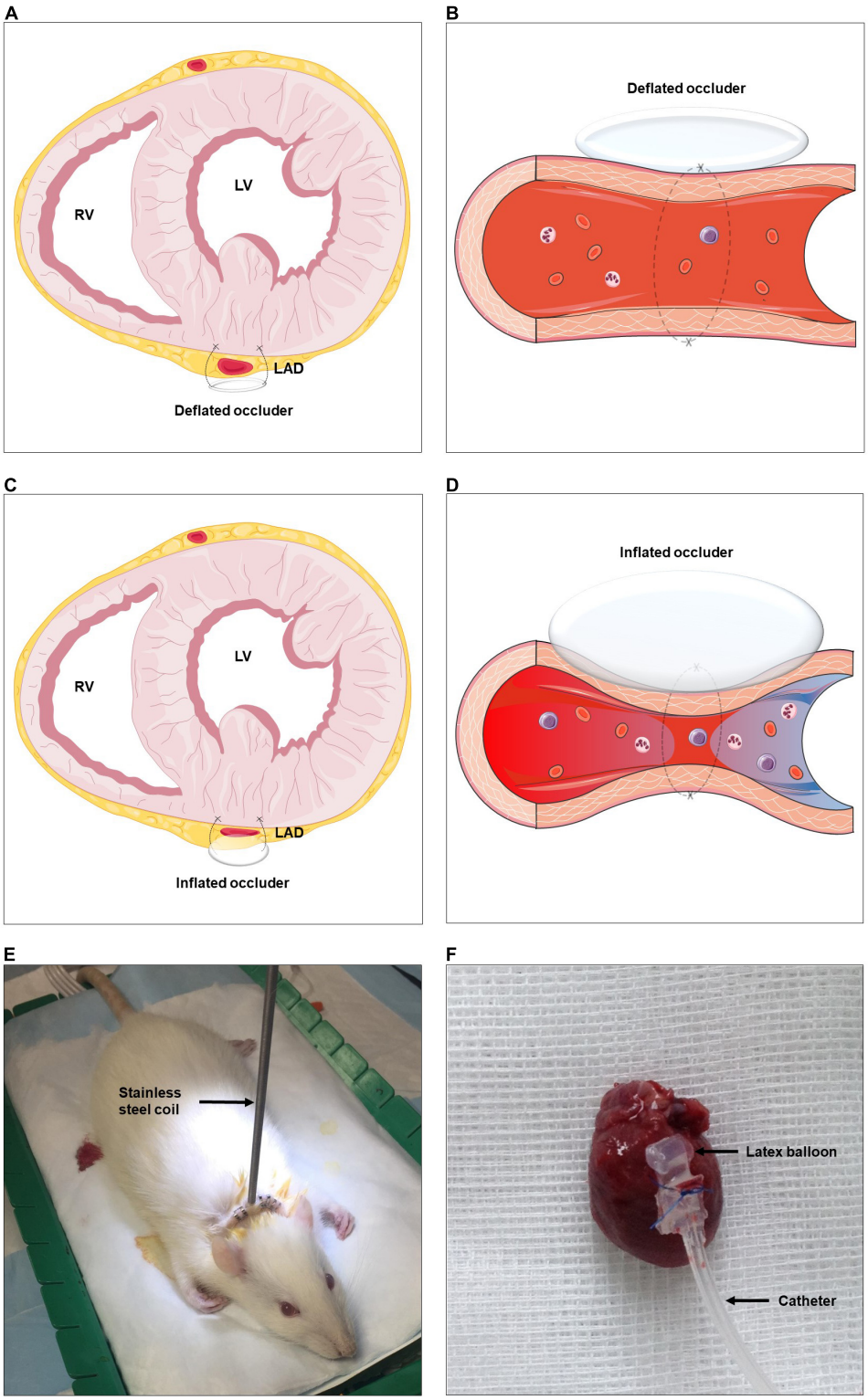

FIGURE 2
Schematic representation of rat model of coronary arteriogenesis. RV, right ventricle; LV, left ventricle; LAD, left anterior descending artery. **(A–D)** A highly flexible latex balloon catheter is fixed around the proximal LAD, compressed air is used to briefly and temporarily inflate the catheter, repetitively ligating the LAD, and thus stimulating coronary collateral development. **(E)** Established rat model with the stainless steel coil. **(F)** Sample of excised rat heart with the occluder. The figures were partly generated using Servier Medical Art, provided by Servier, licensed under a Creative Commons Attribution 3.0 unported license.

outside of the animal cage. The machine was pumping according to a relevant procedure described hereinafter and supplying air through the catheter to the latex balloon. Consequently, the LAD was cyclically blocked and unblocked during the inflation and deflation of the latex balloon (**Figure 2** and **Supplementary Video**).

Repetitive occlusion procedure

It has been verified that the repetitive occlusion of a main coronary artery is an optimal method to establish animal models of coronary arteriogenesis (13). In addition, a moderate intensity and duration of myocardial ischemia are necessary to initiate collateral development (14). The repetitive occlusion procedure (ROP) began on the next day of occluder implantation surgery. The preset ROP consists of 7 × 24-h repetitive routines, and each 24-h individual routine again consists of 3 × 8-h repetitive routines, and each 8-h individual routine again consists of a 2-h and 20-min stimulating stage and followed by a 5-h and 40-min resting stage. Further, each stimulating stage again consists of 7 × 20-min repetitive routines, and each 20-min individual routine again consists of a 40-s balloon inflation and followed by an 18-min and 20-s balloon deflation.

Microspheres–based myocardial perfusion measurement

The sensitivity and ability to measure myocardial perfusion in intact tissue using the stable isotope-labeled microspheres have been validated by comparison with the standard conventional radioactive method (15). Since the injected microspheres circulate in the blood and finally deposit in the region supplied by its corresponding artery, the deposited microsphere concentration is proportional to the blood flow. Given that the occluder was implanted around the LAD and the aim of our experiment was to evaluate coronary collateral perfusion, the LAD-dependent myocardial region distal to the occluder was referred to as the collateral dependent zone (CZ), and the left circumflex artery-dependent myocardial region was referred to as the normal zone (NZ). In order to ensure as many microspheres as possible enter the CZ, microspheres were injected rapidly during the occluder was inflated. In brief, 15 μl of 5×10^5 isotope-labeled 15 μm-diameter microspheres were injected twice into the left ventricle (LV) on Day 0 (the day of occluder implantation) (Samarium STERIspheres, BioPAL, Inc.), and Day 7 (the day of animal sacrifice) (Gold STERIspheres, BioPAL, Inc). After sacrificing, 100 mg of NZ and CZ were collected, respectively and sent to BioPAL, Inc., for further analysis.

During the measurement of microspheres-based myocardial perfusion (MMP), the microsphere activity concentration was expressed as disintegrations per minute per gram (dpm/g). Here, MMP of different myocardial regions (CZ and NZ) at different time points (Day 0 and Day 7) were recorded, respectively. Specifically, MMP of CZ at Day 0, MMP of CZ at Day 7, MMP of NZ at Day 0 and MMP of NZ at Day 7 were represented by $MMP_{CZ(D0)}$, $MMP_{CZ(D7)}$, $MMP_{NZ(D0)}$, and $MMP_{NZ(D7)}$, respectively. MMP at Day 0 was regarded as a reference at baseline, and the difference value of MMP between Day 7 and Day 0 was represented by ΔMMP. Specifically, the difference value of MMP_{CZ} between Day 7 and Day 0 was represented by ΔMMP_{CZ} $[MMP_{CZ(D7)} - MMP_{CZ(D0)}]$; similarly, the difference value of MMP_{NZ} between Day 7 and Day 0 was represented by ΔMMP_{NZ} $[MMP_{NZ(D7)} - MMP_{NZ(D0)}]$.

Animal grouping and treatment protocol

All experimental animals were randomly assigned to the following groups (n = 6–8/group): (1) SHAM group: the occluder was implanted but without any procedures of inflation or deflation for 7 days, meanwhile, distilled water (0.5 ml per day) was administrated *via* gavage. (2) ROP-Ctrl group: ROP procedure was conducted for 7 days, meanwhile, distilled water (0.5 ml per day) was administrated *via* gavage. (3). ROP+ARB group: ROP procedure was conducted for 7 days, meanwhile, Valsartan (31 mg/kg per day) (Novartis International AG) was dissolved in 0.5 ml distilled water and administrated *via* gavage. (4). ROP+ACEi group: ROP procedure was conducted for 7 days, meanwhile, Ramipril (1 mg/kg per day) (AbZ-Pharma GmbH) was dissolved in 0.5 ml distilled water and administrated *via* gavage. (5) ROP+ARNi group: ROP procedure was conducted for 7 days, meanwhile, Sacubitril/Valsartan (68 mg/kg per day) (Novartis International AG) was dissolved in 0.5 ml distilled water and administrated *via* gavage.

Analysis for mRNA expression of membrane receptors and key enzymes

Tissue samples from CZ (n = 6/group) were snap frozen and stored in liquid nitrogen before RNA isolation. Two cubic millimeter tissue from CZ was homogenized using the liquid nitrogen grinding method. Total RNA was extracted using the Trizol reagent (Thermo Fisher Scientific) in compliance with the manufacturer's instructions. Quantitative analysis of RNA was performed using the Nanodrop™ Microvolume Spectrophotometer (Thermo Fisher Scientific). 1 μg of total RNA was reverse transcribed into cDNA by using the QuantiTect Reverse Transcription Kit (QIAGEN) and the peqSTAR thermal cycler (VWR International). The obtained cDNA was diluted in 60 μl RNAse/DNAase-free water. The quantitative polymerase chain reaction (qPCR) based analysis was performed by using the LightCycler® 96 Real-Time PCR

System (Roche). Each reaction system consists of 1 μl cDNA, 1 μl of forward/reverse primer each, 7 μl RNase/DNase-free water and 10 μl PowerTrack SYBR Green Master Mix (Thermo Fisher Scientific). 40 cycles of three-step qPCR were performed, all samples were run in triplicate. All of the primers were synthesized by the Eurofins Genomics Germany GmbH, the detailed sequences of primers are showed in **Table 1**.

Immunoblot assay

Total proteins were extracted from CZ by using the Minute™ total protein extraction kit (Invent Biotechnologies). Protein samples were separated on 10% SDS-PAGE and transferred to PVDF membranes (Merck Chemicals GmbH). After incubation in 5% milk (Carl Roth GmbH) in TBST for 1 h at room temperature, membranes were incubated overnight at 4°C with diluted primary antibodies: Anti-NPR-A+NPR-B antibody (ab139188) (1:300), Anti-NEP1 antibody (ab79423) (1:1000), Anti-ACE1 antibody (ab254222) (1:1000), Anti-ACE2 antibody (ab108252) (1:200), Anti-KLK1 antibody (ab131029) (1:1000), Anti-beta Actin antibody (ab115777) (1:1000) and Anti-alpha Tubulin antibody (ab7291) (1:5000). After washing with TBST three times, membranes were incubated with 1:5000 diluted conjugated peroxidase-labeled secondary antibodies Goat Anti-Mouse IgG H&L (HRP) (ab205719) or Goat Anti-Rabbit IgG H&L (HRP) (ab205718) at room temperature for 1 h, followed by washing with TBST three times. The PVDF membrane was reacted with the Pierce™ ECL Western Blotting Substrate (Thermo Fisher Scientific) for 1 min at room temperature. After absorbing the liquid, blots were visualized by using the VWR® Imager CHEMI Premium (VWR International) system, and analyzed by using the Quantity One Software (Bio-Rad Laboratories). All the primary and secondary antibodies were purchased from Abcam. Each experiment for target protein analysis was repeated three times.

Enzyme-linked immunosorbent assay

Total proteins were extracted from CZ by using the Minute™ total protein extraction kit (Invent Biotechnologies). Quantification of total proteins was achieved by using the Pierce™ BCA™ Protein-Assay (Thermo Fisher Scientific). Measurements of protein concentrations of granulocyte-macrophage colony-stimulating factor (GM-CSF), monocyte chemoattractant protein-1 (MCP-1) and vascular endothelial growth factor (VEGF) were performed by using the Rat GM-CSF ELISA Kit (Assay Genie, RTFI00020), MCP1 (CCL2) Rat ELISA Kit (Abcam, ab100778) and VEGF Rat ELISA Kit (Abcam, ab100787), respectively. Concentrations were measured spectrophotometrically by light absorbance using the Spark multimode microplate reader (Tecan Group AG). All samples were run in triplicate. The final concentration was expressed as pg/μg total protein.

Analysis of mitochondrial DNA copy number

Two cubic millimeter tissue from LV were homogenized by using the liquid nitrogen grinding method. Genomic DNA was extracted by using the DNeasy Blood & Tissue Kit (Qiagen) according to the manufacturer's instructions. Quantitative analysis of DNA was performed using the Nanodrop™ Microvolume Spectrophotometer (Thermo Fisher Scientific). DNA was further diluted to a final concentration of 50 ng/μl. The mitochondrial copy number (mtDNA-CN) was expressed relative to a nuclear DNA specific gene proliferator-activated receptor-γ coactivator-1α (PGC-1α). Here, mtDNA-CN was calculated according to the formula: mtDNA-CN = $2 \times 2^{\Delta Ct}$, $\Delta CT = CT_{PGC-1\alpha} - CT_{mtDNA}$. 60 cycles of a two-step qPCR were performed.

Cell culture and treatment

Murine heart endothelial cells (MHEC5-T) (Leibniz Institute DSMZ-German Collection of Microorganisms and Cell Cultures GmbH) were grown in RPMI 1640 medium (Thermo Fisher Scientific) containing 10% fetal bovine serum (Sigma-Aldrich Chemie GmbH). Cells were treated with 0.01, 0.1, 1, 10, and 20 μM of the compounds as follows: Ramipril (ACEi) (Sigma-Aldrich Chemie GmbH), Valsartan (ARB) (Sigma-Aldrich Chemie GmbH), Sacubitril calcium salt (NEPi) (Sigma-Aldrich Chemie GmbH), Valsartan and Sacubitril calcium salt (ARNi), R715 [antagonist of BDKRB1 (BDKRB1i)] (Tocris Bioscience) and HOE 140 [antagonist of BDKRB2 (BDKRB2i)] (Enzo Life Sciences GmbH) to determine the optimal concentration.

Cell proliferation assay

MHEC5-T were cultured in a 96-well plate with 4000 cells per well. After 4 h attachment, cells were cultured in RPMI-1640 medium alone as control or containing 0.01 μM Ramipril (ACEi), 0.01 μM Ramipril and 0.01 μM R715 (ACEi + BDKRB1i), 0.01 μM Ramipril and 0.01 μM HOE 140 (ACEi + BDKRB2i), 0.01 μM Ramipril, 0.01 μM R715 and 0.01 μM HOE 140 (ACEi + BDKRB1i + BDKRB2i); 0.01 μM Sacubitril calcium salt (NEPi), 0.01 μM Sacubitril calcium salt + 0.01 μM R715 (NEPi + BDKRB1i), 0.01 μM Sacubitril calcium salt and 0.01 μM HOE 140 (NEPi + BDKRB2i), 0.01 μM Sacubitril calcium salt, 0.01 μM R715 and 0.01 μM HOE 140 (NEPi + BDKRB1i + BDKRB2i). Cell proliferation was assessed by using the WST-1 Assay Kit (Cell Proliferation) (Abcam) according to the manufacturer's instructions. Absorbance was spectrophotometrically measured at 450 nm by using the Spark multimode microplate reader (Tecan Group AG), and expressed as optical density (O.D.).

TABLE 1 List of qPCR primers sequences.

Gene	Accession no.	Forward	Reverse
NPRA	NM_012613.1	CCTTTCAGGCTGCCAAAAT	ATCCTCCACGGTGAAGTTGA
NPRB	NM_053838.1	TCTATGCCAAGAAGCTGTGG	CCAGGCCTTCCAAGTAGAAA
NPRC	NM_012868.1	TGACACCATTCGGAGAATCA	CATCTCCGTAAGAAGAACTGTTGA
NEP1	NM_012608.2	GGATCTTGTAAGCAGCCTCAGC	AGTTGGCACACCGTCTCCAG
NEP2	NM_001107997.1	AAGGCGGCAGAGACCAGAGAC	CTTGATGGACTGGATGGCGAACTC
AGTR1a	NM_030985.4	GCTTCAACCTCTACGCCAGTGTG	CGAGACTTCATTGGGTGGACGATG
AGTR2	NM_012494.3	TAGTCTCTCTCTTGCCTTGG	CTGACCTTCTTGGATGCTCT
MAS1	NM_012757.2	TGACAGCCATCAGTGTGGAGA	GCATGAAAGTGCCCACAGGA
ACE1	NM_012544.1	GACGGAAGCATCACCAAGGAGAAC	CTAGGCACTGGAGGGCAGAGAC
ACE2	NM_001012006.1	AAGCCACCTTACGAGCCTCCTG	ACAATGCCAACCACTACCGTTCC
BDKRB1	NM_030851.1	CCAAGACAGCAGTCACCATCAA	CAGCAGGTCCCAGTCTTCTAG
BDKRB2	M59967.2	ATCACCATCGCCAATAACTTCGA	CACCACGCGGCACAG
KLK1	NM_012593.1	GGAGAGTTGGAAGGAGGCAAAGAC	TTGGTGTAGATGGCTGGCATGTTG
KLK10	NM_001004100.1	TCCAGAGCGAGCAACTGAGGTC	GTCGTGTTCATCTGAGCGGAGTG
GAPDH	NM_017008	AGACAGCCGCATCTTCTTGT	CTTGCCGTGGGTAGAGTCAT
18S	X00686	TCAACTTTCGATGGTAGTCGCCGT	TCCTTGGATGTGGTAGCCGTTTCT
mtDNA	NC_001665.2	ACACCAAAAGGACGAACCTG	ATGGGGAAGAAGCCCTAGAA
PGC-1α	NM_031347.1	ATGAATGCAGCGGTCTTAGC	AACAATGGCAGGGTTTGTTC

Statistical analysis

All statistical analyses were performed by using IBM SPSS 26 or Graphpad prism 9. Relative mRNA expression fold change and mtDNA-CN were given as mean ± standard error of the mean (SEM), other parameters were given as mean ± standard deviation (SD). Kolmogorov–Smirnov test was performed to analyze the distribution of quantitative variables. Normally distributed data (ΔMMP, protein expression levels, O.D. values of cytokines concentrations and cell proliferation) were analyzed by one-way analysis of variance (Fisher's protected least significant difference test), abnormally distributed data (Relative mRNA expression fold change and mtDNA-CN) were analyzed by Kruskal–Wallis test. Comparison of MMP between Day 0 and Day 7 was performed using a paired *t*-test. *P*-values less than 0.05 ($\leq$0.05) were considered to be statistically significant.

Results

Angiotensin receptor-neprilysin inhibitors markedly improve coronary collateral perfusion

First, $MMP_{CZ(D7)}$ was significantly higher than $MMP_{CZ(D0)}$ in all ROP groups, but it was unchanged in the SHAM group (**Figure 3A** and **Table 2**). Moreover, ΔMMP_{CZ} in all ROP groups were significantly greater than in the SHAM group. In addition, ΔMMP_{CZ} in the ROP+ARNi group was significantly greater than in the ROP-Ctrl group and ROP+ARB group. Although ΔMMP_{CZ} in the ROP+ARB group was significantly greater than in the SHAM group, it remained unchanged when compared with the ROP-Ctrl group (**Figure 3B** and **Table 2**). In contrast, $MMP_{NZ(D7)}$ was unchanged compared with $MMP_{NZ(D0)}$ in all groups (**Figure 3A**). With regard to ΔMMP_{NZ}, no significant difference was detected between all groups (**Table 2**).

Angiotensin receptor-neprilysin inhibitors regulate natriuretic peptide system, renin-angiotensin-aldosterone system, and kallikrein-kinin system

mRNA and protein expression levels of the membrane receptors and key enzymes in NPS, RAAS, and KKS were analyzed, respectively (**Figure 1**). With regard to NPS, results showed that the mRNA expression levels of natriuretic peptide A receptor (NPRA), natriuretic peptide B receptor (NPRB) and natriuretic peptide C receptor (NPRC) in the ROP+ARNi group were highest among all groups, but these results were statistically non-significant. The mRNA expression levels of neprilysin-1 (NEP1) in the ROP+ACEi group (0.60-fold ± 0.06) were significantly lower than in the SHAM group (1.00-fold ± 0.19)

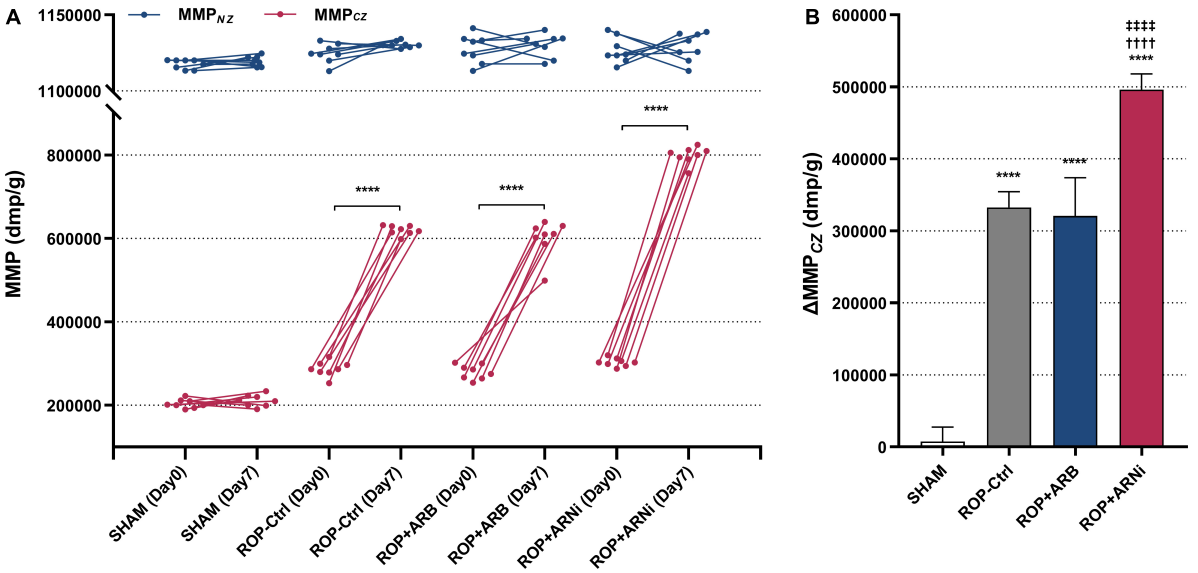

FIGURE 3
Measurement of myocardial collateral perfusion. MMP, microspheres-based myocardial perfusion; MMP$_{CZ}$, MMP of CZ; MMP$_{NZ}$, MMP of NZ; ΔMMP$_{CZ}$, difference value of MMP$_{CZ}$ at Day 7 and Day 0. **(A)** Microspheres-based myocardial perfusion at Day 0 and Day 7. Blue lines indicate changes of MMP$_{NZ}$ from Day 0 to Day 7, red lines indicate the changes of MMP$_{CZ}$ from Day 0 to Day 7. $^{****}P \leq 0.0001$, compared to Day 0. **(B)** Difference value of MMP$_{CZ}$ among groups. $^{****}P \leq 0.0001$, compared to SHAM, $^{††††}P \leq 0.0001$, compared to ROP-Ctrl, $^{‡‡‡‡}P \leq 0.0001$, compared to ROP+ARB.

TABLE 2 Measurement of the coronary collateral perfusion.

Group	MMP$_{CZ(D0)}$ (dmp/g)	MMP$_{CZ(D7)}$ (dmp/g)	Δ MMP$_{CZ}$ (dmp/g)	MMP$_{NZ(D0)}$ (dmp/g)	MMP$_{NZ(D7)}$ (dmp/g)	Δ MMP$_{NZ}$ (dmp/g)
SHAM	203626 ± 10391	211218 ± 14218	7591 ± 19957	1117493 ± 3072	1119576 ± 3299	2084 ± 4451
ROP-Ctrl	287118 ± 18279	619780 ± 11321$^{####}$	332663 ± 21728****	1124653 ± 6334	1130470 ± 2118	5818 ± 6984
ROP+ARB	279846 ± 17332	600495 ± 44262$^{####}$	320649 ± 53317****	1127521 ± 9373	1130063 ± 7646	2541 ± 11744
ROP+ARNi	303161 ± 10094	799348 ± 20406$^{####}$	496186 ± 21723****††††‡‡‡‡	1126644 ± 8494	1128854 ± 9321	2210 ± 16523

MMP, microspheres-based myocardial perfusion; MMP$_{CZ(D0)}$, MMP of CZ at Day 0; MMP$_{CZ(D7)}$, MMP of CZ at Day 7; ΔMMP$_{CZ}$, difference value between MMP$_{CZ(D7)}$ and MMP$_{CZ(D0)}$; MMP$_{NZ(D0)}$, MMP of NZ at Day 0; MMP$_{NZ(D7)}$, MMP of NZ at Day 7; ΔMMP$_{NZ}$, difference value between MMP$_{NZ(D7)}$ and MMP$_{NZ(D0)}$. $^{####}P \leq 0.0001$, compared to Day 0, $^{****}P \leq 0.0001$, compared to SHAM, $^{††††}P \leq 0.0001$, compared to ROP-Ctrl, $^{‡‡‡‡}P \leq 0.0001$, compared to ROP+ARB.

(P = 0.0372). In addition, the mRNA expression levels of neprilysin-2 (NEP2) in the ROP+ARNi group (0.45-fold ± 0.06) were significantly lower than in the SHAM group (1.00-fold ± 0.28) (P = 0.0275) and the ROP+ACEi group (1.04-fold ± 0.18) (P = 0.0052) (**Figure 4A**). Moreover, results from immunoblot assay indicated that the protein expression levels of NPRA + NPRB were unchanged between all groups. However, the protein expression levels of NEP1 in the ROP+ACEi group (0.42-fold ± 0.18) were significantly lower than in the SHAM group (1.00-fold ± 0.38) (P = 0.0023), ROP-Ctrl group (0.75-fold ± 0.18) (P = 0.0489), and ROP+ARNi group (1.11-fold ± 0.25) (P = 0.0004), respectively (**Figures 4D, E**).

With regard to RAAS, results showed that the mRNA expression levels of angiotensin II receptor type 1a (AGTR1a) in either the ROP+ACEi group or the ROP+ARNi group were higher than in the ROP-Ctrl group, but no significant differences were detected. In contrast, the mRNA expression levels of angiotensin II receptor type 2 (AGTR2) in the ROP+ARNi group (0.29-fold ± 0.17) were significantly lower than in the ROP-Ctrl group (0.90-fold ± 0.42) (P = 0.0412). In consequence, the relative mRNA expression ratios of AGTR1a/AGTR2 in the ROP+ARNi group were highest among all groups. In addition, the mRNA expression levels of angiotensin converting enzyme 1 (ACE1) in the ROP+ACEi group (3.00-fold ± 0.81) were significantly higher than in the ROP-Ctrl group (0.63-fold ± 0.17) (P = 0.0037) and in the SHAM group (1.00-fold ± 0.22) (P = 0.0275). Moreover, ACE1 mRNA expression levels were also significantly higher in the ROP+ARNi group (2.84-fold ± 0.59) compared with the ROP-Ctrl group (P = 0.0033) and the SHAM group (P = 0.0247). Similarly, the mRNA expression levels of angiotensin converting enzyme 2 (ACE2) in the ROP+ACEi

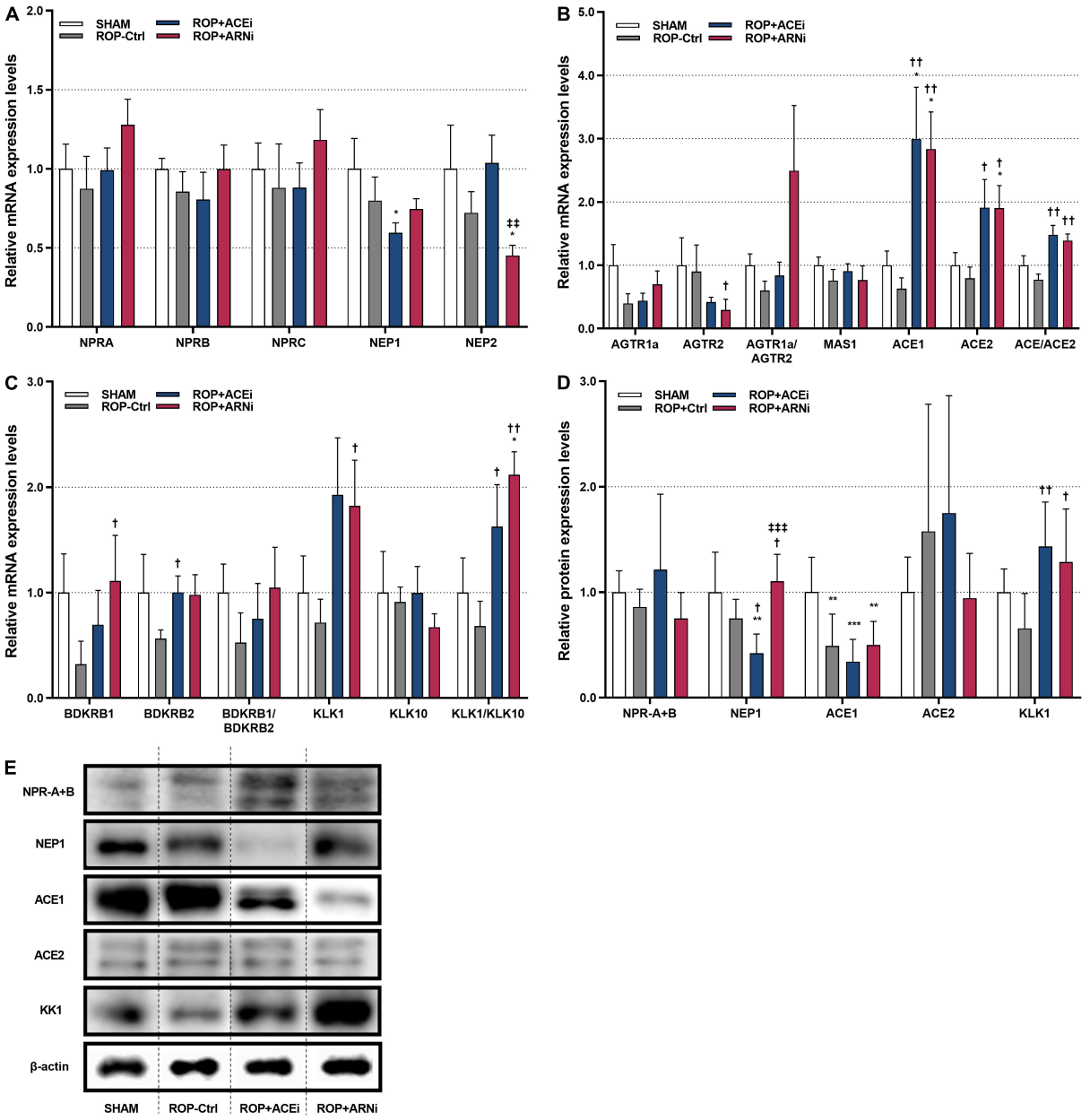

FIGURE 4
Molecular and biochemical quantification of target molecules of NPS, RAAS, and KKS. **(A)** Relative mRNA expression levels of membrane receptors and key enzymes in NPS. **(B)** Relative mRNA expression levels of membrane receptors and key enzymes in RAAS. **(C)** Relative mRNA expression levels of membrane receptors and key enzymes in KKS. **(D,E)** Relative protein expression levels of target molecules. **(A–C)** Data were given as mean ± standard error of the mean (SEM) and presented here as $2^{-\Delta CT}$ values and normalized against SHAM. $^{*}P \leq 0.05$, $^{**}P \leq 0.01$, $^{***}P \leq 0.001$, compared to SHAM. $^{\dagger}P \leq 0.05$, $^{\dagger\dagger}P \leq 0.01$, compared to ROP-Ctrl. $^{\ddagger\ddagger}P \leq 0.01$, $^{\ddagger\ddagger\ddagger}P \leq 0.001$, compared to ROP+ACEi.

group (1.91-fold ± 0.44) were significantly higher than in the ROP-Ctrl (0.79-fold ± 0.18) (P = 0.0373). Besides, ACE2 mRNA expression levels were significantly higher in the ROP+ARNi group (1.91-fold ± 0.36) compared with the SHAM group (1.00-fold ± 0.20) (P = 0.0373) and the ROP-Ctrl group (P = 0.0143). As a consequence, the relative mRNA expression ratios of ACE1/ACE2 in either the ROP+ACEi group (1.48-fold ± 0.15) (P = 0.0017) or the ROP+ARNi group (1.39-fold ± 0.11) (P = 0.0023) were significantly higher than in the ROP-Ctrl group (0.77-fold ± 0.09) (**Figure 4B**). Moreover, the protein expression levels of ACE1 in the SHAM group (1.00-fold ± 0.33) were significantly higher than in the ROP-Ctrl group (0.49-fold ± 0.30) (P = 0.0058), ROP+ACEi group (0.34-fold ± 0.21) (P = 0.0008), and

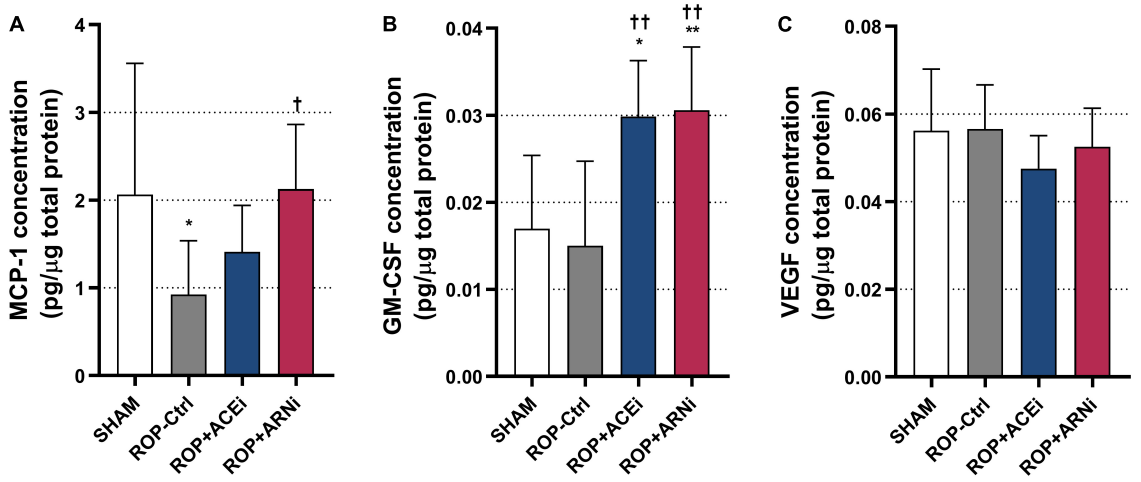

FIGURE 5
Analysis of pro-arteriogenic cytokines. **(A–C)** Protein concentrations of pro-arteriogenic cytokines. $^{*}P \leq 0.05$, $^{**}P \leq 0.01$, compared to SHAM. $^{\dagger}P \leq 0.05$, $^{\dagger\dagger}P \leq 0.01$, compared to ROP-Ctrl.

the ROP+ARNi group (0.50-fold ± 0.22) (P = 0.0086), respectively (Figures 4D, E).

Finally, with regard to KKS, the mRNA expression levels of BDKRB1 in the ROP+ARNi group (1.11-fold ± 0.43) were significantly higher than in the ROP-Ctrl group (0.32-fold ± 0.22) (P = 0.0367). BDKRB1 mRNA expression levels were also higher in the ROP+ACEi group compared with the ROP-Ctrl group, but the results were without any statistical significance. In addition, the mRNA expression levels of BDKRB2 in the ROP+ACEi group (1.00-fold ± 0.15) were significantly higher than in the ROP-Ctrl group (0.56-fold ± 0.08) (P = 0.0453). BDKRB2 mRNA expression levels were slightly higher in the ROP+ARNi group compared with the ROP-Ctrl group. In addition, the relative mRNA expression ratios of BDKRB1/BDKRB2 in either the ROP+ACEi group or the ROP+ARNi group were higher than in the ROP-Ctrl group, but no statistical significance was reached. Moreover, the mRNA expression levels of kallikrein 1 (KLK1) in the ROP+ARNi group (1.82-fold ± 0.43) were significantly higher than in the ROP-Ctrl group (0.72-fold ± 0.22) (P = 0.0500). In addition, the mRNA expression levels of kallikrein 10 (KLK10) were unchanged between all groups. As a consequence, the relative mRNA expression ratios of KLK1/KLK10 in the ROP+ACEi group (1.63-fold ± 0.40) were significantly higher than in the ROP-Ctrl group (0.68-fold ± 0.24) (P = 0.0275). The KLK1/KLK10 mRNA expression ratios were also significantly higher in the ROP+ARNi group (2.12-fold ± 0.22) compared with the SHAM group (1.00-fold ± 0.33) (P = 0.0412) and the ROP-Ctrl group (P = 0.0019) (Figure 4C). Furthermore, the protein expression levels of KLK1 in both the ROP+ACEi group (1.43-fold ± 0.42) (P = 0.0043) and the ROP+ARNi group (1.29-fold ± 0.50) (P = 0.0165) were higher than in the ROP-Ctrl group (0.66-fold ± 0.33) (Figures 4D, E).

Angiotensin receptor-neprilysin inhibitors increase pro-arteriogenic cytokines concentrations

MCP-1 concentration in the ROP+ARNi group (2.13 ± 0.74 pg/μg total protein) was significantly higher than in the ROP-Ctrl group (0.92 ± 0.61 pg/μg total protein) (P = 0.0359). Moreover, MCP-1 concentration in the ROP-Ctrl group was markedly lower than in the SHAM group (2.06 ± 1.50 pg/μg total protein) (P = 0.0457) (Figure 5A). In addition, GM-CSF concentration in the ROP+ACEi group (0.0299 ± 0.0064 pg/μg total protein) was significantly higher than in the SHAM group (0.0170 ± 0.0084 pg/μg total protein) (P = 0.0116) and the ROP-Ctrl group (0.0150 ± 0.0097 pg/μg total protein) (P = 0.0045). GM-CSF concentration was significantly higher in the ROP+ARNi (0.0306 ± 0.0072 pg/μg total protein) compared with the SHAM group (P = 0.0081) and ROP-Ctrl (P = 0.0031) (Figure 5B). Regarding VEGF concentration, results showed that there was no statistical significance between all groups (Figure 5C).

Angiotensin receptor-neprilysin inhibitors hardly affect mitochondrial genome synthesis

mtDNA-CN in either the ROP+ACEi group (0.73-fold ± 0.07) or the ROP+ARNi group (0.77-fold ± 0.12) was slightly lower than in either the SHAM group (1.00-fold ± 0.10) or the ROP-Ctrl (0.98-fold ± 0.11), however, these results were not statistically significant.

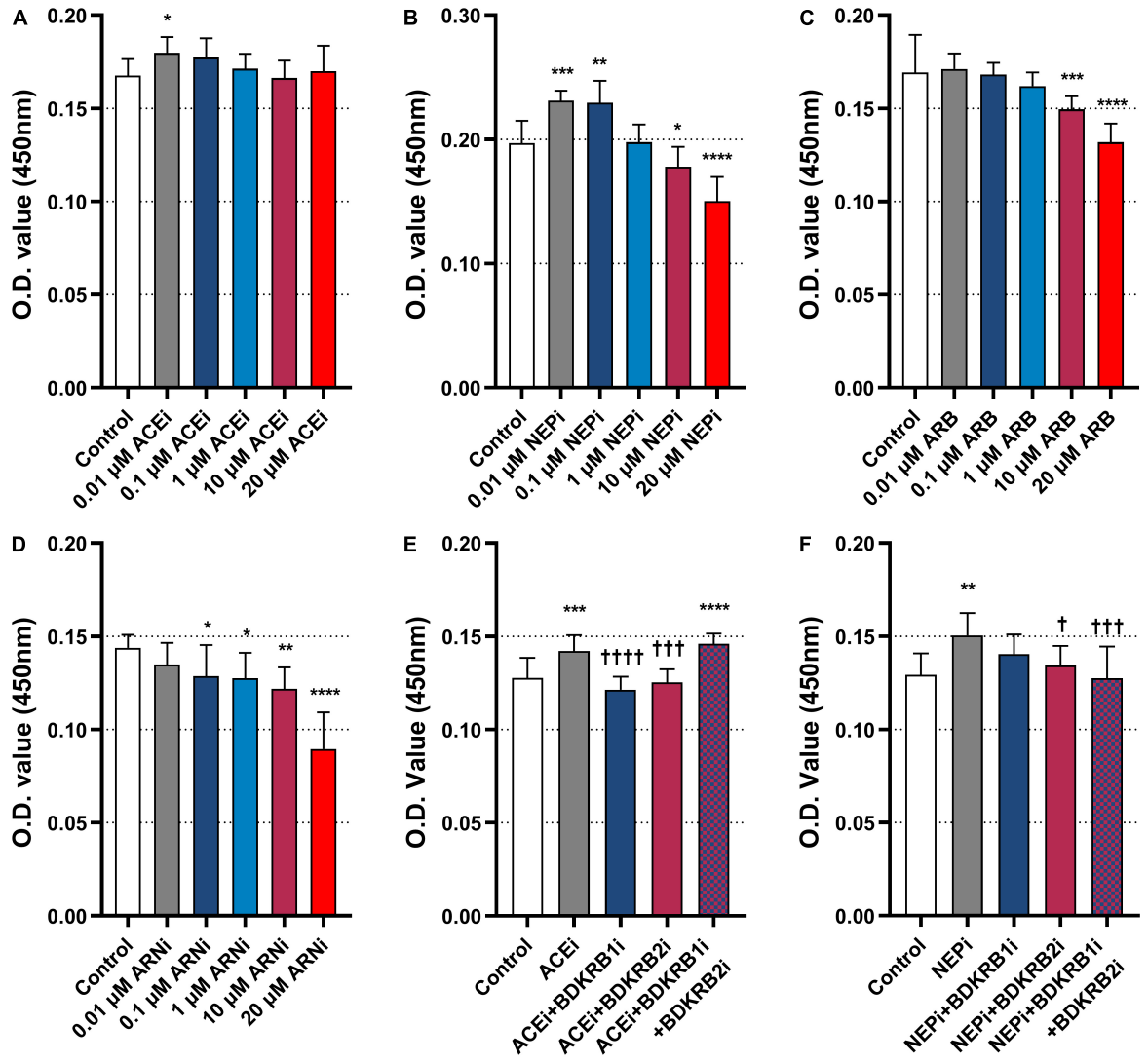

FIGURE 6
Effects of ACEi, NEPi, ARB, ARNi, and antagonists of bradykinin receptors on MHEC5-T proliferation. **(A–D)** Effects of ACEi, NEPi, ARB, ARNi on MHEC5-T proliferation at different concentrations, $^{*}P \leq 0.05$, $^{**}P \leq 0.01$, $^{***}P \leq 0.001$, $^{****}P \leq 0.0001$, compared to control. **(E)** Effects of ACEi and antagonists of bradykinin receptors on MHEC5-T proliferation. $^{***}P \leq 0.001$, $^{****}P \leq 0.0001$, compared to control. $^{\dagger\dagger\dagger}P \leq 0.001$, $^{\dagger\dagger\dagger\dagger}P \leq 0.0001$, compared to ACEi. **(F)** Effects of NEPi and antagonists of bradykinin receptors on MHEC5-T proliferation. $^{**}P \leq 0.01$, compared to control. $^{\dagger}P \leq 0.05$, $^{\dagger\dagger\dagger}P \leq 0.001$, compared to NEPi.

Neprilysin inhibitors exert pro-arteriogenic effects through the bradykinin receptor signaling pathway

In vitro experiments were performed to investigate the roles of ACEis, ARBs, NEPis, and ARNis on MHEC5-T proliferation. The results showed that 0.01 μM ACEi (0.1797 ± 0.0086) significantly promoted cell proliferation compared with the control (0.1677 ± 0.0088) ($P = 0.0196$) (Figure 6A). Similarly, both 0.01 μM NEPi (0.2311 ± 0.0080) ($P = 0.0009$) and 0.1 μM NEPi (0.2294 ± 0.0177) ($P = 0.0014$) significantly promoted cell proliferation compared with the control (0.1969 ± 0.0180) (Figure 6B). In contrast, both 10 μM ARB (0.1495 ± 0.0069) ($P = 0.0008$) and 20 μM ARB (0.1318 ± 0.0101) ($P < 0.0001$) significantly inhibited cell proliferation compared with the control (0.1693 ± 0.0202) (Figure 6C). Moreover, ARNi (NEPi + ARB) significantly inhibited cell proliferation in a concentration-dependent manner from 0.01 to 20 μM (Figure 6D).

Then, we functionally validated whether the pro-arteriogenic effects of ACEis and ARNis were mediated through the bradykinin signaling pathway. The results showed that ACEi (0.1421 ± 0.0086) significantly promoted cell proliferation compared with control (0.1276 ± 0.0109)

(P = 0.0010). In contrast, ACEi in combination with BDKRB1i (0.1213 ± 0.0070) (P < 0.0001) or BDKRB2i (0.1254 ± 0.0069) (P = 0.0002) significantly inhibited cell proliferation compared with ACEi alone. However, ACEi in combination with BDKRB1i and BDKRB2i (0.1460 ± 0.0055) showed a markedly increased cell proliferation when compared with control (P = 0.0001) (**Figure 6E**). Furthermore, NEPi (0.1505 ± 0.0119) significantly promoted cell proliferation compared with control (0.1294 ± 0.0115) (P = 0.0018). In contrast, NEPi in combination with BDKRB2i (0.1344 ± 0.0105) (P = 0.0141), or NEPi in combination with BDKRB1i and BDKRB2i (0.1276 ± 0.0169) (P = 0.0008) significantly inhibited cell proliferation compared with NEPi alone (**Figure 6F**).

Discussion

In case of coronary occlusion, collateral growth is the most efficient compensatory mechanism to adequately supply blood to ischemic myocardium. This study demonstrated for the first time that ARNis significantly improve coronary collateral perfusion *in vivo*. Furthermore, we demonstrated that NEPis exert pro-arteriogenic efforts *via* the bradykinin receptor signaling pathway *in vitro*.

In our current research, we validated again that ROP is an ideal approach to stimulate coronary collateral growth. Most importantly, administration of 7-day ROP+ARNi significantly increased coronary collateral perfusion compared with ROP alone. In contrast, ROP+ARB had no effect on coronary collateral perfusion. Thus, we confirmed that the ARNi induced improvement in coronary collateral perfusion was due to the NEPi (Sacubitril), rather than the ARB (Valsartan). This result is consistent with our most recent study, in which a beneficial effect of an ARB (Candesartan) on cerebral collateral blood flow was not observed (11).

Neprilysin degrades both BK and NPs, and there is overwhelming evidence that both BK and NPs are the most potent endogenous vasodilators modulating coronary blood flow (CBF). It has been well documented that exogenous BK increased CBF in a dose-dependent manner (16), while NPs enhanced coronary artery dilation and increased coronary flow velocity (17, 18). The results presented here were obtained in an established rat model of coronary arteriogenesis. Hence, the improvement in myocardial perfusion was clearly the result of chronic remodeling of the coronary collateral arteries rather than a transient regulation of vascular tone. BK and NPs exert their biological functions by binding bradykinin receptors and natriuretic peptide receptors, respectively. Indeed, increasing evidence suggests that both bradykinin receptors and natriuretic peptide receptors play critical role in collateral artery development (7, 19, 20).

Therefore, in the second part, by analyzing the relevant membrane receptors and key enzymes in NPS, RAAS and KKS, we aimed to understand the underlying molecular mechanism and cross-talk in these three hormonal systems under the administration of ACEis or ARNis. First, NPS is the most prevalent system regulated by ARNis. Hence, we analyzed three major membrane receptors (NPRA, NPRB, NPRC) in NPS, and the results showed that their mRNA expression levels were highest in the ROP+ARNi group among all groups, but a statistical significance was not confirmed. NEP1 is one of the key degradative enzymes in NPS. Our results showed that ACEis, but not ARNis, significantly inhibited NEP1 expression at both mRNA and protein expression levels. Yet, ARNis significantly inhibited the mRNA expression levels of NEP2. Currently, there are no specific studies that clarify the effect of ACEis on the NEP family. However, Pare et al. analyzed the candidate genes associated with ACEi-induced angioedema in a genome-wide study, and the results showed that NEP variants were likely involved in ACEi-induced immunoregulation (21), which may explain the putative ACEi-modulated downregulation of NEP1 mRNA expression observed in our study. Regarding NEP2, Bland et al. demonstrated a high expression of NEP2 in the soluble melanogaster embryo fraction (22). Our previous *in vivo* study also demonstrated that embryonic stage is the most critical phase for arterial identity (23). To date, however, little is known about NEP2 in the context of vascular adaptations.

Second, with respect to RAAS, the main membrane receptors are AGTR1a (AGTR1 consists of AGTR1a and AGTR1b, the first subunit is strongly expressed in the heart) and AGTR2 (24). Our results showed that ARNis significantly downregulated AGTR2 mRNA expression and led to an upregulation of the AGTR1a/AGTR2 ratio. In principle both Ang I and Ang II are cleaved by NEP, so inhibition of NEP increases their concentrations in the circulation system. Indeed, it was reported that NEPis increased blood pressure in normotensive subjects (25), which was identified as an Ang II-dependent effect (26). Although both AGTR1 and AGTR2 have the similar binding affinity for Ang II, they exert opposite biological functions in cardiovascular homeostasis (27). However, an imbalance of the AGTR1/AGTR2 ratio should be theoretically reversed when the ARB (Valsartan) is combined with the NEPi (Sacubitril). In this regard, numerous studies have shown that the cardiovascular protective function of ARBs was partly due to the enhancement of the biological effect of AGTR2 (28). In addition, recent preclinical studies indeed demonstrated that ARNis downregulated AGTR1 expression but upregulated AGTR2 expression at the transcriptional level (29, 30), which are in contrast to our finding. Here, the underlying mechanism is still not clear.

With regard to the key enzymes in RAAS, our results showed that the mRNA expression levels of both ACE1 and ACE2 were upregulated under the administration of either ACEis or ARNis, and a greatly increased ACE1/ACE2 ratio was observed. Indeed, early in the development of ACEis, it was reported that administration of ACEis upregulated ACE mRNA (31, 32),

which was considered as a negative feedback effect of inhibited ACE activity and decreased Ang II levels (33). However, studies subsequently reported that ACEis decreased ACE1 mRNA expression but increased ACE2 (34, 35). It is now generally accepted that ACE2 converts Ang II to Ang-(1-7), which is a potent vasodepressor that counteracts the vasopressor Ang II. Therefore, ACEis exert an important cardiovascular protective function by regulating the imbalance of the ACE1/ACE2 ratio (36). In contrast, Emilsson et al. recently reported that ACEis even increased serum protein levels of ACE1, whereas ACE2 levels remained unchanged (37). Still, the roles of ACEis and ARNis on ACEs expression in this context remain controversial.

Third, to verify our hypothesis that ARNis functionally activate KKS like ACEis, we analyzed the mRNA expression of bradykinin receptors and two members of the tissue kallikrein family. Our results showed that the gene expression of bradykinin receptors was modulated by both ARNis and ACEis. Notably, an upregulated mRNA expression of BDKRB1 was observed in the ROP+ARNi group, while an upregulated mRNA expression of BDKRB2 was observed in the ROP+ACEi group, respectively.

The mechanism of ACEis on bradykinin receptor activation has been intensively investigated in numerous studies. In summary, as agonists, ACEis directly active BDKRB1 by binding the zinc finger motif of the second extracellular loop. As allosteric enhancers, ACEis indirectly resensitize BDKRB2 by altering the conformation of ACE domains of the ACE-BDKRB2 receptor heterodimer. Here, the possible molecular mechanisms of NEPis on bradykinin receptor activation seem conceivable. First, inhibition of NEP leads to increased BK concentration levels, which thereby stabilizing and activing BDKRB1 and BDKRB2. Second, it is speculated that NEP may also associate with BDKRB2 to form a "NEP-BDKRB2 heterodimer," thereby enhancing peptide ligand binding and activating BDKRB2 (38). Intriguingly, it has been reported that NEP was much more responsible for kininase function (68 $\pm$ 2%) than ACE (9 $\pm$ 0.4%) in the murine kidney (39). If NEP has a stronger effect on BK degradation than ACE in the heart, we speculate that NEPis may be more efficient than ACEis to stimulate coronary arteriogenesis therapeutically in ischemic cardiovascular disease, and likely through the bradykinin receptor signaling pathway.

Previous research demonstrated that NEPis could augment the beneficial effect of KKS by particularly stimulating BDKRB2. Ura et al. reported that NEPi-induced increase in renal kinin levels were blocked by the BDKRB2 antagonist (HOE140) (40). In addition, Deddish et al. demonstrated that NEPis resensitized BDKRB2 in human pulmonary fibroblasts (38). However, in our current study, only an upregulated BDKRB1 mRNA expression was detected under the administration of ARNi, suggesting that BDKRB1 plays a greater role than BDKRB2 in ARNi-induced arteriogenesis. Indeed, we previously observed a large reduction in peripheral arteriogenesis in BDKRB1 knock out mice, and a minor reduction in BDKRB2 knock out mice (7). Therefore, BDKRB1 can be regarded as a novel pro-arteriogenic therapeutic target in GPCR drug discovery.

Furthermore, our work showed that both ACEis and ARNis regulated gene expression of the kallikreins, KLK1 and KLK10. KLK1 converts low-molecular-weight kininogen (LMWK) to KD. KD is the ligand of BDKRB2, which is known to exert numerous biological processes implicated in vascular growth (41). In contrast, several studies concluded that KLK10 is a tumor suppressor gene, which is a major modulator of inhibition of vascular cell proliferation and migration (42, 43). Theoretically, downregulation of KLK10 mRNA levels could be associated with vascular cell proliferation and migration, which are the prerequisites of arteriogenesis. Therefore, we considered the mRNA expression ratio of KLK1/KLK10 as a pro-arteriogenic indicator. Here, our results showed for the first time that both ACEis and ARNis significantly upregulated this pro-arteriogenic ratio. In addition, our results also showed that both ACEis and ARNis upregulated KLK1 at the translational level.

Many research has been made regarding the expression ratio of AGTR1/AGTR2, ACE1/ACE2, and BDKRB1/BDKRB2 (44–46). Upregulation or imbalance of these ratios was considered a hallmark of cardiac decompensation and arterial inflammation. Most investigators attributed the pharmacological benefits of ACEis or ARBs to rebalancing of these ratios (34). However, arteriogenesis is a process in which immune activation and inflammatory activation play crucial roles. In particular, leukocyte extravasation is triggered after arterial occlusion. Subsequently, monocytes adhere and transmigrate across vascular endothelium, and differentiate into macrophages, which release numerous cytokines (e.g., GM-CSF, MCP-1, and VEGF). These pro-arteriogenic cytokines significantly promote ECs proliferation *via* the paracrine signaling processes (47). In summary, at the mechanistic level, there are both beneficial and adverse effects of ACEis and ARNis therapy, but ultimately the beneficial effects predominate, leading to improved collateral formation.

Because paracrine factors play a critical role in arteriogenesis, we analyzed whether administration of ACEis or ARNis would result in therapeutic modulation of three main pro-inflammatory cytokines at the protein level. Our results suggested that the pro-arteriogenic cytokines were strongly induced during therapeutic modulation of arteriogenesis. Here, we demonstrated that ARNis, but not ACEis, significantly increased MCP-1 concentration, and that both ACEis and ARNis increased GM-CSF concentration. It has been reported that MCP-1 plays an important role in monocyte/macrophage activation, and that GM-CSF stimulates the release of pluripotent monocyte cells from the bone marrow into the collateral circulation (48–50). The therapeutic and pro-arteriogenic roles of GM-CSF and granulocyte colony-stimulating factor (G-CSF) have been demonstrated in a

variety of animal models of coronary, cerebral, and peripheral arteriogenesis, respectively (13, 51, 52). Yet, a modulation of VEGF at the protein level by ACEis or ARNis was not confirmed in our current study.

Vascular regeneration can be regarded as a plastic process, in which physiological and pathophysiological processes work against each other, ultimately the former gains the upper hand (53). Mitochondrial dysfunction is a hallmark of age-related cardiovascular disease. In fact, the heart is a "muscle pump" that constantly has an extraordinarily high demand for adenosine triphosphate, which is why it has a high density of mitochondria (54). Sabbah et al. demonstrated that ARNis could ameliorate left ventricular mitochondrial dysfunction (55). However, there was no study demonstrating the role of ARNis in mitochondrial biogenesis, whereas previous research has shown that administration of ACEis increased mtDNA-CN (56, 57). Yet, a beneficial effect of ARNis or ACEis on myocardial mitochondrial biogenesis was not confirmed in our current study.

To verify our hypothesis that ARNis exert pro-arteriogenic effects *via* the bradykinin receptor signaling pathway, additional *in vitro* experiments were performed in this study. Because it was confirmed here that NEPis, rather than ARBs, promoted endothelial proliferation, the NEPi (Sacubitril) was analyzed for the possible stimulation of bradykinin receptors. Hence, in subsequent *in vitro* experiments, we verified our hypothesis that NEPis, like ACEis, exert their biological function on ECs through the bradykinin receptor signaling pathway. Here, we have shown for the first time that NEPis significantly promoted MHEC5-T proliferation, which can be abrogated by antagonists of bradykinin receptors. Thus, it can be demonstrated that NEPis exert pro-arteriogenic effects *via* the bradykinin receptor signaling pathway. In particular, since a stronger inhibition of cell proliferation was observed in the NEPi + BDKRB2i treatment group compared with the NEPi + BDKRB1i treatment group, BDKRB2 plays a greater role than BDKRB1 in NEPi-induced endothelial proliferation.

Vascular proliferation and migration play crucial roles in various contexts of arterial remodeling. The endothelium is a thin monocellular layer that lines the inner surface of the heart and blood vessels. As a receptor-effector, the endothelium has the property to respond to physical or chemical stimuli. It maintains vasomotor balance and vascular homeostasis by producing agonistic and antagonistic substances (58). Conversely, endothelial dysfunction is characterized by an imbalanced vasodilation and vasoconstriction (59). It has been demonstrated that endothelial dysfunction precedes atherosclerosis (60). Because atherosclerotic lesions result in the migration of vascular smooth muscle cells from the media to intima (61, 62), and endothelial integrity is maintained by replacement of damaged ECs (63), atherosclerosis is characterized by pathologic intimal thickening. In contrast, with regard to arteriogenesis, collateral arterioles undergo active outward remodeling, which is associated with wall thickening and lumen enlargement. Here, ECs proliferation and migration are essential for collateral artery formation. It is speculated that novel medications for cardiovascular disease may shift the process of pathologic atherosclerosis toward physiological arteriogenesis (64). Recent research has shown that arterial network expansion complemented collateral arterial development to recover from an ischemic insult, in which endothelial function plays an important role in arterial flow recovery (65, 66).

From bench to bedside, ARNis were used only for HF patients with reduced ejection fraction (HFrEF) at the very beginning after it appeared. On the positive side, the indications of ARNis were expanded for both HF with preserved ejection fraction (HFpEF) (approved by the U.S. Food and Drug Administration) (67) and hypertension (approved by the China Food and Drug Administration) (68) in 2021. In addition, results of the PARADISE-MI trial (n = 5661) showed that administration of ARNis reduced the composite outcome by 10% compared with ACEis, and provided additional clinical benefits in patients with acute MI (69). Meanwhile, results from another multi-center randomized control clinical trial conducted in China (n = 7556) showed that ARNis were superior to ACEis in reducing major adverse cardiovascular events after MI (70). Considering that our current study suggests that ARNis significantly facilitate coronary collaterals development, which is the most effective mechanism for maintaining stable blood perfusion after arterial stenosis or occlusion, ARNis may improve the prognosis of patients post-MI HF (tertiary prevention), or even reduce the incidence of new-onset MI (secondary prevention). More research is still needed to provide a rationale for the clinical efficacy and safety of ARNi in MI.

Conclusion

In summary, the results presented here indicate that (1) ARNis improve coronary collateral perfusion by stimulating arteriogenesis therapeutically. (2) NEPis promote endothelial proliferation *via* the bradykinin receptor signaling pathway.

Limitations

First, since our primary finding clearly showed that ARNis significantly increased coronary arteriogenesis, it would be supportive to demonstrate the increase in vessel lumen of collateral arteries angiographically. We have already

successfully verified the morphological features by visualizing angioarchitecture in a rat model of cerebral arteriogenesis (7, 47). However, anatomically, the situation of rat coronary collaterals is more complicated. Second, it would be more promising to evaluate the role of ARNis on coronary collateral perfusion by using the bradykinin receptor knock out mouse model. However, it is too challenging to perform microsurgery and set up ROP system in the heart of a mouse. Finally, because antibodies against some targets are not available, and the specificity of some antibodies has been controversial, the analysis of these targets at the translational level could only be partial.

Data availability statement

The original contributions presented in this study are included in this article/**Supplementary material**, further inquiries can be directed to the corresponding authors.

Ethics statement

The animal study was reviewed and approved by the State Office for Health and Social Affairs (Landesamt für Gesundheit und Soziales), Berlin, Germany.

Author contributions

All authors discussed and participated to draft, revise, and submit the manuscript.

Funding

This work was supported by the Faculty of Health Sciences Brandenburg (Fakultät für Gesundheitswissenschaften Brandenburg, FGW). The open-access publishing was funded by the Brandenburg Medical School Theodor Fontane (Medizinische Hochschule Brandenburg Theodor Fontane, MHB) publication funding supported by the German Research Foundation (Deutsche Forschungsgemeinschaft, DFG).

Conflict of interest

The authors declare that the research was conducted in the absence of any commercial or financial relationships that could be construed as a potential conflict of interest.

Publisher's note

All claims expressed in this article are solely those of the authors and do not necessarily represent those of their affiliated organizations, or those of the publisher, the editors and the reviewers. Any product that may be evaluated in this article, or claim that may be made by its manufacturer, is not guaranteed or endorsed by the publisher.

Supplementary material

The Supplementary Material for this article can be found online at: https://www.frontiersin.org/articles/10.3389/fcvm.2022.981333/full#supplementary-material

References

1. Lam C, Donal E, Kraigher-Krainer E, Vasan R. Epidemiology and clinical course of heart failure with preserved ejection fraction. *Eur J Heart Fail.* (2011) 13:18–28. doi: 10.1093/eurjhf/hfq121

2. Rubattu S, Triposkiadis F. Resetting the neurohormonal balance in heart failure (HF): the relevance of the natriuretic peptide (NP) system to the clinical management of patients with HF. *Heart Fail Rev.* (2017) 22:279–88. doi: 10.1007/s10741-017-9605-8

3. Díez J. Chronic heart failure as a state of reduced effectiveness of the natriuretic peptide system: implications for therapy. *Eur J Heart Fail.* (2017) 19:167–76. doi: 10.1002/ejhf.656

4. Hubers S, Brown N. Combined angiotensin receptor antagonism and neprilysin inhibition. *Circulation.* (2016) 133:1115–24. doi: 10.1161/circulationaha.115.018622

5. Hartupee J, Mann D. Neurohormonal activation in heart failure with reduced ejection fraction. *Nat Rev Cardiol.* (2017) 14:30–8. doi: 10.1038/nrcardio.2016.163

6. Hillmeister P, Persson P. The kallikrein-kinin system. *Acta Physiol (Oxf).* (2012) 206:215–9. doi: 10.1111/apha.12007

7. Hillmeister P, Gatzke N, Dülsner A, Bader M, Schadock I, Hoefer I, et al. Arteriogenesis is modulated by bradykinin receptor signaling. *Circ Res.* (2011) 109:524–33. doi: 10.1161/circresaha.111.240986

8. Buschmann I, Schaper W. Arteriogenesis versus angiogenesis: two mechanisms of vessel growth. *News Physiol Sci.* (1999) 14:121–5. doi: 10.1152/physiologyonline.1999.14.3.121

9. Persson A, Buschmann I. Vascular growth in health and disease. *Front Mol Neurosci.* (2011) 4:14. doi: 10.3389/fnmol.2011.00014

10. Schaper W. Therapeutic arteriogenesis has arrived. *Circulation.* (2001) 104:1994–5.

11. Hillmeister P, Nagorka S, Gatzke N, Dülsner A, Li K, Dai M, et al. Angiotensin-converting enzyme inhibitors stimulate cerebral arteriogenesis. *Acta Physiol (Oxf).* (2022) 234:e13732. doi: 10.1111/apha.13732

12. Erdös E, Tan F, Skidgel R. Angiotensin I-converting enzyme inhibitors are allosteric enhancers of kinin B1 and B2 receptor function. *Hypertension.* (2010) 55:214–20. doi: 10.1161/hypertensionaha.109.144600

13. Carrão A, Chilian W, Yun J, Kolz C, Rocic P, Lehmann K, et al. Stimulation of coronary collateral growth by granulocyte stimulating factor: role of reactive

oxygen species. *Arterioscler Thromb Vasc Biol.* (2009) 29:1817–22. doi: 10.1161/atvbaha.109.186445

14. Kersten J, McGough M, Pagel P, Tessmer J, Warltier D. Temporal dependence of coronary collateral development. *Cardiovasc Res.* (1997) 34:306–12. doi: 10.1016/s0008-6363(97)00019-9

15. Reinhardt C, Dalhberg S, Tries M, Marcel R, Leppo J. Stable labeled microspheres to measure perfusion: validation of a neutron activation assay technique. *Am J Physiol Heart Circ Physiol.* (2001) 280:H108–16. doi: 10.1152/ajpheart.2001.280.1.H108

16. Aptecar E, Teiger E, Dupouy P, Benvenuti C, Kern M, Woscoboinik J, et al. Effects of bradykinin on coronary blood flow and vasomotion in transplant patients. *J Am Coll Cardiol.* (2000) 35:1607–15. doi: 10.1016/s0735-1097(00)00583-0

17. Chu A, Morris K, Kuehl W, Cusma J, Navetta F, Cobb F. Effects of atrial natriuretic peptide on the coronary arterial vasculature in humans. *Circulation.* (1989) 80:1627–35. doi: 10.1161/01.cir.80.6.1627

18. Tesic M, Seferovic J, Trifunovic D, Djordjevic-Dikic A, Giga V, Jovanovic I, et al. N-terminal pro-brain natriuretic peptide is related with coronary flow velocity reserve and diastolic dysfunction in patients with asymmetric hypertrophic cardiomyopathy. *J Cardiol.* (2017) 70:323–8. doi: 10.1016/j.jjcc.2017.02.008

19. Bubb K, Aubdool A, Moyes A, Lewis S, Drayton J, Tang O, et al. Endothelial C-type natriuretic peptide is a critical regulator of angiogenesis and vascular remodeling. *Circulation.* (2019) 139:1612–28. doi: 10.1161/circulationaha.118.036344

20. Li N, Rignault-Clerc S, Bielmann C, Bon-Mathier A, Déglise T, Carboni A, et al. Increasing heart vascularisation after myocardial infarction using brain natriuretic peptide stimulation of endothelial and WT1(+) epicardial cells. *eLife.* (2020) 9:e61050. doi: 10.7554/eLife.61050

21. Pare G, Kubo M, Byrd JB, McCarty CA, Woodard-Grice A, Teo KK, et al. Genetic variants associated with angiotensin-converting enzyme inhibitor-associated angioedema. *Pharmacogenet Genomics.* (2013) 23:470–8. doi: 10.1097/FPC.0b013e328363c137

22. Bland N, Thomas J, Audsley N, Shirras A, Turner A, Isaac R. Expression of NEP2, a soluble neprilysin-like endopeptidase, during embryogenesis in *Drosophila melanogaster*. *Peptides.* (2007) 28:127–35. doi: 10.1016/j.peptides.2006.08.032

23. Buschmann I, Pries A, Styp-Rekowska B, Hillmeister P, Loufrani L, Henrion D, et al. Pulsatile shear and Gja5 modulate arterial identity and remodeling events during flow-driven arteriogenesis. *Development.* (2010) 137:2187–96. doi: 10.1242/dev.045351

24. Wolf K, Della Bruna R, Bruckschlegel G, Schunkert H, Riegger G, Kurtz A. Angiotensin II receptor gene expression in hypertrophied left ventricles of rat hearts. *J Hypertens.* (1996) 14:349–54. doi: 10.1097/00004872-199603000-00012

25. Ando S, Rahman M, Butler G, Senn B, Floras J. Comparison of candoxatril and atrial natriuretic factor in healthy men. Effects on hemodynamics, sympathetic activity, heart rate variability, and endothelin. *Hypertension.* (1995) 26(6 Pt 2):1160–6. doi: 10.1161/01.hyp.26.6.1160

26. Motwani J, Lang C, Cramb G, Struthers A. Natriuretic response to neutral endopeptidase inhibition is blunted by enalapril in healthy men. *Hypertension.* (1995) 25(4 Pt 1):637–42. doi: 10.1161/01.hyp.25.4.637

27. Gallinat S, Busche S, Raizada M, Sumners C. The angiotensin II type 2 receptor: an enigma with multiple variations. *Am J Physiol Endocrinol Metab.* (2000) 278:E357–74. doi: 10.1152/ajpendo.2000.278.3.E357

28. Wu L, Iwai M, Nakagami H, Li Z, Chen R, Suzuki J, et al. Roles of angiotensin II type 2 receptor stimulation associated with selective angiotensin II type 1 receptor blockade with valsartan in the improvement of inflammation-induced vascular injury. *Circulation.* (2001) 104:2716–21. doi: 10.1161/hc4601.099404

29. Habibi J, Aroor A, Das N, Manrique-Acevedo C, Johnson M, Hayden M, et al. The combination of a neprilysin inhibitor (sacubitril) and angiotensin-II receptor blocker (valsartan) attenuates glomerular and tubular injury in the Zucker Obese rat. *Cardiovasc Diabetol.* (2019) 18:40. doi: 10.1186/s12933-019-0847-8

30. Zhao Y, Ma R, Yu X, Li N, Zhao X, Yu J. AHU377+valsartan (LCZ696) modulates renin-angiotensin system (RAS) in the cardiac of female spontaneously hypertensive rats compared with valsartan. *J Cardiovasc Pharmacol Ther.* (2019) 24:450–9. doi: 10.1177/1074248419838503

31. Lear W, Ruzicka M, Leenen F. ACE inhibitors and cardiac ACE mRNA in volume overload-induced cardiac hypertrophy. *Am J Physiol.* (1997) 273(2 Pt 2):H641–6. doi: 10.1152/ajpheart.1997.273.2.H641

32. King S, Oparil S, Berecek K. Neuronal angiotensin-converting enzyme (ACE) gene expression is increased by converting enzyme inhibitors (CEI). *Mol Cell Neurosci.* (1991) 2:13–20. doi: 10.1016/1044-7431(91)90035-m

33. Schunkert H, Ingelfinger J, Hirsch A, Pinto Y, Remme W, Jacob H, et al. Feedback regulation of angiotensin converting enzyme activity and mRNA levels by angiotensin II. *Circ Res.* (1993) 72:312–8. doi: 10.1161/01.res.72.2.312

34. Ferrario C, Jessup J, Chappell M, Averill D, Brosnihan K, Tallant E, et al. Effect of angiotensin-converting enzyme inhibition and angiotensin II receptor blockers on cardiac angiotensin-converting enzyme 2. *Circulation.* (2005) 111:2605–10. doi: 10.1161/circulationaha.104.510461

35. Ocaranza M, Godoy I, Jalil J, Varas M, Collantes P, Pinto M, et al. Enalapril attenuates downregulation of Angiotensin-converting enzyme 2 in the late phase of ventricular dysfunction in myocardial infarcted rat. *Hypertension.* (2006) 48:572–8. doi: 10.1161/01.hyp.0000237862.94083.45

36. Santos R, Sampaio W, Alzamora A, Motta-Santos D, Alenina N, Bader M, et al. The ACE2/angiotensin-(1-7)/MAS axis of the renin-angiotensin system: focus on angiotensin-(1-7). *Physiol Rev.* (2018) 98:505–53. doi: 10.1152/physrev.00023.2016

37. Emilsson V, Gudmundsson E, Aspelund T, Jonsson B, Gudjonsson A, Launer L, et al. Antihypertensive medication uses and serum ACE2 levels: ACEIs/ARBs treatment does not raise serum levels of ACE2. *medRxiv* [Preprint]. (2020) doi: 10.1101/2020.05.21.20108738.

38. Deddish P, Marcic B, Tan F, Jackman H, Chen Z, Erdös E. Neprilysin inhibitors potentiate effects of bradykinin on b2 receptor. *Hypertension.* (2002) 39(2 Pt 2):619–23. doi: 10.1161/hy0202.103298

39. Ura N, Carretero O, Erdös E. Role of renal endopeptidase 24.11 in kinin metabolism in vitro and in vivo. *Kidney Int.* (1987) 32:507–13. doi: 10.1038/ki.1987.239

40. Ura N, Shimamoto K, Kuroda S, Nomura N, Iwata M, Aoyama T, et al. The role of kinins and atrial natriuretic peptide on the renal effects of neutral endopeptidase inhibitor in rats. *Clin Exp Hypertens.* (1994) 16:799–808. doi: 10.3109/10641969409078026

41. Nurmi L, Heikkilä H, Vapaatalo H, Kovanen P, Lindstedt K. Downregulation of bradykinin type 2 receptor expression in cardiac endothelial cells during senescence. *J Vasc Res.* (2012) 49:13–23. doi: 10.1159/000329615

42. Luo L, Rajpert-De Meyts E, Jung K, Diamandis E. Expression of the normal epithelial cell-specific 1 (NES1; KLK10) candidate tumour suppressor gene in normal and malignant testicular tissue. *Br J Cancer.* (2001) 85:220–4. doi: 10.1054/bjoc.2001.1870

43. Hu J, Lei H, Fei X, Liang S, Xu H, Qin D, et al. NES1/KLK10 gene represses proliferation, enhances apoptosis and down-regulates glucose metabolism of PC3 prostate cancer cells. *Sci Rep.* (2015) 5:17426. doi: 10.1038/srep17426

44. Haywood G, Gullestad L, Katsuya T, Hutchinson H, Pratt R, Horiuchi M, et al. AT1 and AT2 angiotensin receptor gene expression in human heart failure. *Circulation.* (1997) 95:1201–6. doi: 10.1161/01.cir.95.5.1201

45. Wang J, Li N, Gao F, Song R, Zhu S, Geng Z. Balance between angiotensin converting enzyme and angiotensin converting enzyme 2 in patients with chronic heart failure. *J Renin Angiotensin Aldosterone Syst.* (2015) 16:553–8. doi: 10.1177/1470320315576257

46. Dell'Italia L, Oparil S. Bradykinin in the heart: friend or foe? *Circulation.* (1999) 100:2305–7. doi: 10.1161/01.cir.100.23.2305

47. Buschmann I, Busch H, Mies G, Hossmann K. Therapeutic induction of arteriogenesis in hypoperfused rat brain via granulocyte-macrophage colony-stimulating factor. *Circulation.* (2003) 108:610–5. doi: 10.1161/01.cir.0000074209.17561.99

48. Buschmann I, Hoefer I, van Royen N, Katzer E, Braun-Dulleaus R, Heil M, et al. GM-CSF: a strong arteriogenic factor acting by amplification of monocyte function. *Atherosclerosis.* (2001) 159:343–56. doi: 10.1016/s0021-9150(01)00637-2

49. Kovacic J, Muller D, Graham R. Actions and therapeutic potential of G-CSF and GM-CSF in cardiovascular disease. *J Mol Cell Cardiol.* (2007) 42:19–33. doi: 10.1016/j.yjmcc.2006.10.001

50. Anzai A, Choi J. The infarcted myocardium solicits GM-CSF for the detrimental oversupply of inflammatory leukocytes. *J Exp Med.* (2017) 214:3293–310. doi: 10.1084/jem.20170689

51. Duelsner A, Gatzke N, Glaser J, Hillmeister P, Li M, Lee E, et al. Granulocyte colony-stimulating factor improves cerebrovascular reserve capacity by enhancing collateral growth in the circle of Willis. *Cerebrovasc Dis.* (2012) 33:419–29. doi: 10.1159/000335869

52. Grundmann S, Hoefer I, Ulusans S, Bode C, Oesterle S, Tijssen J, et al. Granulocyte-macrophage colony-stimulating factor stimulates arteriogenesis in a pig model of peripheral artery disease using clinically applicable infusion pumps. *J Vasc Surg.* (2006) 43:1263–9. doi: 10.1016/j.jvs.2006.02.049

53. Hillmeister P, Buschmann E, Persson P, Bondke Persson A. Exercise for healthy flow. *Acta Physiol (Oxf).* (2017) 219:3–8. doi: 10.1111/apha.12831

54. Moslehi J, DePinho R, Sahin E. Telomeres and mitochondria in the aging heart. *Circ Res.* (2012) 110:1226–37. doi: 10.1161/circresaha.111.246868

55. Sabbah H, Zhang K, Gupta R, Xu J, Singh-Gupta V. Effects of angiotensin-neprilysin inhibition in canines with experimentally induced cardiorenal syndrome. *J Card Fail.* (2020) 26:987–97. doi: 10.1016/j.cardfail.2020.08.009

56. Ederer K, Jin K, Bouslog S, Wang L, Gorman G, Rowe G, et al. Age- and genotype-specific effects of the angiotensin-converting enzyme inhibitor lisinopril on mitochondrial and metabolic parameters in *Drosophila melanogaster*. *Int J Mol Sci.* (2018) 19:3351. doi: 10.3390/ijms19113351

57. Ferder L, Inserra F, Romano L, Ercole L, Pszenny V. Effects of angiotensin-converting enzyme inhibition on mitochondrial number in the aging mouse. *Am J Physiol.* (1993) 265(1 Pt 1):C15–8. doi: 10.1152/ajpcell.1993.265.1.C15

58. Esper R, Nordaby R, Vilariño J, Paragano A, Cacharrón J, Machado R. Endothelial dysfunction: a comprehensive appraisal. *Cardiovasc Diabetol.* (2006) 5:4. doi: 10.1186/1475-2840-5-4

59. Gallo G, Volpe M, Savoia C. Endothelial dysfunction in hypertension: current concepts and clinical implications. *Front Med (Lausanne).* (2021) 8:798958. doi: 10.3389/fmed.2021.798958

60. Gimbrone M Jr., García-Cardeña G. Endothelial cell dysfunction and the pathobiology of atherosclerosis. *Circ Res.* (2016) 118:620–36. doi: 10.1161/circresaha.115.306301

61. Schwartz S, Ross R. Cellular proliferation in atherosclerosis and hypertension. *Prog Cardiovasc Dis.* (1984) 26:355–72. doi: 10.1016/0033-0620(84)90010-0

62. Intengan H, Schiffrin E. Vascular remodeling in hypertension: roles of apoptosis, inflammation, and fibrosis. *Hypertension.* (2001) 38(3 Pt 2):581–7. doi: 10.1161/hy09t1.096249

63. Itoh Y, Toriumi H, Yamada S, Hoshino H, Suzuki N. Resident endothelial cells surrounding damaged arterial endothelium reendothelialize the lesion. *Arterioscler Thromb Vasc Biol.* (2010) 30:1725–32. doi: 10.1161/atvbaha.110.207365

64. Li K, Zemmrich C, Bramlage P, Persson A, Sacirovic M, Ritter O, et al. Effect of ACEI and ARB treatment on nitric oxide-dependent endothelial function. *Vasa.* (2021) 50:413–22. doi: 10.1024/0301-1526/a000971

65. Craps S, Van Wauwe J, De Moudt S, De Munck D, Leloup A, Boeckx B, et al. Prdm16 supports arterial flow recovery by maintaining endothelial function. *Circ Res.* (2021) 129:63–77. doi: 10.1161/circresaha.120.318501

66. Kumar S, Andueza A, Jo H. Is endothelial dysfunction a therapeutic target for peripheral artery disease?: PRDM16 is going out on a limb. *Circ Res.* (2021) 129:78–80. doi: 10.1161/circresaha.121.319448

67. Novartis. *Novartis Entresto® Granted Expanded Indication in Chronic Heart Failure by FDA*. (2021). Available online at: https://www.novartis.com/news/media-releases/novartis-entresto-granted-expanded-indication-chronic-heart-failure-fda (accessed February 16, 2021).

68. Novartis. *Novartis Entresto® Indicated for Treatment of Hypertension in China*. (2021). Available online at: https://www.novartis.com/news/novartis-entresto-indicated-treatment-hypertension-china (accessed June 10, 2021).

69. Pfeffer M, Claggett B, Lewis E, Granger C, Køber L, Maggioni A, et al. Impact of sacubitril/valsartan versus ramipril on total heart failure events in the PARADISE-MI trial. *Circulation.* (2022) 145:87–9. doi: 10.1161/circulationaha.121.057429

70. She J, Lou B, Liu H, Zhou B, Jiang G, Luo Y, et al. ARNI versus ACEI/ARB in reducing cardiovascular outcomes after myocardial infarction. *ESC Heart Fail.* (2021) 8:4607–16. doi: 10.1002/ehf2.13644

Frontiers in
Cardiovascular Medicine

Innovations and improvements in cardiovascular treatment and practice

Focuses on research that challenges the status quo of cardiovascular care, or facilitates the translation of advances into new therapies and diagnostic tools.

Discover the latest Research Topics

See more →

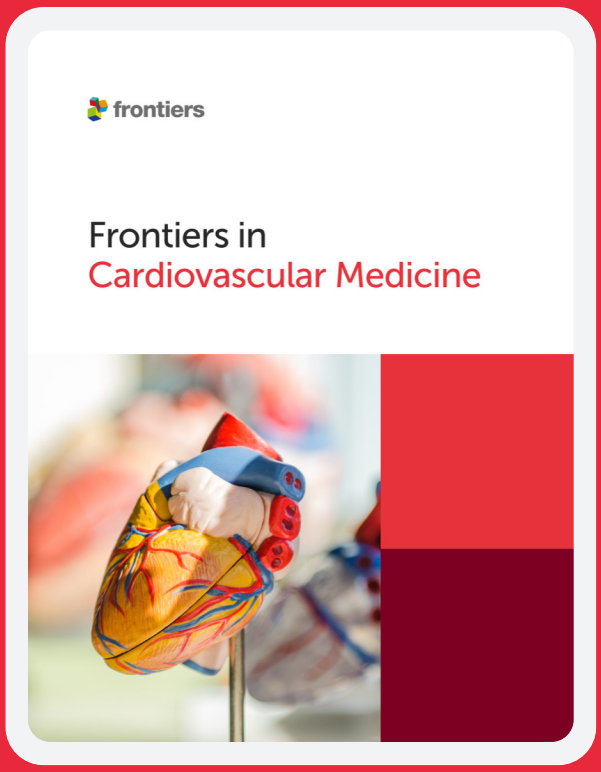

Frontiers

Avenue du Tribunal-Fédéral 34
1005 Lausanne, Switzerland
frontiersin.org

Contact us

+41 (0)21 510 17 00
frontiersin.org/about/contact